Including stochastic rainfall distributions in a probabilistic modelling approach for compound flooding due to tropical cyclones

A case study for Houston, Texas

D.J. Bader

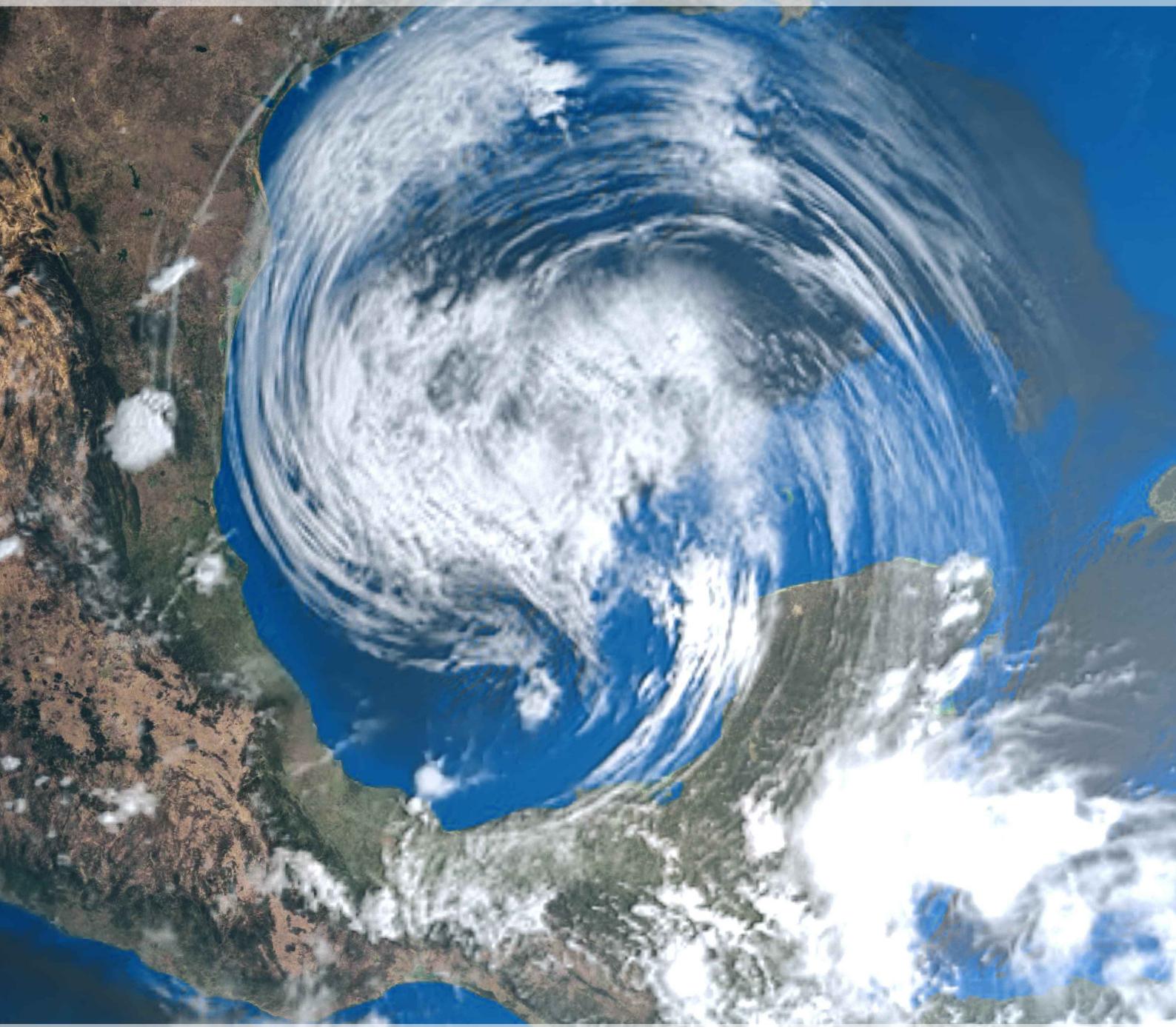

TU Delft Delft University of Technology

Deltares Enabling Delta Life

Including stochastic rainfall distributions in a probabilistic modelling approach for compound flooding due to tropical cyclones

A case study for Houston, Texas

by

D. J. (Daan) Bader

In partial fulfilment of the requirements for the degree of

Master of Science
in Hydraulic Engineering

at the Delft University of Technology (TU Delft),
to be defended publicly on Wednesday September 25, 2019 at 14:00h.

Student number:	4288335	
Project duration:	October 2018 - September 2019	
Chair committee:	Prof. dr. ir. S. G. J. Aarninkhof,	Delft University of Technology
Thesis committee:	Prof. dr. ir. M. Kok,	Delft University of Technology
	Dr. ir. J. D. Bricker,	Delft University of Technology
	Dr. A. G. Sebastian,	Texas A&M University
	Ir. C. M. Nederhoff,	Deltares USA
	Ir. T. W. B. Leijnse,	Deltares

An electronic version of this thesis is available at
`http://repository.tudelft.nl/`.

Cover:
Detailed and realistic high resolution 3D illustration of a hurricane approaching Texas.

TU Delft Delft University of Technology

Deltares
Enabling Delta Life

Acknowledgements

This MSc. thesis concludes six years as a student at the Delft University of Technology. Last year, I have spend working on this MSc. thesis research. Now, the moment is finally there that I am graduating as a Coastal Engineer. In these acknowledgments I want to thank the people that supported me over the last few years and contributed to making my life as a student amazing!

First of all, I want to thank Deltares for giving me the opportunity to carry out this thesis at their office. They provided me with the tools and working environment that I needed to make the most of this project. I want to thank Tim Leijnse and Kees Nederhoff specifically. As daily supervisors, they provided me with all kinds of ideas and suggestions. They always made time to answer any questions I had, even when there was an ocean between us! Furthermore, I would like to thank my fellow students at Deltares for many 'bakkies' and discussions, both relevant and irrelevant.

I also want to thank the people from Delft University of Technology. Stefan Aarninkhof, Jeremy Bricker and Matthijs Kok provided me with useful insights, feedback and a critical view on my work. The meetings we had were very fruitful, formal and efficient, but at the same time very entertaining.

Moreover, I want to thank the professors and students at the Department of Civil and Environmental Engineering at Rice University. I took the opportunity to carry out part of this research in Houston. I want to give special thanks to Antonia Sebastian, she was the one initiating this visit! She put a lot of effort into this trip and was ready for questions and field visits at every moment of time. Furthermore, I want to mention my American house mates Ferne and Danielle for making my time in Texas great!

Lastly, I would like to thank my family and friends for the shared moments over the past six years. I met many people during my time in Delft, you guys definitely made my time as a student better than I could ever wished for. During this research I had my ups and downs, but my friends and family pulled me through. Special thanks to Charlotte, for all her feedback on my report and for all the discussions and talks we had concerning my thesis topic.

So, this is the report that concludes my time in Delft. Being student at Delft University of Technology offered me amazing opportunities, like traveling to Australia and the USA. But now, I am ready to close this chapter of my life and ready for the next steps of my career in the field of Civil Engineering. Enjoy reading!

D. J. (Daan) Bader
Delft, September 2019

Abstract

Tropical Cyclones impose great threats on coastal settlements, in terms of hazard and impact. Recent examples, like Hurricane Barry (New Orleans, 2019) and Typhoon Idai (Mozambique, 2019), emphasize the global character of this threat. In 2017, Hurricane Harvey tied with Hurricane Katrina as costliest Tropical Cyclone on record in the United States, inflicting up to 125 billion United States Dollars of damage. Extreme rainfall of up to 1,500 millimeters in six days, in combination with surge and high river discharges, caused flooding of up to one third of Houston.

Current generation coastal flood early warning systems are often not designed to account for the combined effects of pluvial, fluvial and marine flooding (e.g. the ADCIRC + SWAN model deployed by the Coastal Emergency Risks Assessment group ignores pluvial flooding). Moreover, the advanced models applied in these systems are computationally demanding and can therefore not be used in probabilistic real-time forecasting applications in order to include uncertainty in meteorological conditions. Furthermore, current probabilistic modelling approaches, like the flood plain maps derived by the Flood Emergency Management Agency, do not always account for all components of compound flooding.

In this research, a framework is proposed to carry out an efficient probabilistic flood risk study to assess the joint probability of pluvial, fluvial and marine flooding. The semi-advanced SFINCS model is used for the hydrodynamic assessment. SFINCS includes all components of compound flooding and furthermore optimizes the computational demand. Moreover, the Delft-FIAT model is used to make an exposure assessment in terms of damage and affected people. Delft-FIAT is based on the unit loss methodology, which relates flood quantities to damage at unit level. This tool translates hydrodynamic values to social values in a matter of minutes, which could be useful for policy- and decision-makers. The main research question answered in this study is phrased as follows:

How can a probabilistic flood risk study, including stochastic rainfall distributions, for compound flooding due to Tropical Cyclones be executed?

The focus of this study is on the city of Houston, Texas. First, a SFINCS model validation study is carried out for the flooding due to Hurricane Harvey (2017) in terms of hydrodynamics and exposure. Secondly, a generic parametric observation-based rainfall model is derived, to enable the creation of a spatial rainfall field. Current TC precipitations models are either computationally heavy, or dependent on many parameters, which are not always available in archives. Furthermore, these rainfall models are not always applicable a priori. An observation-based parametric rainfall model is a useful tool to carry out a climate variability study including pluvial flooding. The last line of research is a climate variability assessment for the city of Houston. Here, synthetic Tropical Cyclones are created by the TCWiSE tool, offshore water levels for each of the generated storms are generated by a Delft3D-FM model. Subsequently, the hydrodynamic and exposure assessment are carried out by SFINCS and Delft-FIAT respectively.

For the validation study a SFINCS model is setup to assess the model performance for Hurricane Harvey. Observed offshore water levels, a spatial rainfall field and the reservoir release are forced on a 25-meter resolution model. The model is capable of reproducing water level time-series at 21 United States Geological Survey observation points with good accuracy. For a lower resolution model (100 meters) peak water levels are still reproduced with similar accuracy. However, the full details of the flood wave are no longer captured. This shows that a low resolution model can be used to assess maximum water levels in a probabilistic climate variability study. Moreover, the damage, as assessed by Delft-FIAT, overestimates reported damage to great extent. This is because of the use of global datasets, a generalized depth-damage curve and no value-difference between commercial, industrial or residential buildings.

To parametrize Tropical Cyclone rainfall using main characteristics of Tropical Cyclones, a bivariate analysis method is applied to the QSCAT-R dataset. The QSCAT-R dataset contains over 8,000 independent (oceanic) observations of Tropical Cyclones of all over the world during the period of 1999 to 2009. The bivariate analysis leads to fitting of a Frank Copula to the observations of maximum rainfall intensity and maximum sustained wind speed. Opposite to least-square fitting procedures, a copula offers the opportunity to retrieve statistics like the median and confidence interval bands. Usage of a conditional sampling method indicates that the sampled maximum rainfall intensities for low maximum sustained wind speeds show close resemblance with the data. With the acquired maximum rainfall intensity, a fitting procedure similar to the Holland wind profile is used to create a radial rainfall rate profile. The long tail of this exponential profile seems to overestimate rainfall rates at large radii from the Tropical Cyclone's eye. A solution is proposed to set all rainfall rates lower than 10 mm/hr (in the radial rainfall profile) equal to zero. This causes the radial rainfall profile to be more restricted, because these lower values are mostly observed at large radii. However, further research into this adjustment is necessary, because this adjustment is based on a variability study for Hurricane Harvey only.

Subsequently, a model train is setup to execute a climate variability assessment for the city of Houston. A combination of TCWiSE (track generation tool), Delft3D-FM (large-scale circulation model), SFINCS and Delft-FIAT is used to assess flood risk for Houston. Moreover, the parameterized rainfall model is used to generate Tropical Cyclone rainfall. To further improve the underlying statistics of historical hurricanes, the TCWiSE tool generates synthetic hurricane tracks based on historical data and a Monte Carlo sampling method. The generated hurricanes can be forced upon the Delft3D-FM and SFINCS model and further analyzed with Delft-FIAT. The model train is capable of carrying out a flood risk assessment, derive flood maps for given return periods (e.g. 1 in 100-year flood) and make an exposure assessment for the joint occurrence of pluvial, fluvial and marine flooding. Currently, the proposed model could be improved in terms of computational efficiency.

The main result of the probabilistic flood risk assessment is that Houston is very prone to compound flooding due to Tropical Cyclones. The 1 in 100-year flood plain as delineated by the Flood Emergency Management Agency underestimates the extent of a 1 in 100-year flooding as derived in this study. This research shows that the spatial rainfall distribution is an important component in assessing compound flooding events. Furthermore, the annual expected damage for Houston is 8.6 billion United States Dollars and 500,000 people are expected to be affected annually.

This first framework for assessing the joint probability of pluvial, fluvial and marine flooding due to Tropical Cyclones shows that the semi-advanced model SFINCS is capable of assessing flood risk for coastal communities. Furthermore, with Delft-FIAT the translation from hydrodynamic values to social values is carried out within minutes. This framework could therefore be important for inland flooding modellers, policy- and decision-makers.

Contents

Acronyms and Abbreviations

Acronym / Abbreviation	Description
AIC	Akaike Information Criterion
AoI	Area of Interest
BIC	Bayesian Information Criterion
BTD	Best Track Data
CDF	Cumulative Distribution Function
CRM	Coastal Relief Model
CVA	Climate Variability Assessment
Delft-FIAT	Flood Impact Assessment Tool
Delft3D-FM	Delft3D Flexible Mesh
DEM	Digital Elevation Model
EAAP	Expected Annual Affected People
EAD	Expected Annual Damage
ETM	Empirical Track Model
FEMA	Federal Emergency Management Agency
HWM	Highwatermarks
LFP	LISFLOOD-FP
PHRaM	Parametric Hurricane Rainfall Model
MAE	Mean Absolute Error
MSR	Modified Smith for Rainfall
MvCAT	Multi-variate Copula Analysis Toolbox
NED	National Elevation Dataset
NMSE	Normalized Mean Square Error
NOAA	National Oceanic and Atmospheric Administration
NRMSE	Normalized Root Mean Square Error
NSE	Nash Sutcliffe model Efficiency
PDF	Probability Density Function
pmax	Maximum Rainfall Intensity
QSCAT-R	QuikSCAT Tropical Cyclone Radial Structure
R35	Radius at the 35 knots wind speed
R-CLIPER	Rainfall-CLImatology and PERsistance
RMSD	Root Mean Square Difference
RMSE	Root Mean Square Error
RMW	Radius of Maximum Winds
SFINCS	Super-Fast INundation of CoastS
SLOSH	Sea, Lake and Overland Surges from Hurricanes
STM	Simple Track Model
TC	Tropical Cyclone
TCWiSE	Tropical Cyclone Wind Statistical Estimation
TRaP	Tropical Rainfall Potential
TX	Texas
USA	United States of America
USACE	United States Army Corps of Engineers
USD	United States Dollars
USGS	United States Geological Survey
UTC	Coordinated Universal Time
vmax	Maximum Sustained Wind Speed

1 Introduction

1.1. Context

Tropical Cyclones (TCs) are natural hazards, which are known for their destructive character. A TC imposes great threats on coastal communities in terms of hazard and impact, through extreme sustained wind speeds, surge and heavy precipitation. A fully developed TC covers a broad spectrum of wind speeds and can cause damage from uprooting trees to wiping away entire buildings. Recent TCs, like Hurricane Barry (New Orleans, 2019) and Typhoon Idai (Mozambique, 2019), emphasize the increasing impact and global character of this natural phenomenon. During the 2017 Atlantic Hurricane Season, Hurricane Harvey tied with Hurricane Katrina as costliest storm ever recorded by the National Oceanic and Atmospheric Administration (NOAA), inflicting up to 125 billion United States Dollars (USD) in damage (NOAA, 2018a). In the same hurricane season, Hurricane Maria (2017) and Hurricane Irma (2017) entered as third and fifth costliest hurricanes ever recorded in the United States of America (USA).

Reported damage values refer to a combination of damage due to extreme wind speed (e.g. damage to roofs) and damage due to (compound) flooding. Compound flooding is defined as flooding due to a combination of marine, fluvial and pluvial components (Wahl et al., 2015), see Figure 1.1. Wave-driven flooding is not included in this research. Different combinations of these components can lead to flooding. For example, landfall of Hurricane Katrina (2015) caused flooding due to the simultaneous occurrence of storm surge and high tidal water levels in New Orleans. Another example is Hurricane Harvey (2017), which hovered over the state of Texas for six days. Most of Houston experienced over 700 millimeters (mm) of rainfall during this time, with extreme observations in Texas of almost 1,500 mm (van Oldenborgh et al., 2017).

The impact of TCs on coastal settlements is likely to increase into the future. Development and utilization of coastal zones will lead to socio-economic and environmental changes in the upcoming years (Neumann et al., 2015). The shift of population from non-coastal zones to coastal-zones induces an increase of exposed objects and therefore an increase in damage during compound flooding events in the future (Pielke Jr. et al., 2008). Several studies have also found that the risk of compound flooding is likely to increase in the future due to sea-level rise and an increase of intensity of TCs (Emanuel, 2013; Knutson et al., 2015; Wahl, 2017). This increase in hazard, combined with increasing exposure will potentially lead to higher reported damages from future storms.

To enable for living safely along coasts, there is need to effectively protect against marine, pluvial and fluvial threats. Design and management procedures have become more complex and require an integrated approach. For this purpose, multiple types of modelling software have been developed. Current modelling approaches are able to reproduce a compound flooding event to great detail in a hind-casting study. Therefore, this approach can be used to draw conclusions for design and management procedures based on a single simulation. However, the computational efficiency of current models is low, and therefore their application in probabilistic risk-based studies is limited.

The Federal Emergency Management Agency (FEMA) produces maps that indicate the current coastal flood hazard areas in the USA. These maps provide for setting insurance rates and enable communities to develop flood plain management regulations like zoning and emergency management. Risk of flooding is visualized in flood plain maps for the 100-year and 500-year return period flood. These flood plain domains are based on historic storms and do not account for future developments like climate change and increase in TC intensity (FirstStreetFoundation, 2019). Furthermore, the maps are mostly based on coastal flooding, because of the limited attention given to the importance of pluvial and fluvial flooding. As a result, the fluvial and pluvial flooding delineated maps are not available for all areas (Wing et al., 2018). Moreover, the FEMA flood zone maps are of varying age and quality (HomelandSecurity, 2017). This means that communities who rely on these maps could be more flood-prone than expected. Another example of the current approach for flood early warning systems is the ADCIRC + SWAN (Simulating WAves Nearshore) model deployed by the Coastal Emergency Risks Assessment group. This system is not capable of taking into account the combined effects of fluvial, pluvial and marine flooding, because it ignores flooding due to rainfall. However, recent TCs like Typhoon Idai and Hurricane Harvey show that rainfall is an important element in flooding events. In short, current flood risk assessment methodologies lack the computational efficiency or do not account for all aspects of compound flooding.

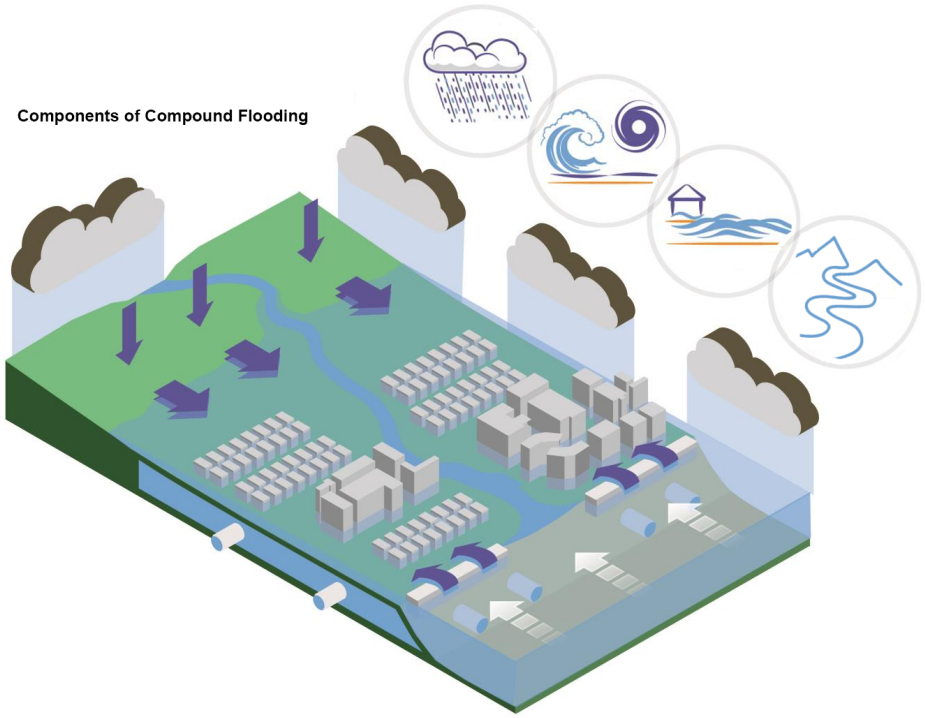

Figure 1.1: Schematic representation of compound flooding. The circles represent (from left to right): precipitation, surge, tides and river discharge. Modified from City of Fort Lauderdale (2018).

1.2. Complication

The before-mentioned examples of Hurricane Katrina and Hurricane Harvey show that different types of forcing can each result in flooding of coastal communities. However, it is also possible that different types of forcing occur at the same moment. This so-called compound flooding can increase the impact of TCs drastically. At the same time, it is not known beforehand which forcing is dominant. For modelling-purposes it is therefore required to include all types of forcing to be able to perform an accurate flood risk assessment.

Current modelling approaches are not suited for this accurate and correct flood risk assessment for various reasons. The simplistic models (i.e. static) are unable to incorporate all types of forcing (with reasonable accuracy). The advanced models are capable of implementing all before-mentioned types of forcing, but this results in a high computational demand. Consequently, the use of these models in a probabilistic assessment

is limited. For this reason, more recent modelling approaches focus on the development of semi-advanced models. An example is the Super-Fast INundation of CoastS (SFINCS) model, which, in a way, is a merger between the two previously mentioned modelling approaches. This model can include different types of forcing, while at the same time optimizing computational demands. SFINCS can be up to two magnitudes faster than an advanced model (e.g. Delft3D (Lesser et al., 2004)), while producing similar hydrodynamic performance (Leijnse, 2018). The SFINCS model shows potential to serve as an operational hazard assessment system and to carry out probabilistic flood risk assessments (i.e. Climate Variability Assessment (CVA)).

A TC can be described by a spatial wind field, a spatial pressure field, a spatial precipitation field and the TC track. When track and intensity of an individual TC are known, spatial surface wind speeds and spatial atmospheric pressure can be reproduced with relatively simple parametric wind models (e.g. Holland et al. (2010)). However, for precipitation, no empirical (stochastic) relationship exists that describes the amount of rainfall as a function of a TC parameter (e.g. intensity, storm motion). Recent events (e.g. Hurricane Harvey (2017)) show the importance of rainfall for events of inland flooding. Developing a basic parametric precipitation field model could contribute to further improvement of current modelling approaches and their computational efficiency. Existing precipitation models use, for example, computationally heavy climate models, which are not suited for a computational efficient probabilistic modelling approach. Furthermore, more computational efficient methods proposed in literature are often dependent on many parameters, which are not frequently available in archives (e.g. Snaiki and Wu (2017)).

1.3. Research Objective

The aim of this research is to develop a methodology, which enables the quick assessment of impact and hazard of compound flooding due to TCs. This is done by assessing the joint probability of pluvial, fluvial and marine components of flooding. By using a semi-advanced numerical model in combination with a large scale circulation model, the influence of different (synthetic) tracks and varying rainfall characteristics is determined in a probabilistic climate variability study. The research objective has been converted into the following main research question:

How can a probabilistic flood risk study, including stochastic rainfall distributions, for compound flooding due to Tropical Cyclones be executed?

The main research question is supported by means of three lines of research:

1. How accurate can SFINCS reproduce the compound flooding event in Houston as a result of the arrival of Hurricane Harvey in terms of hazard and impact?
2. How can the spatial rainfall distribution of a Tropical Cyclone be parametrized using the main characteristics of a Tropical Cyclone?
3. What is the result of a climate variability study for Houston when using synthetic Tropical Cyclone tracks and a schematization of Tropical Cyclone rainfall?

1.4. Outline

Chapter 2 contains an overview of the literature review. This includes definitions of flood risk, an overview of important meteorological and hydrodynamic processes during TCs and a short description of currently available modelling approaches. Chapter 3 sets out the case study and its results, which is used for the validation of the SFINCS model. Hurricane Harvey, which made landfall in 2017, serves as a case study. Chapter 4 presents the derivation of the stochastic observation-based parametric rainfall model. In Chapter 5, the schematization of the precipitation is applied in a climate variability study for Houston in combination with synthetically generated hurricane tracks. This chapter shows the results of this climate variability study. Chapter 6 contains an overview of the limitations of the used methods and acquired results in a discussion. In Chapter 7, the main conclusions of this research are summarized. This chapter is concluded with an overview of potential future research suggestions.

2

Literature Review

This literature review addresses four main elements. In Section 2.1, the basic definitions of flood risk are given. In Section 2.2, the main meteorological processes during TCs are described: wind and atmospheric pressure, hurricane tracks and precipitation. In Section 2.3, the main hydrodynamic processes during TCs are presented: offshore processes, near-shore processes and hinterland processes. In Section 2.4 the currently available inland flooding modelling approaches are discussed, as well as a short description of the SFINCS model.

2.1. Definition of Flood Risk

Risk is a term that is prone to various interpretations. For this research a consistent definition is defined based on (Kron, 2005). Here, the term flood risk is described as follows:

$$"Risk = Hazard \cdot Exposure \cdot Vulnerability" \tag{2.1}$$

This relationship is adapted by other studies (e.g. Jongman et al. (2014)) and organizations, for example the Intergovernmental Panel on Climate Change. The exact definitions for the different elements in Equation 2.1 of Kron (2005) have been slightly adjusted by Field et al. (2012):

- Hazard is the potential occurrence of a natural disaster event, which could cause damage, harm and losses (Field et al., 2012). An example is a flood hazard map;
- The total of people, infrastructure, social or economic assets and environmental services which are present and, simultaneously, can possibly be affected by a natural hazard is defined as exposure. Thus, they can cause potential damage, harm and losses (Field et al., 2012); and
- Vulnerability represents the extent to which an exposed element can be affected by a natural disaster. This includes the characteristics of an element (e.g. person, group, building) and its situation. So vulnerability is the extent to which behavior, anticipation, resistance and recovery are affected from the effects of a natural disaster.

Table 2.1: Different types of damage. Courtesy of Merz et al. (2010)

Damage Type	Examples
Direct, tangible	Damage to buildings and infrastructure. Costs for clean-up.
Direct, intangible	Loss of life, damage to ecosystems.
Indirect, tangible	Costs of disruption of public services and traffic.
Indirect, intangible	Loss of trust in authorities, trauma.

Flood risk can be quantified with the amount of exposed elements. Per definition, the exposure components encompass all flood impact on exposed elements in the flooded area (Field et al., 2012). This includes both direct and indirect damages, see Table 2.1. Damages related to direct contact with flood water are defined as direct damages. Indirect damages are the result of losses outside of the flood event itself, for example the impact of loss of electricity in the area. If damage can be expressed in a monetary value, it is referred to as a tangible damage, else an intangible damage (Merz et al., 2010). Direct damages are quantifiable, therefore this research focuses on direct tangible damages.

2.2. Meteorological Processes during Tropical Cyclones

In this section the main meteorological processes related to TCs are discussed. Section 2.2.1 discusses wind and atmospheric pressure. Section 2.2.2 explains TC tracks. Subsequently, Section 2.2.3 discusses the rainfall patterns resulting from TCs. Each section consists out of the following components: a short introduction, underlying theory and existing models which apply this theory.

2.2.1. Wind and Atmospheric Pressure

TCs are known to be low-pressure systems, in which the pressure drops to significantly lower values compared to the atmospheric pressure (Zehnder, 2018). This pressure drop initiates a hydrodynamic response underneath the eye of the TC, because it can cause temporary sea water level rise (i.e. surge). This is discussed in Section 2.3.1. TCs tend to be more intense when having a larger central pressure deficit. At the same time, hurricane intensity is linked with the sustained wind speeds. Mean sustained winds are wind speeds that are averaged over certain time-scales (e.g. 1-minute average) and measured at certain altitudes (e.g. the 10-meter wind speed) by buoys or weather stations. In the USA, the mean measured wind speed is related to the intensity of a TC by means of the Saffir-Simpson Hurricane Wind Scale as presented in Table 2.2. An increase in rank on the Saffir-Simpson Scale is equal to a factor four increase of the total damage (Pielke Jr. et al., 2008). However, the damage scale only addresses wind speeds, and does therefore not account for other TC threats, like storm surge and precipitation (i.e. flooding)

Table 2.2: Saffir-Simpson Hurricane Wind Scale in kilometers per hour (km/h). Modified from Schott et al. (2012).

Category	Wind speed [km/h]	Damage
1	119-153	Some damage
2	154-177	Extensive damage
3 (major)	178-208	Devastating damage
4 (major)	209-241	Catastrophic damage
5 (major)	> 252	Catastrophic damage

Wind and atmospheric pressure deficit are two meteorological processes connected to a TC. The two processes have a dependency. Chavas et al. (2017) state that pressure drop is a function of maximum sustained wind speeds, storm dimensions and latitude. The following sections discuss background theory on wind-pressure relationships and subsequently the models which apply the theory.

Theory Knaff and Zehr (2007) identify five basic factors that can influence the connection between wind and pressure. Similar to Chavas et al. (2017), they identify storm size and latitude. Furthermore, environmental pressure, storm motion and intensification trends are recognized as influential parameters.

As previously mentioned and substantiated by other studies, a decrease in environmental pressure leads to an increase of the maximum surface wind speeds. Knaff and Zehr (2007) show a linear fit between the two parameters, indicating a positive dependency. Moreover, the effect of the storm motion has been identified by Schwerdt et al. (1979). Faster storm translation has shown to be accompanied by larger maximum surface wind speeds. The influence of these two effects on the wind-pressure relationship however, is limited (Knaff and Zehr, 2007). At the same time, the effect of the position on Earth is of larger influence. As latitude increases, the Coriolis force tends to increase as well. The result is that lower tangential winds are needed to balance the gradient of the pressure force. Thus, storms with an equal radial wind profile have lower pressures at higher latitudes. In other words, for a given maximum sustained wind speed, a TC at low latitude has a higher pressure deficit, compared to a TC at a high latitude (Holland, 2008; Knaff and Zehr, 2007).

According to the gradient in wind balance, larger TCs tend to have a smaller maximum surface wind speed value for a given drop in pressure. In other words, the pressure gradient is distributed over larger radial distance. Thus, this indicates that storm dimensions do influence the wind-pressure relationship (e.g. Willoughby and Rahn (2004)). Knaff and Zehr (2007) use the R35 (radius at the 35 knots (kt) wind speed) as a dimension parameter to substantiate this hypothesis. However, this quantity is difficult to measure during field observations (Holland, 2008) and therefore not frequently available in archives. This is the reason that in model schematizations the impact of this parameter is neglected most of the time. The effect is significant, espe-

cially for the difference between large storms and smaller storm sizes (see Figure 2.1). At higher maximum surface winds (V_{srm} > 100 kt) however, a slight discontinuity can be noticed. This is related to the mean latitude of high intensity storms, which also influences wind-pressure relationships (Knaff and Zehr, 2007).

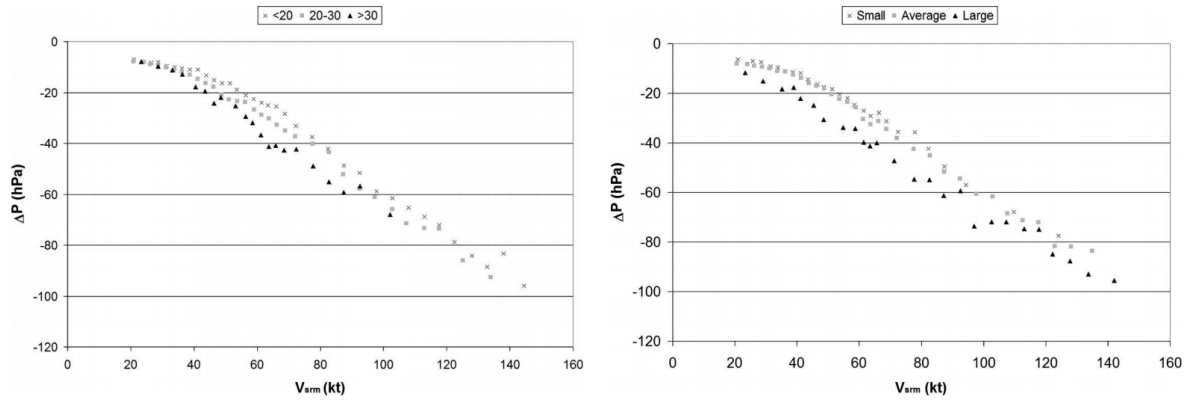

Figure 2.1: Plots of the pressure deficit (ΔP) and the maximum surface winds (V_{srm}) for left) three latitude-scales, right) three storm size quantities. Courtesy of Knaff and Zehr (2007).

Based on Koba et al. (1990), Knaff and Zehr (2007) state that the wind-pressure relationships are dependent on changes in intensity. In general, a TC which is intensifying, tends to have higher pressure deficits below intensities of 40-65 kt, compared to lower pressure deficits at intensities higher than 65 kt. Furthermore, weakening or steady storms tend to have lower pressure below this threshold and higher pressures above the 40-65 kt wind speeds (the opposite compared to TCs with increasing intensity). Nevertheless, these results cannot be seen independent of latitude and storm dimensions. Opposite to Koba et al. (1990), Knaff and Zehr (2007) conclude that the difference in wind-pressure relationships for different trends in intensity is the result of differences in latitude and storm dimensions. A storm is more likely to intensify during its early stages, when at low latitude. Moreover, a storm weakens at the end of its lifetime when at higher latitude. This pattern suggests that intensity trend is not likely to be an important process for the wind-pressure relationship.

Models Different wind-pressure relationships have been developed. These relationships provide a critical analysis tool for assessment of maximum winds and thus maximum possible damage. Almost all pressure-wind models (for a summary see Harper (2002)) are of the form:

$$v_m = a\Delta p^x \tag{2.2}$$

Where the maximum wind v_m is described by a pressure drop Δp scaled with two empirical constants x and a. An example is the model introduced by Knaff and Zehr (2007):

$$p_c = 23.286 - 0.483 v_{srm} - (\frac{v_{srm}}{24.254})^2 - 12.587S - 0.483\phi + p_n \tag{2.3}$$

Where v_{srm} is the maximum sustained surface wind speed excluding TC translation speed, S is a dimension parameter, ϕ the latitude and p_n is the environmental pressure. Opposite to other approaches, this relationship allows for parameter variability (Harper, 2002). Therefore, this relationship takes into account the considerable scatter in the wind-pressure data.

A second example of such model is the Holland (2008) wind-pressure model. The suggested relationship is an extension of the generic wind-pressure relationship (see Equation 2.2) and it incorporates the deviation in the pressure gradient near the maximum sustained wind speeds as established by Holland (1980). The following equation is proposed:

$$v_m = (\frac{b_s}{\rho e}\Delta p)^{\frac{1}{2}} \tag{2.4}$$

Where v_m is the maximum surface wind speed, e is the base of natural logarithms, Δp the pressure deficit between the environmental pressure and the pressure at the TC's center. The air density is represented by ρ and b_s is the surface winds parameter. In this b_s, the central pressure, latitude, intensification trend and storm

motion velocity are accounted for (Holland et al., 2010). This model reproduces the scatter as observed in wind-pressure data. This relation outperforms the suggested relationship by Knaff and Zehr (2007) (Holland, 2008). Furthermore, the wind-pressure relation of Holland et al. (2010) is generically valid. Opposite to the Knaff and Zehr (2007) relationship which is only valid for a specific set of data.

Based on observations and wind-pressure relationships, spatial wind speed fields can be generated. In general, multiple techniques are used to create spatial wind fields. In hind-casting studies, surface winds are mostly derived by data-assimilation techniques to acquire detailed knowledge of the wind speeds at locations in time and space. However, for forecasting studies, climate variability studies or multi-hazard risk assessments the spatial wind field is usually not known beforehand. To model the behavior and impact of TCs, an accurate description of this spatial wind field is desired. Numerous computationally heavy methods are developed to reproduce the spatial wind field of a TC. Nguyen (2015) presents methods as the kinematic analysis wind approach and the steady-state slab Planetary Boundary Layer model. However, the most widely used approach to generate wind fields, is the parametric wind profile, which is based on Best Track Data (BTD, Knapp et al. (2010)). A parametric radial profile of TC winds is often used for reconstructing TC winds. The relative uniformity and consistent behavior of TC circulations make this basic approach valid (Holland et al., 2010).

Several descriptions of parametric wind profiles (Chavas and Lin, 2016; Knaff and Zehr, 2007; Willoughby et al., 2006) exist in literature, of which the Holland et al. (2010) model is the most commonly applied model for its relative simplicity. A parametric wind profile is characterized by the exponentially increasing wind speeds towards the eye-wall and at the same time a drop in sustained wind speeds near the calmer eye. An important parameter in the description of the parametric wind model is the radius of maximum winds (RMW, Holland et al. (2010)). The RMW is described as the distance between the TC's eye and the strongest axially symmetric wind (Nederhoff et al., 2019). The Holland et al. (2010) relationship builds upon the established Holland (2008) model (see Equation 2.4). Including outer wind and surface pressure, central pressure, sea surface temperature and the RMW leads to a more detailed description of the spatial wind and pressure profiles. All of these quantities are regularly available in archives. So, this indicates that this model is suited for multi-hazard risk assessments.

The Holland et al. (2010) model schematizes the spatial wind field as axisymmetric, whereas in reality this can deviate. In fact, the axisymmetric representation is an idealized scenario. Actually, the spatial wind field is a combination of the axisymmetric wind field proposed by Holland et al. (2010) and background environment parameters influencing this axisymmetry. Lin and Chavas (2012) already proposed a correction factor for this phenomenon. For simplicity and applicability this research does not include this correction factor. However, to account for the interaction of the TC with steering flow a correction is made. Based on Chan and Gray (1982), the TC motion velocity is added to the parametric wind field schematization. On the Northern hemisphere for example, this would increase maximum sustained wind speed on the right side of the TC, while reducing the winds on the left-hand side (see Figure 2.2). This creates an azimuthally asymmetric wind field.

Furthermore, parametric wind models create an axisymmetric wind speed profile without any information on the direction of background winds (Zhang and Uhlhorn, 2012). In this case, the wind direction is assumed to have a constant inflow angle and subsequently the asymmetry is implemented as proposed by Chan and Gray (1982). Based on observations, the mean inflow angle is estimated to be 22° (Zhang and Uhlhorn, 2012). Moreover, Schwerdt et al. (1979) proposes another deviation from the axisymmetric wind profile based on storm motion velocity. Based on observations he suggests a correction factor as follows:

$$a = 1.5 * v_{storm}^{0.63} \tag{2.5}$$

These three elements are included in model applications of the parametric wind profile model of Holland et al. (2010). This makes the originally axisymmetric profile deviate to an azimuthally asymmetric profile.

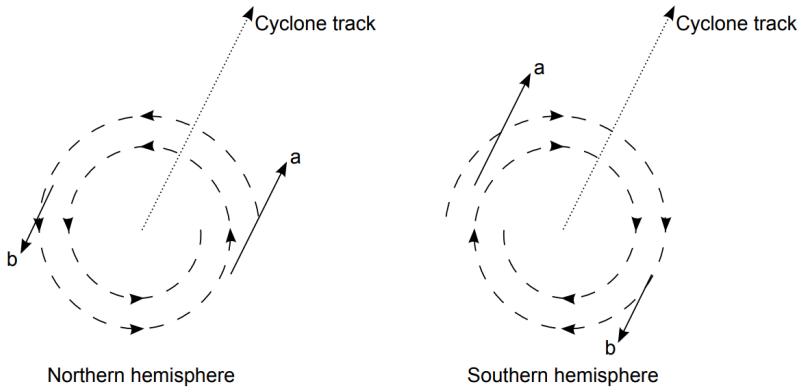

Figure 2.2: Impact of the steering flow on the wind symmetry, for both the left) Northern hemisphere, right) Southern hemisphere. Courtesy of Deltares (2014).

2.2.2. Hurricane Tracks

The affected area and hydrodynamic behavior is, for a large part, determined by the storms intensity and dimensions. Moreover, the exact track of a TC is also important. Small changes in a TC track can cause great variability in landfall location and therefore cause great spatial variability of damage and affected people. First, the background theory of hurricane tracks is discussed. Secondly, an overview of the existing models is given.

Theory Current models for track determination are based on historical cyclone data. This data is gathered by multiple meteorological institutes all over the world (e.g. NOAA). This data is contained in a database that can be used to create understanding about the distribution, frequency and intensity of TCs. This so-called BTD record (Knapp et al., 2010) is freely accessible. Over 6-hour intervals the storm center position and storm intensity are registered with the following variables: latitude, longitude, central pressure and maximum sustained wind speeds (Knapp et al., 2010). Three main components can be recognized for every single recorded historical TC: the genesis, propagation and termination. These are the three components which form a hurricane track.

TCs can form in regions with light winds, high sea surface temperatures (over 26.5°Celsius) and high humidity. Under these conditions the initial cluster of thunderstorms can be generated (Zehnder, 2018). A cluster can possibly intensify into a TC. The given conditions only occur at certain locations on the globe, which are referred to as oceanic basins. The genesis of a TC is therefore restricted geographically.

After generation, the movement of a TC is dynamic. TC intensity is based on the amount of energy it can subtract from the ocean (Zehnder, 2018). When the TC encounters warm waters it is likely to intensify, but when colder waters are encountered, de-intensification occurs. Cold waters are often encountered when the storm travels to higher latitudes. Furthermore, when the TC makes landfall, there is no source of water available which fuels the storm. This initiates weakening of the TC. The magnitude and direction of travel is dependent on more environmental parameters. For example, if a TC enters the proximity of the equator, the Coriolis force is no longer sufficient to maintain the rotational motion. Therefore, weakening or dissipation is likely to occur. The exact description of these physics is beyond the scope of this research. But to conclude, storm motion is dynamic and uncertain. This makes hurricane track estimation a difficult task, but models have been developed to answer for this uncertainty.

Models In literature, a variety of synthetic track generation models is used to recreate hurricane tracks (Emanuel et al., 2006; Hall and Jewson, 2014; Kriesche et al., 2014; Rumpf et al., 2008). In this research the main focus is on the Tropical Cyclone Wind Statistical Estimation (TCWiSE) tool (Hoek, 2018). This model is based on the Simple Track Model (STM, Russell (1968)) and the Empirical Track Model (ETM, Vickery et al. (2000)), which are briefly discussed in the following paragraphs. The use of the TCWiSE tool is further elaborated in Chapter 5.

The STM was first introduced by Russell (1968). His basic idea has been used by other researchers, each with their own approach (e.g. Vickery and Twisdale (1995)). Although different approaches are used, the basic principles are the same for every variation (Nguyen, 2015). First, a statistical distribution of essential parameters (e.g. heading, maximum sustained wind speed) are estimated for a specific location. Then, a Monte Carlo sampling method is used to create the initial synthetic TC conditions. This simulated TC is assumed to follow a straight line with a sampled heading and a constant intensity till landfall. After landfall, the intensity decreases by means of a decay model. However, this method has its disadvantages. The statistical background is based on site specific data and therefore this method is not applicable for all over the globe. Secondly, the straight-line track is a crude assumption, causing a limitation in the variability of TCs. Moreover, by using a Monte Carlo sampling method, the parameters are assumed to behave independently of each other. This can cause unrealistic combinations of TC parameters (Emanuel et al., 2006; Nguyen, 2015).

The more sophisticated ETM is developed by Vickery et al. (2000). Contrary to the STM, this method simulates a full track of a synthetic TC, sampling the heading, central pressure and translation speed for a six-hour interval. Main improvement compared to the STM is the fact that key parameters like heading and maximum sustained wind speeds are sampled every six hours. The track is no longer straight as the result of a STM. Furthermore, the method is less dependent on single location observations. Since all observed tracks are fully used, the area of interest is not restricted. Thus, the ETM is a more statistically reliable method and can provide for a wider range of synthetic tracks (Nguyen, 2015).

The ETM uses Markov chains for generating track data. An example of a Markov chain is the non-returning random walk (Emanuel et al., 2006). Basically, a Markov chain is a list of random samples of which the probability at a certain time interval depends on the value at a previous time. So, each six-hour sample depends on the properties of the previous time step and the probabilistic distribution of rates of change of displacement in direction (Emanuel et al., 2006). This ensures that the tracks are created according to the variability in direction and speed of historical TCs.

2.2.3. Rainfall

Besides high wind speeds and a drop of atmospheric pressure, TCs are often accompanied by (heavy) rainfall. For example, Hurricane Harvey (2017) tied with Hurricane Katrina (2005) as costliest TC on record in the USA (NOAA, 2018a), even though Hurricane Katrina was a surge-dominant TC (Robertson et al., 2007), where Hurricane Harvey a rainfall-dominant TC (Sebastian et al., 2017). Significant amounts of rainfall can cause overtopping of riverbanks and subsequently cause flooding. Inland fresh water flooding is the main cause of fatalities during landfall of a TC (Rappaport, 2000).

At the same time, rainfall due to hurricanes has a great influence on regional water budgets. This positive element is mostly overruled by all negative aspects coming with a TC. At certain locations, TC precipitation contributes 10-15% to the total annual rainfall (Rogers et al., 2009). Therefore, this can impact agricultural management and planning. The dynamic behavior of TCs and its associated rainfall can have a significant impact, both positive and negative. Lowman and Barros (2016) show for example, that TC rainfall can recharge aquifers, impact photosynthesis and take up carbon from the atmosphere. However, rainfall characteristics (i.e. intensity, amount, spatial and temporal distribution) can differ for every single hurricane and location around the world. The rest of this section contains background theory and current modelling approaches for TC precipitation.

Theory Rainfall due to TCs can be divided into two categories: convective precipitation and stratiform precipitation. Convective precipitation is associated with formation of hydro-meteors at low levels. Hydrometeors are water particles formed from the product of condensation or deposition of atmospheric water vapor. Upward air motions carry hydro-meteors vertically. This results in stacked convective clouds which fall out when they reach sufficient size. Convection clouds are associated with the inner core of a TC. The strong updraft interacts with the rapid (wind) fluctuations in and around the eye-wall of the TC (Rogers et al., 2009). Convective regions are associated with heavy precipitation rates (Hong et al., 1999). On the other hand, stratiform precipitation is related to weak vertical air motions and precipitation particles that drift down from upper reaches of the cloud as they grow simultaneously (Rogers et al., 2009). Stratiform precipitation drifts away from the eye of the TC. The homogeneity is much larger compared to the convective cloud system and the rainfall rates are lower (Hong et al., 1999).

As for the structure of a TC, a clear difference in these precipitation features can be distinguished. The ring of heavy precipitation around the eye wall is the result from purely convective clouds accompanied by high sustained wind speeds. Therefore, this area is marked as the most destructive part of a TC. The spiral rain bands which form around the eye-wall contain a mixture of precipitation following from convective and stratiform features. Areas of rainfall which are not in the eye-wall or rain band regions are mostly classified as purely stratiform precipitation (Rogers et al., 2009). A schematization of this can be seen in Figure 2.3. In this schematization an inner and outer eye wall can be distinguished. This feature is called the eye wall replacement cycle. At this moment a new eye is developed around the old eye, usually accompanied by a decrease in intensity (Sitkowski et al., 2011). Nevertheless, the mixture between convective and stratiform rainfall can be recognized.

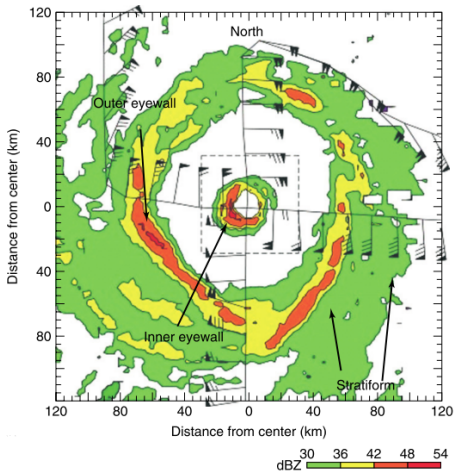

Figure 2.3: Top view radar image of Hurricane Gilbert (1988), in which a distinction is made between convective and stratiform clouds by means of reflectivity. Red indicates convective clouds (i.e. high reflectivity), the green and yellow color indicate stratiform rainbands. Courtesy of Rogers et al. (2009).

In agreement with the before-mentioned, Lonfat et al. (2004) show that TC rainfall primarily varies by radius and intensity of a TC. In Figure 2.4, the radial radial profiles for different storm intensities are ranked after the Saffir-Simpson Hurricane Wind Scale (see Table 2.2, Schott et al. (2012)). As discussed previously, peak rainfall rates are located near the center of the TC and gradually reducing with increasing radial distance. For larger radial distances, the differences in mean rainfall rate between different storm categories vanishes. Figure 2.4 shows the radial rainfall distribution (if assumed axisymmetric) of TCs. This radial distribution of rainfall can be seen as an idealized scenario. In reality, there are many influential factors, which can lead to departure of this axisymmetry.

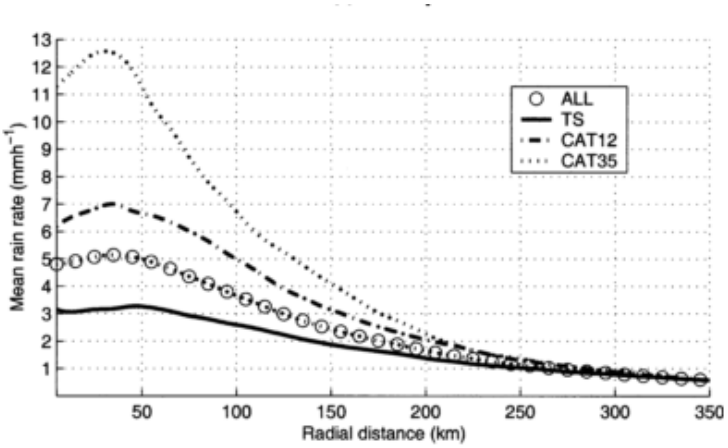

Figure 2.4: Mean rainfall rates (in millimeters per hour (mm/hr)) as function of storm intensity and plotted against the radial distance from the eye of the TC. Courtesy of Lonfat et al. (2004).

Multiple processes are recognized to influence the spatial TC rainfall distribution. The idealized case of axisymmetric distribution mostly converts to the form of azimuthal asymmetric rainfall distributions due to strong tangential flows (i.e. cross-flow) in these systems (Lonfat et al., 2004; Rogers et al., 2003 2009). Other primary physical processes that lead to a shift in spatial rainfall distribution are:

- Topography;
- Storm motion;
- Storm intensity;
- Vertical wind shear; and
- Interaction with baro-clinic systems (i.e. extratropical transition).

Topographical barriers influence the spatial precipitation distribution by forcing air in an upward motion. Upward airflow causes destabilization of the system and subsequently rainfall on the windward side of the topographic barrier (Rogers et al., 2009). The magnitude to which the topography enhances rainfall distribution is dependent on many elements such as intensity of the storm, structure of the winds, fetch of the winds, angle of incidence and moisture content (Smith and Barstad, 2004). Furthermore, surface roughness is of influence according to Lu et al. (2018). Mountainous areas have a higher surface roughness compared to surrounding areas and therefore initiate larger precipitation rates.

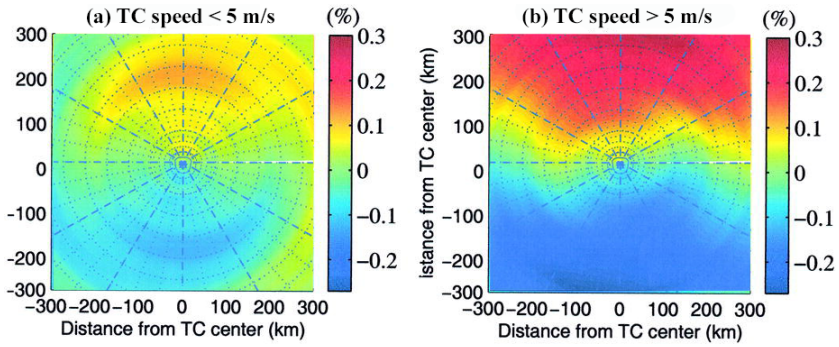

Figure 2.5: Rainfall asymmetry as a function the storm motion velocity: a) for slow moving systems, b) for fast moving systems. The color scale indicates the amplitude of the normalized asymmetry. The blue indicates the minimum rainfall within the storm whereas the red indicates the maximum positive anomaly. Courtesy of Lonfat et al. (2004).

Moreover, multiple studies link storm motion with precipitation rate and distribution (Chen et al., 2006; Lonfat et al., 2004). Lonfat et al. (2004) show that slow-moving systems (< 5 meters per second (m/s)) and fast-moving systems (> 5 m/s) have the same spatial distribution of rainfall, only the intensity differs (see Figure 2.5).

As mentioned previously, storm intensity influences the mean rainfall rates. Furthermore, storm intensity influences the spatial distribution of rainfall. Lonfat et al. (2004) show that the convergence is strongest in the front quadrants for the overall storm composite, equal to tropical storm categories individually. However, a shift from the front-left to the front-right quadrant is recognized for increasing storm intensities (see Figure 2.6).

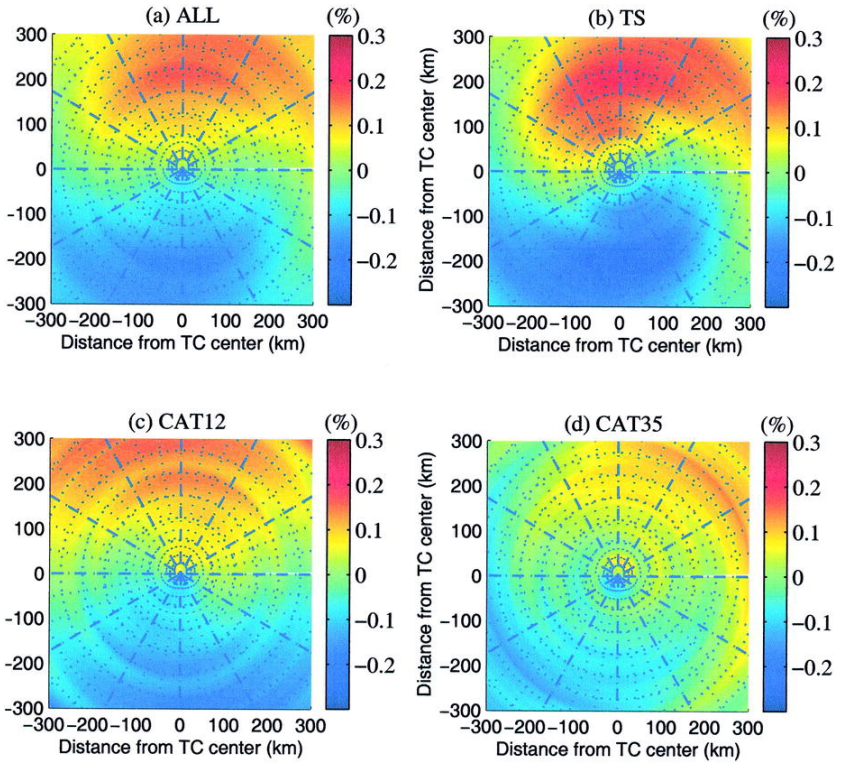

Figure 2.6: Rainfall asymmetry as function of the storms intensity: a) for all observed storms, b) for tropical storms, c) for Saffir-Simpson Scale Category 1 and 2 storms, d) for Saffir-Simpson Scale Category 3, 4 and 5 storms. The blue indicates the minimum rainfall within the storm, whereas the red indicates the maximum positive anomaly. Courtesy of Lonfat et al. (2004).

Moreover, the presence of environmental (wind) shear and storm translation influences the spatial rainfall distribution. Vertical environmental (wind) shear (sometimes referred to as wind gradient (NOAA, 2018b)) is defined by Chen et al. (2006) as: "the difference between the mean wind vectors of the 200- and 850-hectopascal levels over an outer region extending from the radius of 200-800 kilometers (km) around the storm center." (i.e. change in velocity and/or direction of wind with height). For the Northern hemisphere, Chen et al. (2006) show that when the shear vector is aligned with storm motion the rainfall asymmetry is concentrated in the two front quadrants. Subsequently, this leads to an accumulated rainfall maximum in front of the storms eye. When the wind shear vector and storm translation vector are orientated perpendicular, the rainfall asymmetry shifts to the right-back quadrant (see Figure 2.7). To conclude, the wind gradient influences the spatial distribution of rainfall.

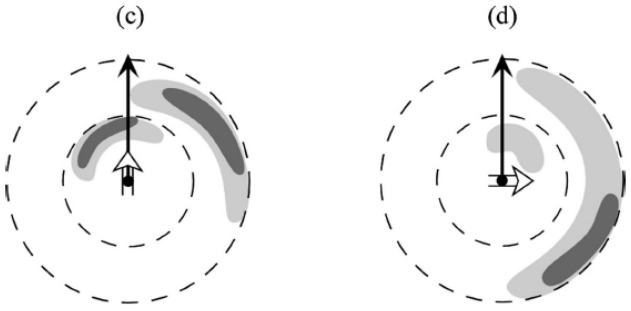

Figure 2.7: Rainfall asymmetry as function of the environmental shear with the black arrow indicating the storm motion and the white arrow indicating the environmental shear: a) for an aligned situation, b) for a perpendicular situation. The dark color indicates a larger positive anomaly compared to the minimum rainfall. Courtesy of Chen et al. (2006).

Furthermore, the interaction with baro-clinic systems and the accompanied extratropical transition can also cause asymmetries in the spatial precipitation distribution. When the TC is moving poleward, it encounters so-called frontal boundaries. This results in an uplift and torrential rainfall. The behavior is similar to the behavior under the influence of topographical barriers (Lonfat et al., 2007; Rogers et al., 2009).

In conclusion, the idealized scenario of an axisymmetric rainfall distribution does not hold. Multiple processes can cause asymmetries in the rainfall distribution of a TC. Multiple schematization efforts are carried out to represent TC precipitation in modelling studies.

Models The framework for spatial precipitation fields is linked to multiple different modelling approaches to give an estimate for tropical cyclone rainfall. This section contains an overview of some common TC precipitation models.

In the 1950s, R. H. Kraft proposed a rule of thumb. The Kraft's Rule of Thumb is one of the simplest techniques to forecast the maximum rainfall (in inches per 24 hours) that is produced by a hurricane (Pfost, 2000). This rule of thumb consists of a constant value of 100 which is divided by the translation speed of the TC (in kt). This gives an estimate of the maximum rainfall (in inches) expected at a given location and time period. This technique does account for the translation speed of the TC as stressed by Lonfat et al. (2004), but does, for example, not include any information on the structure of the spatial distribution of the rainfall and many other quantities.

$$\text{maximum total rain in 24h} = \frac{100}{v_{storm}} \tag{2.6}$$

Miles (1958) proposed a more analytic method, where hourly rainfall amounts of multiple hurricanes are plotted relative to the storm center. Subsequently, the mean areal rainfall rates around the storms center are obtained by using local rain gage data. A frequency distribution of various hourly rainfall amounts for local stations was used. This resulted in an estimate of the expected rainfall due to TCs, when assuming a constant storm motion velocity. The method applied was free of external influences like topographic effects, extratropical transformation and surface roughness. Furthermore, this method uses local storms only. Therefore, the model is only valid for the area in which these storms occurred.

A more complex method is the Tropical Rainfall Potential (TRaP) Method. TRaP includes real-time TC precipitation observations to improve accuracy (Kidder et al., 2005). This method is effective for short-term forecasts. The method makes use of satellite-estimated precipitation fields in combination with storm motion. This results in a 24hour-rainfall accumulation prediction. Computational efficiency is one of the main advantages of this method, while at the same time it takes into account all information about precipitation asymmetry due to the usage of satellite imagery. Downside of this method is that it uses a steady-state precipitation field, which implies that it can only be used for short-term prediction (i.e. < 24 hours).

Tuleya et al. (2007) propose a simple rainfall model based on persistence and climatology called the Rainfall-CLImatology and PERsistence (R-CLIPER) model. According to Tuleya et al. (2007), this model should be seen as a first parametric rainfall model. The rainfall rate along the storm track is determined based on hourly gage data of storms from 1948 to 2000. Main reason for a decrease in average rainfall rate is the weakening of a storm, as mentioned in theory. This observation suggests that the rainfall intensity as a function of radius and storm intensity should be included to improve the R-CLIPER model (Tuleya et al., 2007). The implementation is based on the work of Lonfat et al. (2004). Thus, this model assesses rainfall along the storm track based on intensity and track characteristics. Literature shows the importance of environmental shear for the distribution of the rainfall field (Chen et al., 2006; Rogers et al., 2009). Nevertheless, the R-CLIPER model does not take this effect into account (Tuleya et al., 2007) and assumes the spatial rainfall distribution to be symmetric.

R-CLIPER creates a symmetric rainfall footprint based on storm dimensions and storm intensity. The total rainfall is an integration of this footprint at each time step over the entire lifetime of the storm. The model shows a Mean Absolute Error (MAE) of 23 mm per gage (for 32,784 gage sites for a combined total of 25 USA TC cases). The authors state that this error could decrease when the model forecast is initialized a short period before landfall. Moreover, landfalling TCs are subject to topographical and extratropical influences, which are not included in R-CLIPER. Including these processes would make rainfall forecasting more difficult, yet

it would also decrease the error. Tuleya et al. (2007) recognize that a combination with the TRaP approach would further improve the precipitation forecast. In this case, initial rainfall rates would be adjusted to satellite imagery.

The Parametric Hurricane Rainfall Model (PHRaM) builds on the original R-CLIPER algorithm (Lonfat et al., 2007). In this model, topography and shear effects are included. The PHRaM can be described by:

$$R_{PHRaM} = R_{R-CLIPER} + R_{shearmod} + R_{topography} \tag{2.7}$$

Where R_{PHRaM} is the total rain field as generated by the PHRaM, $R_{R-CLIPER}$ the precipitation field as generated by the R-CLIPER model and $R_{shearmod}$ and $R_{topography}$ the rain field as generated by the environmental shear effects and the influence of the topography respectively. Without going into much detail, PHRaM includes the effect of vertical shear by means of statistical relationships derived from satellite imagery. Subsequently it adds a term proportional to the elevation change to replicate the impacts of topographical uplift (Lonfat et al., 2007). The inclusion of these quantities shows to improve the accuracy of the modelled rainfall compared to the R-CLIPER model (Lonfat et al., 2007). Including environmental shear only raises the prediction skill minimally. Including topography effects leads to significant improvement, as can be seen in Figure 2.8. The authors recognize that not all processes are accounted for in the PHRaM model. The inclusion of extratropical transition would have a positive impact on modelling skill. Furthermore, effects of moisture contents could also influence the rainfall amounts as estimated by the model (Lonfat et al., 2004 2007).

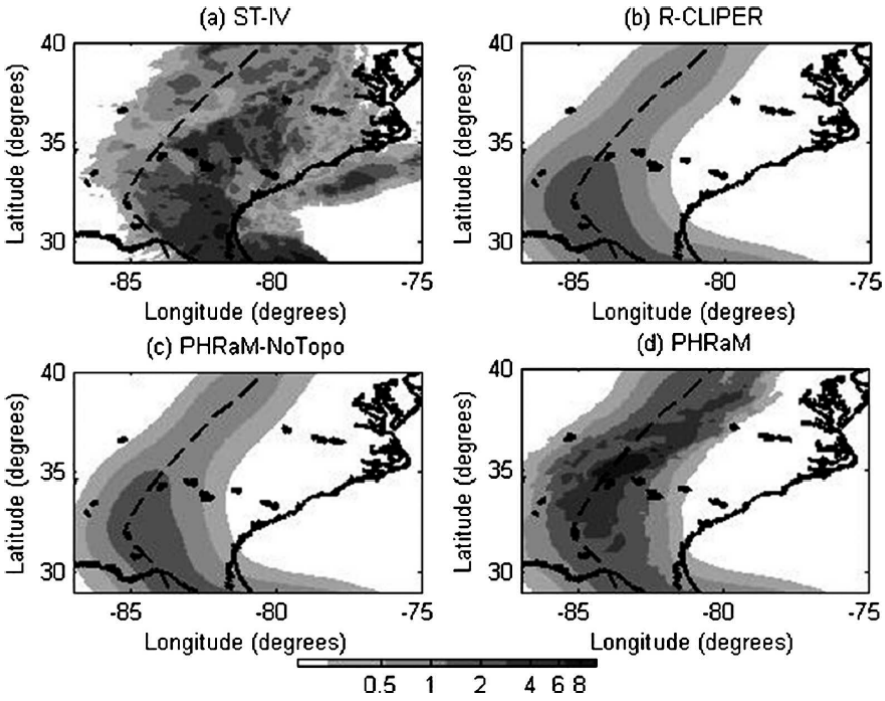

Figure 2.8: Accumulated rainfall (in inches) during Hurricane Frances (2004) for the second USA landfall; a) stage-IV observations, b) R-CLIPER, c) PHRaM without topography effects, d) PHRaM with topography effects. The best track for Hurricane Frances (2004) is indicated by the black dashed line. Courtesy of Lonfat et al. (2007).

R-CLIPER and PHRaM are using an incomplete storm parametrization due to data limitations (Langousis and Veneziano, 2009). Especially, because the RMW is only implicitly taken into account by allowing the maximum precipitation rate to be dependent on storm intensity (Lonfat et al., 2004). Therefore, factors as surface roughness, radial wind speed profile and storm motion velocity are ignored. R-CLIPeR and PHRaM include research of Lonfat et al. (2004) (see Figure 2.4). In other words, ensambled averages of storms with different RMW are used. The dependence between the RMW and the peak rainfall intensity is therefore ignored and furthermore this averaging decreases the estimate for maximum rainfall rate (Langousis and Veneziano, 2009). For this reason, the Modified Smith for Rainfall (MSR) model is proposed (Langousis and Veneziano, 2009). The MSR creates axisymmetric precipitation field, which is solely dependent on: the storm motion

velocity, the maximum tangential wind speed, the *b*-parameter of the Holland (1980) profile, the surface drag coefficient, the average temperature of the boundary layer, the vertical diffusion coefficient of the horizontal momentum and the saturation ration inside the TC boundary layer. Asymmetries are defined based on storm motion, not on the vertical wind shear as proposed in the PHRaM. The MSR model displays good prediction skill when compared to the R-CLIPER model. The asymmetries as a result of storm motion are close to observed asymmetries (Langousis and Veneziano, 2009). However, the model is only valid for open water sites and can therefore not be applied for landfalling hurricanes. Furthermore, the MSR model is depending on a high number of variables, which are not always present in archives.

A more recently developed model is presented by Snaiki and Wu (2017). A physics-based rainfall model is based on the surface boundary condition where the total surface stress was subdivided in two components: a contribution of wind and a contribution of precipitation. The model depends on storm characteristics as: motion velocity, pressure deficit distribution, RMW, approach angle, geographic location, the surface drag coefficient and turbulence diffusivity (Snaiki and Wu, 2017). The proposed model shows close resemblance to the observations as presented in a sensitivity analysis, but no further validation is carried out (yet).

2.3. Hydrodynamic Processes during Tropical Cyclones

Besides meteorological processes, TCs are also accompanied by several hydrodynamic processes. The offshore processes are discussed in Section 2.3.1. The near-shore processes are presented in Section 2.3.2. The processes taking place in the hinterland are discussed in Section 2.3.3.

2.3.1. Offshore Processes

The two offshore hydrodynamic processes during TCs that are of importance for the quantification of flood impact on land are: wave generation and atmospheric driven setup. Each of these processes is explained in more detail in this section.

Wave generation The wind of a hurricane initiates the generation of wind waves. Initial generation is induced due to resonance of a propagating wind-induced pressure wave (i.e. air pressure) at the surface of a water body and freely propagating waves (Phillips, 1957). This turbulent pressure field can be seen as a superposition of many harmonic air-pressure waves. If this component has the same velocity, direction and wavelength as the water waves, this will cause an energy transfer to the water waves by resonance, generating initial waves. Miles (1957) found that the wind profile at the water surface will be disturbed by these harmonic water waves. This disturbance causes a positive feedback mechanism, because the air pressure reaches a maximum at the windward side of the wave crest and a minimum at the lea-side. This causes the wave to grow, subsequently enforcing this mechanism and therefore grow further. This development continues if the wind blows continuously.

Atmospheric driven setup Storm surge can be defined as the change in water level generated by atmospheric forcing (Paul and Rashid, 2017). The atmospheric forcing can be the wind-induced drag on the water surface, like discussed previously, but can also be the result of variations in the surface atmospheric pressure. The magnitude of surge is dependent on water depth, topography, the storm's angle of approach, storm size and propagation speed (Irish et al., 2008). For this reason, storm surge is different for every single storm. Near the coast, where the water depth reduces, the water piles up, leading to elevated water levels and subsequently coastal flooding. The effect is magnified in shallow estuaries or bays in the coastal areas. The magnitude of these two types of water level raise is difficult to predict, because both are dependent on numerous parameters as storm track, storm intensity, wind direction and local bathymetry.

2.3.2. Near-shore Processes

The difference between offshore and near-shore is in part related to the distance from the shore and the local water depth. When a wave travels from offshore to near-shore water, it starts to feel the bottom and other processes start to become important for quantifying the impact on land: wave transformation and wind-driven setup. Although, these processes are not included in this research, this section briefly elaborates on these processes, which are schematically visualized in Figure 2.9, to get a complete overview of important processes for inland flooding.

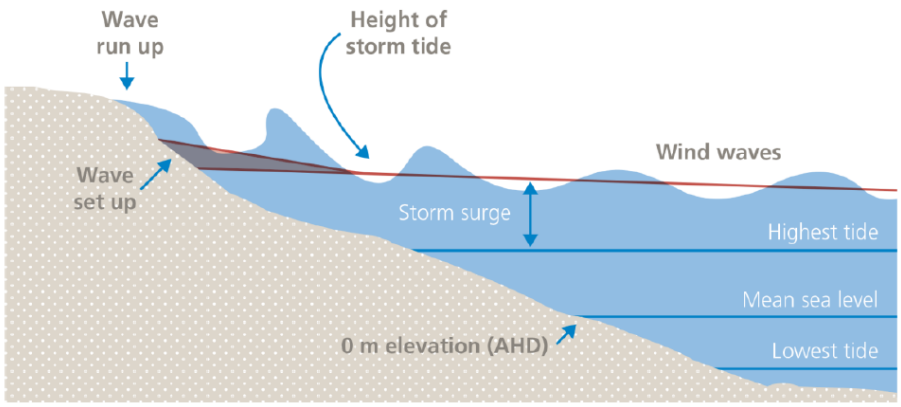

Figure 2.9: Schematization of different hydrological near-shore processes during TCs. Courtesy of Hughes (2016).

Wave transformation The offshore processes determine the incoming forcing upon the coast from the open ocean. When this forcing enters shallow water different processes take place, which initiate marine and inland flooding in the case of extreme forcing, as shown by Roeber and Bricker (2015). The following wave-related processes are discussed: shoaling, wave set-up, wave run-up and overtopping.

When waves travel from deep water to intermediate and shallow water they tend to transform, i.e. the wave height, length and direction will change. For marine flooding, especially the change in wave height is important, also known as shoaling. In shallower water the waves start to be affected by the bottom and are slowed down. This drop in velocity indicates that higher velocity waves, which are traveling behind the first waves are catching up. Due to concentration of wave energy, the wave height increases, which leads to wave breaking due to shoaling. Wave set-up is defined as the increase of mean water level due to breaking waves, which is present in the coastal zone. Wave run-up is the process of the waves traveling up a slope at the coastline. The run-up height is defined as the difference between the mean water level and the highest point of wave run-up (Van der Meer, 2002). In combination with storm surge, wave run-up can cause overtopping of coastal protection structures. Hurricane Katrina is a perfect example of this simultaneous occurrence of storm surge and wave run-up.

Wind-driven setup Wind-driven setup is another main process occurring in the near-shore region. Moving air is exerting a shear stress on the water surface, which initiates movement of the upper parts of the water layer. This can be captured in the following equation:

$$\tau_{wind} = C_d \rho_a W^2 \tag{2.8}$$

Where the wind shear stress τ_{wind} is defined as the product of the drag coefficient C_d, the air density ρ_a and the wind velocity at the water surface W. A landward directed wind generates a landward directed current in the upper water layers. The coastline will act as a barrier for this current, which initiates a water level setup near the coast (see Figure 2.10, Bosboom and Stive (2015)).

2.3.3. Hinterland Processes

Besides sea-originated processes like waves and storm surge, hinterland processes can also contribute to compound flooding events. Extreme river discharges (i.e. fluvial) and extreme precipitation events (i.e. pluvial) can contribute to the magnitude of a compound flooding event. Moreover, local wind set-up could impact the overland flooding. These processes are discussed in this section.

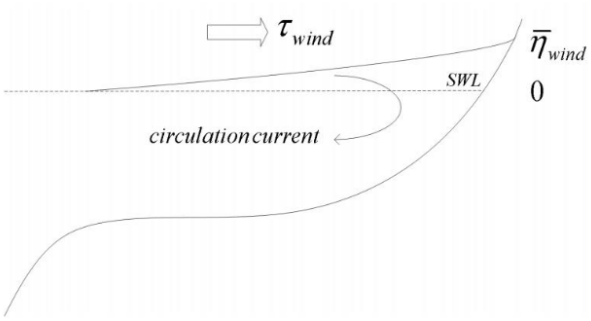

Figure 2.10: Schematization of wind-driven setup. Courtesy of Bosboom and Stive (2015).

Precipitation In case of flow or precipitation in an area, part of this water infiltrates into the subsoil. The amount of infiltration during a precipitation event is, amongst others, dependent on the level of saturation of the soil. A high saturation rate prevents all the water from infiltrating and therefore imply flooding. Furthermore, infiltration is dependent on the rate of infiltration. An infiltration rate is dependent on for example soil type, moisture level and presence of vegetation (USDA, 2019). Moreover, the spatial distribution of rainfall influences the distribution of infiltrated water and saturation rate. Furthermore, the urbanization of coastal areas also implies that most of the soil is covered with low-infiltration materials (e.g. asphalt, concrete). This affects the dynamics of flooding. In urban areas, sewer systems are used to redirect precipitation water. The impact of sewer systems on compound flooding is outside the scope of this research and therefore not taken into account.

The amount of rainfall could have its impact on the river system in the local area. Large watersheds mostly carry the water downstream towards one single water body. During events with high precipitation rates the rivers conveyance capacity is often not large enough to contain all water, so the water overtops the river banks and subsequently flooding the adjacent areas.

Local wind set-up The local wind set-up is particularly important in case of the presence of a shallow lake, basin or estuary in the area of interest. It could also occur at a local wetland inundated by compound flooding. The wind set-up is inversely related to the water depth, so a smaller water depth leads to a larger wind set-up (Bezuyen et al., 2012). This could have implications for the flooding dynamics in the hinterland.

2.4. Modelling Approaches

Modelling inland flooding is a compromise between accuracy and efficiency. The trade-off between these characteristics is one of the difficulties of computational modelling in general. At the moment, three different types of models are often used to model inland flooding. These models can be categorized in static, semi-advanced and advanced models, which are all briefly discussed in this section.

2.4.1. General

Static The simplest way to produce storm tide flooding maps is using a static model (e.g. bathtub model). The static models compare hydraulically connected locations to the elevation of the storm tide. If storms water level is higher than the bathymetry, the location is indicated as flooded, and vice versa. Due to the simplicity of this kind of model, the computational effort is low and a quick assessment can easily be made. However, important characteristics and dynamic behavior of storm tide flooding are not accounted for (Ramirez et al., 2016). Some physical processes not included in a static model are: conservation of mass and effect of landscape roughness (Ramirez et al., 2016).

Advanced Compound flooding can also be modelled in an advanced process-based model like XBeach (Roelvink et al., 2010) or Delft3D (Lesser et al., 2004). Advanced process-based models are computationally expensive, but at the same time capable of modelling coastal flooding to great detail. The models are capable of modelling near-shore wave processes and long-term morphology. At the same time, such model is not capable of solving individual (incident) waves. Full-physics models solve the full non-linear shallow water equations. These formulations express the full physical principles of conservation of mass, momentum and volume. This is the main reason that advanced models are computationally demanding compared to semi-advanced models. In the semi-advanced models (non-linear) terms are simplified or neglected.

Semi-Advanced A third way to model compound flooding is by the use of semi-advanced models. Semi-advanced models are less computationally intensive than advanced models, but at the same time show high accuracy compared to static models. LISFLOOD-FP (LFP, Bates et al. (2010)) is an example of a semi-advanced model. LFP is designed for modelling rivers and flood plain inundation. The model neglects the advection and viscosity terms. Precipitation and wind-induced set-up can not be solved by the model. Nevertheless it is possible to nest the LFP model within an XBeach model to account for wave related processes.

Another example is the Sea, Lake and Overland Surges from Hurricanes (SLOSH) model developed by the National Weather Service (NHC, 2018). The SLOSH model estimates storm surge heights of TCs by including parameters such as atmospheric pressure, forward speed, track data and TC size. SLOSH is seen as a computational efficient model. However, SLOSH is not capable of explicitly model impact of waves on top of surge levels and it does not account for pluvial flooding and normal river flow either. Another recently developed semi-advanced numerical model, that does account for all these processes, is the SFINCS model. The SFINCS model is used in this research and therefore a more detailed description of this model is given in the next section.

2.4.2. SFINCS

SFINCS is an efficient semi-advanced process-based hydrodynamic model to simulate compound flooding (morphology is not included). In particular, SFINCS computes the simplified shallow water equations (see Equations 2.9, 2.10 and 2.11), which are based on the equations of Bates et al. (2010):

$$\frac{\partial \zeta}{\partial t} + \frac{\partial q_x}{\partial x} + \frac{\partial q_y}{\partial y} = 0 \tag{2.9}$$

$$\frac{\partial q_x}{\partial t} + gh\frac{\partial \zeta}{\partial x} + \frac{gn^2 q_x^2}{h^{7/3}} = 0 \tag{2.10}$$

$$\frac{\partial q_y}{\partial t} + gh\frac{\partial \zeta}{\partial y} + \frac{gn^2 q_y^2}{h^{7/3}} = 0 \tag{2.11}$$

In which the free surface elevation with respect to a reference level ζ and the fluxes per unit with in x or y-direction q_x, q_y are the three unknowns. These can be solved every time step with the three presented equations. The third term in Equation 2.10 (or Equation 2.11) represents the bottom friction in which g is the gravitational acceleration, n is the Mannings roughness coefficient and h is the water depth given by $\zeta + d$.

In a way, SFINCS is a merger between two modelling approaches: static and advanced. SFINCS is able to model the interaction between fluvial, pluvial and marine flooding. SFINCS simulates water levels near-shore to the inland region. The current version of SFINCS allows to solve the traditional types of compound flooding, being high offshore water levels, wind-induced set-up and precipitation.

The SFINCS model uses a set of input parameters. At first, the near-shore water levels can be specified at different locations along the coast including tides and storm levels. These water levels often come from a more extensive large scale circulation model like Delft3D (Lesser et al., 2004), but local observations can also be used. Secondly, inland drivers like wind- and rainfall fields can be specified in different ways (e.g. spatially varying spiderweb diagrams, spatially uniform time-series). Finally, local processes like infiltration rate and spatial roughness field can be easily implemented.

The swash-zone in SFINCS is modelled by forcing the model at the offshore boundary. This offshore boundary is set at a water depth of 2 meters (m) along the shore, because at this depth most wave energy has been

dissipated according to Van Engelen (2016). This indicates that the model domain starts at the 2-meter water depth contour, which significantly reduces the model domain area compared to more extensive models (e.g. Delft3D (Lesser et al., 2004)). This in combination with the simplified shallow water equations makes SFINCS a computational efficient model. Earlier research shows that SFINCS produces very similar flooding results compared to full-physics models (Leijnse, 2018; Torres Duenas, 2018).

Four main simplifications are made to create the previously mentioned set of equations (Equations 2.9, 2.10 and 2.11). The Coriolis force is neglected, because SFINCS is used for near-shore regions starting at the 2-meter water depth contour. The effect of this gravitational pull on this relatively small water domain is significantly small, therefore this assumption is valid. Furthermore, the pressure distribution over the depth is seen as hydrostatic and the vertical variation in horizontal flow are assumed to be negligibly small. Thirdly, the viscosity term is not included in the momentum equations. It is assumed that most wave energy is dissipated at the domain boundary, which is located at the 2-meter water depth contour (Van Engelen, 2016). This implies that the amount of turbulence due to viscosity is relatively small and can therefore be neglected. Finally, the advection term is left out of the momentum equation. This is acceptable in case of flood waves in low land rivers with slow changes, because both inertia terms (local and advective) are very small compared to the resistance term (Leijnse, 2018).

3

Model Validation: Case Study of Hurricane Harvey

In this chapter the SFINCS model is validated for Hurricane Harvey which made landfall at the coast of Texas in 2017. An assessment is made based on hydrodynamics and exposure. This chapter is divided in five sections. In Section 3.1 a short summary of Hurricane Harvey's arrival in 2017 is given. Section 3.2 elaborates on the materials and methods used in this validation study. Section 3.3 contains the hydrodynamic model validation. In Section 3.4 the exposure model results are described. To conclude, Section 3.5 summarizes the main findings of this validation study.

3.1. Introduction

The Atlantic Ocean experiences TCs from the 1st of June till the 30th of November every year. The number of TCs occurring in this region varies significantly each season, but the annual peak takes place in August and September (Sebastian et al., 2017). During the annual peak of 2017, Hurricane Harvey hit the coast of Texas.

Hurricane Harvey started as a tropical wave, which formed in the early days of August 2017 on the coast of Africa. A tropical wave is described as a band of low pressure, mostly accompanied by thunderstorms (NOAA, 2018b). Traveling across the Atlantic Ocean it was gaining strength and subsequently developed into a low pressure system. On the 17th of August, the system arrived just east of the Lesser Antilles (Blake and Zelinsky, 2018), approximately 4,000 km south-east of Houston. As it was passing the Caribbean, it briefly intensified into a TC, but subsequently degenerated into a tropical wave on the 18th of August. On the 23rd of August, after crossing the Yucatan Peninsula, it regained strength and regenerated into a tropical depression. The unusually warm waters of the Gulf of Mexico fueled Harvey to develop when approaching the Texas coast (Sebastian et al., 2017). Hurricane Harvey made landfall with maximum sustained wind speeds of around 210 km/h, making it a fourth category TC. Harvey made landfall just before 22:00h (Coordinated Universal Time (UTC)) on the 25th of August, at the northern end of San Jose Island, which is located approximately 200 km south-west of Houston. Winds extended outward up to 65 km from the eye. Peak wind gusts of up to 230 km/h were measured (Sharp, 2018).

Harvey continued moving land inwards at about 11 km/h, simultaneously degenerating into a tropical storm. A second landfall occurred at Copano Bay on August 26, but the storms center stayed offshore, moving towards Louisiana in eastward direction. The warm waters of the Gulf of Mexico allowed Harvey to keep harvesting energy, causing the moisture content to be high. High humidity in combination with the low translatory motion of the TC caused record-breaking rainfall across the coast of Texas. The third and final landfall was made near Cameron on August 30, approximately 200 km east of Houston. Summed up, Harvey hovered above the state of Texas for six days, making it the longest land-falling storm in Texas history (Sharp, 2018). On average, records showed over 700 mm of rainfall in most of the state of Texas. Extreme observations showed 1,500 mm of rainfall during a six-day period (Nederland (Texas), 130 km north-east of Houston, van Oldenborgh et al. (2017)).

3.2. Materials and Methods

This section elaborates on the materials and methods used in this validation study. The first subsections contain information on the input for the SFINCS model used in the hydrodynamic model validation. Furthermore, the components used for the Flood Impact Assessment Tool (Delft-FIAT) are discussed. With the provided elements an analysis can be carried out based on hydrodynamics and exposure.

3.2.1. Study Area

A SFINCS model is created to cover the extent of the inland flooding in the city of Houston during Hurricane Harvey's landfall in 2017. The study area covers the Galveston Bay area till the Addicks and Barker Reservoirs, see Figure 3.1. The model covers the extent of the urban areas of Houston and the majority of the catchment area of the main bayous. The main bayous are the Buffalo Bayou, Brays Bayou and the White Oak Bayou. The Buffalo Bayou flows from west to east. The Buffalo Bayou springs at the Barker and Addicks Reservoirs and flows downstream to the point were the Buffalo and Brays Bayou meet and feed into the Houston Ship Channel. The Brays Bayou and its tributaries are located south of the Buffalo Bayou. The White Oak Bayou is located north of both the Buffalo and Brays Bayou. Just like the other bayous, this river flows from west to east. The confluence of the Buffalo and White Oak Bayou is located in the city center of Houston. All water eventually flows out into the Galveston Bay located south-east of Houston. The model covers the majority of the main bayou catchment areas, however it should be noted that the watersheds of the northern bayou catchments (Greens Bayou and White Oak Bayou) are not fully captured (Seaber et al., 1987). This could influence hydrodynamic model performance.

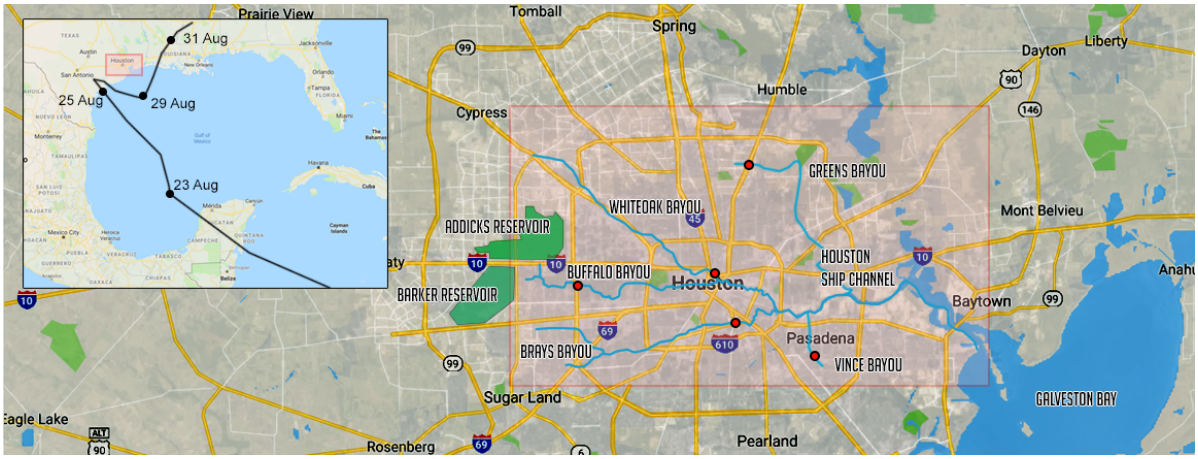

Figure 3.1: The extent of the study area (and hydrodynamic model domain). The red box in the main figure indicates the boundaries of the model grid. The top left input indicates the location of Houston with respect to the Gulf of Mexico, with in black the track of Hurricane Harvey is visualized. The main channels (Buffalo Bayou, Brays Bayou, Greens Bayou, Vince Bayou, White Oak Bayou and the Houston Ship Channel) are highlighted with blue. The Addicks and Barker Reservoirs are indicated with the green polygons. The red dots indicate five observation points which are discussed in Section 3.3.

3.2.2. Topography and Bathymetry

To retrieve the local elevation, two datasets containing bed level information are used, the National Elevation Dataset (NED) and the Coastal Relief Model (CRM). First, the NED is obtained from the United States Geological Survey (USGS) (FEMA, 2007). The data is available on 1/3 arc second (roughly 10 m) resolution for the entire model domain. However, since the NED only provides for overland data (i.e. topography) a second dataset is required to capture the marine and river bed bathymetry.

Including the CRM offers the opportunity to integrate the river and coastal bathymetry with onshore topography. For the Western Gulf of Mexico the resolution is 3 arc seconds (roughly 90 m). The vertical accuracy of this dataset is no better than 1.0 m. Nevertheless, for this specific geographic area, this is the best available dataset.

The two datasets are combined by means of an integration procedure, which results in a full topography and bathymetry map (from now on referred to as Digital Elevation Model (DEM)) as given in Figure 3.2. Both datasets have been converted to NAVD88, a local vertical reference level. The conversion is performed at the difference between the vertical datums at Morgans Point, Barbours Cut (see red cross in Figure 3.2, NOAA (2019)). Due to the coarser CRM, the integrated bathymetry is manually adjusted to remove any integration flaws, such as removing existing infrastructure as bridges which were modelled as obstructions in the bayous. Furthermore, missing river bed elevations are derived based on interpolation between realistic river bed values.

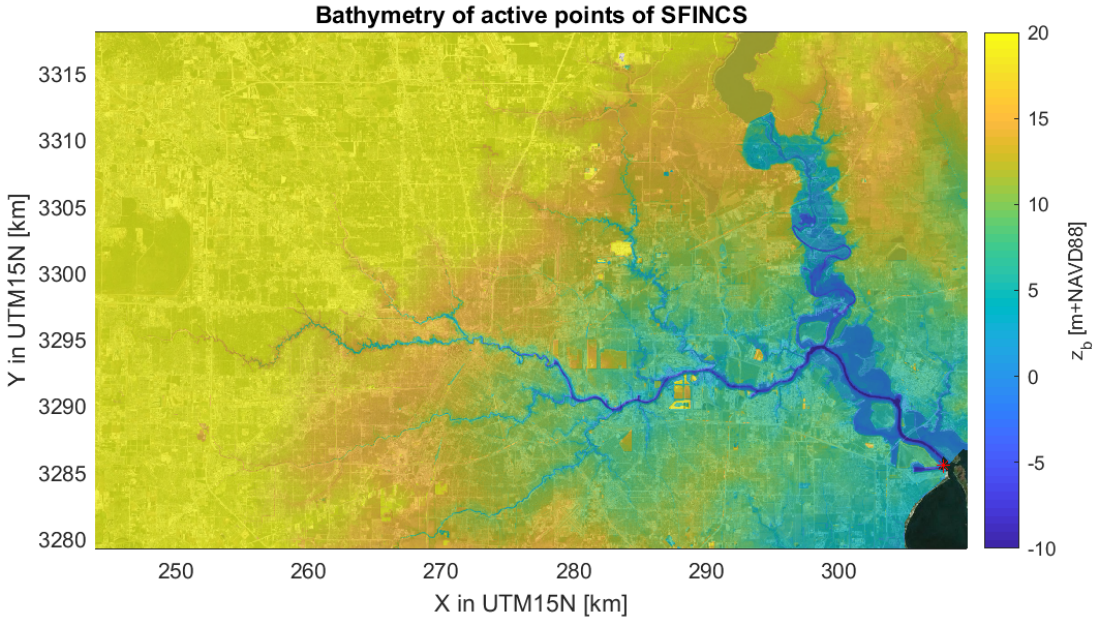

Figure 3.2: Active points of the bathymetry of the SFINCS model domain according to the CRM and NED. The red cross (south-east) indicates the location of the Morgans Points, Barbours Cut observation point.

3.2.3. Land-Use Data

In this study, the parcel level land-use data of the Houston-Galveston Area Council (Houston-Galveston Area Council, 2015) is used to derive the spatial distribution of infiltration and roughness values. This dataset has a spatial resolution of 30 m and was developed in 2014. The data is classified in 14 main land-use classes: open water, developed (high intensity), developed (medium intensity), developed (low intensity), developed (open space), barren lands, forest, pasture and grasslands, cultivated and wetlands. These land-use type designations are specified on a parcel resolution scale. The land use data is used to establish a spatially varying roughness map. The Manning roughness coefficient is used to represent the surface friction for this hydrological model. The surface roughness influences water run-off response. Manning's coefficients for every land-use type are based on Kalyanapu et al. (2009). For the infiltration a similar procedure is followed. For the different land cover types an infiltration value is established (USDA, 2019). These values are set as default, no further calibration is carried out. A full overview of the values and the spatial distribution of the values can be found in Appendix A.1.

3.2.4. Meteorological Data

TCs are accompanied by various meteorological processes as discussed in Chapter 2. Meteorological elements are used to create an accurate model schematization of Hurricane Harvey, a so-called spiderweb diagram. The data for hurricane characteristics as wind speed, atmospheric pressure drop and track is all retrieved from one source. The HURDAT2 dataset (Landsea and Franklin, 2013) is a comma-delimited database which contains the location, maximum winds, central pressure and the size of all known TCs in the Atlantic, Caribbean and Gulf of Mexico registered at a six-hour interval. This data can be used to generate a spiderweb diagram, which contains the conic profile of Hurricane Harvey with spatial information about the winds, pressures and track (Deltares, 2014).

The spatial distribution of the precipitation is generated by using weather station observations. The local district (i.e. Harris County) contains 83 weather station in the Houston urban area as can be seen in Figure 3.3 (HCFCD, 2018). The weather stations are evenly distributed over the study area and the observations can therefore be used as input for the rainfall which is forced on the SFINCS model. Furthermore, the weather stations recorded rainfall rates on a 15-minute interval. To create a spatial rainfall field an interpolation is carried out. The rainfall rates are interpolated on the study area (i.e. the red box in Figure 3.1) on an hourly time scale. A natural neighbor interpolation results in a Root Mean Square Error (RMSE) of 20 mm and bias of -5.1 mm over all observation stations for the cumulative rainfall over a six-day period. With an averaged total of 1,050 mm, this error is considered small. The spatial cumulative rainfall field can be seen in Figure 3.3.

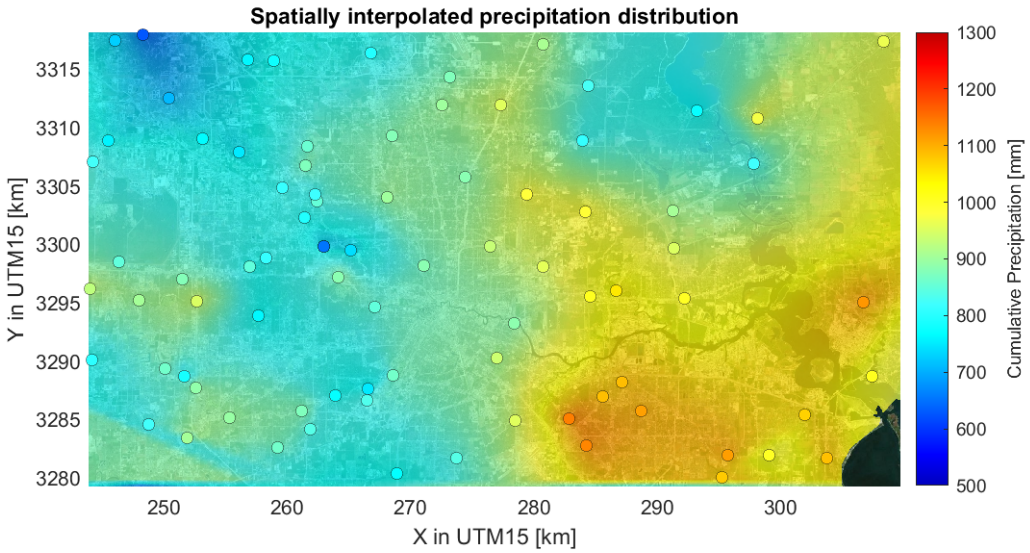

Figure 3.3: Spatial precipitation distribution resulting from the natural neighbor interpolation as used to force SFINCS. The dots indicate the geographic location of weather stations in the area. The color scale indicates the total cumulative rainfall for the period August 25 to August 31, 2017.

3.2.5. Hydrodynamic Data

The Addicks and Barker Reservoirs (see Figure 3.1) capture and store excess rainwater from upstream areas. The reservoirs are a flood protection mechanism for the urban areas of Houston. During Harvey however, unprecedented amounts of water caused the water level in the reservoirs to raise, affecting upstream urban areas. Furthermore, because of fear for failure of the gates, the United States Army Corps of Engineers (USACE) decided to release water at a controlled discharge-rate through the outlet gates (see Figure 3.5, Sanchez-Gomez (2018)). The amount of released water however, exceeded the capacity of Buffalo Bayou, resulting in downstream flooding (Sebastian et al., 2017). The raise in water levels in the Addicks and Barker Reservoirs cannot be reproduced by the model, because upstream areas are not included in the model domain. Nevertheless, to reproduce the reservoir release in the model an artificial discharge point is added at the upstream end of Buffalo Bayou (west), based on the operation schedule of the USACE (Sanchez-Gomez, 2018).

As explained before, hurricanes are accompanied by wave generation, atmospheric driven setup, wave transformation and wind-driven setup. For this study, wave effects are not taken into account. The surge causes the water levels to deviate from normal tidal motion. NOAA has deployed multiple observation stations in the Galveston Bay, which record the water levels with a six-minute interval (NOAA, 2018b). The geographic location of Houston protects the city from heavy storm surge. Moreover, Houston is located behind two barrier islands (Galveston Island and Goat Island). These islands dampen most of the wave energy and surge coming into the Galveston Bay. The observed offshore water levels at a NOAA observation station (Morgans Point, Barbour Cut, see Figure 3.6) is taken. These observations are assumed to be representative for the entire Galveston Bay during Hurricane Harvey. For reference, the water levels during Hurricane Harvey's arrival and under normal conditions are compared in Figure 3.4. It can be concluded that, with respect to the normal conditions, there is about 1 m of residual storm surge.

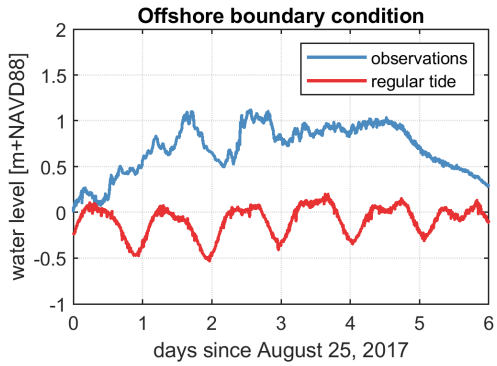

Figure 3.4: The offshore water level condition including tide and storm surge at Morgans Point, Barbours Cut, Texas (TX, NOAA (2018b)). An arbitrarily chosen water level time series of this observation point is given to compare the water levels during storm and non-storm conditions.

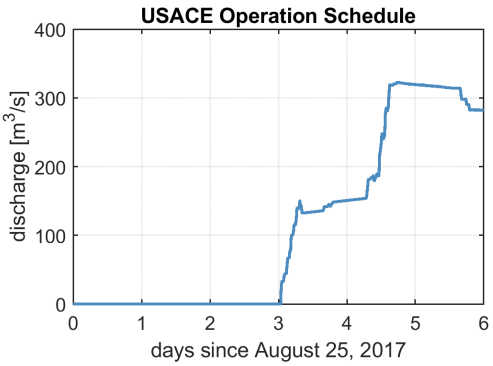

Figure 3.5: Water release in cubic meters per second (m^3/s) for Barker and Addicks Reservoirs combined. Modified from Sanchez-Gomez (2018)

To assess the hydrodynamic performance of the SFINCS model, observed water levels at gages are used as a reference. In the study area, 24 USGS observation station are located. The stations are distributed over the study area as can be seen in Figure 3.6. For this study the water level observations have been converted to the vertical datum NAVD88, equal to the topography and bathymetry. Several stations (1, 3 and 18) can not be seen as representative, because upstream run-off is not included due to model domain limitations. These stations are left out of this analysis.

Secondly, over 300 highwatermarks (HWM) are located in the study area. These HWM represent the highest raise of a body of water over land over a given time at a certain location. The HWM are located mostly on the western part of the study area, see Figure 3.6. The HWM are also used to assess the hydrodynamic behavior of the model.

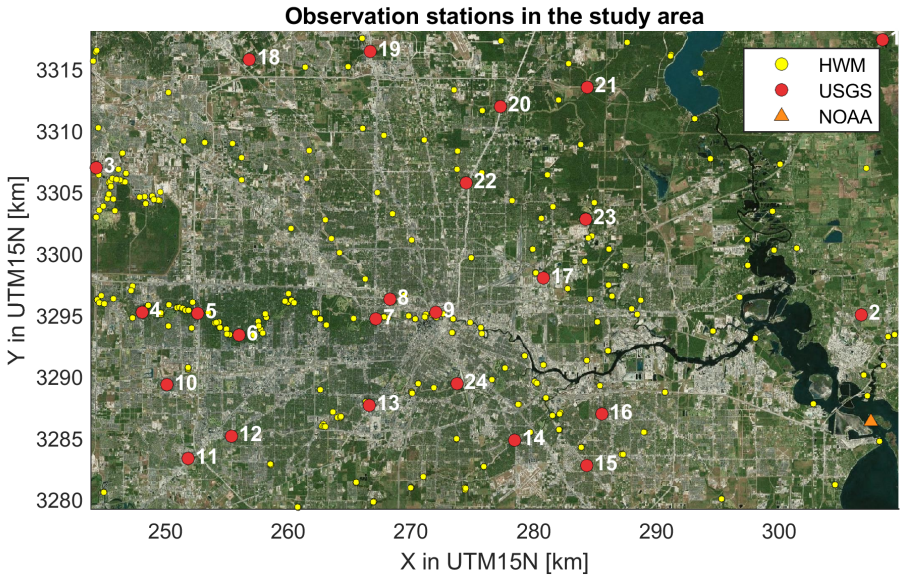

Figure 3.6: The model domain including the different observation points used in the validation study. The USGS observations points are numbered for easy referencing in Section 3.3. The NOAA observation point indicated with the orange triangle is located at Morgans Point, Barbours Cut.

3.2.6. Flood Impact Assessment Tool

Delft-FIAT is a tool to create and run impact models (Slager et al., 2016; Wagenaar et al., 2019). Delft-FIAT is based on the unit-loss methodology, which relates flood quantities to damage at unit level according to De Bruijn (2005). Delft-FIAT is able to calculate damage due to flooding according to the following relationship:

$$\text{Damage} = \sum_{i=1}^{m} s_i \sum_{j=1}^{n} f_{ij} d_j n_{ij} \tag{3.1}$$

Where the damage is a function of the maximum potential damage of an object s_i, the water depth d_j, the damage function used f_{ij} and the number of objects n. Main advantages of Delft-FIAT are its flexibility and applicability. Furthermore, it is computational efficient.

The Delft-FIAT model includes a basic configuration file which is used to get all components together and subsequently run the model. The output of the model contains a damage grid file and an impact report. The damage grid file can be used to visually identify the damage done spatially. It is stressed that Delft-FIAT only takes into account direct damage as a result of flooding. Direct damage due to wind is not included.

FIAT Accelerator When creating an impact model in Delft-FIAT, the most time consuming part is the creation of the exposure dataset. Often data is scarcely available and multiple data sources are needed, therefore a lot of preprocessing is necessary. Furthermore, most uncertainty is incorporated in the damage function and the maximum damage values. For this reason a more workable model is developed: FIAT Accelerator. This model is able to assess the number of people affected and give an estimate of the damage based on global datasets. The global datasets are based on low resolution data sources. Therefore, the results contain more uncertainty.

According to literature, flood risk is the combination of three components: hazard, exposure and vulnerability (Kron, 2005). The SFINCS model output is used as a hazard input for the Delft-FIAT model. With the maximum water depths given by the model an assessment can be made on the number of affected people and damage. According to Field et al. (2012), the exposure is defined as the presence of people, assets and infrastructure in the area of interest. These items can experience potential damage, losses and harm. Information about people is retrieved from two different data sources. The Global Urban Footprint (DLR, 2019) is a worldwide mapping effort to capture all settlements along the globe on a high resolution ($\backsim$12 m). This data is based on remote sensing and uses satellite imagery of 2011 to 2014. Furthermore, the open-source Global Human Settlement (JRC, 2019) database is accessed. This dataset contains a world population map on a 250-meter resolution. It should be noted that this coarse model results in the fact that smaller population settlements are mostly overlooked. Values of buildings and their location are retrieved from the World Settlement Footprint (ESA, 2015). No distinction, in terms of value, is made between different categories of buildings (e.g. residential, commercial, industrial).

For the vulnerability, it is assumed that people are affected by a water depth exceeding 0.15 m. Calibration tests showed that a vulnerability threshold at 0 m water depth would indicate that for every event (no matter what flood extent) all people in the area are affected. SFINCS does not account for sewer systems to run-off storm water. In reality however, sewer systems are present and can handle the first storm water. Therefore, it can be assumed that people and assets are affected from (modelled) water depths starting at 0.15 m. Furthermore, this threshold also takes into account that local residents know how to cope with flooding events, which have happened more frequently over the last years (Giardino et al., 2018).

The damage assessment for (residential) buildings is adapted from a depth-damage function defined by Huizinga et al. (2017), as can be seen in Appendix A.7. The original depth-damage curve includes a positive damage factor at zero flood depth. This is because of the fact that the North American model HAZUS includes damage done to basements (Huizinga et al., 2017). This indicates that for a 0 m water depth damage is calculated by Delft-FIAT. For this study this is not desired and therefore the original depth-damage curve has been inter- and extrapolated to get the desired curve presented in Figure A.19.

3.3. Hydrodynamic Modelling

In this section the performance of the hydrodynamic model is discussed. In the first part a quick outline of the model is given. Subsequently, the model results are discussed and compared to local observations. In the third section, a sensitivity analysis is carried out.

3.3.1. Model Setup

A SFINCS model is created to reproduce the impact of Hurricane Harvey. SFINCS version v052 build on April 2, 2019 is used. The simulation time for the model is from August 25 to August 31, 2017. An equidistant grid with a grid cell size of 25 m is applied. The dimensions of the study area are roughly 70 km by 40 km (see Figure 3.1), resulting in a grid configuration of 2,632x1,555 cells. The geographic coordinate system used is WGS 84 / UTM Zone 15N. Furthermore, the vertical datum is NAVD88.

The model is forced by the following elements:

- The downstream boundary condition is given by the observed water level at Morgans Point, Barbours Cut. This water level time-series is forced on the complete downstream boundary (see Figure 3.4);
- The upstream boundary condition is given by the hydrograph of the reservoir release at Addicks and Barker Reservoirs as a discharge point (see Figure 3.5);
- The characteristics of the hurricane (wind, pressure, track) are retrieved from the HURDAT2 database and have subsequently be rewritten to a spatially varying spiderweb with the Wind Enhancement Scheme (Deltares, 2014); and
- A spatial precipitation field (updating every hour) is interpolated from the observations of 83 weather stations (see Figure 3.3).

3.3.2. Validation

To validate the hydrodynamic performance of the model, the model output is compared to the USGS observation stations and the HWM. The performance is assessed by three performance metrics which are explained first. Secondly, the assessment on both the USGS observations points as well as the HWM is discussed.

Validation Criteria The modelled water levels at USGS observation points are assessed on two different performance metrics: the MAE and the Nash-Sutcliffe model Efficieny (NSE, Nash and Sutcliffe (1970)). The MAE is taken at the peak water level according to the observations. At this point in time the absolute difference between the observed value and the modelled value is taken, see Equation 3.2. When averaging this value over all assessed observation stations a MAE is acquired. A MAE of zero would indicate a perfect match between the modelled and the observed values.

$$\mathrm{MAE} = \frac{\sum_{i=1}^{n} |y_i - x_i|}{n} \tag{3.2}$$

Moreover, the total volume of water which passes at an observation point can be assessed by the NSE (see Equation 3.3). The NSE is used to assess the predictive power of the SFINCS model. It compares the observed and modelled water levels over the entire time-series. An efficiency of 1 (NSE = 1) corresponds to a perfect match of the modelled water level over time with the observed values. Threshold values that indicate a model of sufficient quality are 0.5 < NSE < 0.65, with values higher than 0.65 indicating an excellent model (Ritter and Munoz-Carpena, 2013). A negative value indicates that the mean of the observed water level time-series would be a better predictor than the model itself. Nevertheless, in some cases this can be rejected when visual comparison proofs otherwise. Legates and McCabe (1999) show that the NSE is sensitive to extreme values, which can be explained by the squared elements in Equation 3.3. The NSE is a tool which could be used to make an assessment on total volume of water, but at the same time accounts for the timing of the flood wave.

$$\mathrm{NSE} = 1 - \frac{\sum_{T=1}^{T} (Q_m^t - Q_0^t)^2}{\sum_{T=1}^{T} (Q_m^t - \overline{Q_0})^2} \tag{3.3}$$

The water levels at the HWM locations are assessed by a RMSE (see Equation 3.4). The RMSE is a standard deviation for the residuals, which are the errors at a single observation point. The residuals are squared, so one single outlier can influence the value of the RMSE tremendously. The RMSE is always larger than or equal to zero. A value of 0 indicates a perfect model.

$$\text{RMSE} = \sqrt{\overline{(y_i - x_i)}^2} \tag{3.4}$$

Presentation of Performance Metrics For the sensitivity analysis, the above mentioned criteria will be presented in table-format. An example is shown in Table 3.1.

Table 3.1: Layout of a table used in the sensitivity analysis

run	MAE	bias	RSME (HWM)	positive NSE	average NSE
x	[m]	[m]	[m]	n/21	x

The content of column one to four is explained previously. The fifth column ('positive NSE') contains the amount of USGS stations with a positive NSE value. A score of 5/21 indicates that for 5 of the 21 USGS observation stations a positive NSE is scored. The sixth column indicates the average of all NSE values ('average NSE'). To come up with this score, the negative NSE values are taken into account as a null-score. This is due to the fact that a negative number means a bad model performance in any case, so the magnitude of this number is no longer relevant.

Validation USGS Figure 3.7 shows a selection of the 21 USGS observation stations, which are presented in Figure 3.6. The five stations given here are a good representation of the overall model performance. A full overview containing all USGS observation points is given in Appendix A.2.

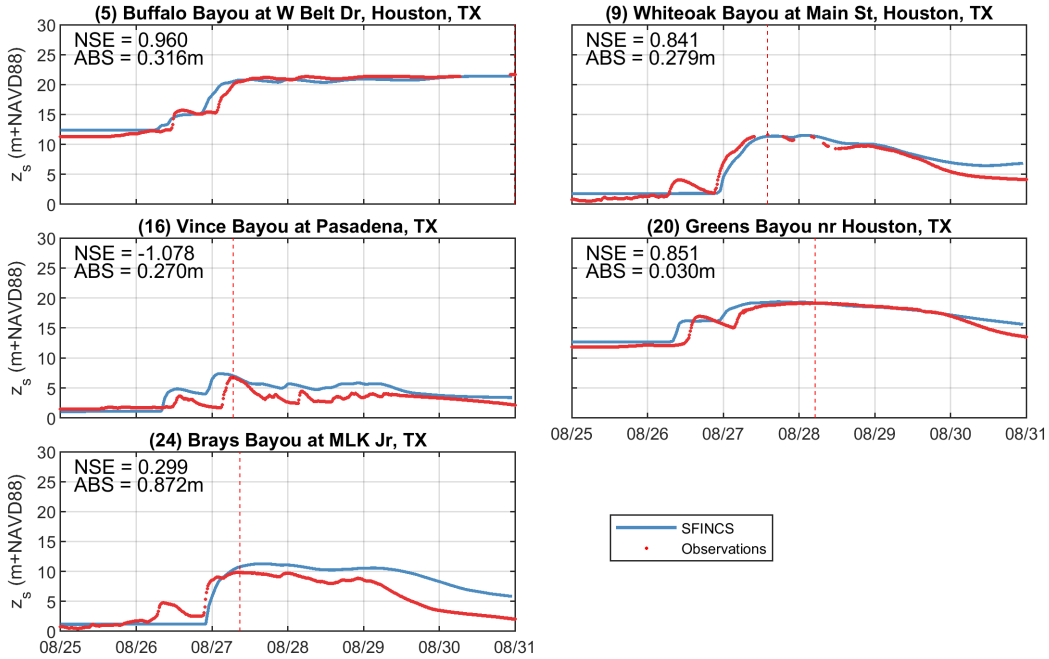

Figure 3.7: Time-series of water levels at selected USGS observation stations expressed in meters above NAVD88. The red line indicates the observed value, whereas the blue line indicates the output of the SFINCS model. The maximum observed water level (peak water level) is indicated with the red dotted vertical line.

The results at the five observation stations are briefly discussed. Station (5) 'Buffalo Bayou at W. Belt Dr., Houston, TX' is representative for the model performance in the Buffalo Bayou. The Buffalo Bayou is sensitive to the hydrograph used for the reservoir release at Addicks and Barker Reservoirs, which is implemented

at the upstream boundary of the Buffalo Bayou. The model (in blue) shows close resemblance with the observed water levels (in red). For station (9) 'White Oak Bayou at Main St., Houston, TX' the same holds. Equal to station (5), it shows an excellent NSE value. At station (16) 'Vince Bayou at Pasadena, TX', which is a smaller tributary of the Houston Ship Channel, rapidly fluctuating water levels were observed. However, in the model, a more smooth water level variation is reproduced. This difference likely be explained by local factors, such as local bathymetry difference which are not resolved in the model, because of the 25-meter grid cell size. This causes the NSE value to be below zero, indicating a poor model performance. However, when visually comparing the model output with the observed values, it can be noticed that the general pattern of water level fluctuations at the observation point is reproduced. Furthermore, the MAE at the peak water level is low. The modelled water levels at gage (20) 'Greens Bayou nr. Houston, TX' show strong resemblance with the observed values. However, the modelled moment of first water level raise is located at a different time compared to the observations. This is a pattern which is recognizable over most of the modelled water levels at observation points and this can most likely be related to the content of the used land-use type dataset. The dataset contains the information about land use on parcel resolution. However, the bayous are not included. Thus, the dataset does not account for differences in bayou characteristics. There is no distinction between a channelized (concrete) bayou and a nature-covered bayou, where in reality different bayous have different characteristics. Therefore, the differences in water run-off dynamics are neglected, because the surface roughness values are equal for bayous (or do not represent a realistic value). This could cause the wrong timing of the first water level raise. Furthermore, this could also explain the model performance for the Brays Bayou. At station (24) 'Brays Bayou at MLK Jr, TX', the water levels are overestimated by the model. This phenomenon can be seen at all observation points in the Brays Bayou. The Brays Bayou is a concrete channel, which means a lower roughness value and therefore higher water run-off values. When the water level time-series is overestimated, it is likely that a higher roughness value has been assigned. This also causes the NSE value to be lower than desired.

These five stations represent the overall model performance. As can be seen, main bayous as the Buffalo and White Oak Bayou show close resemblance with observed water levels. However, the water level in the Brays Bayou is overestimated by the model. It is more difficult to match water levels in smaller tributaries, which can be related to the 25-meter grid cell size (e.g. station (16)). The bathymetry in a grid cell is determined by the mean of the depth at the grid cell points. Therefore, grid cell size is not capable of catching the details in the smallest channels. Nevertheless the model can capture the general flood pattern in these channels as can be seen in Figure 3.7 for station (16). Overall the model shows good correlation with observed hydrodynamic processes. The MAE at peak water levels over all 21 observation points is 0.508 m. With an average water level raise of 7.5 m this is considered a good model performance. Furthermore, the average NSE is 0.55 [-], which indicates a model of sufficient quality according to literature (Ritter and Munoz-Carpena, 2013).

Validation HWM In Figure 3.8 the scatter between observed and modelled water levels at HWM is shown. In the model the observed water levels are matched with a RMSE of 0.977 m. This RMSE is considered as a reasonably accurate model schematization, because of local topography and bathymetry differences.

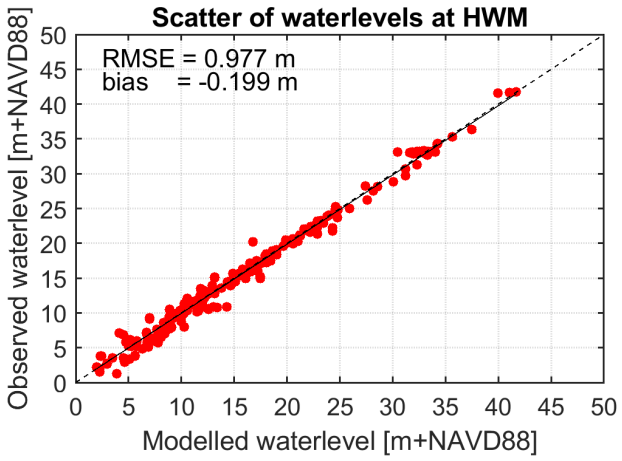

Figure 3.8: Scatter of the observed and the modelled maximum water levels at HWM.

Spatial Overview In Figure 3.9 the total flood extent as retrieved from the SFINCS model can be seen, the maximum water depths during arrival of Hurricane Harvey can be seen. Darker colors indicate larger water depths. Severe overtopping occurs at most of the bayou riverbanks. An exception is the Buffalo Bayou, this bayou flows through a less-urbanized area, indicating that more water can infiltrate. Therefore, the flooding is less severe around Buffalo Bayou.

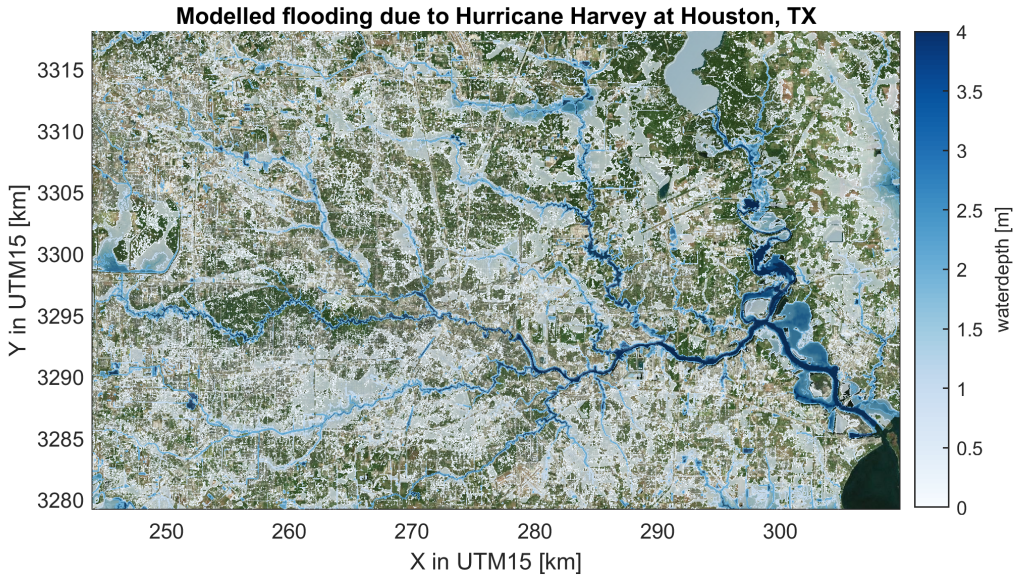

Figure 3.9: Flooding extent (as modelled) due to landfall of Hurricane Harvey in the urban areas of Houston. Maximum water depths lower than 0.15 m have not been plotted for visual purposes. Contour lines are included for the 0.2, 1.0 and 2.0 m water depths.

Opposite to the Buffalo Bayou surroundings, large amounts of water are experienced around the Brays Bayou, which is in line with observations during Hurricane Harvey (Lindner and Fitzgerald, 2018). Figure 3.10 shows a closer look at the Brays Bayou catchment. It can be seen that most urban areas experience high water up to 0.5 m. Areas close to the banks of the Brays Bayou do experience water depths up to two meters. Further upstream (right side of Figure 3.10) is can be seen that the bayou is more meandering and causing even higher water depths close to the banks.

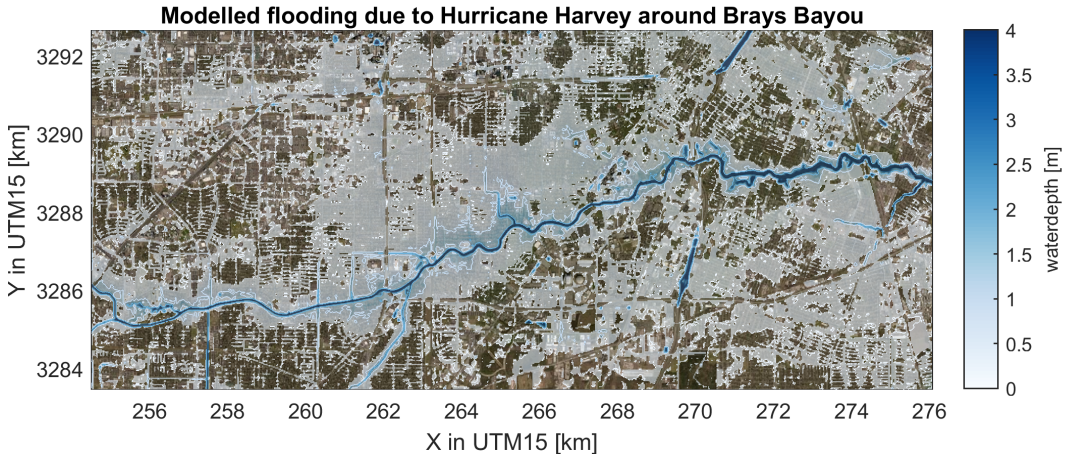

Figure 3.10: Flooding extent (as modelled) in the Brays Bayou catchment area due to landfall of Hurricane Harvey in the urban areas of Houston. Maximum water depths lower than 0.15 m have not been plotted for visual purposes. Contour lines are included for the 0.2, 1.0 and 2.0 m water depths.

3.3.3. Sensitivity

This section contains a sensitivity analysis on: compound flooding, rain and grid resolution. The sensitivity test concerning offshore water levels is presented in Appendix A.4

Contribution to Compound Flooding To assess the contribution of different forcing types (upstream reservoir release, offshore water levels, wind and rain) to the total inundation, several extra runs have been performed. Since one of the elements is turned off for every single run, the significance of the different elements for this compound flooding event can be assessed. The model results for the selected observation points can be seen in Figure 3.11. A full overview can be found in Appendix A.3.

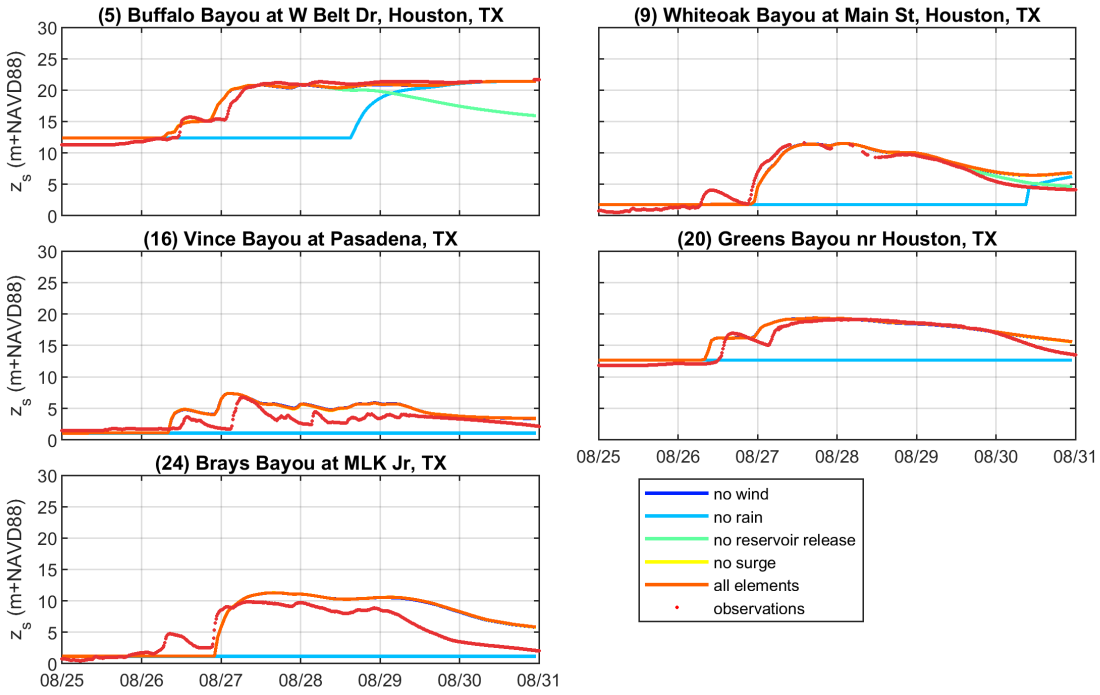

Figure 3.11: Time-series of water levels at selected USGS observation stations expressed in meters above NAVD88 for different configurations of the compound flooding event. The red dotted line indicates the observed value, where the differently colored lines indicate the output of the SFINCS model.

From Figure 3.11, three main conclusions can be subtracted. First, as previously stressed, the rain is the dominant factor in this compound flooding event. If the rain is not taken into account, all observation points would not experience high water at all. The only water level raise that can be distinguished is at Buffalo Bayou due to the reservoir release at the Addicks and Barker Reservoirs. This reservoir release is not likely to happen independently of the rain. So, this underlines the contribution of the rainfall to this compound flooding event. Secondly, the impact of surge on the USGS observation stations is minimal. Since no observation points are located near the coast line, the exact influence of turning off the storm surge cannot be identified. However, the RMSE for the HWM slightly increases, which, in this case, indicates that less water is present overland. A more detailed sensitivity test for the impact of offshore water levels is presented in Appendix A.4. The impact of wind is close to zero. Finally, as recognized by several publications (e.g. Olsen (2018)), the reservoir release had impact on the magnitude of flooding in downstream areas. This can also be seen in the model results, as the water levels in Buffalo Bayou drop significantly when no reservoir release is taken into account. Nevertheless, the reservoir release prevented upstream areas from flooding, but this impact can not be assessed with the current model.

Precipitation As previously stated, the rainfall is the forcing mechanism that caused most of the flooding during landfall of Hurricane Harvey. The model output is expected to be sensitive to deviations in rainfall. To assess this, three extra runs have been executed. First, the North American Regional Reanalysis (NARR) rain model is forced on the SFINCS model (NOAA, 2018b). The precipitation schematization of the NARR model is a gridded rainfall with a spatial resolution of 32 km. Furthermore, it updates the rainfall every 3 hours. The

NARR model rainfall schematization for Hurricane Harvey is characterized by a more axisymmetric distribution (compared to the interpolated spatial precipitation). However, it should be noted that the NARR model is manually modified to better match the observed rainfall rates. This includes an increase in rainfall rates and a shift in longitude and latitude. Nevertheless, the adjusted NARR model underestimates the most extreme rainfall (see Figure 3.12, RMSE of 79.4 mm and a bias of -26.5 mm over all observation stations for the average cumulative rainfall of 900 mm over a six-day period).

Secondly, the rainfall amount as used for the validation is altered. The rainfall rates have been increased (and decreased) by 20 percent. However, the original spatial distribution (see Figure 3.3) is used. The deviation of the rainfall rates is assessed to evaluate the impact of the total rainfall to the compound flooding.

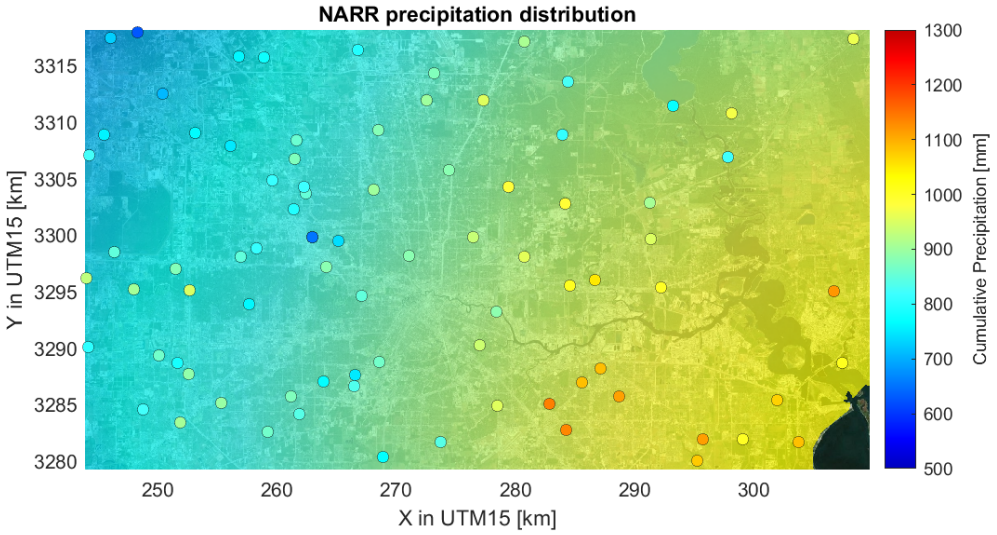

Figure 3.12: Spatial precipitation distribution as retrieved from the NARR model. The dots indicate the geographic location of weather stations in the area. The color scale indicates the total cumulative rainfall for the period August 25 to August 31, 2017.

A full overview of the model results at the USGS observation stations can be found in Appendix A.5. First, the focus is on the increase (decrease) of the amount of rainfall. This leads to higher (lower) peak water levels at different observation points. Furthermore, the pattern of the water levels in time does not change significantly. When looking at the performance metrics, (see Table 3.2) it is notable that the average NSE value is increasing for a decrease in rainfall. This can be explained by the fact that bad scores from the default scenario were mostly due to overestimation of water levels (e.g. in the Brays Bayou or smaller tributaries). For a decrease in rainfall, this effect is less significant and therefore a better NSE score is achieved.

For the SFINCS model forced with the NARR rainfall model, this is not the case. It can be recognized that the pattern of flooding (over time) is different for this axisymmetric rainfall. However, at peak water levels, the NARR model rainfall does not differ tremendously from the model run with a more detailed interpolated rainfall. However, the computational time of the model run decreases, because the NARR model is less detailed compared to the interpolated spatial rainfall. In Table 3.2 the performance metrics are presented. The difference between the default rainfall and the suggested different distribution for the MAE at peak water levels is only 0.131 m. This can mostly be related to the underestimation of the total rainfall in the south-east of the domain. Therefore, it is concluded that peak water levels can also be approximated with a more simple, less computational demanding, representation of the rainfall. However, for the exact dynamics of the flooding over time, a more detailed description of the precipitation is needed.

Resolution To validate whether the SFINCS model is also able to deliver reliable results when a low resolution grid is applied, multiple grid cell sizes have been assessed. This is to analyze whether the model is able to reproduce flooding when the available DEM data is less detailed, for example in less-developed countries. Other input (e.g. rainfall and roughness) is kept constant. An inevitable result of lowering the resolution is the decrease in computational time. For a probabilistic flood risk analysis the model needs to be accurate and computationally inexpensive at the same time. Decreasing the grid resolution from 25 m to 50 m does not

Table 3.2: Performance metrics for the sensitivity analysis of precipitation.

run	MAE	bias	RMSE (HWM)	positive NSE	average NSE
default rain	0.508 m	-0.007 m	0.977 m	18/21	0.55
20% increase	0.542 m	+0.327 m	1.090 m	15/21	0.46
20% decrease	0.653 m	-0.498 m	0.965 m	19/21	0.61
different distribution	0.639 m	-0.396 m	0.943 m	17/21	0.53

influence the MAE significantly, but the runtime decreases by almost 80%, see Table 3.2. Nevertheless, the amount of positive NSE-values is decreasing, which indicates that the total volume of water (and the timing of the flood wave) is off at many observation points. This is caused by the changes in bathymetry. SFINCS uses the average value of the four grid cell corners to appoint a depth to a grid cell. Increasing the size of a grid cell leads to a less accurate description of local bathymetry at an observation point. This results in a (most of the time) higher initial water level at the observation points. The observation points (e.g. (13) Brays Bayou at Houston, TX in Figure A.17) show that the water level at the 25th of August is higher at low resolution grids compared to high resolution grids. This offset will result in a lower NSE-index. In short, for a 100 m resolution model the peak water levels are still reproduced with a MAE of 0.595 m. However, the total volume of water and the details of the flood wave are not modelled accurately.

Table 3.3: Performance metrics for the sensitivity analysis of grid resolution.

Resolution	Configuration	Runtime	MAE	bias	RMSE (HWM)	positive NSE	average NSE
25x25 m	2,632x1,555	14 hr	0.508 m	-0.007 m	0.98 m	18/21	0.55
30x30 m	2,193x1,296	10 hr	0.486 m	0.070 m	1.01 m	16/21	0.53
50x50 m	1,316x778	3 hr	0.496 m	0.148 m	1.05 m	13/21	0.33
75x75 m	877x519	1.5 hr	0.715 m	0.356 m	1.11 m	5/21	0.16
100x100 m	658x389	0.75 hr	0.595 m	0.279 m	1.28 m	6/21	0.15

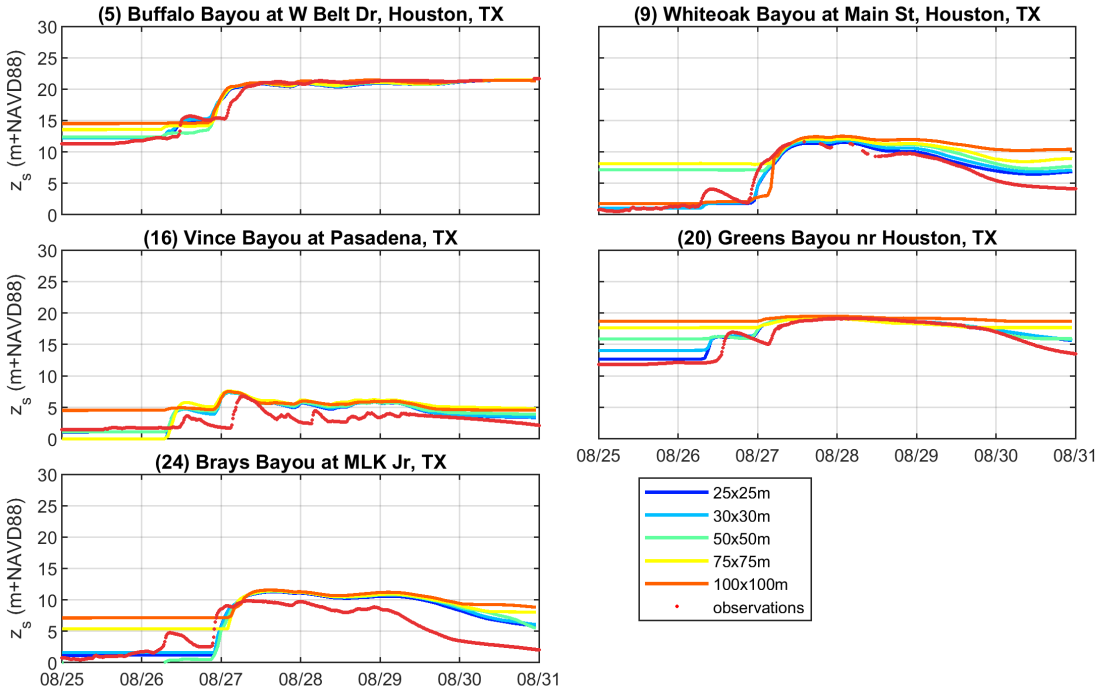

Figure 3.13: Time series of water levels at selected USGS observation stations expressed in meters above NAVD88 for different model resolution. The red dotted line indicates the observed value, where the differently colored lines indicate the output of the SFINCS model.

3.4. Exposure Modelling

In this section the damage and exposure modelling is explained. In the first section the setup of the FIAT Accelerator is briefly discussed. Furthermore, the different input elements are presented. In the second section the results are discussed. Finally, in the third section sensitivity tests are discussed.

3.4.1. Model Setup

The FIAT Accelerator is used to assess the impact of the simulated flooding in terms of affected people and damage to exposed buildings. The model creates a grid with a resolution of 12 m based on the Global Urban Footprint database. Subsequently, the amount of people in a grid cell is calculated and evenly distributed over the grid with the Global Human Settlement data. This gridded population information is now extrapolated to a grid with a resolution equal to the flood hazard input and a calculation is made. For the buildings a similar approach is followed. It is assumed that people are affected at a maximum inundation depth exceeding 0.15 m. Damage to buildings is calculated according to a depth-damage curve, as presented in Appendix A.7 (Huizinga et al., 2017). All buildings are marked as residential, therefore no difference is made between the value of an industrial, a commercial or a residential building.

3.4.2. Model Results

The United States Census Bureau (2018) states that Harris County contained roughly 4.7 million inhabitants in 2017. Harris County is a county in the Texas state and reaches from the Galveston Bay up to 100 km east of the Addicks and Barker Reservoirs. The SFINCS model domain accounts for up to roughly 70% of the entire Harris County. Lindner and Fitzgerald (2018) state that all 4.7 million inhabitants of Harris County were impacted by the flood, both indirect as direct. Over 60,000 residents were rescued from their home and over 300,000 vehicles were flooded. The FEMA assisted 180,000 individuals to recover (so far, at the moment of writing). Furthermore, it was estimated that over 150,000 houses flooded during Hurricane Harvey (Lindner and Fitzgerald, 2018).

The FIAT Accelerator only takes into account direct damages and impact. Moreover, the model domain only contains part of Harris County. This indicates that model results do not match before-mentioned numbers. According to the Delft-FIAT, 3,100,000 people live in the extent of the SFINCS model domain. The Delft-FIAT calculates that up to 1.3 million people were directly affected by the flooding due to Hurricane Harvey. According to Amadeo (2019), over 700,000 people applied for assistance at the FEMA. Furthermore, the damage accumulated up to close to 19 billion USD, according to Delft-FIAT. The spatial distributions of this damage can be seen in Figure 3.14. In line with the observed maximum water depths, the most damage is observed in the Brays Bayou catchment, the part around Sims Bayou (south of the Houston Ship Channel) and near the Addicks and Barker Reservoirs.

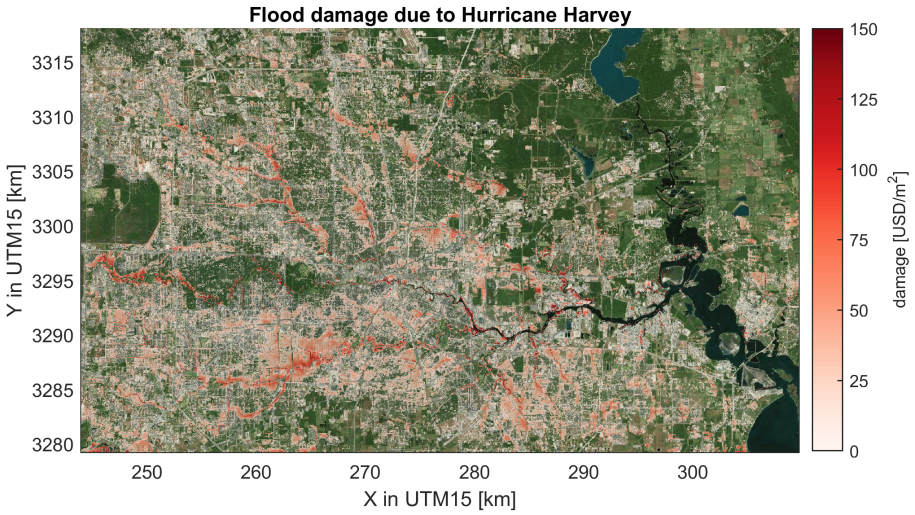

Figure 3.14: Damage in the Houston urban areas due to the flooding event as a result of landfall of Hurricane Harvey. Damage below 10 USD/m^2 is not plotted for visual purposes.

Resilient Texas (2019) shows an overview of the reported damage on zip-code detail level (see Table A.3). The total reported damage adds up to 5.46 billion USD. This indicates that the FIAT model overestimates the reported damages by 400%. However, according to Blake and Gibney (2011), it is expected that the damage estimate of the National Hurricane Center is the sum of double the insured losses estimation, plus an adjusted estimate of flood losses from the National Flood Insurance Program. A conservative assumption could therefore be done to double the insured losses as reported by Resilient Texas (2019). This results in an model overestimation of only 200%. Furthermore, homeowners insurance policies are capped at 250,000 USD, whereas the damage can exceed this value. This indicates that the total reported damage value could be underestimated, because this upper limit is not included in Delft-FIAT. In more detail, Figure 3.15 shows the difference between the modelled damage and the reported damage per zip-code after this adjustment. Here, it can be seen that for most areas the losses are overestimated by large numbers. The areas where the damage is underestimated are mostly located at the edge of the model domain, because not the entire zip-code area is modelled in SFINCS. It should be noted that the losses of Resilient Texas (2019) only account for reported damage and insurance claims, possibly underestimating the total damage done. Furthermore, not all properties are insured for flooding, so for these properties no claim is issued.

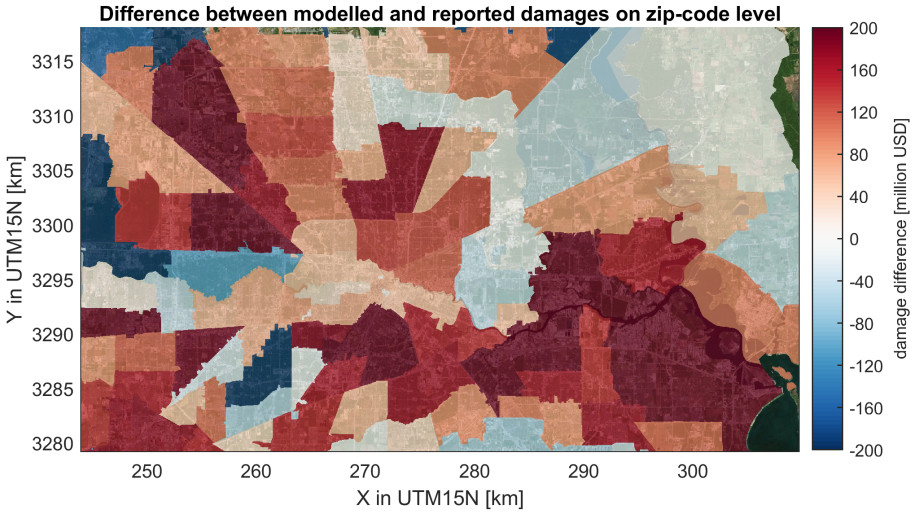

Figure 3.15: The difference between the modelled and reported losses due to Hurricane Harvey.

Furthermore, Figure A.20 shows the percentage of the area which is affected by at least 0.15 m water depth according to Delft-FIAT. Here can be seen for most areas only 50% of the area is affected. When linking this to Figure 3.15, it can be seen that although only part of the area is affected, significant overestimates of the damage value are modelled. Possible explanations are that the depth-damage curve is not suited for the city of Houston or that the maximum potential damage is not represented correctly. Moreover, it is important to notice that the north-eastern part of the model domain does not contain a lot of buildings which can be exposed. Therefore, the affected area reduces significantly. Nevertheless, it can be seen that the area around Brays Bayou experiences the largest impact in terms of area. It can also be seen that the damage values are significantly overestimated in that area.

3.4.3. Sensitivity

This section contains a sensitivity analysis for different model configurations. First, an assessment is made of the impact of the rain in this compound flooding event. Secondly, the axisymmetric rainfall schematization is assessed. Subsequently, the impact of the grid resolution on the model results is validated.

Compound Flooding The hydrological model results suggest that the flood event in Houston was driven by the pluvial component. The impact of the flooding is also greatly influenced by the rain. When the rainfall is removed as forcing on the model, the FIAT Accelerator indicates that only just shy of 30,000 people are affected by the flooding. Furthermore, the total accumulated damage in the case without rain is estimated to be close to 900 million USD, which is a small fraction of the total of 19 billion USD. Therefore, it can be concluded that the impact of Hurricane Harvey was pluvial-driven.

Precipitation Distribution From the hydrodynamic analysis followed that applying the more axisymmetric precipitation schematization from the NARR model, the MAE at peak water levels increased only slightly. This is related to the fact that the NARR schematization underestimated the rainfall rates and therefore the total cumulative rainfall. The resulting underestimation of water levels impacts the exposure analysis as well. The Delft-FIAT indicates damage up to 14 billion USD for the case when a more simple schematization of the precipitation is used. This is an underestimation of 25% compared to the scenario with the precipitation interpolated from weather stations. Furthermore, only 1 million people are affected by a flooding event which is driven by a NARR model rainfall. The used NARR model rain underestimated cumulative rainfall compared to the observations, which inevitably leads to an underestimation of the impact of the resulting flooding event. Nevertheless, it can be stated that a flooding due to the NARR model rain (i.e. an axisymmetric representation of hurricane rainfall) is deemed accurate in reproducing the impact of a compound flooding event.

Grid Resolution Equal to the sensitivity analysis of the hydrodynamic model, the effect of the grid resolution is assessed. The validation suggested that the different grid sizes had minimal impact on the maximum water depth during a compound flooding event like Hurricane Harvey. This can also be seen when taking into account the number of people of people affected by the flood. For different grid cell sizes (30, 50, 75 and 100 m) the total number of affected people is equal to the 25-meter grid model (see Figure 3.16). However, for the damage some slight deviation can be recognized. For example, the model results for a 100-meter grid cell size indicate a 21.2 billion USD of damage, which is an increase of 11 %.

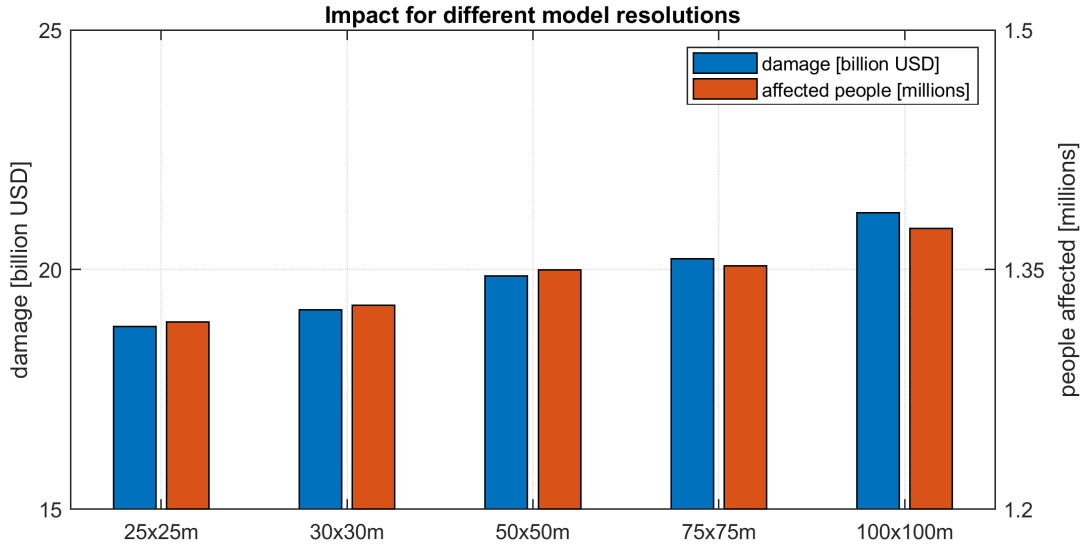

Figure 3.16: Bar-chart indicating the results for different model resolutions on the impact of Hurricane Harvey as modelled with SFINCS and Delft-FIAT.

3.5. Key Points

This case study was performed to assess the capability of a semi-advanced model to reproduce the pluvial-driven flooding event at Houston. This line of research was substantiated by the following research question:

How accurate can SFINCS reproduce the compound flooding event in Houston as a result of the arrival of Hurricane Harvey in terms of hazard and impact?

The following key points discuss the main results of this model validation study:

- A validation study is carried out with the semi-advanced SFINCS model to analysis accuracy of the SFINCS model for the flooding due to Hurricane Harvey. The model domain encloses the catchment areas for most main bayous. Catchment areas of the White Oak and Greens Bayou are not fully included in the model, which could affect the model results. The DEM is retrieved by interpolating the NED and CRM. Subsequently, some manual adjustments have been made to remove interpolation flaws;
- Delft-FIAT is used to carry out an exposure analysis by using flood hazard maps provided by SFINCS. The tool uses coarse global data and it is assumed that people and assets get affected by a water depth of 0.15 m or more;
- SFINCS is deemed accurate in terms of hydrodynamic processes for a 25-meter resolution. The peak water levels are reproduced with a MAE of 0.508 m (with an average water level raise of 7.5 m) and the complete water level time-series are scored with a NSE-value of 0.55 [-], which indicates a good model performance according to Ritter and Munoz-Carpena (2013). FIAT Accelerator gives a first estimate of 19 billion USD of damage and 1.3 million people affected. Compared to reported losses and claims, this is an overestimation of 200% in terms of costs and affected people. However, it can be stated that not all damage is reported. Furthermore, the reported damage is accumulated by adding up insurance claims indicating that non-insured buildings are not included. Moreover, homeowners insurances are capped at 250,000 USD, which is not taken into account in the Delft-FIAT model results. Therefore, the exact accuracy of the Delft-FIAT results is uncertain;
- SFINCS model results are prone to the model resolution used. For a 100-meter resolution, the water level time-series are reproduced with a NSE value of only 0.15 [-]. The peak water levels however, are still approximated with a MAE of 0.595 m. This indicates that the details of the flood wave can not be captured by a low resolution model, but the peak water levels can. Furthermore, lowering the resolution improves computational efficiency by a factor of fifteen. Moreover, in terms of impact, the damage and affected people are overestimated by 11% and 5.7% respectively compared to a 25-meter resolution. In short, a low resolution SFINCS model is suitable for carrying out a climate variability study;
- Sensitivity tests show that using an axisymmetric schematization of the rainfall (NARR model) instead of a high-detailed interpolated rainfall schematization does affect model performance significantly (MAE = 0.639 m, NSE = 0.53 [-]). The performance metrics are not significantly different from the model runs including a detailed interpolated rainfall model. Furthermore, the computational efficiency increases. This suggests that a more axisymmetric rainfall schematization can be used for a climate variability study; and
- Sensitivity tests show that the precipitation and the resulting reservoir release are mainly responsible for the flooding due to Hurricane Harvey. Therefore, it can be concluded that Hurricane Harvey is a pluvial-driven flood event.

4

Derivation of a Stochastic Rainfall Distribution

In this section the development of a parametric observation-based rainfall model is discussed. This chapter is divided in six sections. In Section 4.1 a short introduction is given. In Section 4.2 the materials and methods used for the derivation of rainfall schematization are discussed. Section 4.3 contains the derivation of the relation between maximum rainfall intensity and maximum sustained wind speed. In Section 4.4 the rainfall intensity fit to the radius is described and a validation is carried out. In Section 4.5 the assumption of independence between different observations is validated. To conclude, Section 4.6 describes the main findings of this derivation of the stochastic rainfall distribution.

4.1. Introduction

When the track and intensity of a TC are known, a spatial wind field and a spatial atmospheric pressure field can be reproduced by simple parametric relations (e.g. Holland et al. (2010)). For precipitation no such empirical relation, which is simple, applicable and validated for the entire world, exists. Several approaches to estimate the rainfall of a hurricane have been proposed in literature (for examples, see Section 2.2.3). However, these methods are often restricted geographically, by their computational demand or by availability of data.

Besides the abundance of solid deterministic relationships for the precipitation of TCs, one must also take into account the limited attention given to the stochastic nature of meteorological processes. Natural variability causes the TC parameters to not behave deterministically, but rather stochastically. This indicates that rainfall intensity is not only dependent on BTD (e.g. latitude, maximum wind speed), but also on other external environmental factors as mentioned in Chapter 2. This results in different spatial rainfall patterns for TCs which have the same BTD quantities.

In the last decades, a large amount of high-quality data has become available. The recorded data is mostly based on in-situ observations (e.g. buoy observations), but these high-quality observations are not routinely available. More common is the use of satellite observations. By means of scatterometry, different estimates can be made about TC parameters. Scatterometry is a method of remote sensing with satellites, where microwave sensors send out a signal and subsequently measure how much of the signal returns after interacting with the target (e.g. QuikSCAT, see Chavas and Vigh (2014)).

This data can be used to derive an empirical (stochastic) relationship for a description of TC rainfall in combination with another well-known TC characteristic, as given in BTD. This description can be seen as an observation-based parametric rainfall model.

4.2. Materials and Methods

In this section the materials and methods used in this derivation of a precipitation schematization are discussed. The first section contains a description of the dataset used. Secondly, the methodology to connect a rainfall quantity to another characteristic of the TC is explained. At last, the step towards a radial and spatial rainfall profile is discussed.

4.2.1. QSCAT-R

The QuikSCAT Tropical Cyclone Radial Structure (QSCAT-R) dataset, with data for the period 1999-2009, is used to derive an empirical relationship for maximum rainfall intensity (Chavas and Vigh, 2014). This dataset has been developed at the NASA Jet Propulsion Laboratory. It is derived from the latest version of the QuikSCAT near-surface ocean wind vector database and based on data of the QuikSCAT satellite. The dataset includes 804 unique TC profiles from all over the world and contains data for the radial structure of TCs, including:

- Radial profiles of total wind speeds, including the radial and azimuthal components;
- Gale force winds (e.g. R35), estimated of the radial wind profile;
- Radial profiles of rainfall rate and its radial symmetry; and
- Radial profiles of cloud liquid data.

For a full overview of the included data parameters and the data structure, one is referred to Chavas and Vigh (2014).

According to the World Meteorological Organization, TCs can form in seven basins (NOAA, 2018b). The QSCAT-R dataset accounts for all seven basins. Figure 4.1 gives an indication for these basins and at the same time show all TC tracks that are included in this derivation. The dataset uses near-surface wind vectors with 10-minute averaged wind speed at 10-meter height above surface level. For precipitation, the rainfall rates equal zero artificially in the vicinity of the coastline. To crudely account for this problem all rainfall rate data within 100 km of the coastline has been removed (Chavas and Vigh, 2014). Therefore, the data only includes observations above water surfaces. Furthermore, all rainfall asymmetry is neglected. Nevertheless, over 8,000 single observations are taken into account for this derivation.

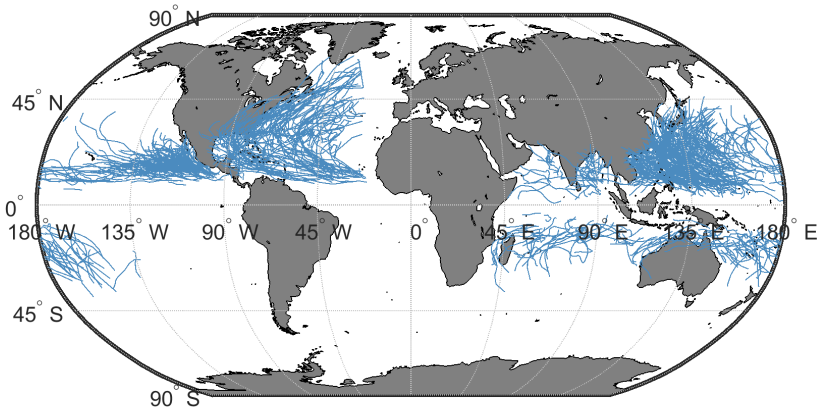

Figure 4.1: All TC tracks contained in the QSCAT-R dataset.

For this analysis, the dataset is split into two subsets which are generated randomly. The calibration-dataset contains 70% of the data and the validation-dataset contains 30% of the data. These datasets contain individual observations and the assumption is made that all observations behave independently from each other. So, for example, from a single TC, every observation is seen as an individual independent realization of TC characteristics.

4.2.2. Copulas

Hydrological and climatological phenomena are often multidimensional and their variables are interdependent. Hence, it requires the joint modelling of these variables to understand their interactions and associa-

tions. Traditionally, this has been done by describing variables as storm surge, precipitation and depth using classical distribution families. Limiting factor of this approach is that the individual behavior of these variables is described by the same distribution family (e.g. normal, log-normal, Genest and Favre (2007)).

Copula models, an example of a multivariate analysis method, avoid this restriction. A copula is a multivariate distribution with uniform (values ranging from 0 to 1) marginal distributions. The copula approach was first presented by Sklar (1959). According to his theorem, the joint cumulative distribution function H(x,y) of any pair of continuous random variables (X and Y) can be rewritten as:

$$H(x,y) = C\{F(x), G(y)\}\text{x,y} \in \mathbb{R} \tag{4.1}$$

Where F(x) and G(y) are any marginal distribution and C represents the copula. Since the margins of a copula are restricted by interval [0,1], it is possible to model the dependence between two variables with their cumulative distribution functions (CDFs). The CDFs are defined in the same interval as the copula, regardless of the chosen marginal distribution for each variable. So, the main advantage of this multivariate analysis approach is that the selection of an appropriate dependence model between X and Y, represented by the copula, can proceed independently from the choice of marginal distributions. However, when sampling from a copula, the values between [0,1] (the copula dataspace) should be reconverted to values from the marginal distribution again (the original dataspace). A copula can be used for multiple different variables without the previously mentioned assumptions to be incorrect. This research focuses on the application of 2-dimensional copulas, mostly referred to as a bivariate analysis.

The bivariate analysis is carried out with the Multivariate Copula Analysis Toolbox (MvCAT, Sadegh et al. (2017)). This MATLAB (The MathWorks, Inc., 2018) toolbox is able to fit 24 different copula families to given data. After analysis, the selected copula families are ranked based on different performance metrics: maximum likelihood, NSE, RMSE, Bayesian Information Criterion (BIC) and Akaike Information Criterion (AIC). Thus, this toolbox provides the best copula fit to given data. A short description of the given performance metrics is given below.

The maximum likelihood value is the most widely used calibration criterion in hydrology according to Thyer et al. (2009). The maximum likelihood minimizes the residuals between model simulations (in this case the copula) and observations. Higher model complexity (more degrees of freedom; more model parameters) provides greater model flexibility, thus a better fit to the observations. Nevertheless, this can also stimulate unnecessary over-conditioning of the model (Sadegh et al., 2017). In contrast to the maximum likelihood, the AIC takes into account both complexity of the model and magnitude of the residuals. The BIC is a similar performance indicator.

Furthermore, the MvCAT is able to fit marginal distribution families to the two variables considered for the bivariate analysis. However, the MvCAT does not provide a ranking based on performance metrics for this marginal distribution fit. To substantiate the decision for the proposed distributions, a comparison is made with other marginal distributions, based on the methodology of Torres Duenas (2018). This includes a comparison based on the probability density function (PDF), CDF, probability of exceedance, Normalized Root Mean Square Deviation (NRMSE) and the Normalized Mean Square Error (NMSE):

$$\text{NRMSE} = \frac{\text{RMSE}}{P_{max} - P_{min}} \tag{4.2}$$

$$\text{NMSE} = \frac{\overline{(P_{obs} - P_{pred})^2}}{\bar{P_{obs}}\bar{P_{pred}}} \tag{4.3}$$

The NRMSE divides the RMSE by the difference between the maximum (P_{max}) and minimum (P_{min}) modelled value. The NMSE compares the observed (P_{obs}) and the predicted (modelled) values (P_{pred}). For both these performance indicators holds that the result can be a value between 0 and 1. A value closer to 1 indicates a better model.

The acquired copula fit can be used to sample a maximum rainfall intensity according to a given maximum sustained wind speed. Subsequently, the sampled maximum rainfall intensity can be fitted to the radius of a TC to create a radial and spatial rainfall distribution.

4.2.3. Radial Rainfall Profile

The best copula fit can be used to sample rainfall data according to another quantity, given the right probability space. To fit this rainfall sample with the radius of the TC a similar formulation as the Holland wind-profile is used (Holland et al., 2010). The Holland profile creates a radial wind-profile depending on the radius of maximum winds and the maximum measured wind speed:

$$v_{wind}(R) = \left(\frac{vmax * \left(\frac{rmax}{R}\right)^{b_s}}{\exp\left(\left(\frac{rmax}{R}\right)^{b_s}\right)}\right)^{x_n} \tag{4.4}$$

In which the wind distribution along the radius v_{wind} is dependent on the maximum sustained wind speed *vmax*, the RMW *rmax*, the radius R and two fitting coefficients b_s, x_n. For the Holland wind-profile, the fitting coefficients have a physical definition linking various parameters to the magnitude and shape of the wind- and pressure-profile. In this application however, the coefficients are fitted according to the data and no longer represent a physical process, as in the wind-profile relationship of Holland et al. (2010). The fit gives an empirical-like distribution of the rainfall over the radius of the hurricane when replacing *vmax* with the maximum rainfall intensity (*pmax*) in the equation presented above. Furthermore, the *rmax* is set equal to the radius of maximum rainfall intensity (opposite to the radius of maximum winds in the Holland wind-profile).

4.3. Maximum Rainfall Intensity (pmax)

The large amount of scatter between the maximum rainfall intensity (*pmax* in mm/hr) and the maximum sustained wind speed (*vmax* in m/s) is shown in Figure 4.2 for all observations. Where *vmax* is a 10-minute averaged wind speed at 10-meter height above a reference level and *pmax* is the maximum rainfall intensity as retrieved from the radial rainfall profile (Knapp et al., 2010). The combinations of *vmax* and *pmax* with a maximum rainfall intensity lower than 10 mm/hr have been removed from the dataset. Furthermore, the QSCAT-R dataset does not include observations with a maximum sustained wind speed under 10 m/s. There is a clear pattern visible which indicates that a larger maximum sustained wind results in a larger maximum rainfall intensity. This is in line with other observations and models, according to literature (e.g. Lonfat et al. (2004), Tuleya et al. (2007)). Furthermore, maximum sustained wind speed is used as an indicator for storm intensity, as well as storm category. This was already seen in Figure 2.4, where a similar connection between the maximum rainfall intensity and the storm intensity can be recognized. Moreover, there seems to be spatial variability in the observations of *pmax* and *vmax* (see Appendix B.2). Nevertheless, it should be noted that the focus of this research is on deriving a generic stochastic rainfall distribution model, so no further research into the spatial variability is carried out.

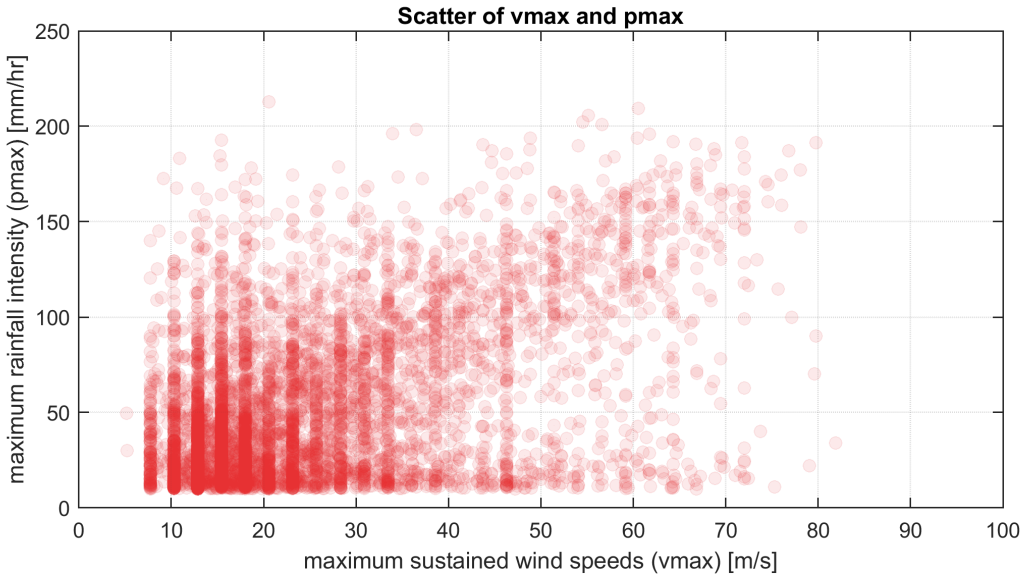

Figure 4.2: Scatter of maximum rainfall intensity (*pmax*) and maximum sustained wind speed (*vmax*) of the calibration dataset. Red dots are individual observations. More frequent observations are shown in darker red.

The dependence between two variables can be expressed with different correlation metrics, see Table 4.1. The Kendall Rank, Spearman Rank-Order and Pearson Product Moment are measures of strength of linear associations between two variables (Taylor, 1997). Moreover, the direction of association between the two variables is taken into account. A correlation metric with value 1 indicates a full positive dependence. In other words, a high value of maximum sustained wind speed correlates with a high value of the maximum rainfall intensity. A correlation metric with value -1 indicates a full negative dependence. In this case, a high value of maximum sustained wind speed correlates with a low value of maximum rainfall intensity. Thus, a strong inverse relationship. A value of zero indicates little, if any, relationship.

Table 4.1: Magnitude of dependence between maximum rainfall intensity (*pmax*) and maximum sustained wind speed (*vmax*) based on three different metrics.

Correlation Metric	Parameter	Value
Kendall's Rank	τ	0.2630
Spearman's Rank-Order	ρ	0.3719
Pearson Product Moment	r	0.4759

The maximum rainfall intensity and the maximum sustained wind speed show a degree of dependence. The correlation metrics indicate a weak positive correlation. Due to the great scatter in the data, which is most likely the result of the stochastic character of meteorological phenomena, the magnitude of dependence is limited. Moreover, the distribution of the data indicates more frequent observations in the south-west quadrant of Figure 4.2 compared to the north-east quadrant. This suppresses the correlation metric values.

Adding other parameters like storm motion or latitude results in very limited skill improvement in the estimation of the maximum rainfall intensity. This can be seen from the different correlation metrics presented in Table 4.2. Furthermore, this is visualized in Appendix B.1. This appendix shows scatter plots of different parameters in combination with *pmax*. Here can be seen that the combination of maximum rainfall intensity and maximum sustained wind speed is the only combination where significant dependence can be recognized.

Table 4.2: Magnitude of dependence between maximum rainfall intensity (*pmax*) and other TC characteristics based on three different metrics.

Correlation Metric	Parameter	Latitude	Longitude	Storm Motion
Kendall's Rank	τ	-0.0207	0.0876	0.0173
Spearman's Rank-Order	ρ	-0.0312	0.1317	0.0182
Pearson Product Moment	r	-0.0573	0.1333	0.1777

4.3.1. Fitting Procedure

Marginal Distribution A marginal distribution is a probability distribution of a variable. It gives the probability of various values of the parameter. To perform a data analysis, a wider set of random variables is generated by the marginal distribution, which are in line with the occurrence probability of observed values. These marginal distributions are used to fit the correct copula family. Moreover, in order to retrieve a value from the original dataspace, the sample from the copula space needs to be inverted to the original marginal distribution (with the inverse CDF). The MvCAT is used to give a first estimate for the best marginal distribution fit to the *pmax* and *vmax* data acquired from the QSCAT-R dataset. Subsequently, this has been validated by a fitting-analysis of other distributions, see Appendix B.3. Based on this comparison, the MvCAT-proposed marginal distribution is the best fit for both the maximum rainfall intensity and the maximum sustained wind speed. These marginal distribution fits are presented in Figures 4.3 and 4.4.

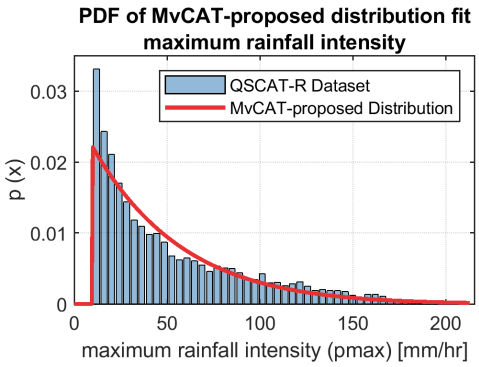

Figure 4.3: The proposed MvCAT distribution (Generalized Pareto) fitted to the maximum rainfall intensity data from the QSCAT-R calibration dataset.

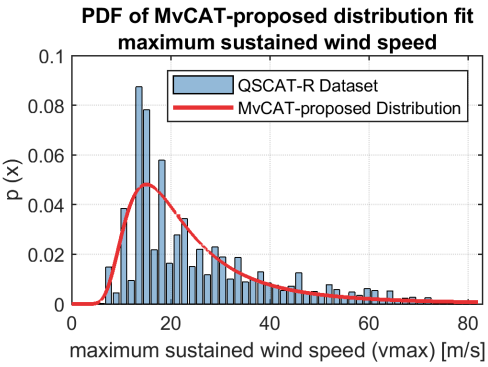

Figure 4.4: The proposed MvCAT distribution (Generalized Extreme Value) fitted to the maximum sustained wind speed data from the QSCAT-R calibration dataset.

To conclude:

- The maximum rainfall intensity (*pmax*) can be described by a Generalized Pareto distribution. The Generalized Pareto distribution is described by three parameters:
  - k = -0.0686 (shape parameter);
  - σ = 45.2829 (scale parameter); and
  - θ = 10.002 (threshold parameter).
- The maximum sustained wind speed (*vmax*) can be described by a Generalized Extreme Value distribution. The Generalized Extreme Value distribution is described by three parameters:
  - k = 0.346 (shape parameter);
  - σ = 8.0676 (scale parameter); and
  - μ = 17.3637 (location parameter).

Copula The MvCAT is able to analyze 24 different copula families and rank them based on performance metrics. Applying the before-mentioned distributions for maximum rainfall intensity and maximum sustained wind speeds, the toolbox is capable of fitting these distributions with a copula family. For a full ranking of the 24 copula families according to maximum likelihood, AIC, BIC, RMSE and NSE, see Appendix B.4. The Frank Copula proves to be the best fit to the data (RMSE = 1.4686 [1] and NSE = 0.9951).

The Frank Copula is part of the Archimedean Copula Family, which contains a large variety of copulas. The Archimedean copula family is a favorable copula family for hydrological analysis. It is easily constructed (described by one parameter) and it can be applied when correlation is both positive and negative (Zhang and Singh, 2007). The Frank Copula is described by the following expression:

$$C(u,v) = -\frac{1}{\theta} \cdot ln(1 + \frac{(e^{-\theta u} - 1)(e^{-\theta v} - 1)}{(e^{-\theta} - 1)}) \tag{4.5}$$

Where u and v are the parameters representing the maximum sustained wind speed and the maximum rainfall intensity respectively. The value for the copula parameter (θ = 3.58) is acquired during the fitting procedure. A decrease of this parameter value would lead to a less defined dependence between *pmax* and *vmax*. The impact of this parameter is further discussed in Section 4.3.3. The Frank Copula is known for its symmetric behavior. This is unlike other Archimedean copulas such as the Gumbel Copula, which shows greater dependence in the positive tail compared to the negative tail. Although Figure 4.2 suggests that tail dependence would be expected, the frequency of observations in the south-west quadrant of the data-plot is much higher than in the north-east domain. For this reason the symmetric Frank Copula is proposed as a better fit, see Figure 4.5.

[1] dimensionless, because dimensions of a multivariate space cannot be made satisfactorily commensurate (Willmott et al., 1985).

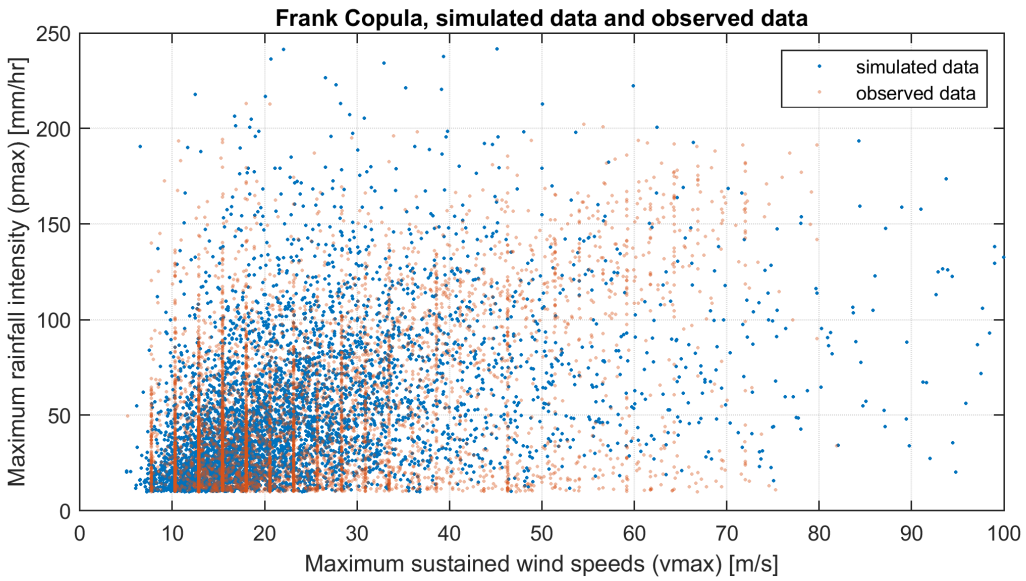

Figure 4.5: The simulated data (5,000 random samples) versus the observed data. Red dots are individual observations, more frequent observations appear in a darker red.

4.3.2. Conditional Sampling

The proposed copula is, in a way, a relationship between the maximum rainfall intensity and the maximum sustained wind speed. A copula represents the joint distribution function H(x,y) as a function of $F(x)$ and $G(y)$ (i.e. $H(x,y) = C\{F(x), G(y)\}$). This is a way to express the joint probability of the two variables. It is straightforward to sample a random combination of the two variables based on their joint probability (i.e. random *vmax* and random *pmax*). For this research however, it is required to sample the maximum rainfall intensity given a maximum sustained wind speed. This is called conditional sampling (i.e. given *vmax*, sampled *pmax*).

A conditional distribution of a copula can be derived. Let $C_1(u,v)$ be the derivative of $C(u,v)$ with respect to argument u (*vmax*). If the joint distribution of X and Y is given by $F(x,y) = C\{F_X(x), F_Y(y)\}$, then the conditional distribution of Y given X=x (i.e. $Y|X = x$) can be defined as (Venter, 2002):

$$F_{Y|X}(y) = C_1(F_X(x), F_Y(y)) \tag{4.6}$$

Thus, in the case of a Frank Copula, the conditional distribution is stated as follows:

$$v = -\frac{1}{\theta} \cdot \ln(1 + \frac{p(e^{-\theta} - 1)}{e^{-\theta u} - p(e^{-\theta u} - 1)}) \tag{4.7}$$

Where u is a representation of the maximum sustained wind speed and p is considered a draw from the conditional distribution of v (*pmax*) given u (*vmax*), within the copula limits of [0,1]. Since this p is distributed with function C_1, the value for v (*pmax*) can be found as $v = C_1^{-1}(p|u)$. This is the parametric form of the formula given in Equation 4.7. When u and v have been extracted, the variables of interest can be inverted to the original sample space with their marginal distributions. An example of a set of random samples of *pmax* given a certain *vmax* can be seen in Figure 4.6.

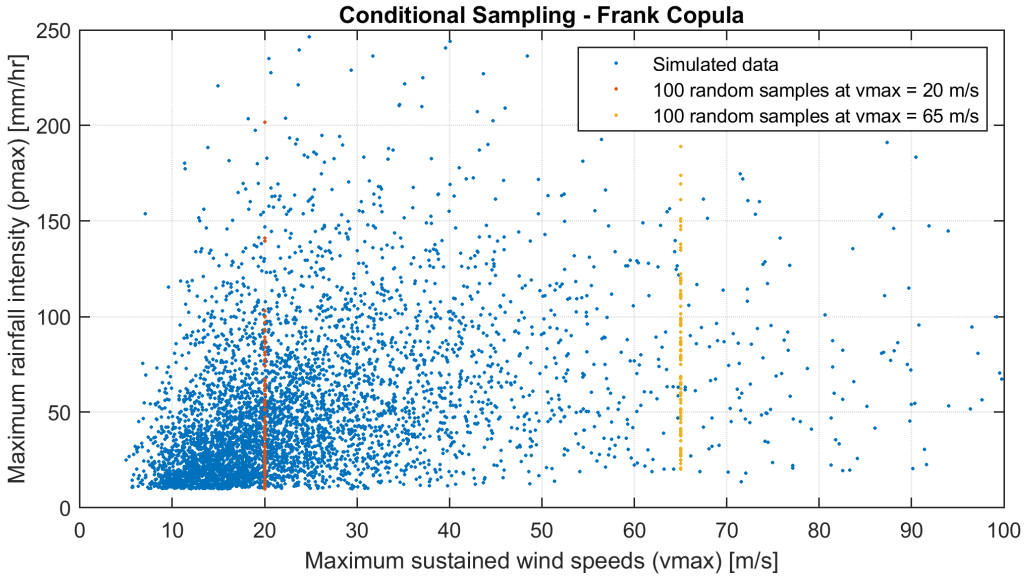

Figure 4.6: 5,000 random realizations of the Frank Copula in blue. The differently colored dots are 100 random samples retrieved with the conditional sampling for a maximum sustained wind speed of 20 m/s and 65 m/s respectively.

The random samples are distributed over a range of maximum rainfall intensities, as the scatter in the original dataset suggests. Nevertheless, due to the difference in joint probability for different combinations of the variables, the pattern of positive dependence can be noticed. In Table 4.3 a quantitative description of the sampled data is given. It can be seen that, in general, high sustained wind speeds result in a higher maximum rainfall intensity. However, as the QSCAT-R data suggests, there is a large natural variability in the data. This indicates that a higher sustained wind speed is not per definition connected with a higher maximum rainfall intensity. This randomness is also recognized in the suggested copula schematization.

Table 4.3: An example of conditional sampling of maximum rainfall intensities (*pmax*) at two different values of maximum sustained wind speed (*vmax*).

Value	$vmax = 20$ [m/s]	$vmax = 65$ [m/s]
5%-sample	11.3 mm/hr	27.2 mm/hr
25%-sample	23.9 mm/hr	51.3 mm/hr
50%-sample	38.6 mm/hr	79.6 mm/hr
75%-sample	61.2 mm/hr	110.6 mm/hr
95%-sample	96.9 mm/hr	161.2 mm/hr

4.3.3. Validation

According to this procedure, a comparison is made with the validation dataset. First, an equal procedure as in Section 4.3.1 is followed to fit a copula family to the data of the validation dataset. This gives a suggested copula fit for the validation set, which can be compared to the fit to the calibration dataset. Secondly, a comparison is made with the observed values in the validation dataset.

Copula Equal to the methodology in Section 4.3.1 a fit is proposed for the validation data. First the marginal distributions are fitted and secondly these distributions are fitted to a copula family with the MvCAT. This results in the following ranking of the copula families. For clarity, only the best three copula fits are given.

Table 4.4: Sorted copulas based on different criteria according to MvCAT (Sadegh et al., 2017) for the validation dataset. A star indicates a warning by the MvCAT. The copula parameter is in this case converging to the parameter boundary and it would therefore be possible that this copula is not a good fit.

Rank	Maximum Likelihood	AIC	BIC	RMSE	NSE
1	Frank	Frank	Frank	0.8790	0.9973
2	Nelsen	Nelsen	Nelsen	0.8790	0.9973
3*	Roch-Alegre	Roch-Alegre	Roch-Alegre	0.9266	0.9970

It can be seen in Table 4.4 that the fitting procedure for the validation dataset gives the same result in terms of best fitted copula as the calibration dataset. The Frank Copula is considered to be the best fit to the given data. The only main difference is the copula parameter θ. For the validation dataset this yields $\theta = 4.42$, where for the calibration dataset $\theta = 3.58$ was established. The influence of this parameter on the probability space of the copula can be seen in Appendix B.5. A lower θ indicates a less defined positive dependence between the two parameters. Further quantification of this difference is given in the next section.

Conditional Sampling Figure 4.7 shows good agreement between the validation dataset and the proposed methodology of random sampling from a copula up until a maximum sustained wind speed of 40 m/s. The blue line indicates the median *pmax* values according to random sampling method, whereas the solid green line represents the median *pmax* as it is contained in the QSCAT-R data. The dotted black lines indicate the 5 and 95 % exceedance values of the dataset, whereas the variance in the random samples is given with the red color fill. The stochastic character is shown by the original dataset and the samples of the proposed methodology. This can be recognized by the location of the confidence interval boundaries. The confidence interval boundaries do show some dissimilarities however. Especially for maximum wind speeds between 20 and 60 m/s, the proposed equations tend to overestimate maximum rainfall intensity up to 20 mm/hr for both the 5%- and 95% sample.

Moreover, for higher wind speeds the similarities between the sampling method and the dataset decrease. The median value of the data exceeds the median value of the samples. This could be explained by the lack of data for high sustained wind speeds and therefore no good representation of the median value. Furthermore, the proposed Frank Copula is a symmetric copula, indicating that it does not show strong tail-dependence. This suggests that the combination of a high *pmax* and *vmax* is not sampled often, which is in line with the observations, because only five observations with a *vmax*-value of 70 m/s are recorded. Although the confidence interval bands are given, more-or-less, correct for the entire *vmax* dataspace, the median *pmax* value could be underestimated by up to 60 mm/hr for the higher sustained wind speeds. Overall, the proposed method indicates a Root Mean Square Difference (RMSD) of 37.9 mm/hr and a bias of -6.79 mm/hr between the median of the dataset and the median of the proposed methodology.

The performance of the proposed copula-fit is dependent on its application. If the value for *pmax* is sampled according to the median value, it is expected that the value of the maximum rainfall intensity is underestimated for higher maximum sustained wind speeds. However, taking into account the randomness in natural phenomena suggests that the *pmax* should be sampled randomly. According to the large variation in the data and the proposed methodology this possibly leads to a more accurate description of the maximum rainfall intensity value. To conclude, the performance of the copula-fit for high maximum sustained wind speed values is dependent on the method of sampling.

The influence of the copula parameter (θ) on the RMSD is negligible. For θ in the range of 2.0 to 5.0, the RMSD only varies 1.6 mm/hr. Therefore, it is concluded to let θ be defined according to the calibration period ($\theta = 3.58$). This value is based on a larger fraction of the QSCAT-R observation dataset.

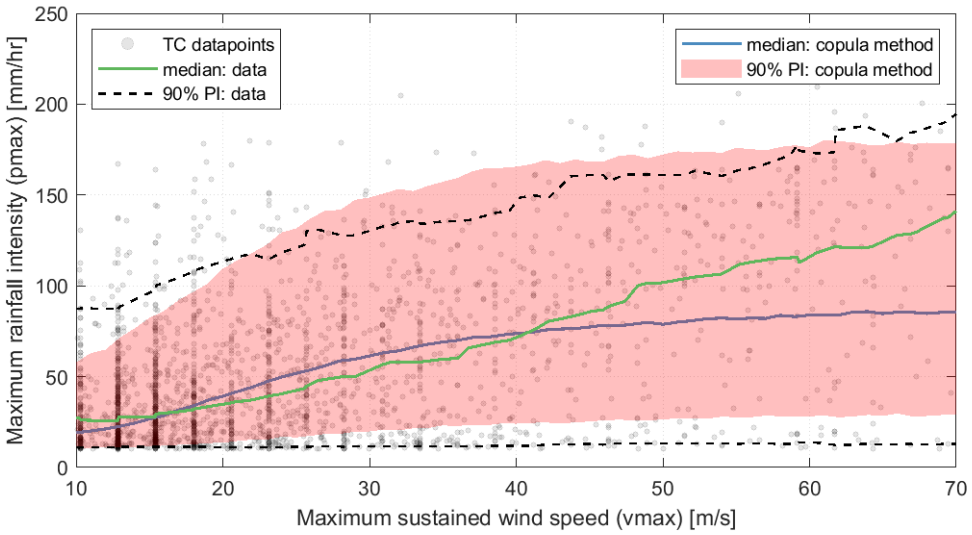

Figure 4.7: Scatterplot describing maximum rainfall intensity (*pmax*, observed and predicted) as function of the maximum sustained wind speed (*vmax*) of the validation dataset. The blue line is the median of the proposed sampling method, whereas the green line indicates the median of the dataset. Gray dots are individual observations, more frequent observations are shown in darker gray.

4.4. The Radial Rainfall Profile

Inspired by Holland et al. (2010), a proposition is done to create a radial rainfall profile. As mentioned in literature (e.g. Lonfat et al. (2007)), rainfall intensity decreases by increasing radius. The radial rainfall profile has an exponential-like fit, which can be described by the following equation. This is based on the relationship used for the wind-profile of Holland et al. (2010):

$$p_r(R) = \left(\frac{pmax * \left(\frac{rmax}{R}\right)^{b_s}}{\exp\left(\left(\frac{rmax}{R}\right)^{b_s}\right)}\right)^{x_n} \tag{4.8}$$

Where p_r is the rainfall intensity at a radius R. The maximum rainfall intensity is defined by *pmax* and *rmax* is equal to the RMW. The fitting parameters are given by b_s and x_n. In this formulation the coefficients are used as shape and scaling parameters, the physical definition as used for the Holland wind-profile is no longer valid. It is assumed that the radius of maximum rainfall intensity coincides with the radius of maximum wind. The data suggests that this holds true for high rainfall intensities, but not for lower maximum rainfall rates, see Figure 4.8. However, a significant fraction of the observations substantiate this assumption, see the density scatterplot in Figure 4.9. Therefore, although this is a pragmatic assumption, this relationship is applied to enable the creation of a radial rainfall profile based on readily available data.

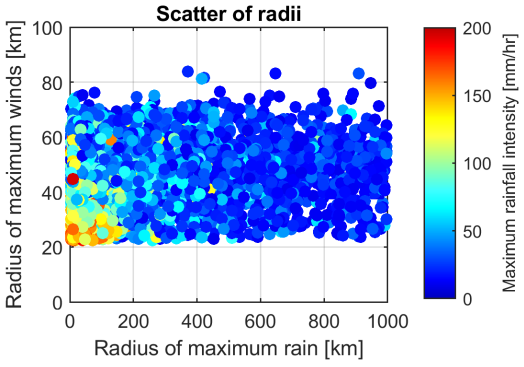

Figure 4.8: The observed RMW and the observed radius of maximum rainfall intensity. The dots are color-coded by the maximum rainfall intensity.

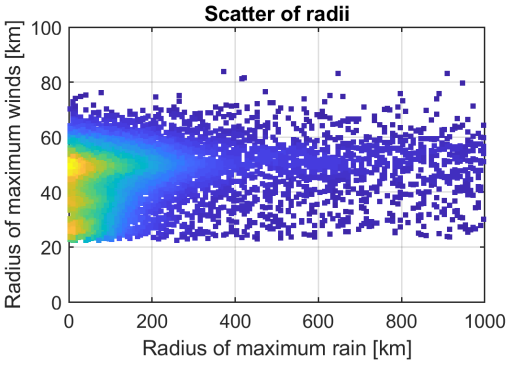

Figure 4.9: The observed RMW and the observed radius of maximum rainfall intensity. The squares are color-coded according to the frequency of the observation, yellow squares indicate more frequent observations.

For every TC included in the QSCAT-R dataset, an empirical fit is made based on Equation 4.8. This indicates that the fitting parameters b_s and x_n can be determined by a least-square fitting procedure. The coefficients are fitted according to $b_s = a \cdot pmax^b$ and $x_n = a \cdot pmax^b$. The results can be seen in Figures 4.10 and 4.11. The fits indicate that a clear pattern is recognizable, but there is some scatter in the data. For the creation of the radial rainfall profile, the equations presented in the bottom right of each figure are used.

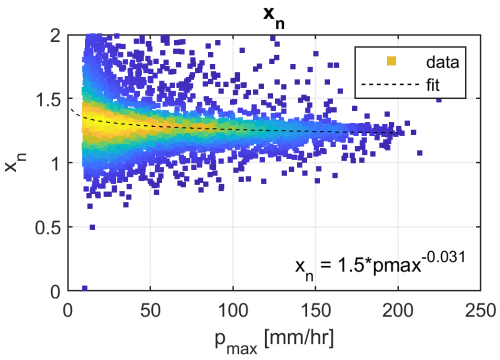

Figure 4.10: Best fit (black dotted line) for the fitting coefficient x_n. The squares are color-coded according to the frequency of the observation, yellow squares indicate more frequent observations.

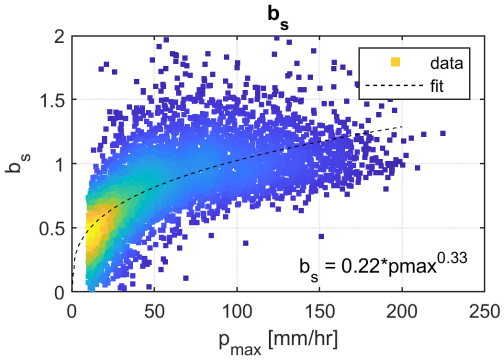

Figure 4.11: Best fit (black dotted line) for the fitting coefficient b_s. The squares are color-coded according to the frequency of the observation, yellow squares indicate more frequent observations.

An example of a radial rainfall intensity profile, as created from this procedure, can be seen in Figure 4.12. The differently colored dotted lines represent fits of different values of maximum rainfall intensity (out of a set of 100,000 sampled *pmax*-values) at the same maximum sustained wind speed. The difference in magnitude between the sample profiles emphasizes the stochastic behavior of meteorological phenomena, which could already be seen in Figure 4.6. At the same time it shows that the proposed model can sample a wide range of values for the same maximum sustained wind speed. The fitting coefficients x_n and b_s are dependent on the value of *pmax*, this is the reason that the fit to the 95%-value of *pmax* shows a higher decrease with increasing radius compared to other *pmax* values. The blue line indicates the observed radial rainfall profile of Hurricane Isabel at 21:41h (UTC) on September 10, 2003.

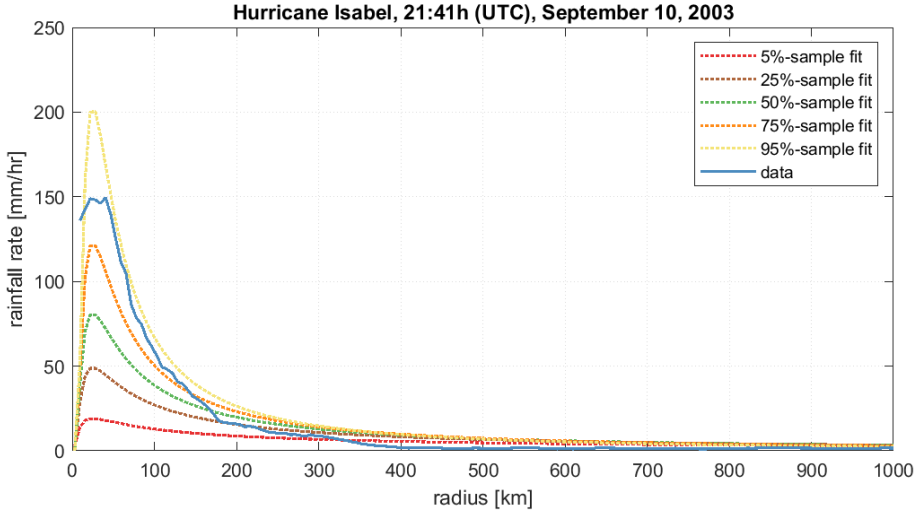

Figure 4.12: An example of rainfall intensity distributed over distance from the hurricane's eye for Hurricane Isabel (2003) at a moment in time. Fits for different sampled values for the maximum rainfall intensity are given. The solid blue line indicates the observed radial rainfall profile from the QSCAT-R dataset.

4.4.1. Validation of the Radial Rainfall Profile

The proposed observation-based parametric rainfall model is validated by means of two performance metrics. First, the sampled and observed *pmax*-value are compared with the maximum rainfall intensity that is created by fitting according to Equation 4.8. Secondly, the total radial rainfall (i.e. the area under the radial rainfall profile) is compared with observations.

Maximum Rainfall Intensity To validate the proposed radial rainfall fit, a comparison is made with the data. To quantify the performance of the rainfall model this assessment consists of two parts. First, the *vmax* observations from the validation dataset are used to sample 100,000 samples of *pmax*. Subsequently, the different *pmax*-samples are fitted to a radial rainfall profile according to Equation 4.8. From the fitted radial rainfall profiles, the *pmax* is retrieved and compared with the *pmax* according to the sampled value and the observed value at the given *vmax* observations in the validation set. This results in three performance metrics for the comparison of different sample fits to the sampled and observed maximum rainfall intensity (see Table 4.5).

Table 4.5: Performance metrics for the fitted *pmax* (for different sample fits) compared to the sampled *pmax* and the observed *pmax* from the validation dataset.

fitted *pmax* - sampled *pmax*	RMSD [mm/hr]	bias [mm/hr]	MAE [mm/hr]
5%-sample fit	9.2	-8.4	8.4
25%-sample fit	4.7	-4.3	4.3
50%-sample fit	3.4	-2.3	3.0
75%-sample fit	5.3	2.0	4.4
95%-sample fit	16.8	14.5	14.5
fitted *pmax* - observed *pmax*	RMSD [mm/hr]	bias [mm/hr]	MAE [mm/hr]
5%-sample fit	62.9	-46.2	46.5
25%-sample fit	52.1	-28.2	35.9
50%-sample fit	47.6	-9.9	35.5
75%-sample fit	54.1	17.8	45.1
95%-sample fit	101.6	83.5	89.1

First, when the sampled *pmax* is fitted according to Equation 4.8, it seems that for the low-end values, the maximum rainfall intensity in the profile is underestimated (negative bias for the 5, 25 and 50-% sample fits) in the fitted profile compared to the sampled value. For the extreme values (75 and 95%-sample fits) the fit causes the sampled *pmax* to be significantly overestimated due to the fitting procedure (positive bias). A possible explanation could be that the fitting coefficient b_s shows large scatter in Figure 4.11, but is represented with a single least-squares fit.

Secondly, for the comparison of the fitted *pmax* compared to the observed maximum rainfall intensity in the validation dataset, it can be seen that the model underestimates the values for the low-end sample fits. For the high-end sample fits, the *pmax* value is overestimated to larger extent. This is related to the large scatter as observed in the data and the proposed sampling method (see Figure 4.6).

To further understand the performance of this radial rainfall profile, the same analysis is carried out for three different categories: *pmax* < 50 mm/hr, 50 mm/hr < *pmax* < 100 mm/hr, *pmax* > 100 mm/hr (see Table 4.6). When looking at the performance metrics for the difference between the fitted and observed *pmax* for the 50%-sample fit, it can be seen that for the first category (*pmax* < 50 mm/hr) the model overestimates the observed value (positive bias of 10.5 mm/hr), but for the other categories greatly underestimates the observed *pmax* (negative bias of up to 68.1 mm/hr). The difference can be explained with Figure 4.6. Here can be seen that the median-value (50%-sample) is underestimating the maximum rainfall intensities at *pmax*-values exceeding 70 mm/hr. For values lower than this threshold this is the other way around. The frequent occurrence of lower *pmax* values (see Figure 4.2) in the complete QSCAT-R dataset, suppresses the bias for the 50%-sample over all observations in Table 4.5.

Table 4.6: Performance metrics for the 50%-sample fit *pmax* (for different sample fits) compared to the sampled *pmax* and the observed *pmax* for different categories.

fitted *pmax* - sampled *pmax*	RMSD [mm/hr]	bias [mm/hr]	MAE [mm/hr]
pmax < 50 mm/hr	24.4	10.5	18.1
50 mm/hr < *pmax* < 100 mm/hr	34.3	-26.4	28.7
pmax > 100 mm/hr	73.6	-68.1	68.1

To conclude, the fitted maximum rainfall intensity is most of the time not equal to the modelled maximum rainfall intensities. This has to do with the performance of the conditional sampling method as presented in Figure 4.6. Here is shown that the model is underestimating observed median values for the high maximum sustained wind speeds and maximum rainfall intensities. Furthermore, a 5% or 95%-sample fit would initiate a large error between the observations and the model results. The most extreme category would show a large underestimation for the 5% sample fit and an overestimation for the 95%-sample fit as can also be seen in Figure 4.6. For future application the *pmax* value is sampled randomly (i.e. not according to a metric like the median or mean value), this could indicate a large variability in the sampled *pmax* and its error.

Total Radial Rainfall Another way to analyze the suggested profile is by looking at the total radial rainfall, which is defined as the area under the radial rainfall profile. With increasing radius, the accuracy of the fit seems to decay. The modelled radial rainfall profile has a long tail (i.e. large radii, $p_r(R)$ still larger than zero). In observations however, the long tail profile is not (always) present. Figure 4.12 can serve as an example. Hurricane Isabel (at 21:41h (UTC) on September 10, 2003) shows a radial rainfall profile, which shows close resemblance with the 75%-sample fit for lower radii. Furthermore, the rainfall rate equals zero for radii equal to or larger than 400 km. For all proposed radial sample fits however, this is not the case. As a result, the total rain in this radial rainfall profile is overestimated at this observation of Hurricane Isabel.

The example of Hurricane Isabel shows a exponential-like observed radial rainfall profile. For radial rainfall profiles with a low maximum rainfall intensity (*pmax* < 50 mm/hr) however, the profile is deviating from the exponential distribution. Furthermore, Figure 4.8 already suggested that for lower rainfall intensities the *pmax* is not located at the radius of maximum winds for all observations. Figure 4.13 shows all observations (*pmax* < 50 mm/hr). Here can be noticed that the profile is no longer exponential per definition and especially that maximum rainfall intensities are no longer concentrated at small radii. This causes the proposed radial rainfall distribution to be overestimating the precipitation intensity at smaller radii. The difference of the radial rainfall profiles of different categories can be seen in Figures B.20 and B.21 in Appendix B.6. It can be noted that these high-end categories do represent an exponential-like profile.

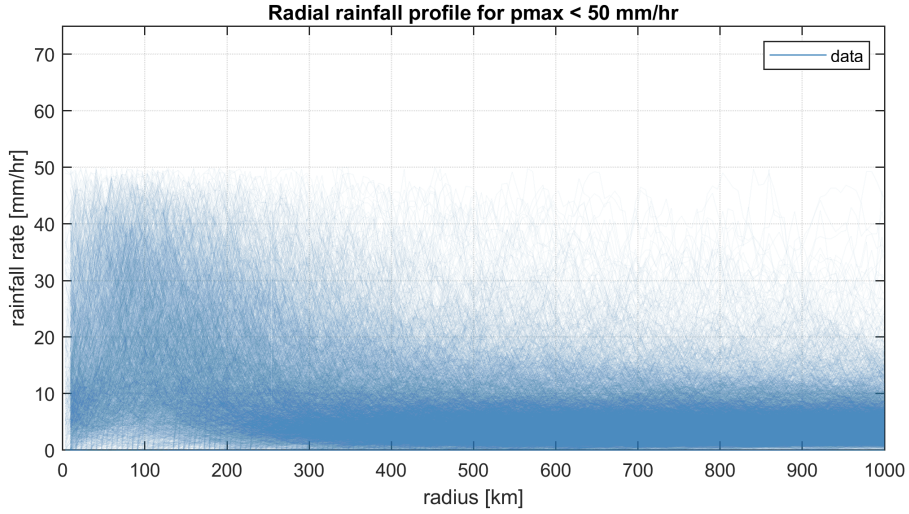

Figure 4.13: Absolute radial rainfall profiles for observations with *pmax* < 50 mm/hr of the QSCAT-R dataset. Blue lines are individuals observations, more frequent observations are shown in darker blue.

In Table 4.7 this explanation is quantified for the complete validation dataset. Every radial fit, based on a sample of the *pmax* is integrated over the radius (up to 1,000 km) to calculate the total rainfall for this radial profile. Subsequently, this is compared to the observations. For simplicity, the total rainfall is calculated for one hour. As can be seen, the total rainfall is significantly overestimated for the 50, 75 and 95%-sample fits (positive bias). This is related to the tail of the exponential distribution, which is not always present for high maximum rainfall intensity profiles (e.g. Figure 4.12). Furthermore, for the low range sample fits the total radial rainfall is underestimated (negative bias). This can be related that for the radial rainfall profiles with low maximum rainfall intensity, the exponential distribution no longer holds. As a result, the rainfall rates at small radii are greatly overestimated and therefore the total radial rainfall is overestimated. The magnitude of the performance metrics is significant, but it should be noted that the radial rainfall profile is integrated over a 1,000 km distance.

Table 4.7: Performance metrics for the total radial rain per hour for different sample fits of *pmax* compared to the observed radial rain profile for a radius of 1,000 km.

modelled radial rain - observed radial rain	RMSD [mm]	bias [mm]	MAE [mm]
5%-sample fit	9,063	-5,133	6,548
25%-sample fit	8,217	-888	6,377
50%-sample fit	8,892	2,585	7,292
75%-sample fit	8,986	3,640	7,556
95%-sample fit	12,009	8,886	10,573

A further quantification and elaboration on these performance metrics can be found in Table 4.8. The error in the total radial rain for different categories (*pmax* < 50 mm/hr, 50 mm/hr < *pmax* < 100 mm/hr and *pmax* > 100 mm/hr) for the 50%-sample fit is given. Here, it can be seen that for each of the categories the total radial rainfall is overestimated by the proposed model (positive bias). This is most likely related to the large tail in the exponential fit that is proposed. Moreover, it can be concluded that the underestimation in the *pmax* value does not prevent the total radial rainfall to be underestimated.

Table 4.8: Performance metrics for the total radial rain per hour for the 50%-sample fit of *pmax* compared to the observed radial rain profile for a radius of 1,000 km for different categories.

modelled - observed radial rain	RMSD [mm]	bias [mm]	MAE [mm]
pmax < 50 mm/hr	8,438	4,447	7,084
50 mm/hr < *pmax* < 100 mm/hr	9,662	6,706	8,397
pmax > 100 mm/hr	12,271	10,276	11,081

To conclude, for high maximum rainfall intensities the exponential radial rainfall profile is in line with the observations visually. However, (mainly) the long tail causes an overestimation of the total radial rain of a TC at one moment in time. For lower maximum rainfall intensities the exponential profile is not always valid, this causes the observed total radial rainfall to be overestimated by the rainfall model.

4.4.2. Variability of the Radial Rainfall Profile

The variability of the proposed model is assessed by an attempt to reproduce Hurricane Harvey. The track of Hurricane Harvey is used as a base and with the proposed methodology a radial precipitation profile is generated for every time step. To give an indication about the variability of the copula samples, 100 different synthetic variations of Hurricane Harvey are created. The realizations have the same track, pressure drop and maximum sustained wind speeds as Hurricane Harvey, but the precipitation is included by using the observation-based rainfall model. The created TCs are forced upon the SFINCS model as setup in Chapter 3. This is to assess the rainfall rate at a fixed observation point in Houston and subsequently substantiate the hypothesis that rainfall rates are overestimated at large radii.

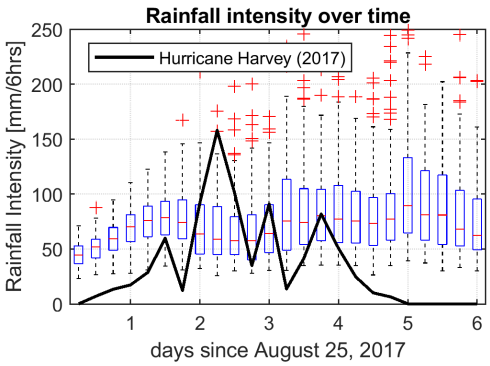

Figure 4.14: Rainfall intensity over time (in millimeters per 6 hours (mm/6hr)) for Hurricane Harvey (black line) and 100 synthetic variations (box- and whisker plots) of Hurricane Harvey.

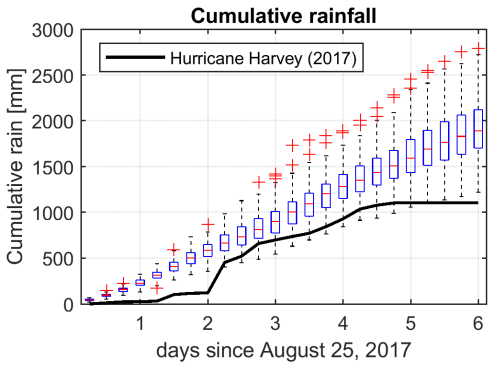

Figure 4.15: Cumulative rainfall over time for Hurricane Harvey (black line) and 100 synthetic variations (box- and whisker plots) of Hurricane Harvey.

A randomly placed observation point in Houston is used to assess the impact of the synthetic variations of Hurricane Harvey. At this observation point the rainfall rates and cumulative rain can be assessed over time. The results can be seen in Figures 4.14 and 4.15. The rainfall intensity shows a near-constant profile over time (looking at the (red) median value in the box- and whisker plots) for the synthetic variations, whereas for Hurricane Harvey the rainfall rate is more dynamic (black line). Furthermore, the synthetic variations show great scatter in the rainfall rates (see whiskers of box plots). This emphasizes the variability of TC rainfall, which was already suggested by Figures 4.6 and 4.12, but also the impact of the random *pmax*-sampling method. It should be noted, that especially for moments where the rainfall rate during Hurricane Harvey is low (see black line in Figures 4.14 and 4.15), the synthetic variations tend to overestimate rainfall tremendously. There could be two explanations for the overestimation of the rainfall rate. First, in line with Section 4.4, the *pmax* is overestimated for the low-end category ($pmax < 50$ mm/hr), which is not exceeded frequently during Hurricane Harvey. Secondly, for all radial rainfall profiles created, a large tail is generated. For that reason, the radial rainfall profile generates a spatial rainfall distribution with a diameter of 2,000 km, which for every radii holds a rainfall rate larger than zero. As a result, the fixed observation point in Houston endures precipitation for every hurricane that enters the Gulf of Mexico. In reality, this is not likely to happen. Furthermore, the validation study shows that a combination of high-roll *pmax*-samples induces great overestimation of both rainfall rates as well as cumulative rainfall.

In short, the extended tail of the radial rainfall profile indicates an overestimation in total rainfall as well as the rainfall rate at a fixed observation point. At 6 hours since August 25, Hurricane Harvey was at a large distance from Houston. Observations indicate that Houston did not experience rainfall due to Hurricane Harvey at that moment (see the black line in Figures 4.14 and 4.15). For the modelled radial rainfall schematization however, the radial extent of the precipitation profile did reach Houston due to the length of the tail. As a result, the rainfall rates are overestimated at the observation point. Moreover, rainfall intensity is linked with the cumulative rainfall (and duration) of a TC. Inevitably, the cumulative rainfall is also overestimated by the synthetic variations.

4.4.3. Modification of the Radial Rainfall Profile

To crudely overcome the overestimation of the rainfall rate at large radii, the proposed rainfall model is modified. All rainfall intensities lower than 10 mm/hr are removed from the generated radial rainfall rate profiles. These lower rainfall intensities are mostly located at larger radii. With this adjustment, a radial rainfall profile does most likely not cover the entire span of 1,000 km. In other words, the spatial precipitation field is restricted at smaller radii and the total radial rain reduces. An example of the impact of this modification on the radial rainfall profile can be seen in Figure 4.16, where an observation of Hurricane Isabel is shown (equal date and time as Figure 4.12). Now, the proposed radial rainfall profiles are restricted by radius and for most sample fits the rainfall rates equal zero at the same radius as in the observation of this example.

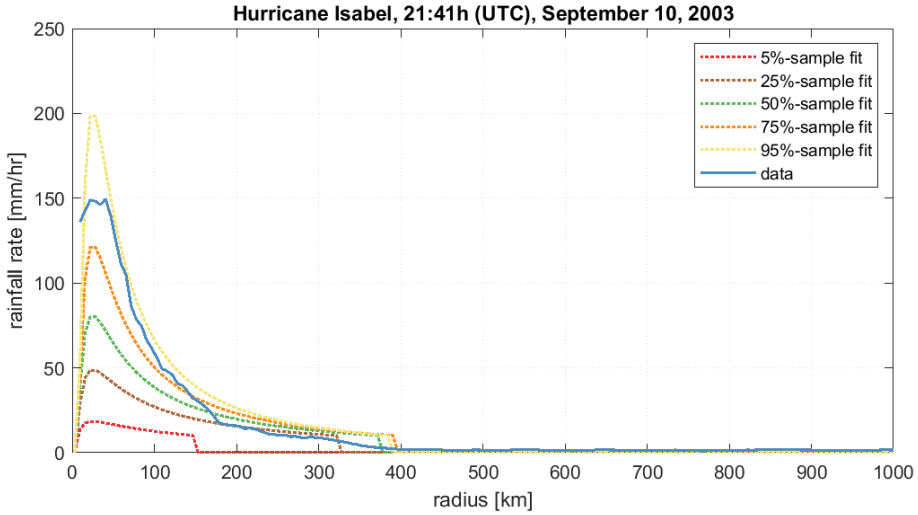

Figure 4.16: An example of rainfall intensity distributed over distance from the hurricane's eye for Hurricane Isabel (2003) at a moment in time. Fits for different sampled values for the maximum rainfall intensity are given, including the proposed adjustment. The solid blue line indicates the observed radial rainfall profile from the QSCAT-R dataset.

Consequently, the observed rainfall rates at a fixed observation point are affected. Figures 4.17 and 4.18 present the rainfall rates and totals as a result of the synthetic variations. Opposite to the previously shown plots, the radial rainfall profiles have been adjusted according to the before-mentioned modification. It can now be seen that the rainfall rates in the first days are significantly reduced. As a result, also the overestimation of total rainfall at a fixed observation point decreased in magnitude. To quantitative impact of this modification is analyzed by performance metrics. The RMSD of the rainfall rate at a fixed observation point drops due to the suggested adjustment from 11.50 mm/hr (for reference in Figure 4.17: 56.22 mm/6hr) to 10.97 mm/hr (for reference in Figure 4.18: 47.22 mm/6hr). This difference is limited, because of the fact that the large variability in the synthetic variations is still present (outliers impact the outcome of the RMSD, as stated in Chapter 3). However, the bias drops from 5.33 mm/hr (34.44 mm/6hr) to 2.77 mm/hr (17.00 mm/6hr), which is a reduction of almost 50 %.

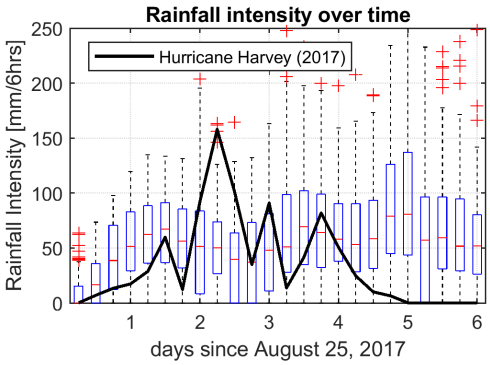

Figure 4.17: Rainfall intensity over time (mm/6hr) for Hurricane Harvey (black line) and 100 synthetic variations (box plots) of Hurricane Harvey. All rainfall rates lower than 10 mm/hr in the radial rainfall profile are set to zero.

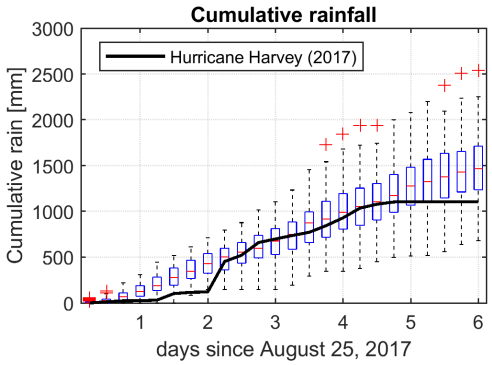

Figure 4.18: Cumulative rainfall over time for Hurricane Harvey (black line) and 100 synthetic variations (box plots) of Hurricane Harvey. All rainfall rates lower than 10 mm/hr in the radial rainfall profile are set to zero.

Table 4.9 shows the performance metrics for the total radial rainfall in one hour for the complete dataset. A similar procedure as in Section 4.4 is used. It can be seen that, for example, a 50%-sample fit value is now underestimating (bias = -1,209 mm) instead of overestimating (bias = +2,585 mm) for the total radial rainfall. Nevertheless, the magnitude of the error has decreased due to the modification. It should be distinguished that the 75%-sample fit looks to be the closest fit according to the validation set, in terms of total radial rainfall. It is concluded that the adjusted rainfall model shows to be a better fit according to the data, for total radial

rain of a TC at one moment in time. However, this adjusted model should be handled with care, because the radial rainfall total seems to decrease, but for the Hurricane Harvey variability case, where rainfall rate is assessed at an fixed observation point, the rainfall rate is still slightly overestimated for the 50%-sample fit (e.g. days 5 and 6 in Figure 4.17). Furthermore, the model has only been analyzed for one hurricane. Moreover, this analysis is carried out a random fixed observation point in Houston, but Hurricane Harvey showed spatial variability in rainfall rates and totals over the entire model domain (see Figure 3.3). This indicates that the performance of the rainfall model for Hurricane Harvey could deviate.

Table 4.9: Performance metrics for the total radial rain per hour for different sample fits of *pmax* compared to the observed radial rain profile for a radius of 1000 km. All rainfall intensities within the radial rain profile lower than 10 mm/hr are removed.

modelled radial rain - observed radial rain	RMSD [mm]	bias [mm]	MAE [mm]
5%-sample fit	12,039	-9,391	9,459
25%-sample fit	9,804	-5,133	7,352
50%-sample fit	8,834	-1,209	6,841
75%-sample fit	8,329	63	6,584
95%-sample fit	9,943	5,704	8,559

Moreover, Appendix B.8 shows three different snapshots of Hurricane Isabel which all serve as an example of one of the previously established categories. On the left side, the results of the original rainfall model are depicted, whereas the figures on the right side indicate the radial rainfall profiles when using the adjusted model. It can easily be distinguished that for these examples the radial rainfall profiles are restricted at smaller radii. For the high *pmax* sample category (50 mm/hr < *pmax* < 100 mm/hr: Figures B.22 and B.23 and *pmax* > 100 mm/hr: Figures B.24 and B.25), this seems to have a positive effect. However it should be noted that the underestimation of the total radial rain at a low sample fit is increasing, because the underestimation is magnified due to the restriction of the radial rainfall profile. For the case of low maximum rainfall intensity (Figures B.26 and B.27) the proposed adjustment only causes a reduction in magnitude of overestimation in terms of the total radial rainfall.

This is further quantified in Table B.4 in Appendix B.7. Here it can be seen that for the 50%-sample fit for different categories the error in the total radial rainfall is reduced by the modification in the radial rainfall profile. Nevertheless, the total radial rainfall is still overestimated for every single category. Especially for the high *pmax* values the overestimation is significant.

To conclude, the originally proposed radial rainfall profile fit is adjusted according to a variability study. As a result, the radial rainfall profile is restricted at a smaller radius and therefore more in line for observations with a high maximum rainfall intensity. However, for low maximum rainfall intensities, this adjustment indicates that the total radial rainfall is underestimated by a larger extent. Furthermore, when looking at the variability study for Hurricane Harvey, the total rainfall at a fixed observation point is still slightly overestimated. This is most likely due to the fact that the tail of the radial rainfall profile is still present in some cases (e.g. rainfall rates of 11 mm/hr). Furthermore, this can be related to the fact that radial rainfall profiles with low *pmax*-values are not correctly captured with the exponential profile. This causes the maximum rainfall rates to occur at a different location in the radial rainfall profile if compared to the observations. More, after the proposed modifications, the variability of rainfall rates is still large (see box plots in Figure 4.17), this is due to the random sampling method used in this model. This indicates that a combination of high-roll *pmax*-samples could still double the observed total rainfall (see whiskers of box plots in Figure 4.18.)

4.5. Time Dependence

A framework is set-up to be able to sample a distribution of rainfall intensity according to a given maximum sustained wind speed. This could potentially serve as a valuable tool in a flood risk analysis or a climate variability studies. A relatively simplistic schematic rainfall distribution can be created and subsequently be forced on a inland flooding model (e.g. SFINCS). In Chapter 3 is shown that SFINCS is capable of creating similar flooding results as observed water levels during Hurricane Harvey. Moreover, the peak water levels and impact of Hurricane Harvey could be reproduced with a low resolution grid and an axisymmetric rainfall schematization. This can be used to set up a climate variability study with SFINCS. Synthetic TC tracks

can be generated with a schematized wind-, pressure and precipitation field, based on maximum sustained wind speed. The assumption of independent observations over time (see Section 4.2) is validated to analyze whether TCs have a general consistent rainfall pattern over time. Furthermore, if dependence is recognized, it could potentially reduce the computational time of a CVA, because the sampling frequency can be reduced.

Taking into account all observation points of the QSCAT-R dataset, the dependence over time is analyzed. For this analysis, only the hurricanes with more than 5 observation points are taken into account. The first observed value (at t = 0) for *pmax* is compared with a threshold value and subsequently assigned to one of the previously mentioned categories: $pmax < 50$ mm/hr, $50 < pmax < 100$ mm/hr and $pmax > 100$ mm/hr. In Figure 4.19, the second case is presented. The absolute difference with the previous time step in maximum rainfall intensity (Δ *pmax*) is plotted in the histograms. It can be seen that the absolute difference in rainfall with the previous step can reach large values. With 90% confidence, it can be concluded that over time, the *pmax* can variate up to 100 mm/hr compared to the previous time step. This difference is considered large, therefore time dependence can not be recognized for this category of initial *pmax* values. The same holds for other two categories shown in Appendix B.9. To conclude, no real pattern in time can be recognized. Sampling is needed at every single time step when creating a synthetic TC. The assumption of independence between different observations holds. Moreover, TC rainfall can be considered dynamic.

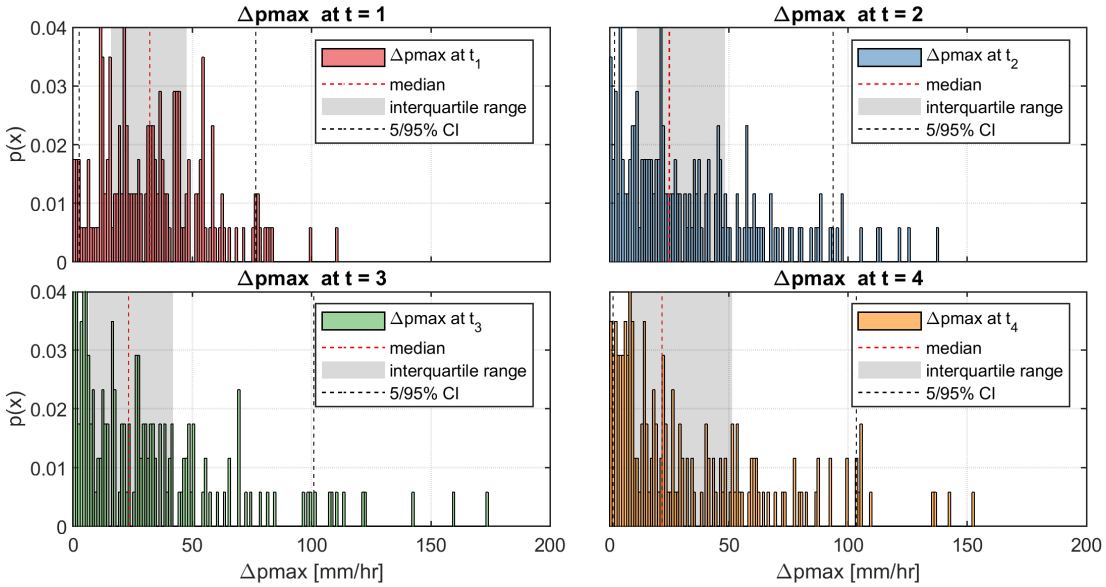

Figure 4.19: Distribution of the difference in maximum rainfall intensities at different time steps. Only hurricanes with an initial pmax between 50 and 100 [mm/hr] are taken into account. The red dashed-line indicates the median value, the gray polygon represents the interquartile range and the black dashed lines indicate the 5% and 95% boundaries.

4.6. Key Points

Previously, only a schematization of pressure and wind speed could be generated based on BTD. Now, with the proposed observation-based rain model a similar profile can be generated for the precipitation of a TC. This line of research was substantiated by the following research question:

How can the spatial rainfall distribution of a Tropical Cyclone be parametrized using the main characteristics of a Tropical Cyclone?

Key points resulting from this derivation are:

- The observations (data from 804 TCs worldwide from 1999 to 2009) from the QSCAT-R dataset are used to create a observation-based parametric rainfall model. All observation are assumed to behave independently. The QSCAT-R dataset does not contain precipitation data in a 100 km vicinity of the coast. A correlation (Pearson Product Moment = 0.476 [-]) is recognized between maximum sustained wind speeds (*vmax*) and maximum rainfall intensity (*pmax*). The *vmax* and *pmax* show large scatter, which is in line with theory and referred to as the stochastic character of TCs;
- Opposite to similar studies, which use a least-squares fitting procedure, a copula fit is proposed. The symmetric Frank Copula family proofs to be the best fit (RMSE = 1.4686 [-], NSE = 0.9951 [-]) to the data. Multiple copula families show similar RMSE and NSE scores, but their influence is not further analyzed. Following a conditional sampling procedure a *pmax* can be sampled according to a given *vmax*. For *vmax* < 40 m/s the proposed method produces very similar results (for the median) compared to the data. For values exceeding the 40 m/s the model underestimates the median value of the data. This results in a RMSD of 37.9 mm/hr and a bias of -6.79 mm/hr for the median value over the entire dataspace. Nevertheless, the 90% confidence interval bands of both the data and the model are similar for the entire range of *vmax* enclosed in the QSCAT-R dataset;
- The sampled *pmax* is fitted with the radius of a TC according to a similar procedure as the exponential Holland wind-profile. Fitting coefficients (b_s and x_n) are defined according to a least-squares fitting procedure. For high *pmax*-values the proposed radial rainfall fit shows close resemblance to the data in terms of the exponential-like radial rainfall profile. For lower *pmax* however, this is not (always) the case. This can be related to the assumption of letting the radius of *pmax* be equal to the RMW. This assumption holds for only part of the QSCAT-R data. Especially for low *pmax* this is not valid;
- After analysis, the proposed radial rainfall profile tends to overestimate rainfall rates at larger radii. To prevent this overestimation a modification has been applied. All rainfall rates in the radial rainfall profile larger than 10 mm/hr are set to zero. This limits the radial rainfall profile to smaller radii;
- For radial rainfall profiles with a maximum rainfall intensity lower than 50 mm/hr, the *pmax*-value is underestimated by the model (bias = 10.5 mm/hr). However, for all other *pmax*-values, the maximum rainfall intensity in the radial rain profile is underestimated significantly. Especially, for the extreme rainfall profiles the maximum rainfall intensity can be underestimated by up to 68 mm/hr for the 50%-sample. This is related to the performance of the Frank Copula as discussed previously;
- Furthermore, the total radial rainfall is analyzed to assess the performance of the proposed rainfall model. Here it can be seen that the total radial rainfall (i.e. the area under the radial rainfall profile) is overestimated for the entire *pmax*-dataspace;
- A variability study assesses the performance of the radial rainfall model by analyzing the rainfall at a fixed observation point in Houston. Multiple variations of Hurricane Harvey are produced by using the original track, pressure and wind characteristics. TC rainfall however, is extracted from the proposed model. These variations show a large variability in rainfall intensity at a fixed observation point. In general, when looking at the median value, the (total) rainfall is overestimated. It should be noted that this conclusion is based on a variability study of one TC only. Moreover, the analysis is carried out at one fixed observation point where the rainfall rates and totals during Hurricane Harvey showed spatial variability. This could indicate that the magnitude of the model error as presented in this study could vary for different locations in the Houston model domain; and
- The assumption of independent observations holds true for the QSCAT-R dataset. No pattern over time can be recognized. Therefore, TC rainfall is considered a dynamic process. For this reason, the decision for a random sampling method is valid.

5

Application: Climate Variability Assessment for Houston, Texas

In this chapter the two previous elements of this research are combined into an application by means of a climate variability study for the urban areas of Houston, Texas. In Section 5.1 a short introduction is given. Section 5.2 contains a description of the material and methods used for this CVA. Furthermore, in Section 5.3 an analysis of the generated input is carried out. Subsequently, in Section 5.4 the probabilistic risk analysis results are discussed. To conclude, Section 5.5 contains the key findings of this chapter.

5.1. Introduction

As stated in the research objectives, the main goal of this research is to develop a methodology to assess the joint probability of pluvial, fluvial and marine flooding in a probabilistic flood risk assessment. In this chapter the capability of SFINCS to carry out this climate variability assessment is shown.

In Chapter 3 the SFINCS model was subjected to a validation case study. The model was validated for Hurricane Harvey which arrived in late August 2017. The model showed to be able to reproduce peak water levels with a MAE of roughly 0.5 m and furthermore, in combination with the Delft-FIAT, an estimate of the impact of Hurricane Harvey in terms of damage and affected people can be given. Sensitivity tests showed that rainfall was the dominant component in this flooding event. Furthermore, to accurately reproduce the flood wave details, an accurate description of the precipitation is needed. However, for reproducing peak water levels, a more generic axisymmetric description is sufficient. Moreover, a sensitivity analysis on the grid resolution showed that with a low resolution grid (100 m), it is also possible to reproduce peak water levels and the impact with reasonable accuracy (relative to the high resolution model results).

To get to a simplified input for the precipitation a schematization of the distribution was derived in Chapter 4. Based on a bivariate analysis method a relationship was established between maximum rainfall intensity and maximum sustained wind speeds. Inspired by the Holland et al. (2010) wind-profile an axisymmetric radial rain profile can be created under the assumption that the RMW is equal to the radius of maximum rainfall intensity. Furthermore, all rainfall rates in the radial rainfall profile lower than 10 mm/hr are set to zero.

These two components can now be combined to carry out a climate variability study. Synthetic tracks can be generated with a track generation tool. The hurricane tracks are provided with a spatial wind and pressure field. Furthermore, with the proposed rainfall model an axisymmetric rainfall profile is generated as function of the maximum sustained wind speed. The SFINCS model is used to assess the impact of these generated TCs in terms of flooding (i.e. maximum water depths). Subsequently, Delft-FIAT is used to analyze the impact.

5.2. Materials and Methods

5.2.1. TCWiSE

For this research the TCWiSE tool as developed by Maarten van Ormondt, Deepak Vatvani and Jasper Hoek (Hoek, 2018) is used to generate synthetic TCs based on a Monte Carlo Simulation. By creating new (extra) TC tracks based on historical data, a much larger representative dataset can be generated, see Figure 5.1. Here, all the hurricanes generated by the TCWiSE tool in the Atlantic Basin are given in the right panel, whereas the historical tracks are given in the left panel. The difference in number of TCs for the historical and synthetic causes the underlying statistics to be much better represented.

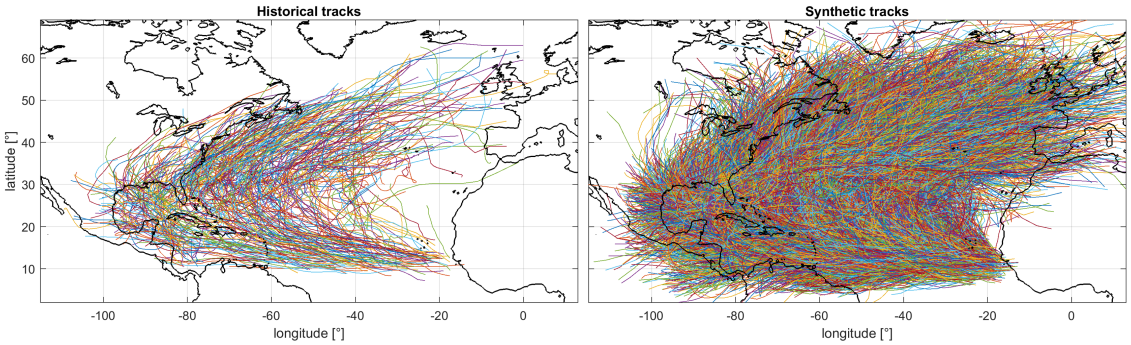

Figure 5.1: Hurricane tracks: left) historic, right) simulated by TCWiSE.

The TCWiSE tool uses historical TCs to create synthetic tracks and spiderweb diagrams based on the statistics from this dataset (Knapp et al., 2010). As highlighted in the literature review (see Section 2.2), the TCWiSE tool is based on the ETM developed by Vickery et al. (2000). This means that the synthetic TCs are created from genesis to termination with sampled values every six hours. The implementation of the Markov chain approach indicates that the sampled values solely depend on the previous time step. The parameters representing the TC track are: maximum sustained wind speed, storm motion and heading like shown in Table 5.1.

Table 5.1: Parameters used to create a synthetic track. The parameters are dependent on the previous time step (t-1), according to the Markov chain method. Courtesy of Hoek (2018).

Description	Parameter	Dependency
Maximum sustained wind speed	$vmax$	$vmax_{t-1}$
Storm motion speed	c	c_{t-1}, θ_{t-1}
Heading	θ	c_{t-1}, θ_{t-1}

The flowchart of TCWiSE tool is given in Figure C.1. First, the number of years has to be specified by the user. This is used to compute the number of storms to be generated, when taking into account the average number of TCs per year in the specified oceanic basin according to the observations (see Figure C.2). The tool then determines the location of genesis of the TC, to subsequently sample the three parameters mentioned above on a six hour interval till termination. Termination is based on a maximum lifetime (30 days) or a lower limit for the maximum sustained wind speed (< 20 kt). A more extensive description of the different steps given in this flowchart is given by Hoek (2018).

The main focus of this chapter is on the 1 in 100-year flood, because this can be compared to existing flood plain maps of the FEMA. Therefore, the track generator tool was used to create 1,000 years of generated synthetic TC tracks. This should create a large enough dataset to create a representative 1 in 100-year compound flooding event due to TCs. The tracks can be seen in Figure 5.1. The generated data is compared with the historical archive for the North Atlantic basin spanning 46 years from 1970-2016. Comparing historical and synthetic genesis and termination locations shows the close resemblance between the two (see Figures 5.2 and 5.3).

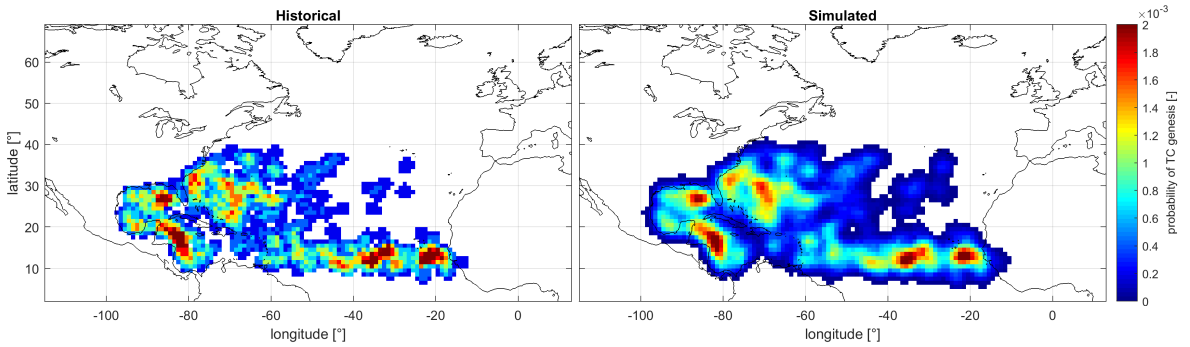

Figure 5.2: Genesis locations of TCs: left) historic, right) simulated by TCWiSE.

The figures for simulated hurricanes show a smooth color change. This is because this dataset contains data for 1000 years of TCs, where the historical dataset contains only 46 years of data. Nevertheless, the main pattern of probability of occurrence is matched. The high probability for the coast of Africa, near Mexico and just west of Florida is present in both the historical dataset and the synthetic simulated tracks. For the termination locations more anomalies can be recognized. Especially the high probability of termination near Mexico is not entirely reproduced. However, this could be the result of the size of the synthetic dataset.

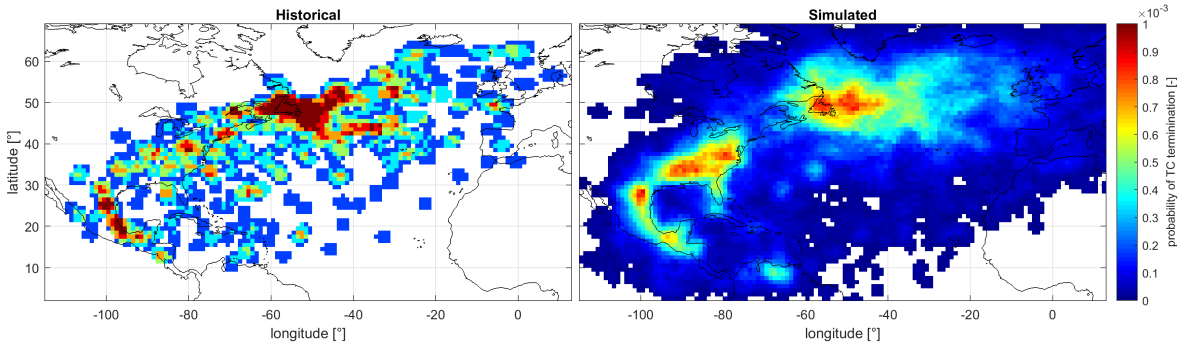

Figure 5.3: Termination locations of TCs: left) historic, right) simulated by TCWiSE.

Besides creating the hurricane track, the TCWiSE tool is able to create a spiderweb diagram based on the Monte Carlo Simulation method. The description above provided a location of the TCs eye and the maximum sustained wind speed. To create a spatial wind field, the Holland parametric spacial wind field model is adopted (Holland et al., 2010). The R35 was used as extra input, to prevent the overestimation of wind speeds at larger radii which occurred frequently in the original Holland (1980) model (Nederhoff et al., 2019). The parametric wind field model is used in combination with the wind-pressure relationship of Holland (2008). Furthermore, TC asymmetry is included according to Schwerdt et al. (1979) and a constant inflow angle of 22° is used (Zhang and Uhlhorn, 2012). For this study, a set of synthetic tracks is created which is representative for the current climate state, no future scenarios are taken into account.

Moreover, the derived (modified) relationship between maximum sustained wind speed and the maximum rainfall intensity is used to create a spatial precipitation profile. This observation based parametric rain model creates a radial fit inspired by the Holland et al. (2010) model and can be used to add a pluvial component to a synthetic TC. The maximum rainfall intensity (*pmax*) is randomly sampled based on the conditional sampling method presented in Chapter 4. Furthermore, this *pmax*-value is fitted with the radius based on Equation 4.8. The asymmetry imposed by the elements mentioned previously also influences the rainfall profile. For example, the Schwerdt correction factor changes magnitude of the maximum sustained wind speed and the location of the RMW for different directional bins (see Section 2.2.1, Nederhoff et al. (2019); Schwerdt et al. (1979)). This will result in a different rainfall distribution for different directional bins (usually four quadrants), resulting in a deviation of the axisymmetric wind profile and thus, the axisymmetric rainfall profile.

5.2.2. Delft3D-FM

For this research a basic Delft3D Flexible Mesh (Delft3D-FM, Deltares (2018); Kernkamp et al. (2011)) model is created to produce the offshore water levels occurring during every generated TC. Key advantage of using a large scale circulation model is the fact that the timing of the surge is in line with the arrival of the TC and according to the continuously differing heading and translatory motion. Downside of using this model is the computational effort needed to generate the offshore water levels. For example, to generate offshore water levels for 500 TCs, the computational time is up to 4 days (Linux-cluster, 4 calculations at the same time).

A brief overview of the model settings can be seen in Appendix C. Furthermore, this appendix contains some model results for the Hurricane Harvey case. Here can be seen that the Delft3D-FM model is not fully validated. In the appendix, different observation points are considered for this calibration. Main observation station of interest is Morgans Point, which will be used as location for the offshore boundary condition for the SFINCS model (equal to the validation study in Chapter 3). The pressure, wind speed and wind direction is evenly matched for all observation points, which suggests that the spiderweb diagram for Hurricane Harvey is correct. When looking at the time series for water levels, the Delft3D-FM model shows close resemblance to the observed water levels at the inlet into the Galveston Bay (8771450 - Galveston Pier). However, when looking at the water levels at observation points inside the basin (8770613 - Morgans Point and 8771013 - Eagle Point), the model is behaving differently in time. Especially, the peak water level at Morgans Point is 0.3 m off. This can be the result of a number of factors, for example the model-resolution, the number of refinements or the used bathymetry dataset. Nevertheless, the model is used to get an indication of an offshore water level for the synthetic hurricane tracks.

5.2.3. SFINCS

For the hydrodynamic analysis of the compound flooding due to the generated TCs a SFINCS model is used. The general model setup is equal as used in Chapter 3. Thus, the model domain still covers the Houston urban areas from Addicks and Barker Reservoirs up to the Galveston Bay (see Figure 3.1). The geographic coordinate system is WGS 84 / UTM Zone 15N and the vertical datum is NAVD88. The meteorological characteristics are retrieved from the TCWiSE tool. The offshore water levels are acquired by the Delft3D-FM model. However, for this climate variability study some adjustments to the original model setup have been made:

Resolution Sensitivity tests have showed that the SFINCS model resolution is important for capturing the exact details of the flood wave. However, when looking at peak water levels, the influence of the resolution is less distinct. Furthermore, the values resulting from the exposure calculation also indicate that a lower resolution grid produces similar numbers in amount of people affected. Besides this, also the computational effort drastically decreases. This effect is magnified by the fact that a more schematic rainfall component is used for this CVA compared to the model validation. The computational time for a SFINCS model with a 100-meter grid cell size decreases significantly due to this simplification of the rainfall schematization compared to the interpolated rainfall in the Hurricane Harvey simulation. The total computational effort for 500 model runs is 10 hours (4 models parallel at the same time), which is equal to 5-10 minutes for each model run. Furthermore, the MAE at peak water levels for a 100-meter resolution model is 0.595 m.

Reservoir Release As stated in Chapter 3, a reservoir release was forced during landfall of Hurricane Harvey. This was the result in unexpected amounts of precipitation and therefore an increase in water levels in the Addicks and Barker Reservoirs. The reservoir release was issued, because of possible failure of the gates. A controlled release was preferred over an unexpected release. The amount of water released from the reservoirs caused flooding downstream. In the model domain used in this study, the increase of water levels in the reservoirs can not be reproduced due to model domain limitations. Furthermore, based on the spiderweb diagrams created by the TCWiSE tool, no prediction can be made about the operation schedule of the Addicks and Barker Reservoirs in case of unprecedented rainfall amounts. Although it could lead to possible underestimation of the impact of a hurricane, a possible reservoir release is neglected in this CVA. Sensitivity analysis for the simulation for Hurricane Harvey showed that water levels can decrease (see Figure 3.11). However, this is dependent on the timing and magnitude of this reservoir release.

5.3. Analysis of Generated Input

This section discusses the input that is generated by the previously-mentioned models. First, the set of TCs included in this analysis is discussed. Subsequently, the hydrodynamic and meteorological forcing and their combinations are assessed.

5.3.1. Area of Interest

Figure 5.1 shows the distribution of historical tracks (left panel) and an overview of all synthetic tracks (right panel) as generated by the TCWiSE tool for the North Atlantic basin. The presented synthetic tracks are generated with the following settings:

- The North Atlantic Basin is the only basin taken into account;
- The hurricanes are simulated for 1,000 years; and
- The TCWiSE model domain ranges from halfway the state of Tamaulipas (Mexico) till the city of New Orleans (Louisiana) and covers most of the Gulf of Mexico, covering an area of roughly 2,000 by 2,000 km.

The Area of Interest (AoI) determines how many cyclones are generated, because if a TC does not enter the AoI with its eye it is terminated (see Figure C.1). The settings as given above result in a sample set of over 8,000 TCs. For this study however, only the TCs in close vicinity of Houston are important. Therefore, it is decided to reduce the AoI to the extent of the red box in Figure 5.4. The red box covers an area of roughly 500 by 500 km with the urban areas of Houston in the center. As a result, the reduced set contains 489 synthetic TCs.

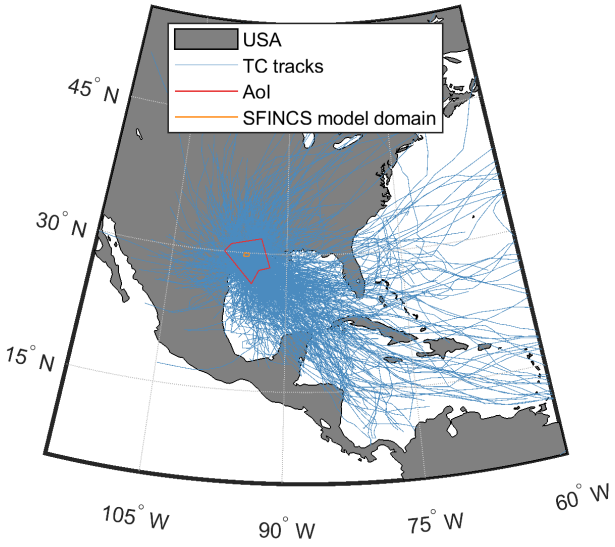

Figure 5.4: The red box indicates the AoI considered for this climate variability study. The black box indicates the SFINCS model domain and the blue lines are the 489 hurricane tracks considered for this study.

5.3.2. Hydrodynamic and Meteorological Forcing

Figure 5.5 shows the offshore water levels generated by the Delft3D-FM model for all 489 synthetically generated hurricanes. The tidal motion is a recognizable pattern. Furthermore, it can be seen that the maximum offshore water level as modelled is 2.61 m above NAVD88 and the minimum water level is 1.25 m below NAVD88. The Morgans Point, Barbours Cut observation point was installed in 1973 (NOAA, 2019) and recorded a maximum water level in 2008 of 2.70 m above NAVD88. A minimum was established in 1996 with a water level of 0.92 m below NAVD88. This indicates that the modelled offshore water levels are in the right order of magnitude according to observed values. The representation of the offshore water levels is in the right range. During 90% of the generated TCs, the maximum offshore water level is in between 0.11 m and 1.25 m above NAVD88.

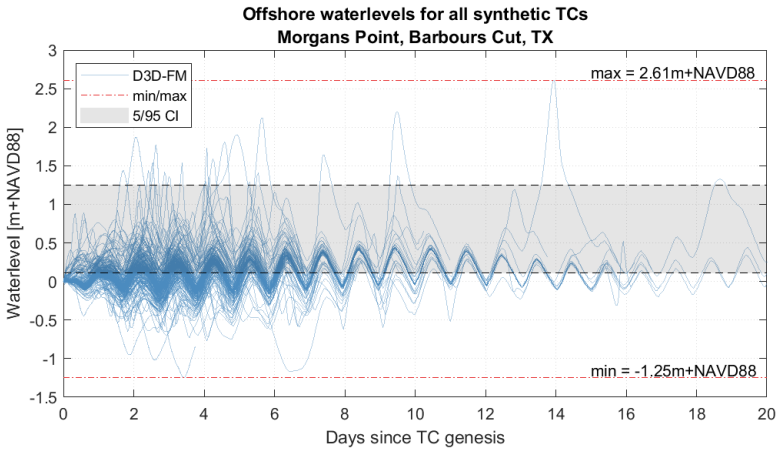

Figure 5.5: The water level time-series (blue lines) at Morgans Point, Barbours Cut for all generated TCs. These offshore water levels are generated by the Delft3D-FM model. The red dotted lines indicate the minimum and maximum water level as generated by Delft3D-FM, whereas the gray box indicate the 90% confidence interval of the maximum offshore water level.

Furthermore, the spin-up time of the Delft3D-FM model can be recognized in Figure 5.5. The tidal signal does not represent reality in the first two days of the time-series. However, the influence of this deviation is assumed to be limited. The tidal signal only had limited impact on the total flooding in Houston due to Hurricane Harvey.

Moreover, all TCs have been generated with respect to January 1, 1970. This means that for all TCs, the moment of genesis coincides with the same moment in the tidal cycle. In other words, no difference is made between hurricanes which arrive during spring tide or those arriving during neap tide. This indicates that, although the simultaneous occurrence of surge and spring tide is random, not all possible combinations are created.

At the same time, different rainfall patterns are recognizable in the created dataset. Figure 5.6 shows the rainfall intensity over time for one fixed observation point in Houston for every single synthetically generated storm. It is valid to represent this with an arbitrarily chosen observation point, because the created spatial rainfall distribution is close to uniformly distribution over the entire model domain for every simulation. It can be seen that significant rainfall intensities are reached over time indicating heavy precipitation and moreover, flooding. In 90% of the scenarios, the maximum rainfall intensity (as recorded at a fixed observation point, so not equal to *pmax*) as generated is in between 12 and 86 mm/hr. For reference, the maximum rainfall intensity as recorded at an observation point during Hurricane Harvey was 73.8 mm/hr.

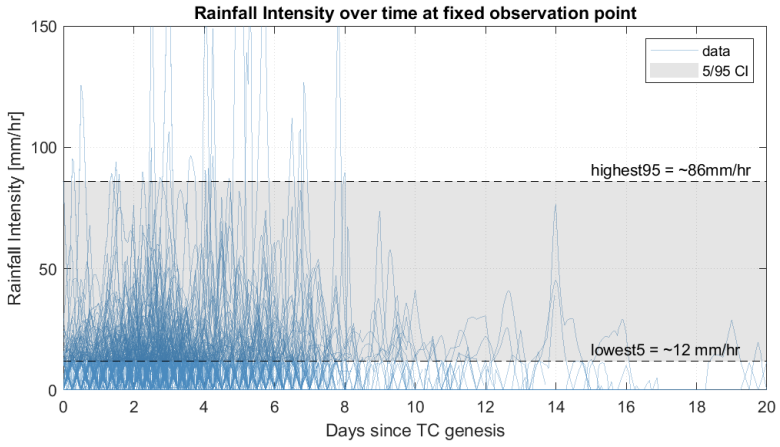

Figure 5.6: Rainfall intensity over time (blue lines) at one observation point in Houston of all generated TCs. The 90% confidence interval of the maximum rainfall intensity observed over time is indicated with the gray box.

An overview of the variability of created SFINCS model realizations is given by means of scatter plots:

- Scatter of the cumulative rain and the lifetime of a TC (Figure 5.7);
- Scatter of the cumulative rain and the maximum offshore water level (Figure 5.8);
- Scatter of the cumulative rain and the maximum rainfall intensity at an observation point (Figure 5.9); and
- Scatter of the maximum rainfall intensity and the maximum offshore water level (Figure 5.10).

The given scatterplots present the configuration of the created SFINCS models for all generated TCs and Hurricane Harvey is indicated with the red dot. For Hurricane Harvey the following parameters are set: maximum rainfall intensity at an observation point = 73.8 mm/hr, cumulative rain = 1,050 mm/hr, TC lifetime = 17.8 days and maximum surge = 1.1 m. These values are retrieved from the SFINCS model validation. It should be noted that the SFINCS model validation is based on a 6-day simulation and does therefore not account for all 17.8 days of Hurricane Harvey. Nevertheless, for Houston, the flooding (and thus precipitation) occurred during these six days. Therefore, it can be validated that for Harvey this combination of TC lifetime and total cumulative rain is correct. Furthermore, van Oldenborgh et al. (2017) stated that maximum cumulative rain observations were close to 1,500 mm. However, according to the data and the simulation time of the SFINCS model for Hurricane Harvey, these observations were not taken in the Houston model domain, but in Nederland, Texas (130 km north-east of Houston). Therefore, a representative cumulative precipitation value of 1,050 mm is assumed, which is considered as a high-end value for the rainfall due to Hurricane Harvey. This is because the spatial precipitation distribution shows some variability over the Houston area (see Figure 3.3).

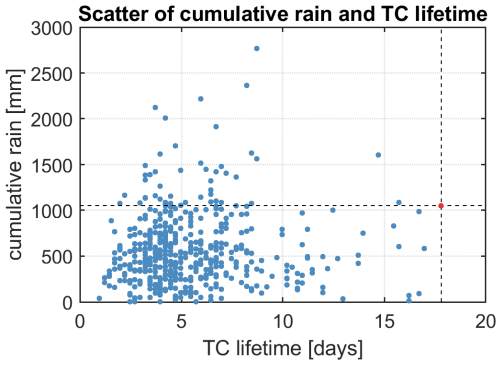

Figure 5.7: Scatter of cumulative rain at an observation point and time between TC genesis and TC termination. Characteristics of Hurricane Harvey are indicated by the red dot.

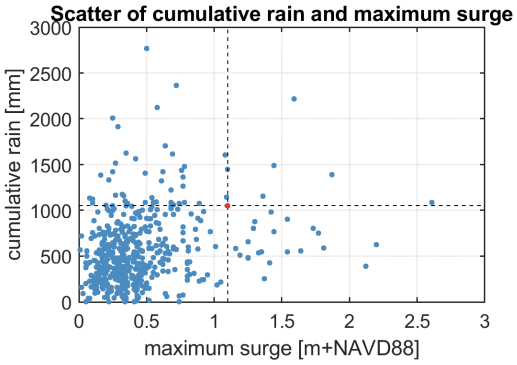

Figure 5.8: Scatter of cumulative rain at an observation point and maximum offshore water level. Characteristics of Hurricane Harvey are indicated by the red dot.

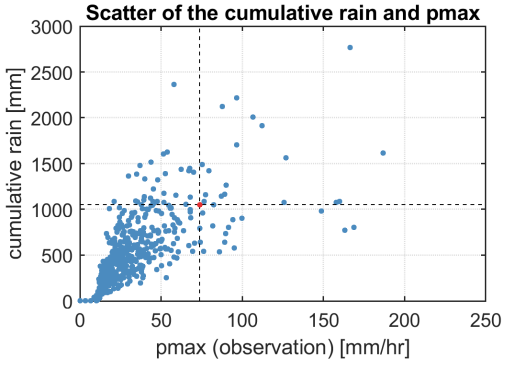

Figure 5.9: Scatter of cumulative rain at an observation point and maximum rainfall intensity at an observation point. Characteristics of Hurricane Harvey are indicated by the red dot.

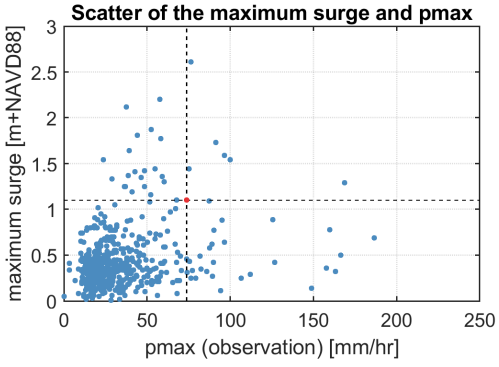

Figure 5.10: Scatter of maximum offshore water level and maximum rainfall intensity at an observation point. Characteristics of Hurricane Harvey are indicated by the red dot.

The scatter plots and the quantitative statistical analysis (see Table 5.2) help to put Hurricane Harvey in perspective. Figure 5.7 indicates that the cumulative rain (1,050 mm) is at the higher range of the cumulative precipitation values for the synthetic TCs. However, this translates to a recurrence interval of less than 25 years, according to:

$$\text{Recurrence Interval} = \frac{\text{years} - 1}{\text{rank}} \tag{5.1}$$

This suggests that, according to the input as generated for this CVA, Hurricane Harvey is a relatively frequently occurring event. However, it should be noted that the observation-based parametric rainfall model overestimates rainfall rates and totals when looking at a fixed observation station (see Section 4.4.3). When accounting for this, the recurrence interval of an event as Hurricane Harvey would be larger. For reference, the 1,500 mm cumulative rainfall would have a return period of almost 100 years. Furthermore, it stands out that the maximum rainfall intensity at an observation point during Hurricane Harvey is a common rainfall intensity during TCs, see Table 5.2. However, the duration of Hurricane Harvey exceeds the 1 in 250-year TC lifetime. This is the main reason of the high cumulative rainfall and therefore the pluvial-driven flooding in Houston.

Table 5.2: Quantitative analysis of generated input. The *pmax* (observation) indicates the maximum observed rainfall intensity at a fixed observation point.

	pmax (observation) [mm/hr]	cum. rain [mm]	max. surge [m]	TC lifetime [days]
Hurricane Harvey	73.8	1,050	1.10	17.8
1 in 25-year	68.1	1,086	0.89	10.2
1 in 50-year	89.8	1,408	1.33	12.0
1 in 100-year	125.6	1,614	1.59	15.7
1 in 250-year	166.4	2,212	1.90	17.0
1 in 500-year	186.7	2,765	2.20	22.0
1 in 1,000-year	313.5	3,105	2.61	28.2

5.4. Probabilistic Flood Risk Assessment

In this section the results of the climate variability study are discussed. First, an analysis of the current mapped flood risk by FEMA is carried out. Secondly, the hydrodynamic results based on the methodology of this research is compared with the FEMA flood plain maps. Thirdly, an exposure analysis is presented based on the flooding due to synthetic TCs.

5.4.1. Current Approach

An example of an existing probabilistic approach to flood risk modelling are the flood plain maps of the FEMA. These maps delineate a 1 in 100-year and 1 in 500-year flood plain based on historical storms. Most of the maps are based on coastal flooding. However, when available, fluvial and pluvial flooding maps are included. Nevertheless, these maps are outdated most of the time (Wing et al., 2018). Figure 5.11 shows the flood risk according to FEMA.

The FEMA flood plain map is shown in Figure 5.11. The map consists out of four different mapped flood plains: floodway (dark blue), 1 in 100-year flood plain (blue), 1 in 500-year flood plain (turqoise) and 1 in 100-year coastal flood plain (orange). The main focus of this research is on the 1 in 100-year flood plain.

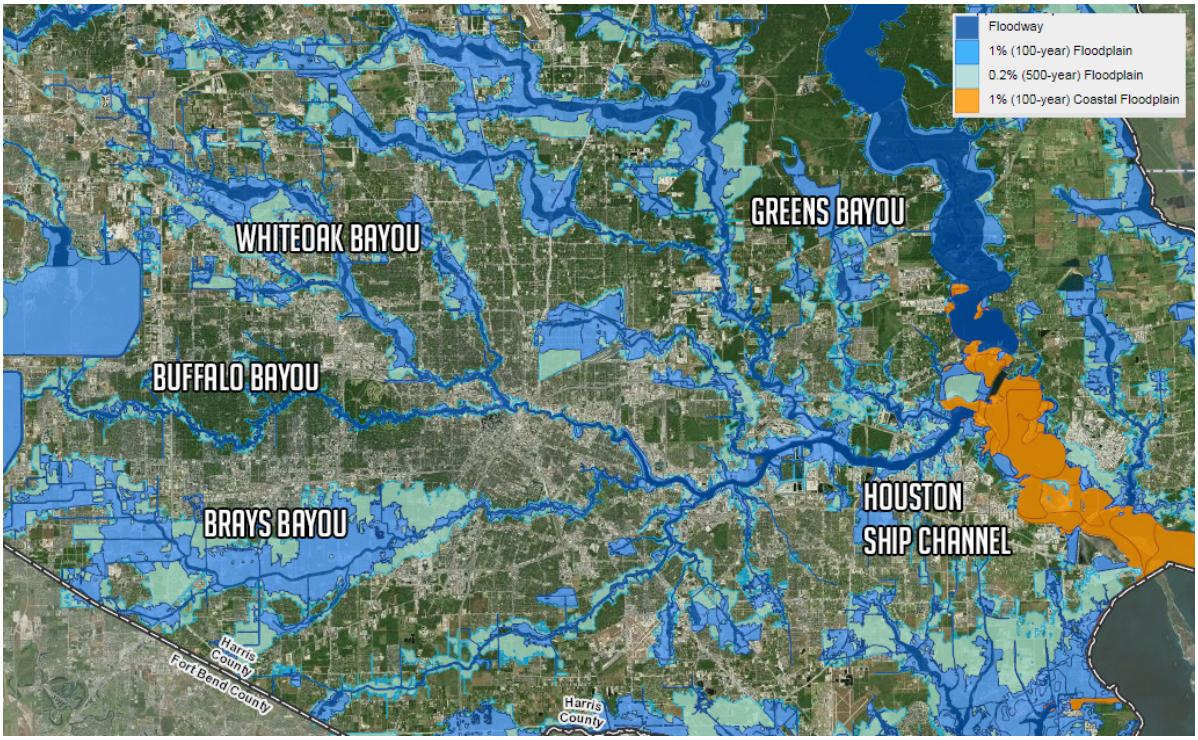

Figure 5.11: The FEMA flood plain map for the city of Houston (HCFCD, 2018).

Several areas are marked as flood prone during a 1 in 100-year flood. Areas which experience severe flooding during such storm are around the Brays Bayou, White Oak Bayou and the Greens Bayou. Especially areas around the Brays and White Oak Bayou are densely populated and therefore marked as flood-prone. Significant impact in terms of damage are to be expected during such storm. Moreover, the areas further downstream of the Brays and White Oak Bayou are less flood prone.

Furthermore, the areas around the Buffalo Bayou are not marked as prone to flooding at all. This can be related to the non-urbanized area around the Buffalo Bayou, just downstream of the Addicks and Barker Reservoirs. Flood water is expected to infiltrate in the ground. Moreover, water from upstream is expected to be hold back by the reservoirs. The events during Hurricane Harvey suggest however, that this is not always the case. The Houston Ship Channel streams in an area with industrial activities. Compared to the expected flooding near Brays and White Oak Bayou, the flood extent is only limited in this area according to the FEMA flood plain maps.

5.4.2. Hydrodynamic Assessment

The model train as presented in Section 5.2 is used to analyze the flood risk due to TCs in the Houston urban area. Based on all 489 model runs, flood maps can be derived for various return periods. The focus of this section is on the 1 in 100-year return period flood map (see Figure 5.12). This flood map can be compared to the delineated flood plain map of the FEMA and to the flood extent of Hurricane Harvey as presented in Figure 3.9. Figure 5.12 is created by assessing the 100-year recurrence interval water depth for every grid cell. No further analysis on the created combinations of water depths in adjacent grid cells is carried out.

From the generated input analysis (see Section 5.3) followed that Hurricane Harvey was not as significant as expected in terms of *pmax* and total cumulative rainfall if compared to the 100-year return period value for these quantities. A 100-year recurrence interval *pmax* (observation) equals 125.6 mm/hr (Harvey: *pmax* (observation) = 73.8 mm/hr) and a 100-year cumulative rain equals an observed 1,614 mm in Houston (Harvey: cumulative rain = 1,050 mm).

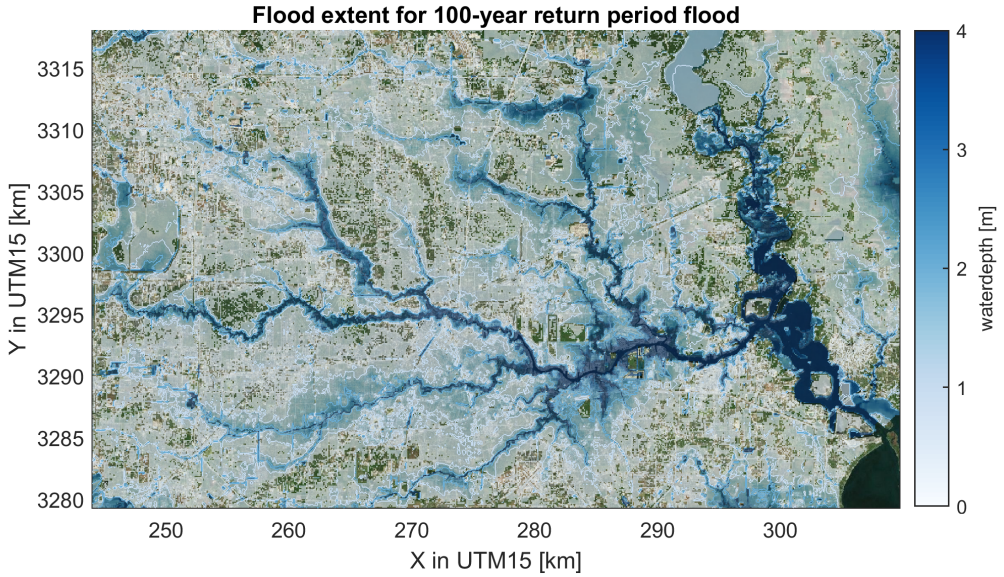

Figure 5.12: The flood extent for a 100-year return period storm in the urban areas of Houston. Water depths lower than 0.15 m have not been plotted for visual purposes. Contour lines are given for the 1.0 and 2.0 m water depths.

The flood extent underlines the difference between the 1 in 100-year flood (see Figure 5.12) and the Hurricane Harvey flood event (see Figure 3.9) according to this CVA. Where the flooding due to Hurricane Harvey was mostly concentrated in and around bayou systems, the 1 in 100-year flood shows the entire model domain to be covered with water. Especially areas around the Brays Bayou, Greens Bayou and Houston Ship Channel experience more than 1.0 m water during a 1 in 100-year flood, whereas during Hurricane Harvey these areas were mostly dry. A visualization of the difference between the flood extent of Hurricane Harvey and the 1 in 100-year flood can be found in Appendix C.5. In the remainder of this section, a more detailed (qualitative) comparison to the FEMA flood plain maps is carried out for the areas around Brays Bayou and the Houston Ship Channel. Appendix C.6 includes a more detailed (qualitative) comparison for the White Oak Bayou, Buffalo Bayou and Greens Bayou.

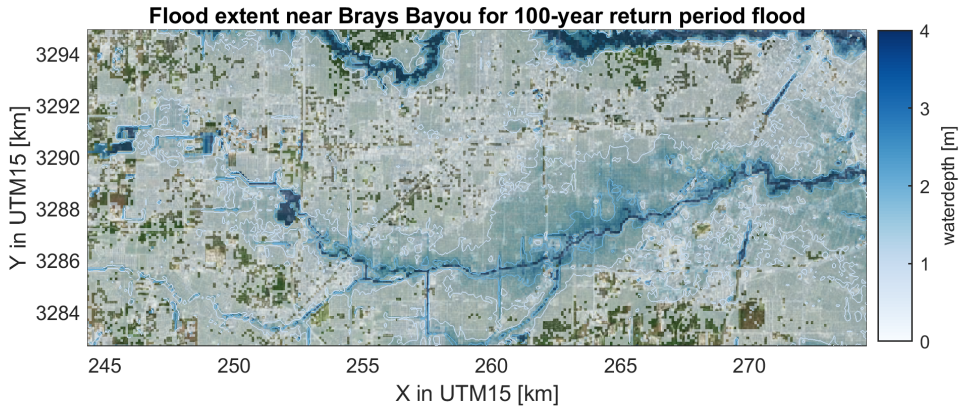

Figure 5.13: The flood extent near Brays Bayou for a 100-year return period storm. Water depths lower than 0.15 m have not been plotted for visual purposes. Contour lines are given for the 1.0 and 2.0 m waters depths.

The flood extent near Brays Bayou is visualized in Figure 5.13. The contour lines indicate the 1.0 and 2.0 m water depth contours. It can be seen that most of the area is flooded with at least 0.15 m (all white colors). The FEMA flood plain map does not mark these areas as prone to flooding during a 1 in 100-year storm, because the underlying model does not account for pluvial flooding. What can be noticed however, is that the 500-year return period flood plain from FEMA shows close resemblance with the area delineated (260 km < X in UTM15 < 270 km) by the 1.0 m depth contour in Figure 5.13. This shows that the FEMA flood plain maps could underestimate the potential flooding during a 1 in 100-year flood. For areas further upstream

this does not hold. Furthermore, the FEMA flood plain shows little to no flooding in areas upstream from 270 km UTM15, whereas the results of this study show that flooding in that area can be severe during a 1 in 100-year flood.

The flood extent for the Houston Ship Channel, ranging from the junction of the San Jacinto River towards the confluence of the Buffalo and White Oak Bayou, is shown in Figure 5.14. The FEMA flood plain (see Figure 5.11) marks the areas close to the river banks prone to flooding. Not much difference can be distinguished between the 100- and 500-year flood plains. Furthermore, it stands out that independent on the significance of the flooding, some industrial areas keep dry at all times. This can also be recognized in the 1 in 100-year flood extent map as a result of this climate variability study. Several areas experience little to no flooding. Nevertheless, the difference with the FEMA flood plains is significant. Besides the wide spread area which experiences water depths up to 1.0 m, as was noticed near the Brays Bayou as well, a large area also experiences water depths exceeding 2.0 m (280 km < X in UTM15 < 290 km). This extreme flooding during a 1 in 100-year event is most likely the result of run-off of all upstream water to one single water body.

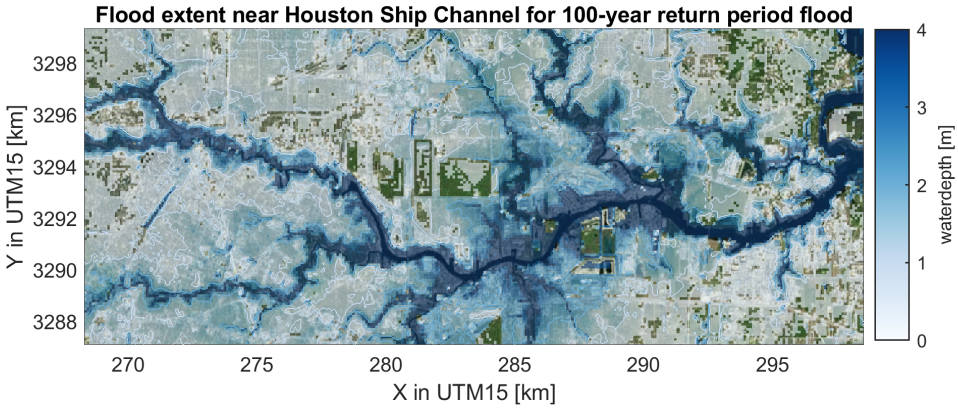

Figure 5.14: The flood extent near the Houston Ship Channel for a 100-year return period storm. Water depths lower than 0.15 m have not been plotted for visual purposes. Contour lines are given for the 1.0 and 2.0 m water depths.

In short, according to this climate variability study, the city of Houston is very prone to flooding due to TCs. The FEMA flood plain map significantly underestimates the flooding extent during a 1 in 100-year flood event. When zooming in on specific areas, this underestimation becomes more clear. The flood plain maps do not account for the spatial distribution of the pluvial component. Areas located at a relatively large distance from water bodies are excluded in the flood zone maps of the FEMA. This causes the flood risk to be underestimated. However, it should be noted that the FEMA does not represent potential water depths magnitudes. Therefore, it is difficult to compare the significance of the flooding in terms of water depth.

Moreover, it should be noted that the SFINCS model used in this CVA is a model with a positive bias of 0.279 m on peak water levels. According to the validation study (which is based on Hurricane Harvey only) this could potentially initiate an overestimation of 0.279 m of the modelled water levels. This suggests that the flooding due to the 1 in 100-year flood could be less significant than depicted in this section. Furthermore, the most extreme synthetically generated compound flooding events are most likely the result of a multiple high-rolls in the *pmax* sampling method. As shown previously, high-rolls (i.e. the 95%-sample fit) causes large overestimation of up to 70 mm/hr compared to observations. This indicates that the flood extent and magnitude could be less significant than presented here.

5.4.3. Exposure Assessment

Similar to the methodology in Chapter 3, Delft-FIAT is used to give an indication for the amount of affected people and the damage due to flooding. As highlighted previously, Delft-FIAT is only used as a first estimate for the impact due to a hurricane. The validation study indicated that the tool is overestimating the reported losses and claims for almost every zip-code area. Figures 5.15, 5.16, 5.17 and 5.18 show scatterplots of the results of the exposure assessment. The red dot in these figures is indicating the impact of Hurricane Harvey. It can immediately be recognized that multiple model runs exceed the damage and impact as experienced during Hurricane Harvey. For cumulative rain as well as for maximum rainfall intensity a strong positive dependence can be seen in relation to the impact of a TC. Moreover, it can be seen that over 25% of the flood-events due to generated storms exceed the damage as calculated for Hurricane Harvey.

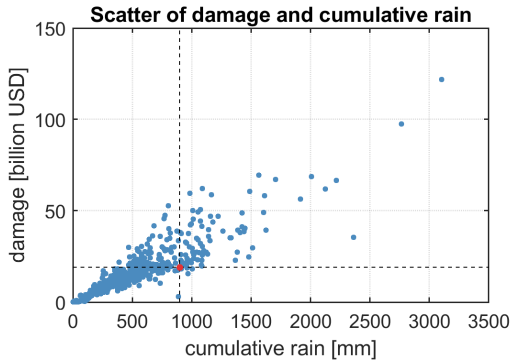

Figure 5.15: Scatter of damage as a result of the flooding and the cumulative rain over the entire lifetime of the TC at an observation point in the model domain. Characteristics of Hurricane Harvey are indicated by the red dot.

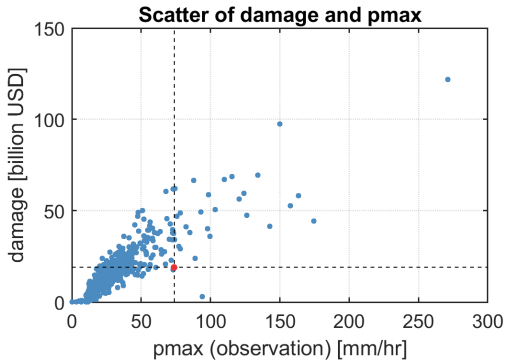

Figure 5.16: Scatter of damage as a result of the flooding and the maximum rainfall intensity over the entire lifetime of the TC at an observation point in the model domain. Characteristics of Hurricane Harvey are indicated by the red dot.

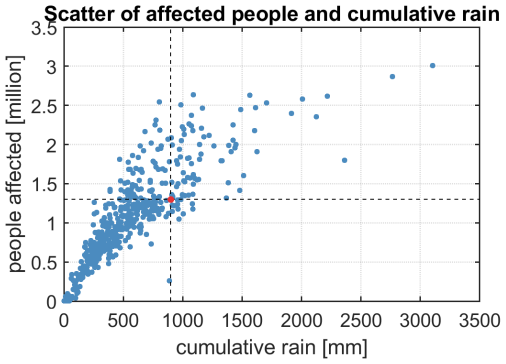

Figure 5.17: Scatter of affected people as a result of the flooding and the cumulative rain over the entire lifetime of the TC at an observation point in the model domain. Characteristics of Hurricane Harvey are indicated by the red dot.

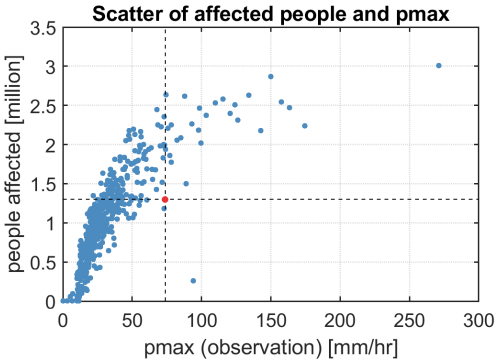

Figure 5.18: Scatter of affected people as a result of the flooding and the maximum rainfall intensity over the entire lifetime of the TC at an observation point in the model domain. Characteristics of Hurricane Harvey are indicated by the red dot.

Furthermore, when the model results are translated to recurrence intervals for damage and affected people due to flooding, it can be seen that the impact due to Hurricane Harvey could potentially be a more frequently occurring event. For a 1 in 100-year event the expected damage is just shy of 60 billion USD and close to 2.5 million people could be affected by a minimum water depth of 0.15 m. Obviously, these numbers are connected with the extent of the flooding due to a 1 in 100-year flood event, which shows to be more severe than the flooding due to Hurricane Harvey.

Table 5.3: Quantitative analysis of the exposure assessment

	Damage [billion USD]	People affected [million]
Hurricane Harvey	19.0	1.300
1 in 25-year	38.1	1.985
1 in 50-year	47.5	2.240
1 in 100-year	59.6	2.469
1 in 250-year	68.6	2.632
1 in 500-year	97.6	2.870
1 in 1,000-year	121.8	3.009

Figures 5.19 and 5.20 present the probability of exceedance and the damages for the climate variability study. An expected annual damage (EAD) can be derived according to this data and the following formula (Skovgard Olsen et al., 2015):

$$\text{EAD} = \int_A \int_p D(p)\,dp\,dA \tag{5.2}$$

The integral consists of the damage $D(p)$ that occurs during the event with probability p in the model domain A (Skovgard Olsen et al., 2015). For the expected annual affected people (EAAP) a similar formulation can be used. This results in an EAD of 8.64 billion USD and an EAAP of 516,590 people, according to the results of this CVA.

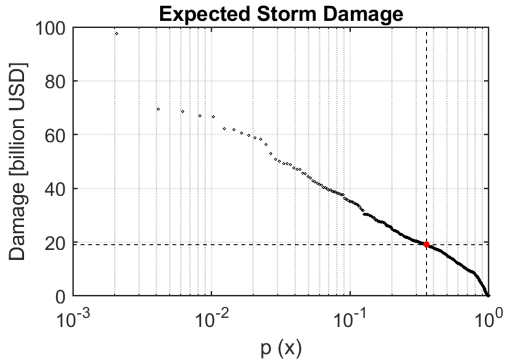

Figure 5.19: Probability of exceedance of damage due to flooding in billion USD. Hurricane Harvey is indicated by the red dot.

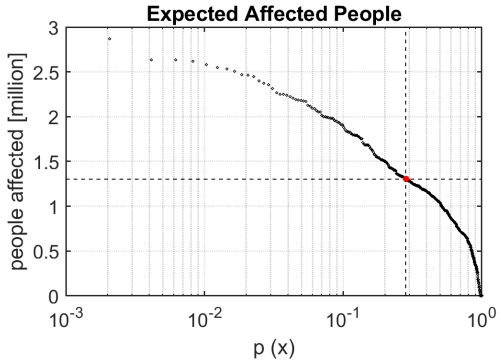

Figure 5.20: Probability of exceedance of affected people due to flooding in billion USD. Hurricane Harvey is indicated by the red dot.

To conclude, in terms of damage and exposure, a flooding as occurred during Hurricane Harvey has a low recurrence interval. This cannot be seen separate from the applied stochastic rainfall distribution model. On the one hand, the rainfall rates at a fixed observation point are overestimated and the randomness of the proposed model causes great variability in the samples. It should be noted however, that this has only been validated for one single TC. Overestimation of rainfall rates inevitably leads to an increase in total cumulative rainfall and therefore the maximum water depths. On the other hand, the maximum rainfall intensities of the most extreme storms are significantly overestimated according to the analysis of the radial rainfall profile. This could affect the climate variability study results as well. Therefore, it is expected that this climate variability study overestimates the impact due to TCs. Nevertheless, the proposed framework is the first model train capable of solving the joint probability of pluvial, fluvial and marine flooding for Houston due to TCs in a dynamic way.

5.5. Key Points

In this chapter a framework is setup which enables to do a climate variability study for Houston, Texas. This line of research was substantiated by the following research question:

What is the result of a climate variability study for Houston when using synthetic Tropical Cyclone tracks and a schematization of Tropical Cyclone rainfall?

The model train exists of the TCWiSE tool, a Delft3D-FM model, a SFINCS model and Delft-FIAT. The key findings as a result of using this framework are:

- A framework is setup to carry out a climate variability study. Houston serves as a case study for this probabilistic flood risk analysis. The framework exists of a model train including: TCWiSE, Delft3D-FM, SFINCS and Delft-FIAT. The model train is capable of carrying out a probabilistic flood risk analysis, where the joint probability of pluvial, fluvial and marine flooding is assessed. For this study, SFINCS models are setup for a set of 489 synthetic TCs. The generated models show great variability in terms of *pmax*, cumulative rain, surge and TC lifetime. The model train as presented here tends to be computationally heavy, especially due to the inclusion of Delft3D-FM model;
- The TCWiSE tool is used to generate synthetic TCs for the North Atlantic Basin. The tool uses a Monte Carlo sampling method and generates TCs sampled from 1,000 years. From this dataset is expected that a representative 1 in 100-year flood can be retrieved. An area of interest is defined to limit the amount of TCs considered in this study. Only TCs which enter in a 250 km radius around Houston are considered in this study, resulting in 489 TCs. Furthermore, future scenarios as a possible increase in intensity and frequency are not taken into account;
- A Delft3D-FM model is used to generate offshore water level time-series which are used as offshore boundary condition for the SFINCS model. The model is poorly-validated for Hurricane Harvey and therefore contains lots of uncertainty. Nevertheless, it proofs to be an excellent tool to get a feeling for the magnitude and the timing of offshore water levels for different TCs. A disadvantage is that all TCs are forced at the same date. Therefore, the difference between different tidal periods can not be analyzed. However, the validation study showed the negligible impact of surge on the compound flooding event. For this reason, the impact of this disadvantage is negligible for the specific case of Houston. Nevertheless, potential future substitutes are one dimensional models or an empirical relation for surge. Furthermore, the inclusion of a Delft3D-FM model increases the computational effort of the climate variability study. Four days of computational time are needed to generate offshore boundary conditions for 489 TCs (4 parallel simulations at the same time);
- Comparing the hydrodynamic character of the generated events to Hurricane Harvey leads to the conclusion that Hurricane Harvey was mostly exceptional in terms of TC lifetime (recurrence interval of more than 1 in 250-year). In combination with relatively low rainfall rates this resulted in significant cumulative rainfall and therefore flooding. The generated events show that the 1 in 100-year maximum rainfall rate at an observation point is equal to 125.6 mm/hr (Harvey: 73.8 mm/hr), the 1 in 100-year cumulative rain = 1,614 mm (Harvey: 1,050 mm), the 1 in 100-year maximum surge = 1.59 m (Harvey: 1.1 m) and the 1 in 100-year TC lifetime = 15.7 days (Harvey: 17.8 days);
- The SFINCS model is based on the model as setup for the validation study in Chapter 3. A 100-meter resolution model is used to suppress the computational effort. This results in a computational time of 10 hours for 489 model runs (4 parallel simulations at the same time). Furthermore, human interventions during a flood event are not taken into account (e.g. a reservoir release);
- The SFINCS model is used to derive a 1 in 100-year flood map. When comparing the derived flood map with the FEMA delineated flood zones for Houston, it can be concluded that the FEMA underestimates the potential 1 in 100-year flood map. This can be the result of a lack of information on pluvial and fluvial flooding. Especially, the widely spread flooding due to precipitation is not marked by the FEMA flood maps. However, it should be noted that the most extreme events are mostly the result of a combination of high-rolls in the sampling method of the maximum rainfall intensity; and
- The FIAT Accelerator enables to compare the impact of the synthetic TCs to the impact of Hurricane Harvey. It is concluded that the impact Hurricane Harvey is an event of frequently occurring magnitude. The damage of 19 billion USD as a result of Hurricane Harvey has a recurrence interval close to 7 years. For reference, a 1 in 100-year damage expectation is close to 60 billion USD. The same holds for the affected people (Hurricane Harvey: 1.3 million, 1 in 100-year: 2.5 million). The expected annual damage for Houston is 8.6 billion USD and the expected annual affected people is 0.5 million.

6
Discussion

This chapter contains a discussion on the methodology and the models used that make up the results of this research. The aim of this research was to set up a generic framework which enables to perform a climate variability study for urban areas. This chapter discusses the uncertainties of this framework, its assumptions and the methodologies applied. The chapter is divided according to the three main lines of research: the validation study, the derivation of the stochastic rainfall distribution model and the climate variability study.

6.1. Validation Study

The findings and results of this research into probabilistic modelling of inland flooding due to TCs are based on a single case study of Hurricane Harvey in Houston, Texas. The validation study was carried out with the combined application of a semi-advanced SFINCS model and the Delft Flood Impact Assessment Tool. The SFINCS model was setup and validated to accurately reproduce the flooding due to Hurricane Harvey in Houston. The model domain encloses most of the catchments areas of the main bayous in the area. However, it did not cover the entire White Oak and Greens Bayou catchments. For the case study of Hurricane Harvey, the results are not significantly affected by this model limitation, because the modelled water levels in the White Oak and Buffalo Bayou show close resemblance to observed water levels. However, it could impact the results of the CVA. For different distributions of rainfall over time and space, different run-off patterns can be expected, influencing the spatial variation of maximum water depths.

An important model component is the DEM. The DEM is based on a cubic interpolation between the low resolution Coastal Relief Model and the high resolution National Elevation Dataset. After interpolation, the digital elevation model is adjusted manually to remove any integration flaws. A nearly seamless DEM is created by this process and it proves to be a great source of data for both the validation and the climate variability study. However, the accuracy of the merger of the two datasets is not assessed.

Model resolution is an important component for both model performance as well as computational efficiency. The model validation study shows highly accurate results for different model resolutions. Peak water levels (and their timing) are captured for small and large grid cell sizes. Hurricane Harvey causes flooding due to extreme input, therefore extreme output is expected. For this reason, this is possibly not the hardest example to reproduce with a low resolution hydrodynamic model. Furthermore, for low resolution models, the characteristics of the flood wave and exact timing first high water can not be fully captured. For the climate variability study as carried out in this research, a correct assessment of peak water levels is sufficient.

Furthermore, the hydrodynamic model results are translated into monetary and social values by Delft-FIAT. This is a needed step to make the results useful for policy-makers. Delft-FIAT makes it possible to carry out a damage assessments based on the unit-loss methodology in a matter of minutes. A simplified Delft-FIAT model (i.e. FIAT Accelerator) is used to perform the damage assessment. FIAT Accelerator uses low resolution global data for the distribution of buildings and people over the model domain. The coarse data is responsible for uncertainty in the model results. Furthermore, a continentally valid depth-damage curve is used to connect water depth with a fraction of the maximum potential damage of a building in North America. The depth-damage curve is therefore not specifically designed for Houston. Moreover, no difference between different types of buildings is taken into account (e.g. the difference between commercial, residential and industrial buildings). As a result, the reported damage is significantly overestimated by the output from Delft-FIAT, on both bulk level as well as zip-code level.

6.2. Stochastic Rainfall Distribution

In this study a generic (stochastic) observation-based parametric TC rainfall model is created based on observations from the QSCAT-R dataset. According to Ahmad et al. (2005), spatial rainfall patterns and rainfall rates are represented accurately in the QSCAT-R dataset. A copula family is fitted, which links the maximum rainfall intensity to the maximum sustained wind speed for worldwide observations. Opposite to a least-squares fitting procedure, as used in similar studies, a copula fit offers the opportunity to make an assessment on statistical quantities (e.g. median, confidence intervals). In a matter of seconds a maximum rainfall intensity can be sampled from the copula. The Frank Copula is used for the parametrization of TC rainfall, but several other copula families prove to be an equally good fit to the data according to the performance metrics from the Multi-Variate Copula Analysis Toolbox. These copulas can possibly show a better fit in the positive tail. Nevertheless, their influence and performance is not further analyzed.

The derived observation-based parametric TC rainfall model is valid for TCs all over the world. Nevertheless, some spatial variability in the occurrence of maximum rainfall intensity and maximum sustained wind speed combinations is recognized. A large portion of the high rainfall intensity observations occurs in the West Pacific Basin for example. For this reason, it could be expected that the copula fit would differ for every oceanic TC basin (see Appendix B.2). This spatial variability however, has not been further analyzed.

Furthermore, it is recognized that the QSCAT-R dataset only includes oceanic observations of TC rainfall, whereas the application of the derived model is focused on overland flooding. Land falling TCs tend to show de-intensification, which suggest a reduction in maximum sustained wind speed and therefore maximum rainfall intensity. However, it should be noted that topographic boundaries and surface roughness also influences TC rainfall. For this reason, it could be expected the scatter of maximum sustained wind speed and maximum rainfall intensity shows different behavior when overland observations of TC rainfall are taking into account. This could lead to a different copula family fit.

The copula allows for sampling maximum rainfall intensity samples for a given maximum sustained wind speed by means of a conditional sampling method. The 90% confidence interval band of the maximum rainfall intensity samples show close resemblance with the 90% confidence interval band of the observations from the QSCAT-R dataset for the entire maximum sustained wind speed dataspace. Therefore, it can be concluded that the variability in TC rainfall is captured with the model. Due to less frequent observations of the combination of high maximum sustained wind speeds and high maximum rainfall intensities, the model accuracy (at the median maximum rainfall intensity values) reduces for maximum sustained wind speeds larger than 40 m/s. Therefore, when sampling at the median of the maximum rainfall intensity samples, the model underestimates the maximum rainfall intensity of a TC. For the climate variability study and other future applications, a random sampling method is suggested. Therefore, it is expected that the performance according to the confidence interval bands is leading, but nevertheless overestimation of the maximum rainfall intensity in a radial rainfall profile is expected. Moreover, the performance of the model is not compared to different TC rainfall models.

To convert the acquired maximum rainfall intensity into a radial rainfall rate profile, an exponential equation based on the Holland wind-profile is used. This basic procedure enables to create a radial (and three dimensional) rainfall profile based on a sampled maximum rainfall intensity according to a given maximum

sustained wind speed. The radial rainfall profile is based on the assumption of equality between the radius of maximum winds and radius of maximum rainfall intensity. This assumption is valid for high maximum rainfall intensities. For lower maximum rainfall intensities, this is not always true. Nevertheless, the error of this assumption is not further assessed into full detail, but it is expected that this causes overestimation of total radial rain and maximum rainfall intensity for low-intensity TCs. Furthermore, the exponential fit results in a long tail in the radial rainfall rate profile (i.e. rainfall rates > 0 mm/hr at large radii). According to observations, this leads to a significant overestimation of the rainfall rates. This holds for both the total rainfall in a radial rainfall profile and the rainfall rates at a fixed observation point. For the climate variability study, all rainfall rates in the radial rainfall profile lower than 10 mm/hr have been set to zero.

Based on a variability study for Hurricane Harvey, this reduces the overestimation of total rain, but does not prevent overestimation of rainfall rates at fixed observation points. This adjustment is based on the performance of the model when assessing Hurricane Harvey only at one fixed observation point only. The rainfall rate and total during Hurricane Harvey showed to be spatially varying. The assessment based on only one observation point is therefore not entirely conclusive.

6.3. Climate Variability Study

This research proposes the first framework for a climate variability study for compound flooding due to TCs. A model train of TCWiSE, Delft3D-FM, SFINCS and Delft-FIAT shows to be capable of making a probabilistic flood risk analysis based on the combination of pluvial, fluvial and marine flooding.

The offshore water level time-series used as input for the SFINCS model are generated by using an extensive full scale circulation model created in Delft3D-FM. On the one hand, this model provides an estimate for the timing and magnitude of offshore water levels for every generated synthetic TC. On the other hand, the Delft3D-FM model is not great in accuracy, since it is poorly calibrated for Hurricane Harvey. Furthermore, the computational efficiency of the Delft3D-FM model is poor. A model run for a single TC takes 45 minutes. However, it should be noted that for general modelling purposes this is considered fast. Due to the variations of angle of incidence and wind speeds, surge levels are generated based on the characteristics of the TC. However, the TCs generated are all initiated on the same day (January 1, 1970). Although the combinations of TC arrival and surge are random, no distinction is made between the timing in different tidal periods, because every single one of the realizations is started on the same day. In a way, this causes variability in the generated timing of simultaneous occurrence of surge and precipitation. However, not all possible combinations are assessed. Since Houston is located at a protected bay, it is expected that this does not have a big influence. However, for the (future) application in a different city, it could potentially lead to an underestimation of offshore water levels. As previously discussed, a low resolution SFINCS model is used to assess the hydrodynamic response to the offshore water levels and TC rainfall. This means that the MAE at peak water levels is larger compared to the results of higher-resolution SFINCS models. This affects the modelled maximum water levels, potentially overestimating the return period flood extent and magnitude. For this analysis, human interventions (e.g. reservoir release) are not taken into account. During Hurricane Harvey, a reservoir release caused significant (extra) flooding in the downstream area. Neglecting similar interventions could also potentially underestimate flooding for synthetically generated flooding scenarios.

Delft-FIAT translates the hydrodynamic results into monetary and social values for 489 model runs within 30 minutes. An expected annual damage and expected annual affected people can be calculated. According to the validation study, modelled damage is overestimated for Hurricane Harvey when comparing to the reported damages. Moreover, it is expected that the hazard and impact due to synthetically generated TCs is overestimated in this research. Storms with a high return period are most likely the result of a sequence of high-rolls in the sampling method for maximum rainfall intensities. This affects the maximum water depths in Houston as a result of these storms. It is expected that the monetary and social values are overestimated due to the combination of these elements, but a detailed validation is not carried out.

The proposed framework to assess the hydrodynamic response consists of several elements: TCWiSE, Delft3D-FM, SFINCS and the proposed observation-based rainfall model. All these elements contribute to the uncertainty in the results of the climate variability study. The TCWiSE generates synthetic TC tracks and terminates hurricanes which do not enter the area of interest. This area therefore limits the amount of TCs taken into account. This limits the variability in the hurricane events, but nevertheless it can be assumed that the most significant events are captured in the area close to Houston. The uncertainty induced for the final results is therefore small. The Delft3D-FM model is poorly validated for Hurricane Harvey and it is therefore expected that offshore water levels forced on the coast of Texas are not entirely correct. However, the validation study showed that the contribution of storm surge on a compound flooding event in Houston was negligible. Therefore, although the uncertainty induced due to Delft3D-FM is large, the impact on the final results is considered small according to the results of the validation study.

More significant are the uncertainties induced due to the developed observation-based parametric rainfall model and the used SFINCS model. The random sampling method for maximum rainfall intensity can result in significantly different radial rainfall rates for the same maximum sustained wind speed. The (maximum) rainfall intensity does have a large influence on the flood extent. This makes the parametric rainfall model a component which induces the most uncertainty in the climate variability study results. Furthermore, a 100 meter resolution SFINCS model is applied. According to the validation study, this can induce a bias of almost +0.3 m on the maximum water depths, potentially overestimating the maximum water depths for every synthetic flood event. Furthermore, the influence of human interventions is neglected. A reservoir release, as during Hurricane Harvey, could potentially occur during events which are more significant. Neglecting human interventions could therefore underestimate the flooding of synthetic events. Therefore, the impact on the final results of the assumptions for the SFINCS model could be significant.

7

Conclusions

The main objective of this research was to develop a methodology to quickly assess the joint probability of pluvial, fluvial and marine flooding due to TCs. The city of Houston serves as a case study. This objective is translated into a main research question:

How can a probabilistic flood risk study, including stochastic rainfall distributions, for compound flooding due to Tropical Cyclones be executed?

The conclusions of this research are summarized in this chapter. First, the main findings for all three lines of research are discussed. Subsequently, recommendations for future work are given.

7.1. Validation Study

The semi-advanced process-based model SFINCS was subjected to a validation case study for Hurricane Harvey. Observed water level time-series at 21 USGS gages are modelled with a MAE of 0.51 m at the peak water level (compared to an average water level raise of 7.5 m). Moreover, the water level time-series show an average NSE of 0.55 [-], which indicates a model of sufficient quality (Ritter and Munoz-Carpena, 2013). A SFINCS model with a 25-meter grid cell size is capable of capturing the characteristics of the flood wave in most of the main bayous in the model domain. The performance of the SFINCS model reduces when the grid cell size increases to 100 m. The characteristics of the run-off flood wave can no longer be captured (NSE = 0.15 [-]). However, the peak water levels are still reproduced with a MAE of 0.60 m. The significant reduction in NSE is related to the low resolution DEM and roughness input, which turn out to be two important components in accurately reproducing the pluvial water run-off, the flood wave and its characteristics. Moreover, sensitivity tests show that the flooding event and impact due to Hurricane Harvey is mainly pluvial-driven. The impact of surge and wind is little to none, accounting for less than 1% of the damage done.

In addition to the hydrodynamic analysis, an exposure assessment is carried out with Delft-FIAT. This tool is able to convert hazard data (from the SFINCS model) into monetary and social values. This conversion can be carried out in minutes and is a valuable tool for policy- and decision-makers. The output of the Delft-FIAT is compared to reported values according to Resilient Texas (2019). This shows that the modelled damage overestimates reported damages by 200%. For the 25-meter resolution model, Delft-FIAT calculates 19 billion USD of damage and up to 1.3 million directly affected individuals due to Hurricane Harvey. For the applicability in a probabilistic flood risk assessment, which desires computational efficiency, the results have been subjected to a sensitivity test for the resolution. For a 100-meter grid resolution, the calculated damage only increases by 11%. Moreover, the calculated amount of affected people only raises for 5.7% compared to the high resolution model. This indicates that Delft-FIAT shows results in the same order of magnitude for different resolutions of the SFINCS model.

For the hind-casting study a detailed precipitation field was constructed and used to force the SFINCS model. Here, the data of 83 weather stations is interpolated in time and space to acquire a highly detailed precipitation schematization (RMSD of 20 mm, for an averaged total of 1,050 mm over six days). The high resolution observed rainfall field is a vital component in accurately simulating the flood wave in this pluvial event. In the case of forcing the SFINCS model with the rainfall fields from a local high-resolution weather model (NARR, NOAA (2018b)), the exact details of the flood wave can no longer be reproduced. The NARR rainfall (RMSE of

79.4 mm and a bias of -26.5 mm over all observation stations for the cumulative rainfall over a six-day period) shows a more axisymmetric rainfall pattern on the model domain. Sensitivity tests are carried out to assess the effect of the application of this model. Performance metrics show a MAE of 0.64 m at peak water levels and a NSE of 0.53, which still indicates a similar model performance compared to the high-detailed interpolated rainfall field. Thus, a more simple representation of TC rainfall does not cause the hydrodynamic response to differ tremendously. Furthermore, using this less-detailed rainfall model reduces the computational demand of the SFINCS model, which is beneficial for a probabilistic flood risk study.

7.2. Stochastic Rainfall Distribution

An observation-based stochastic precipitation model is created based on the TC observations of the QSCAT-R dataset (Chavas and Vigh, 2014). Dependence is recognized between maximum rainfall intensity and maximum sustained wind speed. Opposite to similar studies, that use a least-square fitting procedure, a more statistical approach is used in this research. The proposed 'best-fit' Frank copula (RMSD = 1.47 [-], NSE = 0.9951 [-]) offers the opportunity to retrieve statistical quantities as the mean and confidence intervals. The proposed method of sampling shows good resemblance with the dataset looking at the variability in the samples. The 90% confidence interval band for the QSCAT-R data and the sampled maximum rainfall intensity show close resemblance for the complete maximum sustained wind speed dataspace. However, the median maximum rainfall intensity tends to be underestimated for higher wind speeds ($vmax > 40$ m/s). The RMSD for the median values is 37.9 mm/hr, this is mainly due to the large difference between the observations and the model at higher *vmax*. However, for application, the maximum rainfall intensity is sampled randomly. This indicates that the 90% confidence interval band comparison is more important.

A similar approach as for the Holland wind-profile is used to create a radial rainfall rate profile. As a pragmatic assumption, the radius of maximum winds and the radius of maximum rainfall intensity is set equal. This is only valid for higher *pmax* values. Creating 100 synthetic variations of Hurricane Harvey (track and *vmax* of Hurricane Harvey, *pmax* from proposed model) shows that the proposed observation-based precipitation model overestimates TC rainfall rates at a fixed observation point. This can be explained by the fact that the exponential fit creates a large tail (i.e. rainfall rates larger than zero for large radii), which is incorrect for part of the observations in the QSCAT-R dataset. For this reason, the extent of the created radial rainfall profile is larger than observations suggest. To prevent this, all rainfall rates lower than 10 mm/hr are set to zero. In essence, this cuts off the tail of the exponential radial rainfall profile. By removing these lower rainfall intensities, the precipitation rates due to the synthetic variations of Hurricane Harvey at a fixed observation point decrease. This adjustment reduces the root mean square difference of rainfall rates at a fixed observation point with 0.5 mm/hr to +11 mm/hr and the bias reduces with 50% to +2.77 mm/hr. Nevertheless, the proposed rainfall schematization still overestimates the rainfall rate as observed at a fixed point, as can be concluded from these metrics.

7.3. Climate Variability Study

With the before-mentioned components, a framework is setup to carry out a climate variability study, where the joint probability of pluvial, fluvial and marine flooding is assessed. A model train of TCWiSE, Delft3D-FM, SFINCS and Delft-FIAT is used to assess both hydrodynamic and social impact of TCs. The model train is capable of carrying out a flood risk assessment and derive flood maps for given return periods. When comparing this to the current FEMA approach for flood risk, it can be seen that the flood extent due to compound flooding can be significantly larger than currently expected. Furthermore, for a 100-year return period flood event in Houston, the impact adds up to 2.5 million individuals and 60 billion USD. This is 216% higher than the damage due to flooding that occurred due to Hurricane Harvey. On the one hand, the overestimation of rainfall rates at a fixed observation point due to the proposed observation-based parametric rainfall model, it is expected that the computed impact and flooding extent of a 1 in 100-year flood event is overestimated by this quantity. On the other hand, the maximum rainfall rates in a radial rainfall profile are overestimated to great extent for the most extreme storms in which the rainfall rates are most likely a combination of many high-rolls in the conditional sampling method for the maximum rainfall intensities. Furthermore, the validation study shows a bias of +0.28 m at peak water levels. The overestimated of the maximum rainfall rates is expected to have the largest influence on the results of the climate variability study. Therefore it is expected that the 1 in 100-year flood extent and magnitude could be less severe. Furthermore, the climate variability study does show that flood events as during Hurricane Harvey could possibly happen more often. Therefore,

it can be concluded that Houston is very prone to flooding due to the combined occurrence of pluvial, fluvial and marine flooding. The flood risk study shows an annual expected damage of 8.64 billion USD and an annual expected affected people of over 500,000 individuals.

SFINCS is a semi-advanced model which shows to be rather computationally efficient and at the same time relatively accurate in terms of reproducing peak water levels (roughly 5 minutes for a single model simulation). The model train setup for this climate variability assessment includes the use of a Delft3D-FM model. This model causes the proposed methodology to be rather computational inefficient (roughly 45 minutes for a model simulation). Nevertheless, it can be concluded that the proposed method is a first step towards the assessment of the joint probability of pluvial, fluvial and marine flooding in a CVA.

7.4. Recommendations

This research offers plenty of opportunities for future work. Several recommendations which could help and further develop the given methodology to the observation-based precipitation model are given in this section. The suggested future research is subdivided in suggestions concerning the validation study, the derivation of a stochastic rainfall model and the climate variability study.

Research into the SFINCS model performance

- The coarse resolution model is not capable of reproducing the details of the flood wave. The reason for that is that the initial water level is not reproduced correctly due to a wrong bed level. Local bathymetry difference which are not resolved in the model. The SFINCS model averages the topography level at all grid cell points to set a bed level for that specific cell. The inclusion of a sub-grid feature can be investigated. This allows the user to specify a smaller grid cell size at locations of interest, while at the same time a coarser grid can be used for the rest of the model domain. It is expected that this does not impact the computational demand tremendously.

Research into the proposed stochastic rainfall distribution model

- This study focused on providing a generic precipitation schematization, which is applicable all over the world. Looking at the data however, spatial variability is recognized. More frequent observations of high *pmax* are observed in the West Pacific basin for example. Looking at basin-specific rainfall schematization (e.g. a copula fit per basin) could improve the performance of the developed observation-based precipitation model at different locations around the world;
- The proposed fit for the radial rainfall distribution is based on the fitting procedure of the Holland wind-profile (Holland et al., 2010). For the rainfall fit it was assumed that the radius of the maximum winds equals the radius of maximum rainfall intensity. This however, is not always the case. Especially for lower rainfall intensities the exponential fit does not match observed rainfall distributions. The impact of this assumption should be investigated; and
- Furthermore, to account for the overestimation of total rainfall, all rainfall rates lower than 10 mm/hr were set to zero. The model was adjusted based on a variability study for Hurricane Harvey only. To validate this adjustment, two options are suggested. First, the rainfall model could be tested for different historical TCs. For example, Hurricane Allison (2001) and Hurricane Ike (2008) are two other storms which induced compound flooding in Houston. Secondly, the radial limit of TC rainfall should be investigated. It should be investigated if the radial limit of TC rainfall can be linked (or parametrized) with another characteristic of a hurricane.

Research into the application of a probabilistic flood risk assessment

- The computational efficiency of the proposed methodology can be improved. The use of a Delft3D-FM model to create offshore water level time-series is computationally demanding. To further improve computational efficiency and applicability of the climate variability study framework, an empirical relation which links storm surge, maximum sustained wind speed and distance to the area of interest can be developed; and
- Lastly, this research does not include future climate scenarios for the probabilistic flood risk assessment. It is most likely that future developments would impact offshore water levels, TC intensity and TC frequency. On the one hand, it is interesting to compare the results between different future scenarios. On the other hand, future changes most likely also impact the performance of the proposed rainfall schematization, because observations of high *pmax* and high *vmax* can potentially occur more frequently. The frequency of observed combinations of high maximum rainfall intensity and maximum sustained wind speed in the existing dataset is limited. Therefore, the conditional sampling tends to perform less for more intense hurricanes, which could potentially occur more frequently in the future.

Bibliography

Ahmad, K. A., Jones, W. L., Kasparis, T., Vergara, S. W., Adams, I. S., and Park, J. D. (2005). Oceanic rain rate estimates from the quikscat radiometer: A global precipitation mission pathfinder. *Journal of Geophysical Research: Atmospheres*, 110(D11).

Amadeo, K. (2019). Hurricane Harvey Facts, Damage and Costs. *The Balance*. Accessed on September 16, 2019.

Bates, P. D., Horritt, M. S., and Fewtrell, T. J. (2010). A simple inertial formulation of the shallow water equations for efficient two-dimensional flood inundation modelling. *Journal of Hydrology*, 387(1):33 – 45.

Bezuyen, K. G., Stive, M. J. F., Vaes, G. J. C., Vrijling, J. K., and Zitman, T. J. (2012). *Inleiding Waterbouwkunde*.

Blake, E. S. and Gibney, E. J. (2011). The deadliest, costliest, and most intense united states tropical cyclones from 1851 to 2010 (and other frequently requested hurricane facts). Technical report, National Weather Service, National Hurricane Center. NOAA Technical Memorandum NWS NHC-6.

Blake, E. S. and Zelinsky, D. A. (2018). Tropical Cyclone Report - Hurricane Harvey. Technical report, National Hurricane Center.

Bosboom, J. and Stive, M. J. F. (2015). *Coastal Dynamics I*. VSSD. Lecture Notes CIE4305.

Chan, J. and Gray, W. (1982). Tropical Cyclone Movement and Surrounding Flow Relationships. *Monthly Weather Review*, 110:1354–1374.

Chavas, D. R. and Lin, N. (2016). A Model for the Complete Radial Structure of the Tropical Cyclone Wind Field. Part II: Wind Field Variability. *Journal of the Atmospheric Sciences*, 73(8):3093–3113.

Chavas, D. R., Reed, K. A., and Knaff, J. A. (2017). Physical understanding of the tropical cyclone wind-pressure relationship. *Nature Communications*, 8(1).

Chavas, D. R. and Vigh, J. L. (2014). *QSCAT-R: The QuikSCAT Tropical Cyclone Radial Structure Dataset*. National Center for Atmospheric Research.

Chen, S. S., Knaff, J. A., and Marks, F. D. (2006). Effects of vertical wind shear and storm motion on tropical cyclone rainfall asymmetries deduced from trmm. *Monthly Weather Review*, 134(11):3190–3208.

City of Fort Lauderdale (2018). Stormwater Master Plan. `https://www.fortlauderdale.gov/departments/public-works/engineering/stormwater-design/stormwater-master-plan`.

De Bruijn, K. M. (2005). *Resilience and flood risk management: a system approach applied to lowland rivers*. PhD thesis, Delft University of Technology.

Deltares (2014). *WES - Wind Enhance Scheme for cyclone modelling - User Manual*.

Deltares (2018). Delft3D Flexible Mesh Suite - Manual.

DLR (2019). Earth observation center - global urban footprint. `https://www.dlr.de/eoc/en/desktopdefault.aspx/tabid-9628/16557_read-40454/`. Accessed on 26 June 2019.

Egbert, G. D. and Erofeeva, S. Y. (2002). Efficient inverse modeling of barotropic ocean tides. *Journal of Atmospheric and Oceanic Technology*, 19(2):183–204.

Emanuel, K., Ravela, S., Vivant, E., and Risi, C. (2006). A statistical deterministic approach to hurricane risk assessment. *Bulletin of the American Meteorological Society*, 87(3):299–314.

Emanuel, K. A. (2013). Downscaling CMIP5 climate models shows increased tropical cyclone activity over the 21st century. *Proceedings of the National Academy of Sciences*, 110(30):12219–12224.

ESA (2015). Mapping our global human footprint. `https://www.esa.int/Our_Activities/Observing_the_Earth/Mapping_our_global_human_footprint`. Accessed on 27 July 2019.

FEMA (2007). National Elevation Dataset (NED) and similar USGS Holdings. `https://hazards.fema.gov/femaportal/docs/NationalElevationDataset_2007.pdf`.

Field, C. B., Barros, V., Stocker, T. F., Qin, D., Dokken, D. J., Ebi, K. L., Mastrandrea, M. D., Mach, K. J., Plattner, G. K., Allen, S. K., Tignor, M., and Midgley, P. M. (2012). Managing the risks of extreme events and disasters to advance climate change adaptation. Technical report, IPCC.

FirstStreetFoundation (2019). Understanding FEMA Flood Maps and Limitations. `https://firststreet.org/updates/understanding-fema-flood-maps-and-limitations/`.

Genest, C. and Favre, A. (2007). Everything You Always Wanted to Know about Copula Modeling but Were Afraid to Ask. *Journal of Hydrologic Engineering*, 12(4):347–368.

Giardino, A., Nederhoff, K., and Vousdoukas, M. (2018). Coastal hazard risk assessment for small islands: assessing the impact of climate change and disaster reduction measures on Ebeye (Marshall Islands). *Regional Environmental Change*.

Hall, T. M. and Jewson, S. (2014). Statistical modelling of North Atlantic tropical cyclone tracks. *Tellus*, 59A:486–498.

Harper, B. (2002). Tropical Cyclone Parameter Estimation in the Australian Region: Wind-Pressure Relationships and Related Issues for Engineering Planning and Design - A Discussion Paper. Technical report, Systems Engineering Australia Pty Ltd.

HCFCD (2018). Harris County Flood Warning System. `https://www.harriscountyfws.org/`.

Hoek, J. (2018). Tropical Cyclone Wind Statistical Estimation in Regions with Rare Tropical Cyclone Occurrence. Master's thesis, Delft University of Technology.

Holland, G. J. (1980). An analytic model of the wind and pressure profiles in hurricanes. *Monthly Weather Review*, 108(8):1212–1218.

Holland, G. J. (2008). A revised hurricane pressure–wind model. *Monthly Weather Review*, 136(9):3432–3445.

Holland, G. J., Belanger, J. I., and Fritz, A. (2010). A revised model for radial profiles of hurricane winds. *Monthly Weather Review*, 138(12):4393–4401.

HomelandSecurity (2017). FEMA Needs to Improve Management of Its Flood Mapping Programs. OIG-17-110.

Hong, Y., Kummerow, C. D., and Olson, W. S. (1999). Separation of convective and stratiform precipitation using microwave brightness temperature. *Journal of Applied Meteorology*, 38(8):1195–1213.

Houston-Galveston Area Council (2015). H-GAC Land Cover Data Set. `http://www.h-gac.com/land-use-and-land-cover-data/default.aspx`. Accessed on 23 April 2019.

Hughes, M. (2016). Coastal waves, water levels, beach dynamics and climate change. CoastAdapt.

Huizinga, J., De Moel, H., and Wojciech, S. (2017). Global flood depth-damage functions: Methodology and the database with guidelines. Technical report, JRC Science Hub. EUR 28522 EN.

Irish, J. L., Resio, D. T., and Ratcliff, J. J. (2008). The Influence of Storm Size on Hurricane Surge. *Journal of Physical Oceanography*, 38(9):2003–2013.

Jongman, B., Hochrainer-Stigler, S., Feyen, L., CJH, A., Mechler, R., Botzen, W. W., Bouwer, L., Pflug, G., Rojas, R., and Ward, P. (2014). Increasing stress on disaster-risk finance due to large floods. *Nature Climate Change*, 4.

JRC (2019). GHSL - Global Human Settlement Layer. `https://ghsl.jrc.ec.europa.eu/`. Accessed on 26 June 2019.

Kalyanapu, A. J., Burian, S. J., and McPherson, T. N. (2009). Effect of land use-based surface roughness on hydrological model output. *Journal of Spatial Hydrology*, 9(2):51–71.

Kernkamp, H. W. J., Van Dam, A., Stelling, G. S., and de Goede, E. D. (2011). Efficient scheme for the shallow water equations on unstructured grids with application to the Continental Shelf. *Ocean Dynamics*, 61(8):1175–1188.

Kidder, S. Q., Knaff, J. A., Kusselson, S. J., Turk, M., Ferraro, R. R., and Kuligowski, R. J. (2005). The Tropical Rainfall Potential (TRaP) Technique. Part I: Description and Examples. *Weather and Forecasting*, 20(4):456–464.

Knaff, J. A. and Zehr, R. M. (2007). Reexamination of tropical cyclone wind–pressure relationships. *Weather and Forecasting*, 22(1):71–88.

Knapp, K. R., Kruk, M. C., Levinson, D. H., Diamond, H. J., and Neumann, C. J. (2010). The international best track archive for climate stewardship (ibtracs). *Bulletin of the American Meteorological Society*, 91(3):363–376.

Knutson, T. R., Sirutis, J. J., Zhao, M., Tuleya, R. E., Bender, M., Vecchi, G. A., Villarini, G., and Chavas, D. (2015). Global Projections of Intense Tropical Cyclone Activity for the Late Twenty-First Century from Dynamical Downscaling of CMIP5/RCP4.5 Scenarios. *Journal of Climate*, 28(18):7203–7224.

Koba, H., Hagiwara, T., Asano, S., and Akashi, S. (1990). Relationships between CI number from Dvorak's technique and minimum sea level pressure or maximum wind speed of tropical cyclone. *Journal of Meteorological Research*, 42:59–67.

Kriesche, B., Weindl, H., Smolka, A., and Schmidt, V. (2014). Stochastic simulation model for tropical cyclone tracks, with special emphasis on landfall behavior. *Natural Hazards*, 73:335–353.

Kron, W. (2005). Flood risk = hazard * values * vulnerability. *Water International*, 30(1):58–68.

Landsea, C. W. and Franklin, J. L. (2013). Atlantic Hurricane Database Uncertainty and Presentation of a New Database Format. *Monthly Weather Review*, 141:3576–3592.

Langousis, A. and Veneziano, D. (2009). Theoretical model of rainfall in tropical cyclones for the assessment of long-term risk. *Journal of Geophysical Research: Atmospheres*, 114(D2).

Legates, D. R. and McCabe, G. J. (1999). Evaluating the use of "goodness-of-fit" measures in hydrologic and hydroclimatic model validation. *Water Resources Research*, 35(1):233–241.

Leijnse, T. W. B. (2018). Computationally Efficient Modelling of Compound Flooding due to Tropical Cyclones with the Explicit Inclusion of Wave-Driven Processes. Master's thesis, Delft University of Technology.

Lesser, G. R., Roelvink, J. A., van Kester, J. A. T. M., and Stelling, G. S. (2004). Development and validation of a three-dimensional morphological model. *Coastal Engineering*, 51(8):883 – 915. Coastal Morphodynamic Modeling.

Lin, N. and Chavas, D. (2012). On hurricane parametric wind and applications in storm surge modeling. *Journal of Geophysical Research: Atmospheres*, 117(D9).

Lindner, J. and Fitzgerald, S. (2018). Final Report, Hurricane Harvey. Technical report, Harris County Flood Control District. HCFCD Flood Watch.

Lonfat, M., Marks, F. D., and Chen, S. S. (2004). Precipitation Distribution in Tropical Cyclones Using the Tropical Rainfall Measuring Mission (TRMM) Microwave Imager: A Global Perspective. *Monthly Weather Review*, 132(7):1645–1660.

Lonfat, M., Rogers, R., Marchok, T., and Marks, F. D. (2007). A Parametric Model for Predicting Hurricane Rainfall. *Monthly Weather Review*, 135(9):3086–3097.

Lowman, L. E. L. and Barros, A. P. (2016). Interplay of drought and tropical cyclone activity in se u.s. gross primary productivity. *Journal of Geophysical Research: Biogeosciences*, 121(6):1540–1567.

Lu, P., Lin, N., Emanuel, K., Chavas, D., and Smith, J. (2018). Assessing Hurricane Rainfall Mechanisms Using a Physics-Based Model: Hurricanes Isabel (2003) and Irene (2011). *Journal of the Atmospheric Sciences*, 75(7):2337–2358.

Merz, B., Kreibich, H., Schwarze, R., and Thieken, A. (2010). Assessment of economic flood damage. *Natural Hazards Earth Systems Science*, 10:1697–1724.

Miles, B. I. (1958). Rainfall Rates of Florida Hurricanes. *Monthly Weather Review*, 86(7):258–264.

Miles, J. W. (1957). On the generation of surface waves by shear flows. *Journal of Fluid Mechanics*, 3(2):185–204.

Nash, J. E. and Sutcliffe, J. V. (1970). River flow forecasting through conceptual models part I - A discussion of principles. *Journal of Hydrology*, 10(3):282 – 290.

Nederhoff, K., Giardino, A., van Ormondt, M., and Vatvani, D. (2019). Estimates of tropical cyclone geometry parameters based on best track data. *Natural Hazards and Earth System Sciences Discussions*, 2019:1–26. in review.

Neumann, B., Vafeidis, A. T., Zimmermann, J., and Nicholls, R. J. (2015). Future Coastal Population Growth and Exposure to Sea-Level Rise and Coastal Flooding - A Global Assessment. *PLOS ONE*, 10(3):1–34.

Nguyen, B. M. (2015). *Long-term regional simulation of tropical cyclones using a Generalized Stochastic Empirical Storm Model. A case study in the Western North Pacific.* PhD thesis, Delft University of Technology.

NHC (2018). Sea Lake and Overland Surges from Hurricanes (SLOSH). `https://www.nhc.noaa.gov/surge/slosh.php`.

NOAA (2018a). Costliest U.S. Tropical Cyclones Tables Updated.

NOAA (2018b). National Oceanic and Atmospheric Administration. `https://www.noaa.gov/`.

NOAA (2019). Datums for 8770613, Morgans Point, Barbours Cut TX. `https://tidesandcurrents.noaa.gov/datums.html?id=8770613`.

Olsen, L. (2018). Record reservoir flooding was predicted even before Harvey hit Houston. *Houston Chronicles*.

Paul, B. K. and Rashid, H. (2017). *Chapter Two - Tropical Cyclones and Storm Surges*. Butterworth-Heinemann, Boston.

Pfost, R. L. (2000). Operational Tropical Cyclone Quantitative Precipitation Forecasting. *National Weather Digest*, 24:61–66.

Phillips, O. M. (1957). On the generation of waves by turbulent wind. *Journal of Fluid Mechanics*, 2(5):417–445.

Pielke Jr., R. A., Gratz, J., Landsea, C. W., Collins, D., Saunders, M. A., and Musulin, R. (2008). Normalized Hurricane Damage in the United States: 1900-2005. *Natural Hazards Review*, 9(1):29–42.

Ramirez, J. A., Lichter, M., Coulthard, T. J., and Skinner, C. (2016). Hyper-resolution mapping of regional storm surge and tide flooding: comparison of static and dynamic models. *Natural Hazards*, 82(1):571–590.

Rappaport, E. N. (2000). Loss of Life in the United States Associated with Recent Atlantic Tropical Cyclones. *Bulletin of the American Meteorological Society*, 81(9):2065–2074.

Resilient Texas (2019). Rebuild Texas - The Governor's Commission to Rebuild Texas. `http://resilient-texas.com/`.

Ritter, A. and Munoz-Carpena, R. (2013). Performance evaluation of hydrological models: Statistical significance for reducing subjectivity in goodness-of-fit assessments. *Journal of Hydrology*, 480:33 – 45.

Robertson, I. N., Riggs, H. R., Yim, S. C., and Young, Y. L. (2007). Lessons from hurricane katrina storm surge on bridges and buildings. *Journal of Waterway, Port, Coastal, and Ocean Engineering*, 133(6):463–483.

Roeber, V. and Bricker, J. D. (2015). Destructive tsunami-like wave generated by surf beat over a coral reef during Typhoon Haiyan. *Nature Communications*, 6(7854).

Roelvink, D. J. A., J. H. M. Reniers, A., van Dongeren, A., Thiel de Vries, J., Lescinski, J., and McCall, R. (2010). *XBeach Model – Description and Manual*. Deltares.

Rogers, R., Chen, S., Tenerelli, J., and Willoughby, H. (2003). A Numerical Study of the Impact of Vertical Shear on the Distribution of Rainfall in Hurricane Bonnie (1998). *Monthly Weather Review*, 131(8):1577–1599.

Rogers, R., Marks, F., and Marchok, T. (2009). *Tropical Cyclone Rainfall*. American Cancer Society.

Rumpf, J., Weindl, H., Hoppe, P., Rauch, E., and Schmidt, V. (2008). Tropical cyclone hazard assessment using model-based track simulation. *Natural Hazards*, 48:383–398.

Russell, L. B. (1968). Probability distributions for texas gulf coast hurricane effects of engineering interest. PhD. Thesis.

Sadegh, M., Ragno, E., and Agha Kouchak, A. (2017). Multivariate Copula Analysis Toolbox (MvCAT): Describing dependence and underlying uncertainty using a Bayesian framework. *Water Resources Research*, 53:5166–5183.

Sanchez-Gomez, P. (2018). Risk-based Optimization of Reservoir Emergency Operations. Master's thesis, Delft University of Technology.

Schott, T., Landsea, C., Hafele, G., Lorens, J., Taylor, A., Thurm, H., Ward, B., Willis, M., and Zaleski, W. (2012). The Saffir-Simpson Hurricane Wind Scale.

Schwerdt, R. W., Ho, F. P., and Watkins, R. R. (1979). Meteorological criteria for standard project hurricane and probable maximum hurricane wind fields - Gulf and East Coasts of the United States. Technical report, NOAA. NWS23.

Seaber, P. R., Kapinos, F. P., and Knapp, G. L. (1987). Hydrologic Unites Maps. Water Supply-Paper.

Sebastian, A., Lendering, K., Kothuis, B., Brand, A., Jonkman, S. N., Gelder, P. H. A. J. M., Kolen, B., Comes, T., Lhermitte, S., Meesters, K., Walle, B., Ebrahimi Fard, A., Cunningham, S., Khakzad, N., and Nespeca, V. (2017). A fact-finding effort in the direct aftermath of Hurricane Harvey in the Greater Houston Region.

Sharp, J. (2018). Eye of the Storm - Report of the Governor's Commission to Rebuild Texas.

Sitkowski, M., Kossin, J. P., and Rozoff, C. M. (2011). Intensity and structure changes during hurricane eyewall replacement cycles. *Monthly Weather Review*, 139(12):3829–3847.

Sklar, A. (1959). Fonctions de repartion a n dimensions et leurs marges. *Institut Statistique de l'Universite de Paris*, 8:229–231.

Skovgard Olsen, A., Zhou, Q., Jorgen Linde, J., and Arnbjerg-Nielsen, K. (2015). Comparing Methods of Calculating Expected Annual Damage in Urban Pluvial Flood Risk Assessments. *Water*, 7:255–270.

Slager, K., Burzel, A., Bos, E., de Bruijn, K., Wagenaar, D., Winsemius, H., Brouwer, L., and van der Doef, M. (2016). User Manual Delft-FIAT version 1. `publicwiki.deltares.nl/display/DFIAT/Delft-FIAT+Home`.

Smith, R. B. and Barstad, I. (2004). A linear theory of orographic precipitation. *Journal of the Atmospheric Sciences*, 61(12):1377–1391.

Snaiki, R. and Wu, T. (2017). A theoretical model for rapid estimates of rainfall during tropical cyclones.

Taylor, J. R. (1997). *An Introduction to Error Analysis: The Study of Uncertainties in Physical Measurements*. University Science Books. `https://faculty.kfupm.edu.sa/phys/aanaqvi/Taylor-An%20Introduction%20to%20Error%20Analysis.pdf` (PDF).

The MathWorks, Inc. (2018). MATLAB 2018a.

Thyer, M., Renard, B., Kavetski, D., Kuczera, G., Franks, S. W., and Srikanthan, S. (2009). Critical evaluation of parameter consistency and predictive uncertainty in hydrological modelling: A case study using bayesian total error analysis. *Water Resources Research*, 45(12).

Torres Duenas, L. F. (2018). Flood Risk Assessment of the Clear Creak Watershed considering Compound Events. Master's thesis, Delft University of Technology.

Tuleya, R. E., DeMaria, M., and Kuligowski, R. J. (2007). Evaluation of gfdl and simple statistical model rainfall forecasts for u.s. landfalling tropical storms. *Weather and Forecasting*, 22(1):56–70.

United States Census Bureau (2018). Population estimates, july 1, 2018. `https://www.census.gov/quickfacts/harriscountytexas`. Accessed on 27 June 2019.

USDA (2019). Soil infiltration. `https://www.nrcs.usda.gov/Internet/FSE_DOCUMENTS/nrcs142p2_053268.pdf`. Accessed on July 10, 2019.

Van der Meer, J. W. (2002). Techincal Report Wave Run-up and Wave Overtopping at Dikes. Technical report, Technical Adivsory Committee on Flood Defence.

Van Engelen, T. E. (2016). Towards a rapid assessment flood forecasting system for the Southern California coast. Master's thesis, Delft University of Technology.

van Oldenborgh, G. J., van der Wiel, K., Sebastian, A., Singh, R., Arrighi, J., Otto, F., Haustein, K., Li, S., Vecchi, G., and Cullen, H. (2017). Attribution of extreme rainfall from Hurricane Harvey, August 2017. *Environmental Research Letters*, 12(12):124009.

Venter, G. (2002). Tails of copulas. *Proceedings of the Casualty Actuarial Society*, 89.

Vickery, P. J., Skerlj, P. F., and Twistdale, L. A. (2000). Simulation of Hurricane Risk in the U.S. Using Emprical Track Model. *Journal of Structural Engineering*, 126(10):1222–1237.

Vickery, P. J. and Twisdale, L. A. (1995). Prediction of hurricane wind speeds in the united states. *Journal of Structural Engineering*, 121(11):1691–1699.

Wagenaar, D. J., Dahm, R. J., Diermanse, F. L. M., Dias, W. P. S., Dissanayake, D. M. S. S., Vajja, H. P., Gehrels, J. C., and Bouwer, L. M. (2019). Evaluating adaptation measures for reducing flood risk: A case study in the city of Colombo, Sri Lanka. *International Journal of Disaster Risk Reduction*, 37:101162.

Wahl, T. (2017). Sea-level rise and storm surges, relationship status: complicated! *Environmental Research Letters*, 12(11):111001.

Wahl, T., Jain, S., Bender, J., Meyers, S. D., and Luther, M. E. (2015). Increasing risk of compound flooding from storm surge and rainfall for major US cities. *Nature Climate Change*, 5(12):1093–1097.

Willmott, C. J., Ackleson, S. G., Davis, R. E., Feddema, J. J., Klink, K. M., Legates, D. R., O'Donnell, J., and Rowe, C. M. (1985). Statistics for the evaluation and comparison of models. *Journal of Geophysical Research: Oceans*, 90(C5):8995–9005.

Willoughby, H. E., Darling, R. W. R., and Rahn, M. E. (2006). Parametric representation of the primary hurricane vortex. part ii: A new family of sectionally continuous profiles. *Monthly Weather Review*, 134(4):1102–1120.

Willoughby, H. E. and Rahn, M. E. (2004). Parametric representation of the primary hurricane vortex. part i: Observations and evaluation of the holland (1980) model. *Monthly Weather Review*, 132:3033–3048.

Wing, O. E. J., Bates, P. D., Smith, A. M., Sampson, C. C., Johnson, K., Fargione, J., and Morefield, P. (2018). Estimates of present and future flood risk in the conterminous united states. *Environmental Research Letters*, 13:034023.

Zehnder, J. A. (2018). Tropical Cyclone. `https://www.britannica.com/science/tropical-cyclone`.

Zhang, J. A. and Uhlhorn, E. W. (2012). Hurricane Sea Surface Inflow Angle and an Observation-Based Parametric Model. *Monthly Weather Review*, 140:3587–3605.

Zhang, L. and Singh, V. P. (2007). Bivariate rainfall frequency distributions using Archimedean copulas. *Journal of Hydrology*, 332(1):93 – 109.

A

Validation: Hurricane Harvey

This appendix contains the background information for the validation study of Hurricane Harvey for Houston. Section A.1 contains the distribution of the infiltration and roughness values. Section A.2 provides the water level time-series for all 21 USGS observation stations. Sensitivity analysis for compound flooding, offshore water levels, precipitation and resolution are presented in Sections A.3, A.4, A.5 and A.6. The depth-damage curve used is given in Section A.7. Lastly, Section A.8 gives the reported and modelled damage in table-format.

A.1. Model: Infiltration and Roughness

The infiltration and roughness values are specified on a spatially varying map. For both the infiltration and the roughness, the value are set according to the land-use type present at the location. The land-use type specification is retrieved from Houston-Galveston Area Council (2015). The appointed values can be found in Table A.1. For a full description of different land-use types, see Houston-Galveston Area Council (2015). In Figures A.1 and A.2 the chosen values of Table A.1 are mapped out.

Table A.1: Surface roughness values per land-use type based on Kalyanapu et al. (2009). Infiltration values per land-use type based on the authors knowledge.

Land Use	Infiltration [mm/hr]	Manning Factor [$m^{-1/3}s$]
Open Water	0.0	0.0250
Developed, High Intensity	4.0	0.0404
Developed, Medium Intensity	5.0	0.0678
Developed, Low Intensity	8.0	0.0678
Developed, Open Space	12.0	0.0404
Barren Lands	8.0	0.0113
Forest	14.0	0.0400
Pasture/Hay and Grasslands	14.0	0.3250
Cultivated	14.0	0.3250
Wetlands	14.0	0.1825

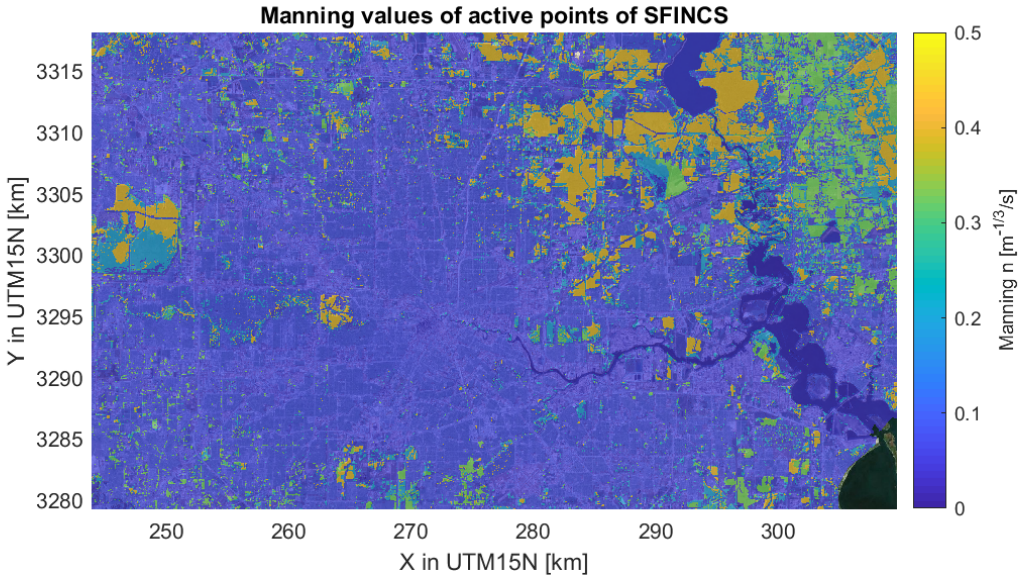

Figure A.1: Spatial varying roughness SFINCS model input.

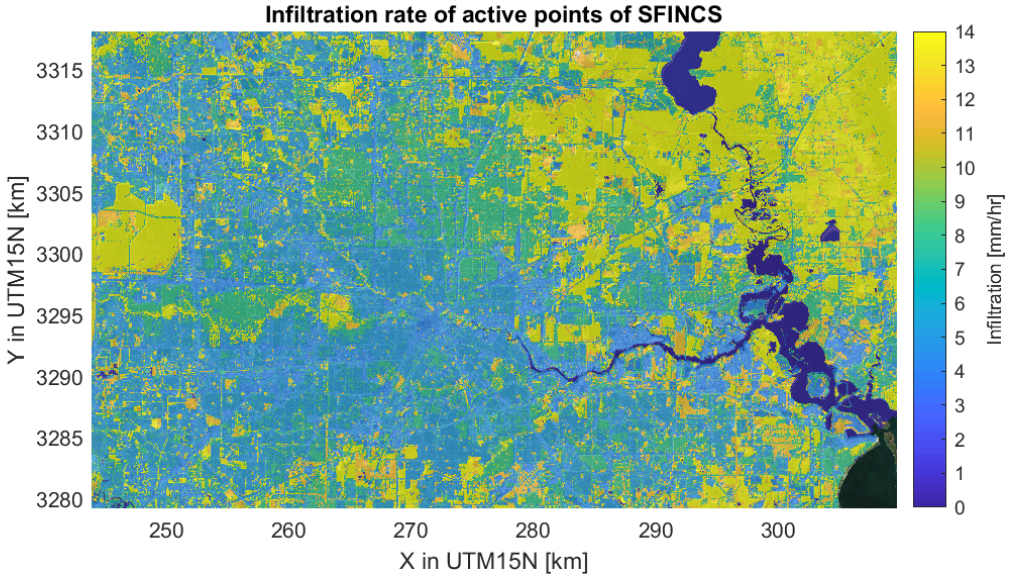

Figure A.2: Spatial varying infiltration SFINCS model input.

A.2. Hydrological Model Performance

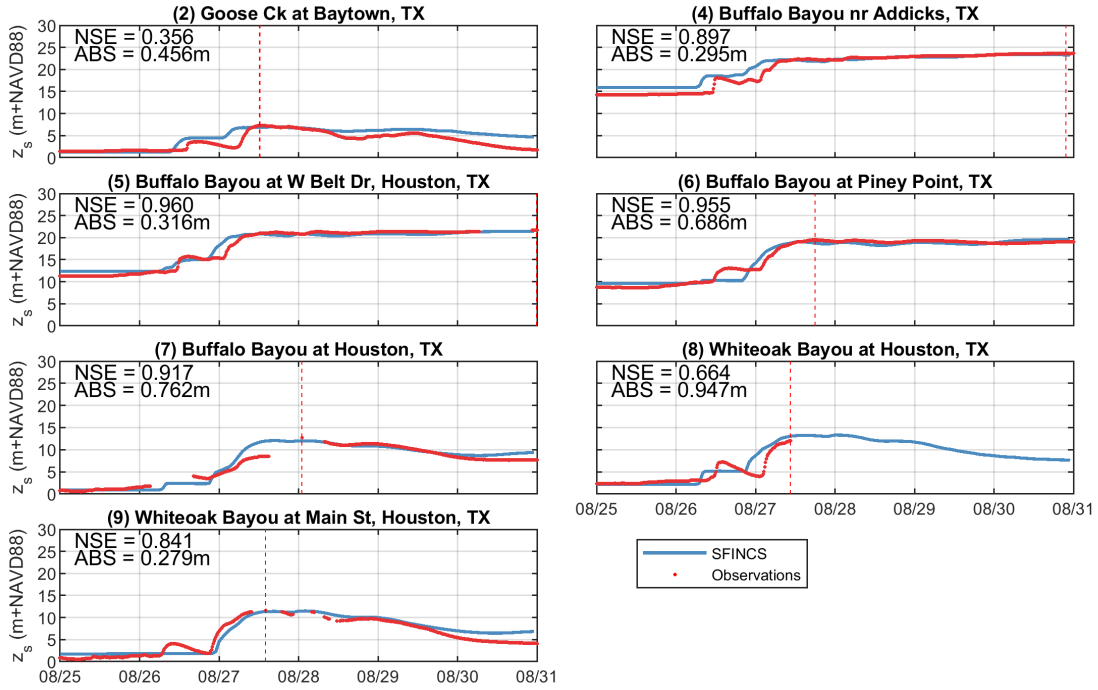

Figure A.3: Time-series of water levels at USGS observation stations expressed in meters above NAVD88. The red line indicates the observed value, where the blue line indicates the output of the SFINCS model. The maximum observed water level (peak water level) is indicated with the red dotted vertical line (1/3).

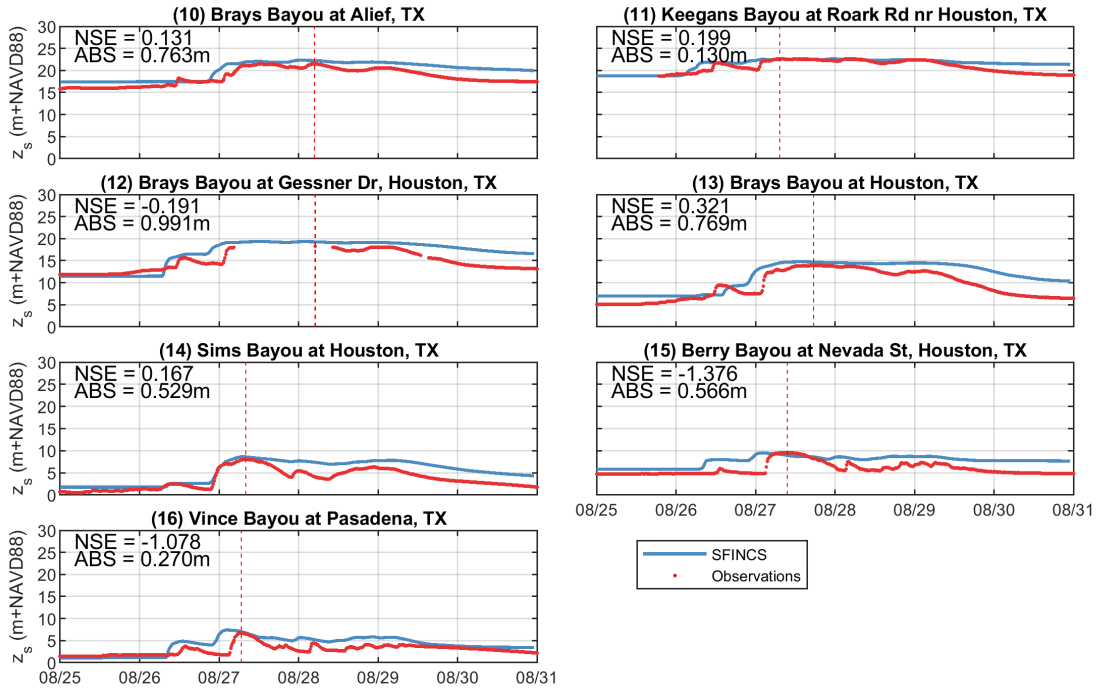

Figure A.4: Time-series of water levels at USGS observation stations expressed in meters above NAVD88. The red line indicates the observed value, where the blue line indicates the output of the SFINCS model. The maximum observed water level (peak water level) is indicated with the red dotted vertical line (2/3).

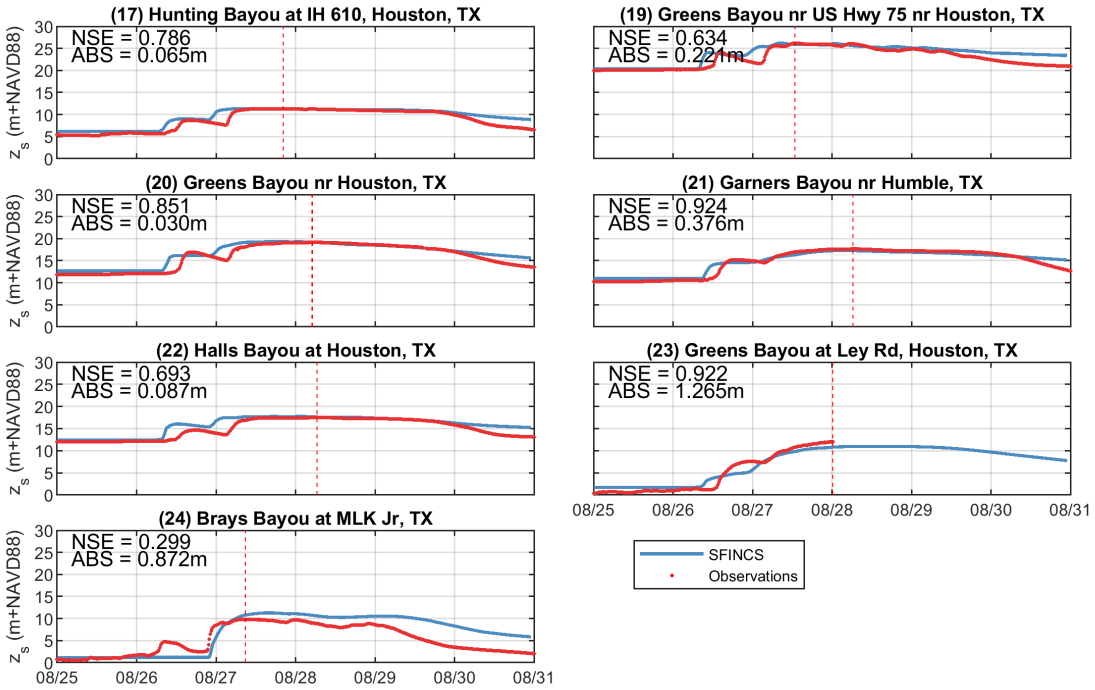

Figure A.5: Time-series of water levels at USGS observation stations expressed in meters above NAVD88. The red line indicates the observed value, where the blue line indicates the output of the SFINCS model. The maximum observed water level (peak water level) is indicated with the red dotted vertical line (3/3).

A.3. Compound Flooding

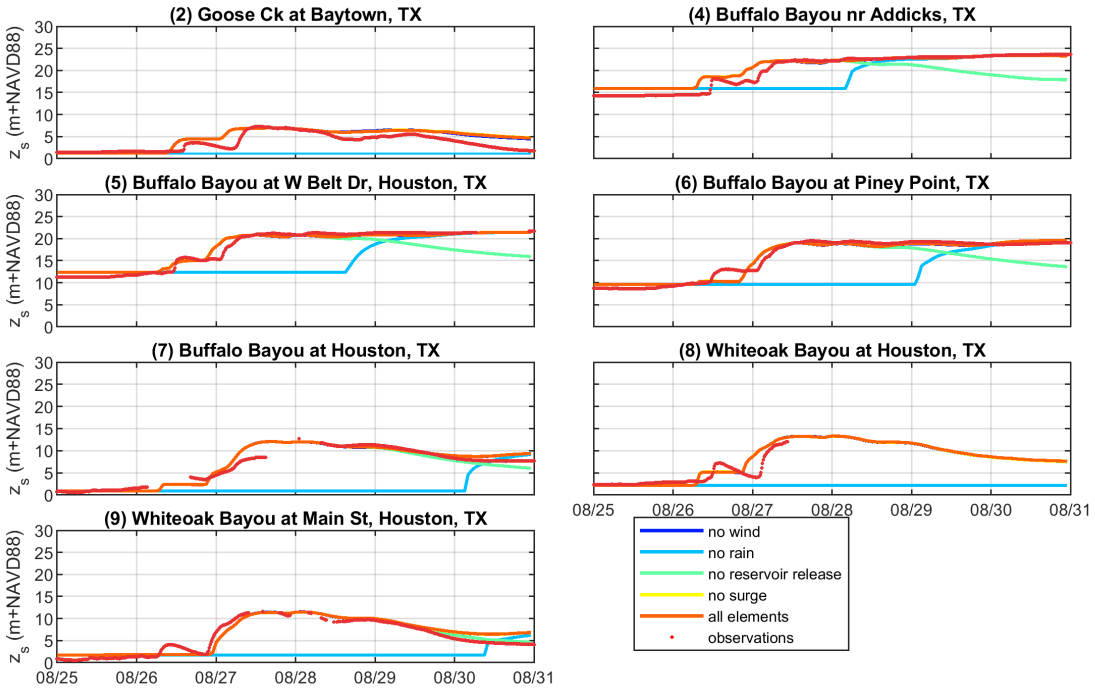

Figure A.6: Time-series of water levels at USGS observation stations expressed in meters above NAVD88 for different configurations of the compound flooding event. The red line indicates the observed value, where the colored lines indicate the SFINCS model output for different scenarios (1/3).

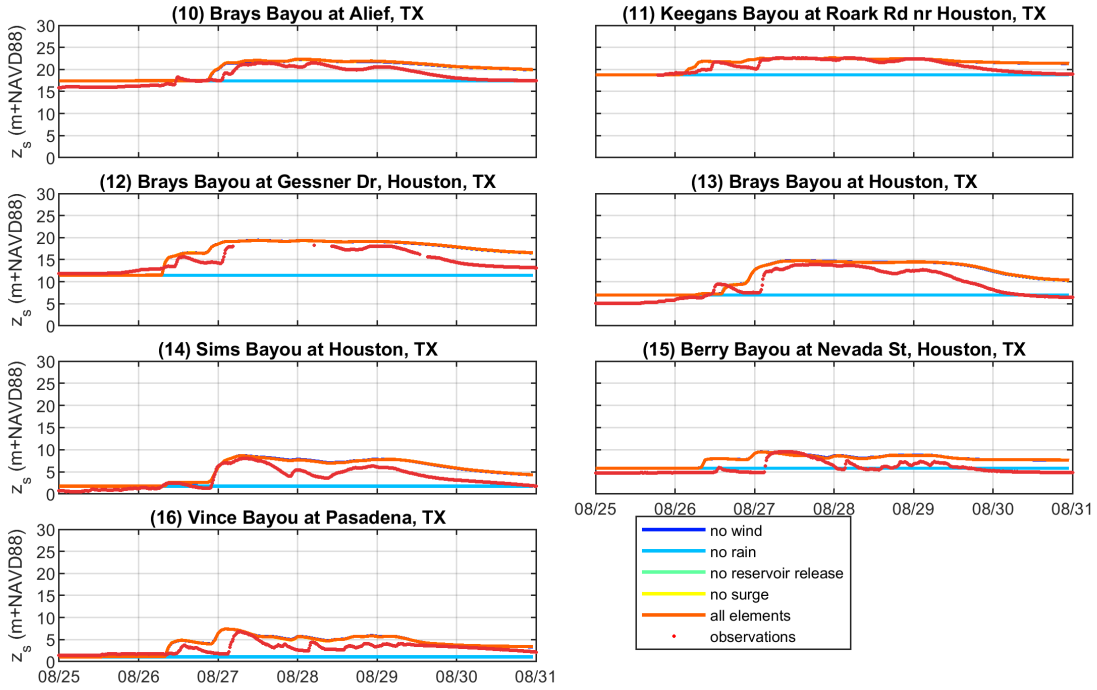

Figure A.7: Time-series of water levels at USGS observation stations expressed in meters above NAVD88 for different configurations of the compound flooding event. The red line indicates the observed value, where the colored lines indicate the SFINCS model output for different scenarios (2/3).

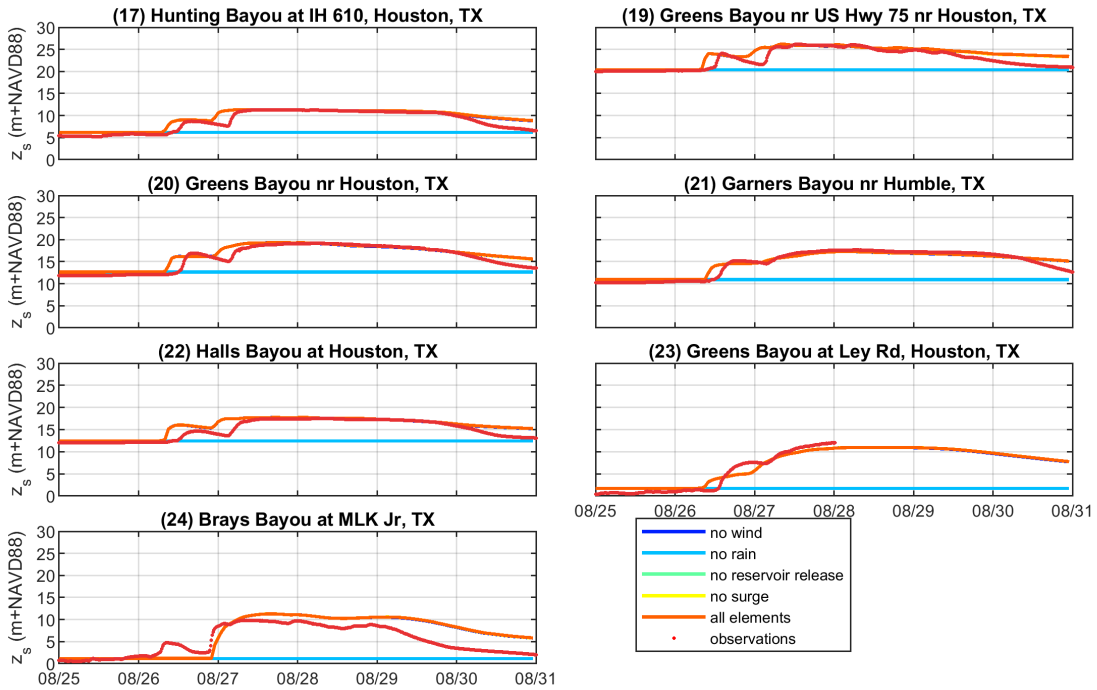

Figure A.8: Time-series of water levels at USGS observation stations expressed in meters above NAVD88 for different configurations of the compound flooding event. The red line indicates the observed value, where the colored lines indicate the SFINCS model output for different scenarios (3/3).

A.4. Sensitivity Offshore Boundary Condition

To assess the impact of the offshore boundary condition, the water levels have been increased with 1.0 m and 2.0 m respectively. As mentioned previously, the impact of the surge could not be quantified by means of an observation point, because none of the USGS observation stations are located in close vicinity of the coast. This is confirmed when looking at the results for the increased downstream boundary condition (forced at Morgans Point, Barbour Cut). The increase in water level at the observation points (see Figures A.10, A.11 and A.12) is barely noticeable visually. This can be explained by the tidal reach of the San Jacinto river, which does not reach one of the USGS observation points. Nevertheless, the MAE at peak water level is increasing slightly as can be seen in Table A.2.

Table A.2: Performance metrics for the sensitivity analysis of offshore water levels.

run	MAE	bias	RSME (HWM)	positive NSE	average NSE
Default	0.512m	-0.007m	0.977m	18/21	0.55
+1.0 m	0.565m	-0.014m	0.980m	18/21	0.55
+2.0 m	0.619m	-0.017m	1.000m	18/21	0.54

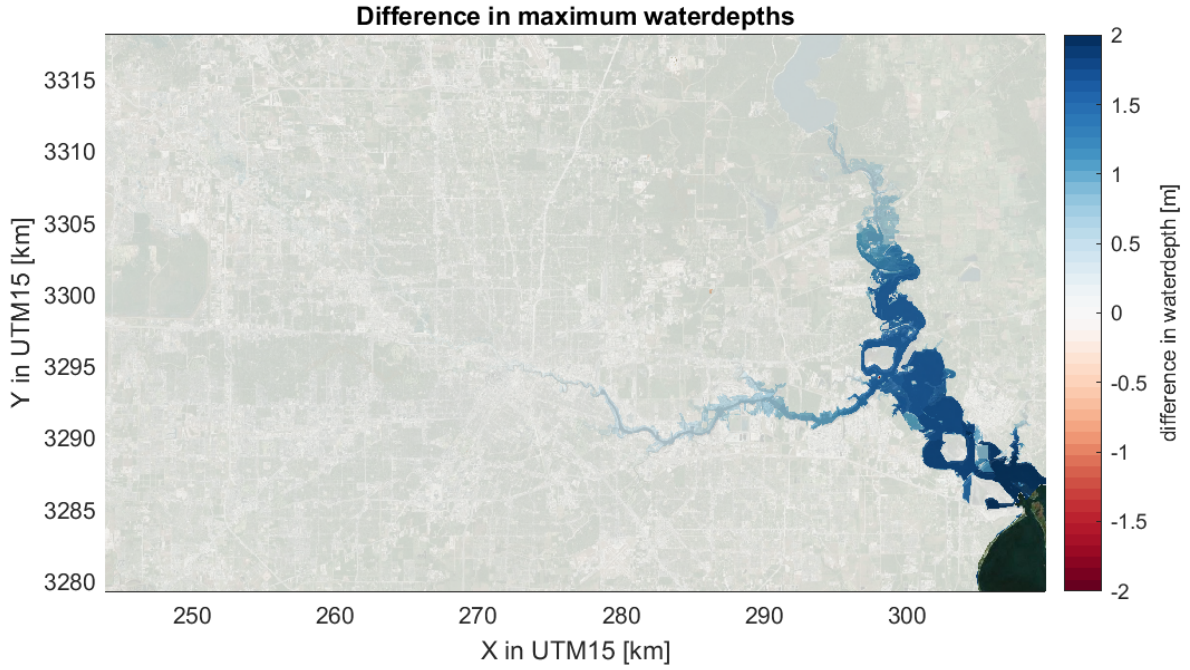

Figure A.9: Spatial overview of the difference in flooding when assessing the default scenario and the scenario where the offshore water levels are increased with 2.0 m. The color scale indicates the absolute difference in maximum water depth compared to the default scenario.

Furthermore, the impact of an increase in offshore water levels can be checked by the HWM. The RMSE of all HWM is increasing slightly with increasing surge levels, indicating a raise in total volume of water in the model domain. The reason that this difference is only small, while the offshore water level is increased with relatively large values, can be explained by the spatial distribution of the HWM. The impact of offshore water levels will affect the inland area close to shore (south-east of model domain) and near the Houston Ship Channel banks. However, as can be seen in Figure 3.6, most HWM are located in the western part of the domain, indicating that they are not affected by an increase in offshore water levels. The effect on the RMSE is therefore limited. When comparing the maximum water depths (see Figure A.9) it can be seen that the water level raise only affects water levels in the Houston Ship Channel. It can be concluded that for a flooding in Houston the effect of surge is small.

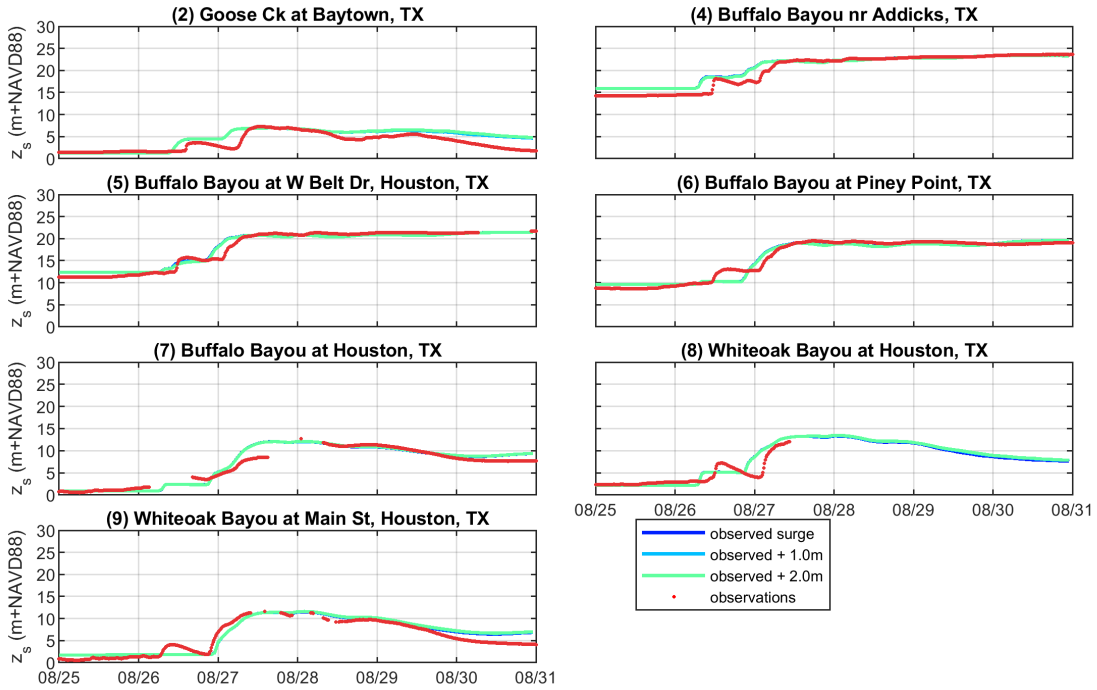

Figure A.10: Time-series of water levels at USGS observation stations expressed in meters above NAVD88 for different offshore boundary conditions. The red line indicates the observed value, where the colored lines indicate the SFINCS model output for different scenarios (1/3).

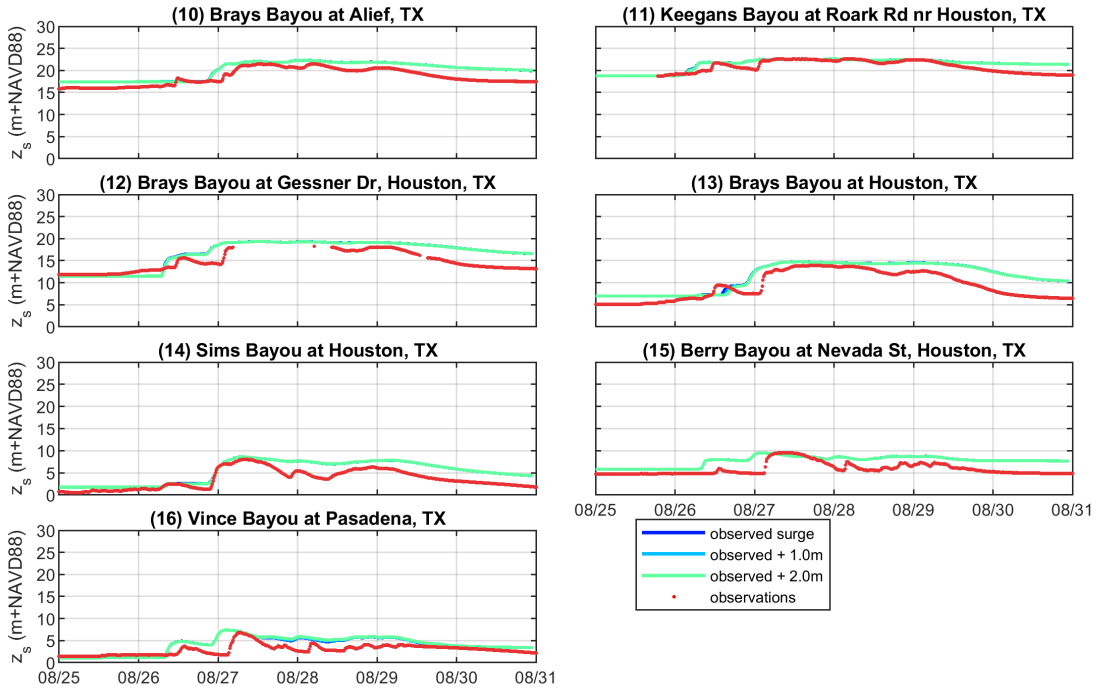

Figure A.11: Time-series of water levels at USGS observation stations expressed in meters above NAVD88 for different offshore boundary conditions. The red line indicates the observed value, where the colored lines indicate the SFINCS model output for different scenarios (2/3).

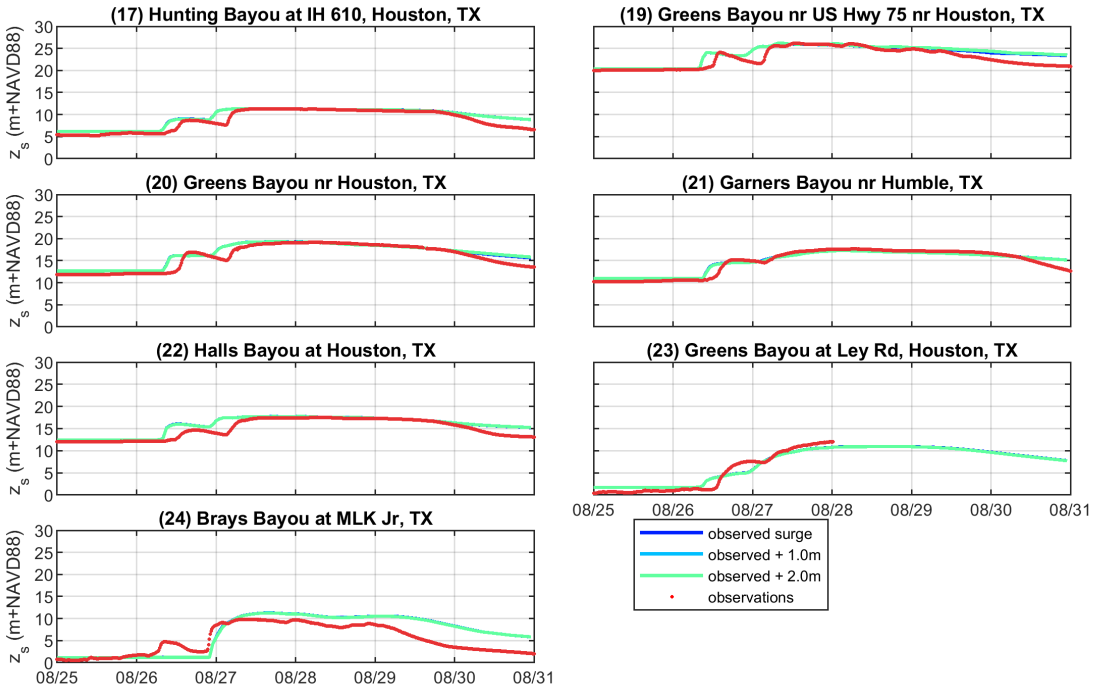

Figure A.12: Time-series of water levels at USGS observation stations expressed in meters above NAVD88 for different offshore boundary conditions. The red line indicates the observed value, where the colored lines indicate the SFINCS model output for different scenarios (3/3).

A.5. Sensitivity Precipitation

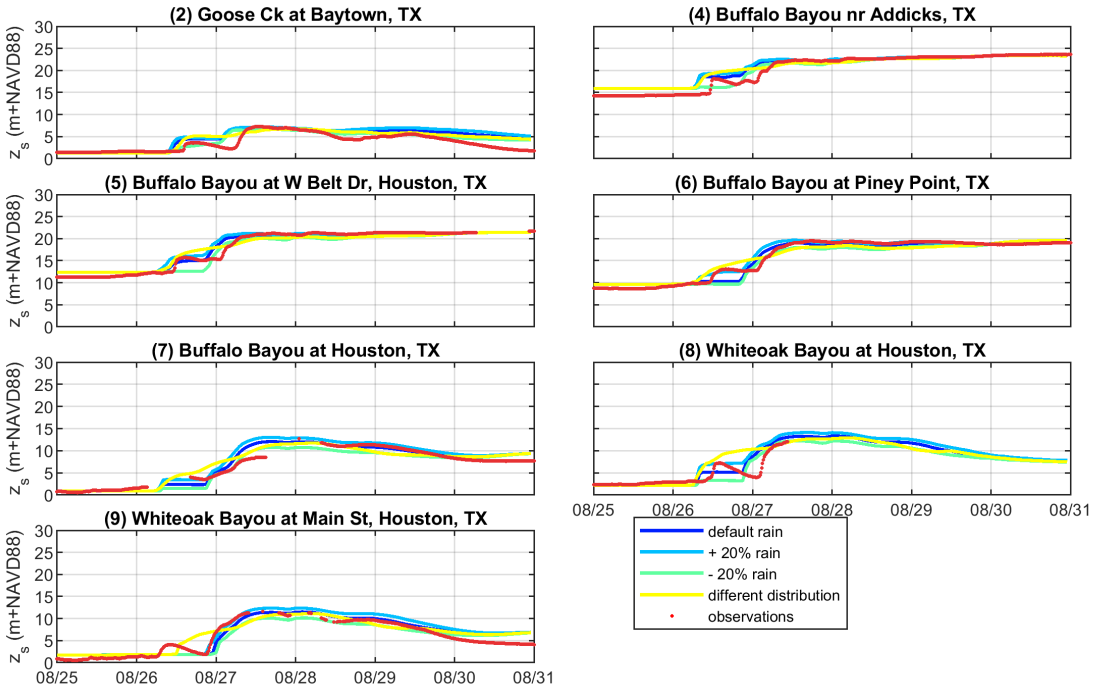

Figure A.13: Time-series of water levels at USGS observation stations expressed in meters above NAVD88 for different configurations of the precipitation. The red line indicates the observed value, where the colored lines indicate the SFINCS model output for different scenarios (1/3).

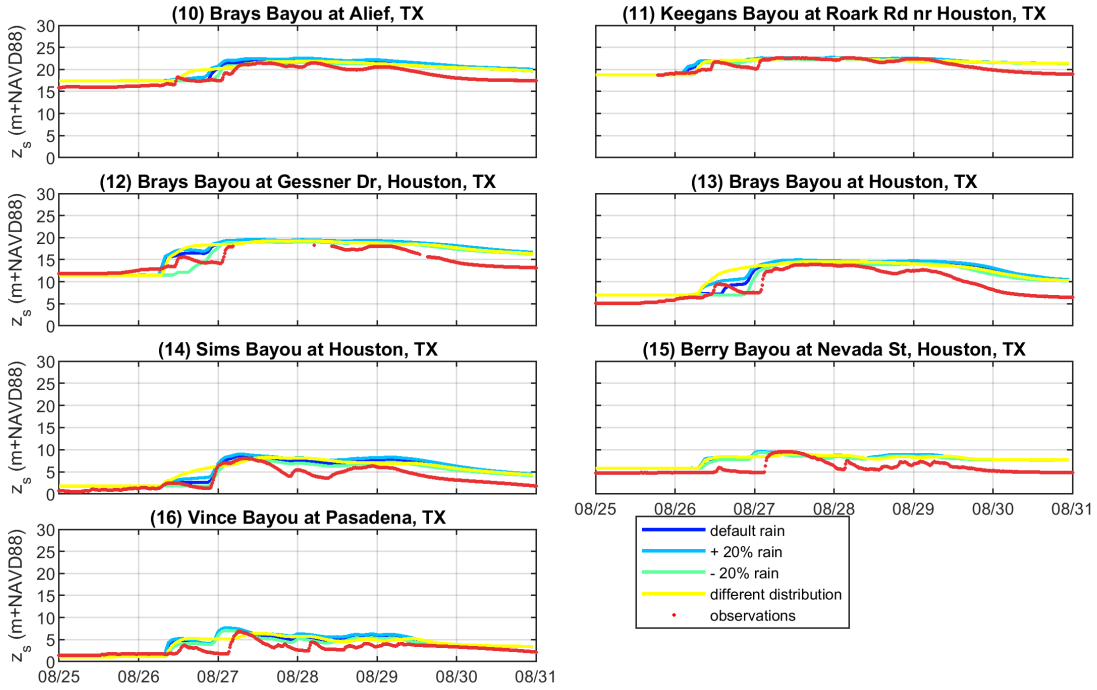

Figure A.14: Time-series of water levels at USGS observation stations expressed in meters above NAVD88 for different configurations of the precipitation. The red line indicates the observed value, where the colored lines indicate the SFINCS model output for different scenarios (2/3).

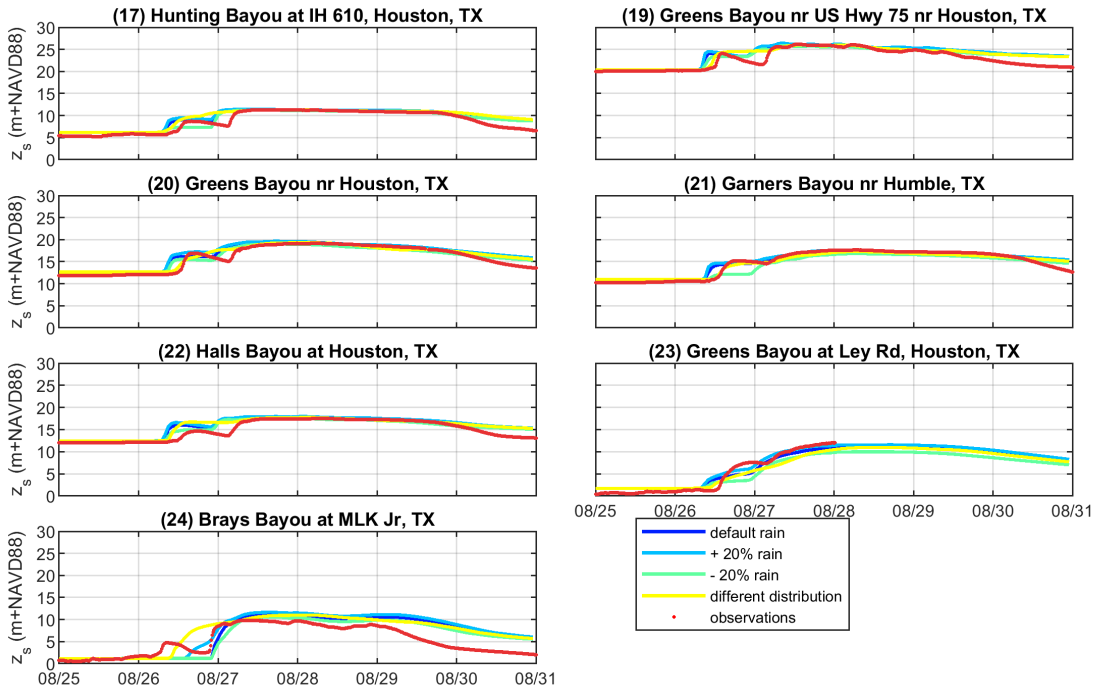

Figure A.15: Time-series of water levels at USGS observation stations expressed in meters above NAVD88 for different configurations of the precipitation. The red line indicates the observed value, where the colored lines indicate the SFINCS model output for different scenarios (3/3).

A.6. Sensitivity Resolution

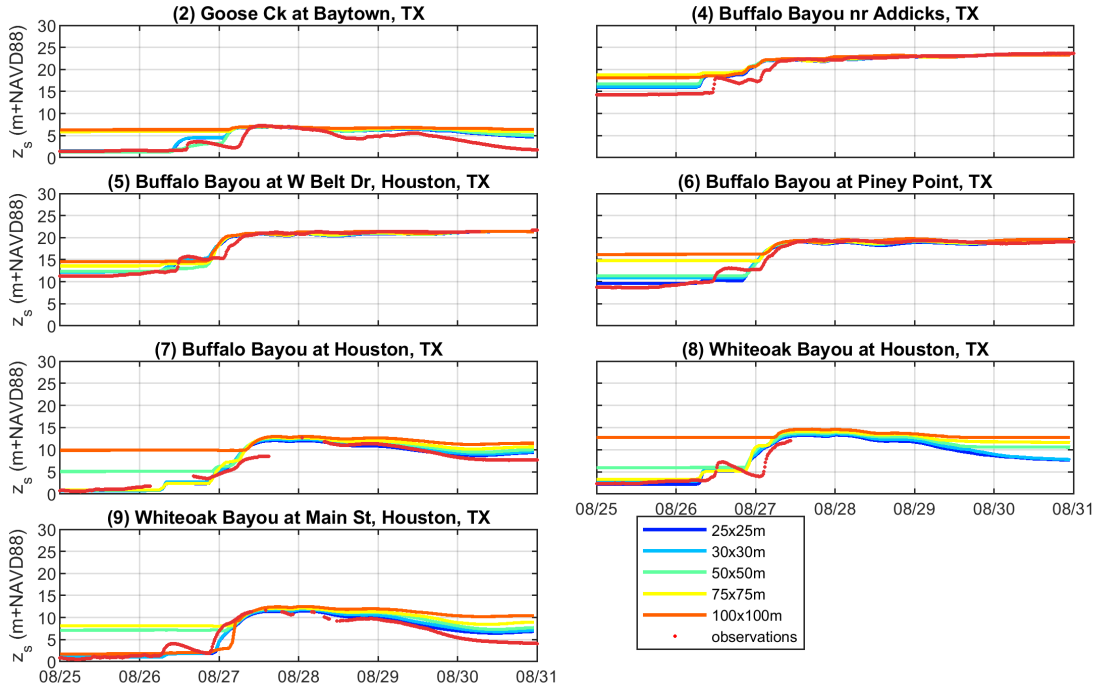

Figure A.16: Time-series of water levels at USGS observation stations expressed in meters above NAVD88 for different model resolutions. The red line indicates the observed value, where the colored lines indicate the SFINCS model output for different scenarios (1/3).

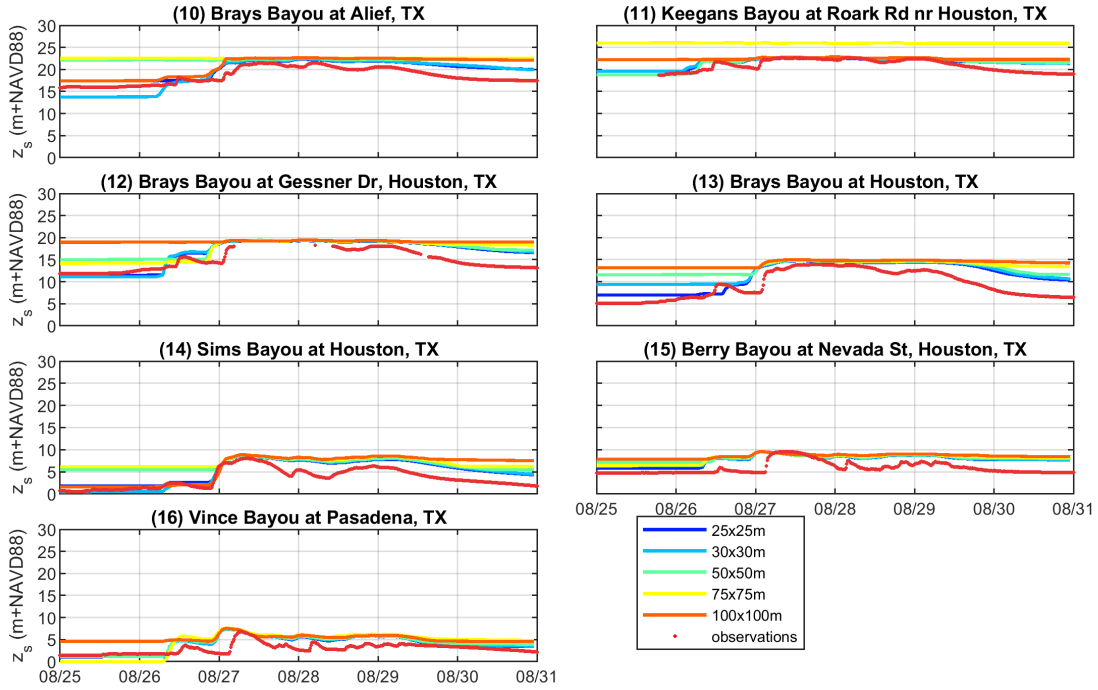

Figure A.17: Time-series of water levels at USGS observation stations expressed in meters above NAVD88 for different model resolutions. The red line indicates the observed value, where the colored lines indicate the SFINCS model output for different scenarios (2/3).

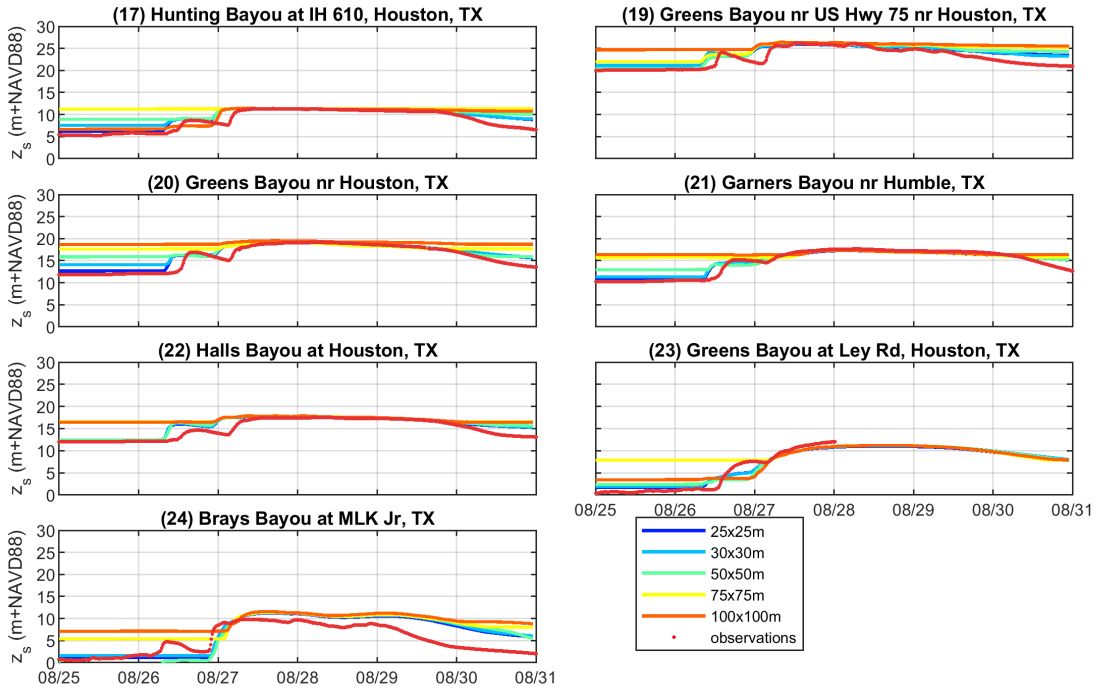

Figure A.18: Time-series of water levels at USGS observation stations expressed in meters above NAVD88 for different model resolutions. The red line indicates the observed value, where the colored lines indicate the SFINCS model output for different scenarios (3/3).

A.7. Depth-Damage Function

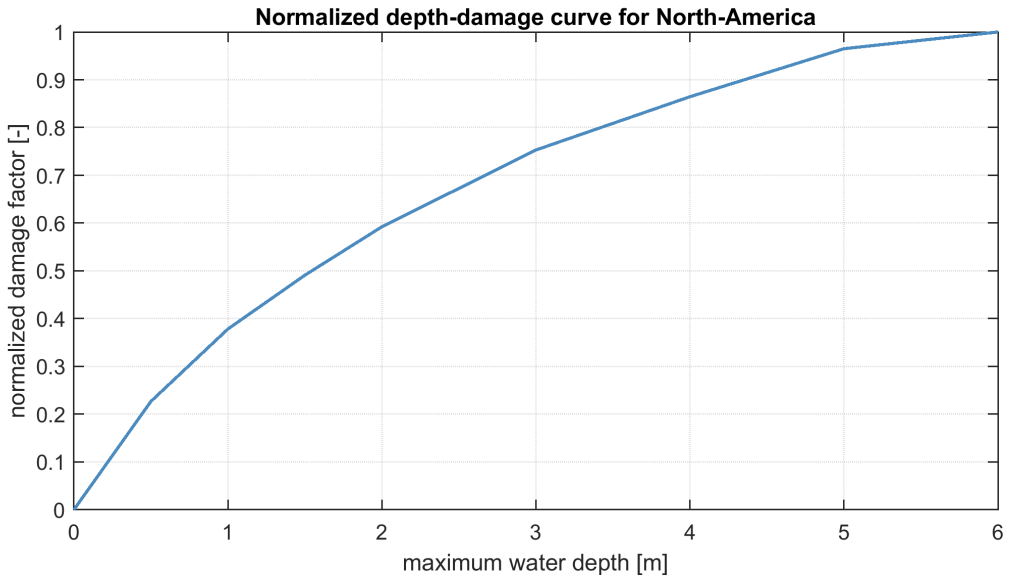

Figure A.19: Normalized damage factor for North America at a given water depth for buildings. Modified from Huizinga et al. (2017)

A.8. Damage on Zip-Code Level

Table A.3: Damage on zip-code level as reported by Sharp (2018) and modelled by FIAT Accelerator. Furthermore. the percentage of the zip-code area affected by a minimum of 0.15 m water depth is given. Moreover, the reported losses are doubled according to Blake and Gibney (2011).

Zip-Code	Reported Loss [USD]	Modelled Loss [USD]	Difference [USD]	Affected Area [%]
77002	1.97E+07	8.44E+07	6.46E+07	36.35
77003	4.50E+06	5.85E+07	5.40E+07	30.15
77004	3.74E+07	2.76E+08	2.38E+08	52.17
77005	2.19E+07	2.04E+08	1.82E+08	58.10
77006	3.86E+06	7.29E+07	6.91E+07	49.10
77007	4.73E+07	9.99E+07	5.26E+07	13.38
77008	9.62E+07	1.62E+08	6.60E+07	28.41
77009	4.05E+07	1.74E+08	1.33E+08	33.49
77010	8.33E+03	6.37E+06	6.37E+06	64.76
77011	5.46E+06	6.25E+07	5.70E+07	18.21
77012	1.12E+07	1.59E+08	1.48E+08	24.13
77013	2.06E+08	1.91E+08	-1.52E+07	21.75
77015	1.19E+08	5.69E+08	4.50E+08	20.60
77016	4.12E+07	1.06E+08	6.51E+07	17.92
77017	2.90E+07	2.86E+08	2.57E+08	31.87
77018	5.69E+07	1.54E+08	9.75E+07	29.45
77019	2.30E+07	5.28E+07	2.97E+07	20.23
77020	1.98E+07	1.39E+08	1.19E+08	28.50
77021	3.02E+07	2.78E+08	2.48E+08	54.06
77022	3.89E+07	2.20E+08	1.82E+08	4.46
77023	8.73E+06	1.66E+08	1.57E+08	30.94
77024	3.68E+08	2.63E+08	-1.05E+08	22.30
77025	3.81E+08	3.65E+08	-1.56E+07	63.63
77026	1.08E+08	2.40E+08	1.32E+08	46.43
77027	2.09E+07	9.71E+07	7.62E+07	41.21
77028	1.17E+08	2.46E+08	1.30E+08	32.90
77029	4.68E+07	3.44E+08	2.97E+08	28.03
77030	1.79E+07	2.23E+08	2.05E+08	68.52
77031	1.96E+07	7.30E+07	5.34E+07	31.13
77032	5.21E+07	1.03E+08	5.08E+07	6.84
77033	2.24E+07	1.95E+08	1.73E+08	47.59
77034	2.15E+08	1.48E+08	-6.78E+07	13.21
77035	2.32E+08	1.76E+08	-5.61E+07	30.45
77036	7.78E+06	2.01E+08	1.93E+08	38.02
77037	1.57E+08	1.84E+08	2.73E+07	37.45
77038	3.48E+07	1.50E+08	1.16E+08	2.46
77039	1.58E+08	1.35E+08	-2.30E+07	20.13
77040	2.39E+07	4.35E+08	4.11E+08	36.04
77041	2.19E+08	2.99E+08	7.97E+07	25.01
77042	2.38E+08	1.97E+08	-4.12E+07	36.86
77043	1.41E+07	1.58E+08	1.44E+08	15.72
77044	2.08E+08	1.72E+08	-3.67E+07	6.28
77045	1.26E+07	1.61E+08	1.48E+08	16.23
77046	3.14E+05	6.30E+06	5.99E+06	68.00

*continues on next page

Zip-code	Reported Damage [USD]	Modelled Damage [USD]	Difference [USD]	Affected Area [%]
77047	2.92E+07	2.16E+07	-7.65E+06	2.56
77048	9.81E+06	4.46E+07	3.48E+07	6.44
77049	1.13E+08	1.96E+08	8.31E+07	12.27
77050	1.40E+07	1.60E+07	1.99E+06	4.72
77051	6.30E+06	6.73E+07	6.10E+07	17.06
77054	5.21E+06	1.70E+08	1.64E+08	38.60
77055	8.20E+06	1.78E+09	1.78E+09	34.43
77056	6.93E+07	1.38E+08	6.83E+07	39.44
77057	3.46E+07	1.05E+08	7.00E+07	32.64
77059	4.17E+07	1.23E+06	-4.05E+07	0.24
77060	1.10E+08	1.39E+08	2.90E+07	25.88
77061	2.90E+07	1.18E+08	8.91E+07	21.07
77063	1.00E+08	1.63E+08	6.30E+07	38.15
77064	4.63E+06	2.05E+08	2.01E+08	20.86
77065	3.88E+07	1.39E+08	1.00E+08	27.65
77066	1.07E+07	1.07E+08	9.63E+07	16.90
77067	3.68E+06	8.67E+07	8.31E+07	23.56
77070	3.60E+08	5.55E+07	-3.04E+08	7.20
77071	3.45E+07	1.45E+08	1.10E+08	37.67
77072	1.26E+07	1.30E+08	1.17E+08	38.95
77074	2.38E+08	2.09E+08	-2.90E+07	41.88
77075	1.31E+08	6.76E+07	-6.32E+07	8.51
77076	1.41E+07	8.21E+07	6.80E+07	31.34
77077	2.37E+08	2.55E+08	1.73E+07	33.55
77078	1.12E+08	1.05E+08	-7.40E+06	10.94
77079	9.79E+08	3.00E+08	-6.79E+08	32.53
77080	8.94E+06	2.38E+08	2.29E+08	31.90
77081	1.17E+07	7.77E+07	6.60E+07	39.17
77082	7.93E+06	2.21E+08	2.13E+08	19.90
77083	1.33E+07	9.73E+07	8.40E+07	13.96
77084	5.82E+08	4.10E+07	-5.41E+08	2.18
77085	1.01E+07	4.60E+07	3.59E+07	12.07
77086	6.53E+06	1.11E+08	1.04E+08	27.09
77087	1.87E+07	1.88E+08	1.69E+08	38.59
77088	1.03E+08	2.36E+08	1.33E+08	30.29
77090	2.00E+08	1.05E+08	-9.51E+07	0.04
77091	5.23E+07	1.65E+08	1.13E+08	28.59
77092	4.22E+07	2.17E+08	1.75E+08	29.63
77093	7.32E+07	2.55E+08	1.82E+08	30.85
77094	6.38E+07	2.97E+05	-6.35E+07	0.06
77095	2.83E+07	9.18E+07	6.35E+07	9.59
77096	9.06E+08	3.45E+08	-5.61E+08	51.86
77098	2.41E+06	6.76E+07	6.52E+07	51.88
77099	2.27E+07	1.81E+08	1.58E+08	37.25
77201	0.00E+00	3.81E+05	3.81E+05	13.74
77338	1.83E+08	1.36E+05	-1.83E+08	0.02
77346	2.10E+08	2.57E+07	-1.84E+08	1.83

*continues on next page

Zip-code	Reported Damage [USD]	Modelled Damage [USD]	Difference [USD]	Affected Area [%]
77396	3.23E+07	1.31E+08	9.84E+07	7.40
77401	4.90E+08	2.61E+08	-2.28E+08	75.89
77429	3.65E+08	2.05E+08	-1.60E+08	2.03
77477	8.32E+06	1.85E+08	1.77E+08	21.93
77478	5.23E+06	1.78E+08	1.73E+08	17.84
77479	1.12E+08	2.45E+06	-1.09E+08	0.04
77489	1.60E+07	1.69E+08	1.53E+08	13.45
77498	2.65E+07	1.69E+08	1.42E+08	13.45
77502	9.42E+07	2.61E+08	1.67E+08	56.26
77503	2.99E+07	1.74E+08	1.44E+08	2.67
77504	4.26E+07	1.27E+08	8.44E+07	34.46
77505	6.96E+07	2.43E+08	1.73E+08	30.49
77506	4.46E+07	3.60E+08	3.15E+08	32.70
77507	3.66E+05	1.14E+08	1.13E+08	8.39
77520	3.94E+07	1.40E+08	1.01E+08	6.32
77521	3.78E+08	3.33E+08	-4.53E+07	10.10
77530	2.11E+07	1.82E+08	1.61E+08	11.91
77532	8.73E+07	8.94E+07	2.04E+06	2.34
77536	4.81E+07	2.69E+08	2.21E+08	26.97
77547	8.00E+06	6.08E+07	5.28E+07	22.28
77562	2.02E+07	7.89E+07	5.86E+07	7.04
77571	7.78E+07	3.87E+08	3.09E+08	12.74
77587	8.28E+07	1.87E+08	1.04E+08	71.79

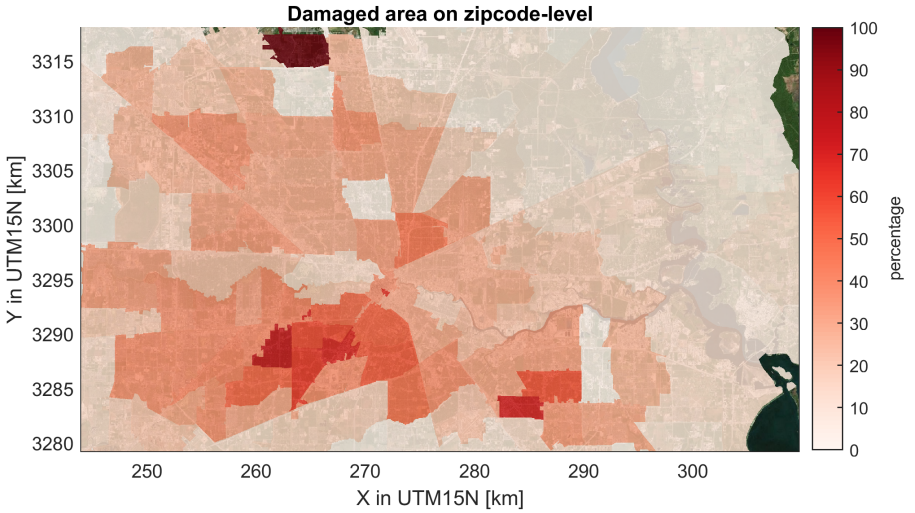

Figure A.20: The (percentual) area of the zip-code that is affected by a 0.15 m water depth according to the model.

B

Schematisation: Precipitation

This appendix contains background information for the derivation of the observation-based parametric rainfall model. In Section B.1 different TC quantities are discussed. Section B.2 shows scatter plots for *pmax*-*vmax* for different oceanic basins. In Section B.3 the decision for the marginal distributions for *pmax* and *vmax* is substantiated. In Section B.4 the ranking of the copula families according to MvCAT is given. Section B.5 shows the sensitivity of the copula parameter. Furthermore, Section B.6 contains the absolute radial rainfall plots for different categories. In Section B.8 different examples visualize the proposed model modification. Lastly, Section B.9 contains the different plots for substantiation of the assumption of independence.

B.1. Classification

The QSCAT-R dataset contains a variety of parameters linked to a TC. For this analysis, five different quantities are taken into account. The advantage of these quantities is that they can all be measured offshore and could potentially be applicable in forecasting applications:

- maximum rainfall intensity;
- maximum sustained wind speed;
- latitude (absolute);
- longitude (absolute); and
- storm motion velocity.

The modelled parameters are explored by analyzing the correlation with the maximum rainfall intensity. When looking at the data, it can be seen that only the maximum sustained wind speed shows any kind of dependence with maximum rainfall intensity (see Figures B.1, B.2, B.3 and B.4). The other parameters do not show any correlation.

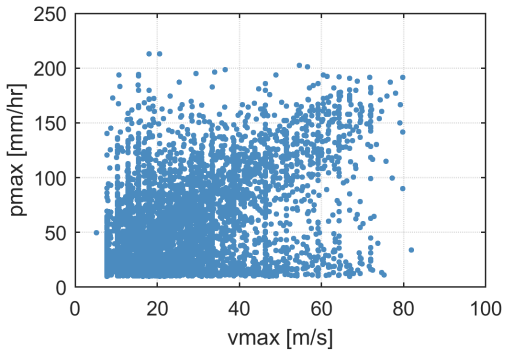

Figure B.1: Scatter of maximum rainfall intensity and maximum sustained wind speeds.

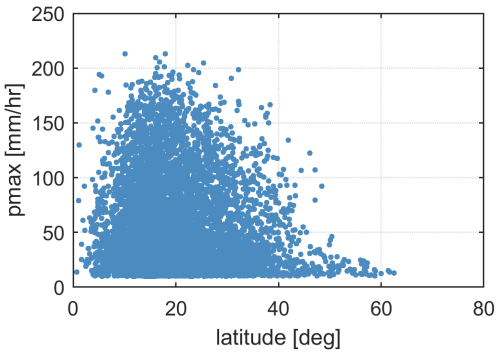

Figure B.2: Scatter of maximum rainfall intensity and latitude.

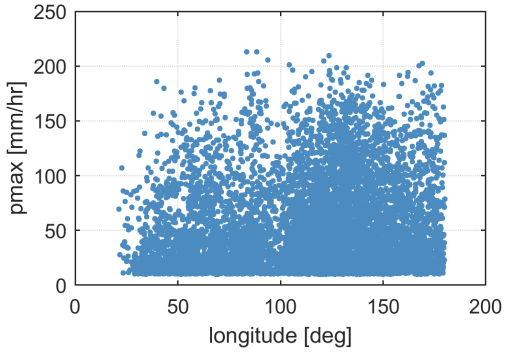

Figure B.3: Scatter of maximum rainfall intensity and longitude.

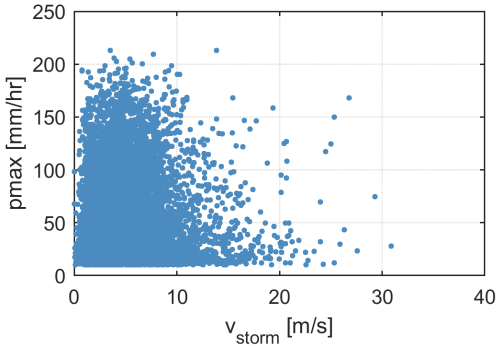

Figure B.4: Scatter of maximum rainfall intensity and storm motion velocity.

B.2. Spatial Variability

Scatter of maximum rainfall intensity and maximum sustained wind speed shows spatial variability. In some basins the dependence is more distinct compared to others. This could indicate that a different copula family could be fitted for every single basin. However, basins as the Central Pacific Basin and the Indian Ocean Basin do not have enough data points to make a decent fit.

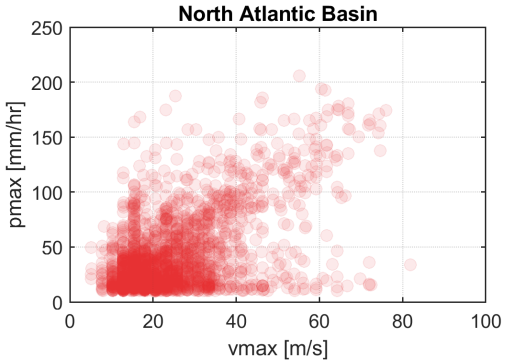

Figure B.5: Scatter of *pmax* and *vmax* for the North Atlantic Basin. Red dots are individual observations. More frequent observations are shown in darker red.

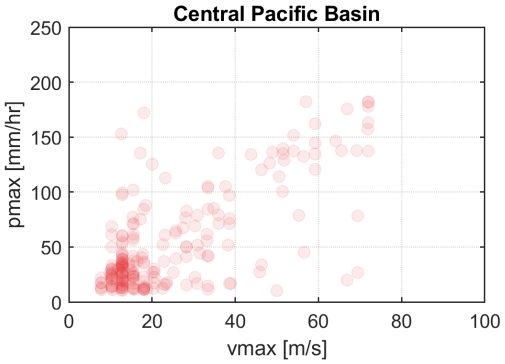

Figure B.6: Scatter of *pmax* and *vmax* for the Central Pacific Basin. Red dots are individual observations. More frequent observations are shown in darker red.

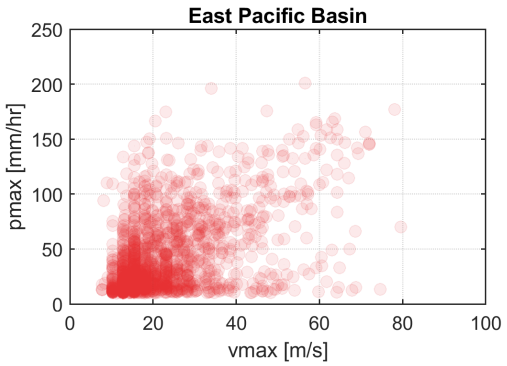

Figure B.7: Scatter of *pmax* and *vmax* for the East Pacific Basin. Red dots are individual observations. More frequent observations are shown in darker red.

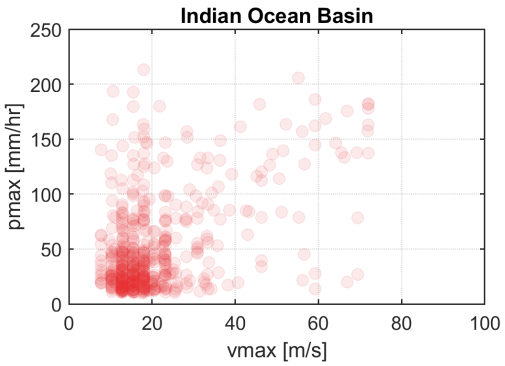

Figure B.8: Scatter of *pmax* and *vmax* for the Indian Ocean Basin. Red dots are individual observations. More frequent observations are shown in darker red.

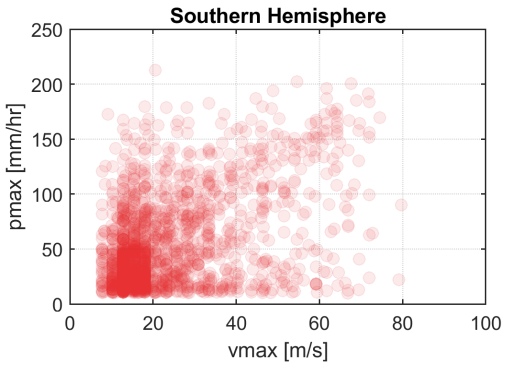

Figure B.9: Scatter of *pmax* and *vmax* for the Southern Hemisphere. Red dots are individual observations. More frequent observations are shown in darker red.

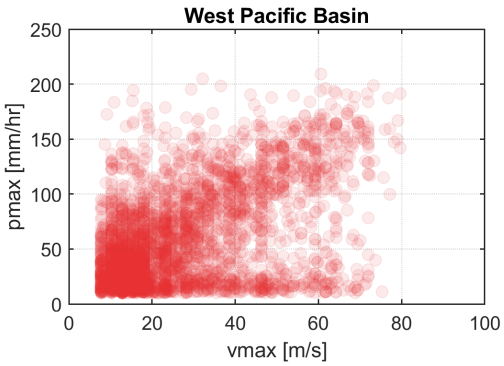

Figure B.10: Scatter of *pmax* and *vmax* for the West Pacific Basin. Red dots are individual observations. More frequent observations are shown in darker red.

The spatial variability can also be assessed on a global scale. Figures B.11 and B.12 show the distribution of maximum rainfall intensity and maximum sustained wind speed on a world map. As mentioned before, there seems to be a more frequent occurrence of high values in the West Pacific Basin compared to other basins.

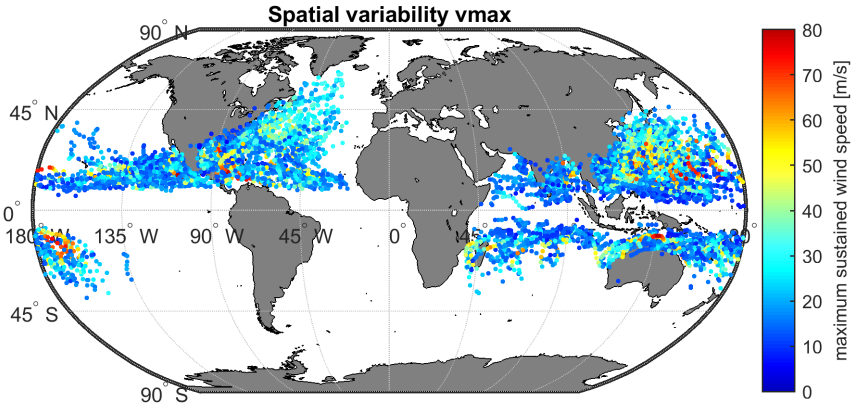

Figure B.11: Distribution of QSCAT-R observations on a world map. The dots are color-coded according to the maximum sustained sustained wind speed.

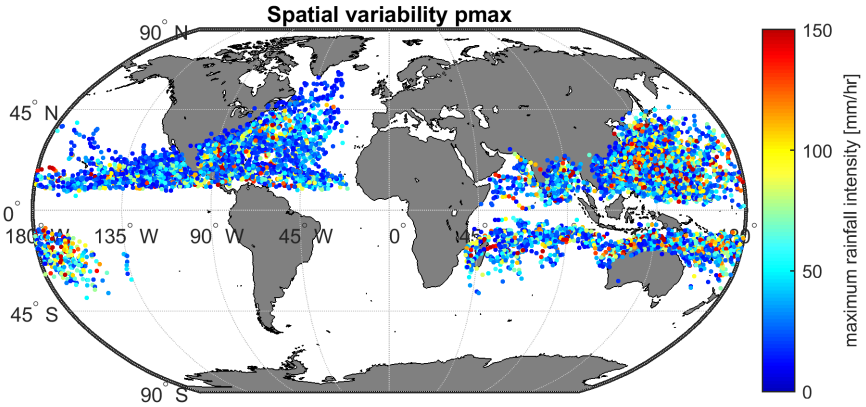

Figure B.12: Distribution of QSCAT-R observations on a world map. The dots are color-coded according to the maximum rainfall intensity.

B.3. Marginal Distributions

To validate whether the proposed marginal distribution by the MvCAT is correct, it is compared to other marginal distributions according to the method applied by Torres Duenas (2018). The Statistical Toolbox of Matlab is used for this (The MathWorks, Inc., 2018). The following marginal distributions are checked for both the maximum rainfall intensity and the maximum sustained wind speeds.

- Birnbaum-Saunders;
- Burr - Type XII;
- Exponential;
- Extreme Value;
- Gamma;
- Generalized Extreme Value;
- Generalized Pareto;
- Half-Normal;
- Inverse Gaussian;
- Logistic;
- Log-Logistic;
- Lognormal;
- Nakagami;
- Normal;
- Rayleigh;
- Ricean;
- Stable;
- T-Location Scale;
- Weibull; and
- MvCAT-proposed.

Maximum Rainfall Intensity (pmax) For clarity, only the five best marginal distribution fits are presented in this appendix. The theoretical probability distributions are fitted with the maximum rainfall intensity data from the calibration dataset of the QSCAT-R dataset (Chavas and Vigh, 2014). The results are compared on the PDF, CDF and probability of exceedance. Furthermore a "goodness-of-fit" test is performed to compare the distribution with the given data, resulting in performance indicators NRMSE and NMSE.

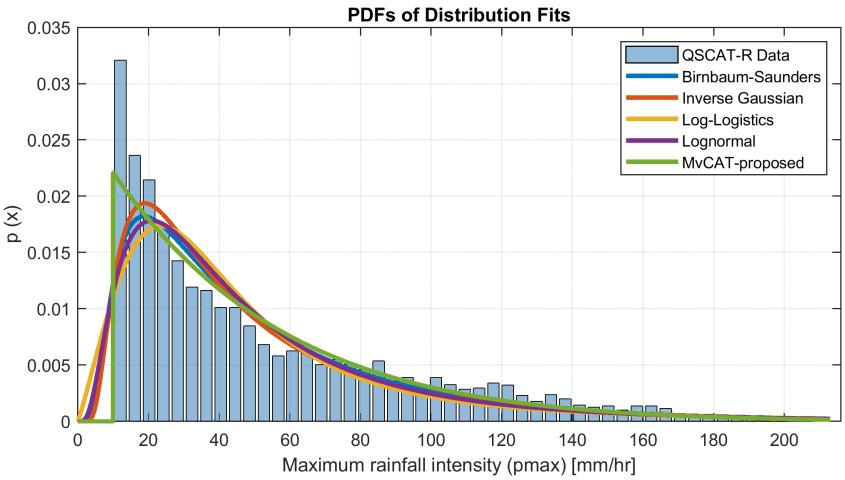

Figure B.13: PDFs of the fitted distributions. The QSCAT-R maximum rainfall intensity data is presented with a histogram.

The fitted distributions are unable to match the probability of low maximum rainfall intensity as can be seen in Figure B.13. The MvCAT-proposed distribution is the only distribution which reproduces the fact that values less than 10 mm/hr are non-existent (because these have been removed from the complete dataset manually). Furthermore, it can be seen that the MvCAT-proposed distribution is closest for the lowest maximum rainfall intensity value. Moreover, this distribution matches the highest end of the probability spectrum to a better extent than other distributions.

If the CDFs are compared instead of the PDFs, one can see that all five distributions show more-or-less similar behavior compared to each other and compared to the empirical data. At the low maximum rainfall intensity values ($pmax < 50$ mm/hr), all distributions are equal. At the medium maximum rainfall intensity values (50 mm/hr $< pmax <$ 150 mm/hr) all distribution overestimates the probability that X takes a value less or equal than x. The MvCAT-proposed distribution shows the least overestimation in this range of the maximum rainfall intensity. At the high-end of the maximum rainfall intensities ($pmax >$ 150 mm/hr) all distributions tend to underestimate the value given by the empirical data. Once again, the MvCAT-proposed distribution shows to be the closest match to the empirical line.

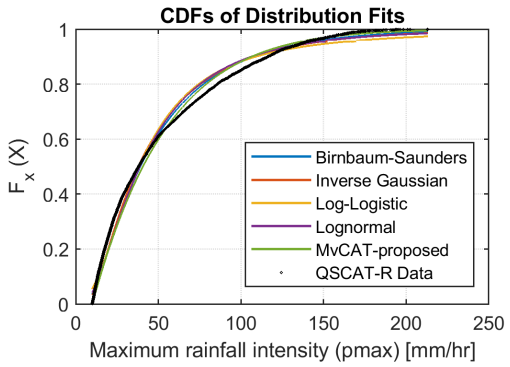

Figure B.14: CDFs of the fitted distributions. The QSCAT-R maximum rainfall intensity data depicted as a black dotted line.

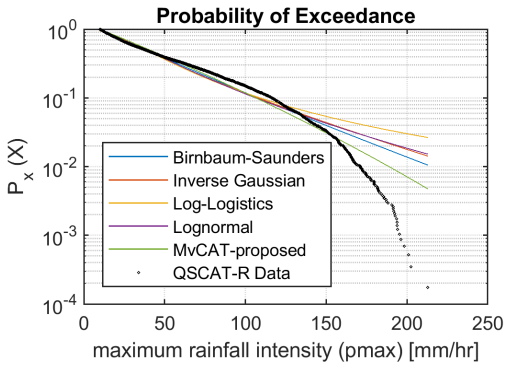

Figure B.15: Probability of exceedance plotted on log-scale. The QSCAT-R maximum rainfall intensity data is depicted as a black dotted line.

All five distributions show almost linear behavior when plotted on a log-scale for the purpose of a probability of exceedance plot, where the empirical data shows non-linear behavior. According to the probability of exceedance, all distributions perform equal. To substantiate performance of the different distribution fits, a "goodness-of-fit" test is performed. The NRMSE and NMSE are shown in Table B.1. A value of 1 would indicate a perfect match between the distribution and the data, a value of 0 indicates no match at all. As can be seen, all five distributions perform roughly equal. Therefore, based on this and visual comparison, the MvCAT-proposed distribution is considered to be the best fit to the QSCAT-R dataset for maximum rainfall intensity

Table B.1: Results of the "goodness-of-fit" tests expressed in NRMSE and NMSE for the QSCAT-R maximum rainfall intensity data

Distribution	NRMSE	NMSE
Birnbaum-Saunders	0.89982	0.98896
Inverse Gaussian	0.89842	0.98986
Log-Logistic	0.88086	0.98581
Lognormal	0.88663	0.98715
MvCAT-proposed	0.88945	0.98778

Maximum Sustained Wind Speed (vmax) For the maximum sustained wind speed the same procedure is followed. Based on a first assessment only the five best alternatives are presented. The distribution fits are assessed on visual comparison between the PDF, CDF and probability of exceedance plots. Furthermore a more quantitative assessment is made based on "goodness-of-fit" tests.

As can be seen in Figure B.16, all distributions are showing an equally shaped PDF. Differences can be noticed in the location of the highest probability around the low wind speeds. Furthermore, distinctions can be noticed in the reproduction of the high wind speeds. All distributions fail to match the high occurrence probability of low maximum wind speeds.

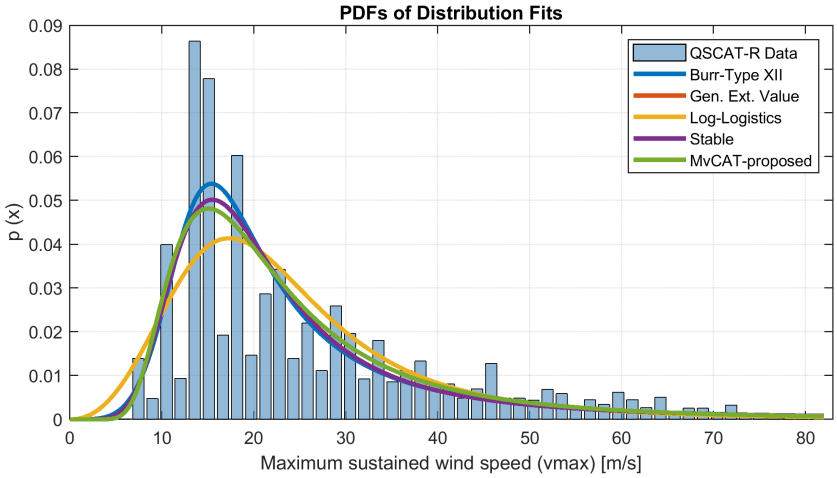

Figure B.16: PDFs of the fitted distributions. The QSCAT-R maximum sustained wind speed data presented with a histogram.

In Figure B.17 can be distinguished that the data is not continuous. This can already be explained from Figure B.16, where big differences in probability of occurrence between adjacent maximum sustained wind speeds can be seen. The different fits perform fairly similar to each other. The other distributions seem to match the data more accurately. The same holds for the probability of exceedance (see Figure B.18).

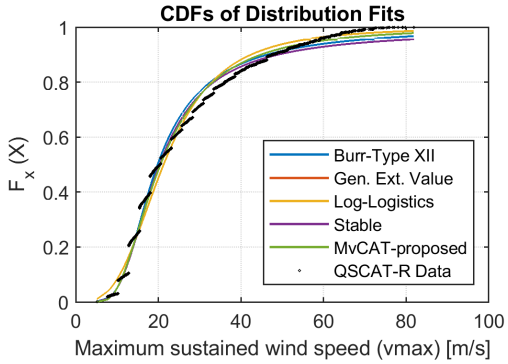

Figure B.17: CDFs of the fitted distributions. The QSCAT-R maximum sustained wind speed data depicted as the black dotted line.

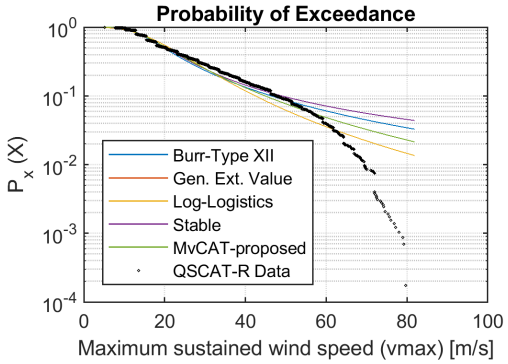

Figure B.18: Probability of exceedance plotted on log-scale. The QSCAT-R maximum sustained wind speed data is depicted as the black dotted line.

The "goodness-of-fit" tests show that all distributions perform equal on this performance metrics. Remarkable is that the Inverse Gaussian fit and the fit as proposed by MvCAT show equal values for NRMSE and NMSE. This indicates that the Statistical Toolbox of Matlab fits the Inverse Gaussian distribution equal to the MvCAT-proposed distribution. For this reason the MvCAT-proposed distribution is set to be the representative distribution for the maximum sustained wind speeds.

Table B.2: Results of the "goodness-of-fit" tests expressed in NRMSE and NMSE for the QSCAT-R maximum sustained wind speed data

Distribution	NRMSE	NMSE
Burr-Type XII	0.87417	0.98417
Generalized Extreme Value	0.89323	0.98860
Log-Logistics	0.86415	0.98154
Stable	0.88708	0.98725
MvCAT-proposed	0.89323	0.98860

B.4. Copula Ranking

The MvCAT is able to rank copula families based on five criteria; maximum likelihood, AIC, BIC, RMSE and NSE. Table B.3 provides the ranking of the different copula families according to these performance metrics for the calibration dataset. Copula families marked with an asterisk are possibly not a good a fit as suggested. This is because of the fact that the copula parameter converges to its boundary value.

Table B.3: Sorted copulas based on different criteria according to MvCAT (Sadegh et al., 2017). A star indicates a warning by the MvCAT. The copula parameter is in this case converging to the parameter boundary and it would therefore be possible that this copula is not a good fit.

Rank	Maximum Likelihood	AIC	BIC	RMSE	NSE
1*	Roch-Alegre	Roch-Alegre	Roch-Alegre	1.4559	0.9952
2	Frank	Frank	Frank	1.4686	0.9951
3	Nelsen	Nelsen	Nelsen	1.4686	0.9951
4	Gaussian	Gaussian	Gaussian	1.5426	0.9946
5	Plackett	Plackett	Plackett	1.5558	0.9945
6*	BB1	BB1	BB1	1.5603	0.9944
7*	AMH	AMH	AMH	1.5839	0.9943
8	Clayton	Clayton	Clayton	1.5851	0.9943
9	Raftery	Raftery	Raftery	1.7335	0.9931
10*	Galambos	Galambos	Galambos	1.8314	0.9923
11*	BB5	BB5	BB5	1.8314	0.9923
12*	Gumbel	Gumbel	Gumbel	1.8427	0.9922
13*	Tawn	Tawn	Tawn	1.8428	0.9922
14*	FGM	FGM	FGM	2.0049	0.9908
15*	Fischer-Kock	Fischer-Kock	Fischer-Kock	2.0049	0.9908
16	Fischer-Hinzmann	Fischer-Hinzmann	Fischer-Hinzmann	2.0484	0.9904
17	Shih-Louis	Shih-Louis	Shih-Louis	2.0489	0.9904
18	Linear-Spearman	Linear-Spearman	Linear-Spearman	2.0489	0.9904
19	Marshal-Olkin	Marshal-Olkin	Marshal-Olkin	2.0574	0.9903
20	Cuadras-Auge	Cuadras-Auge	Cuadras-Auge	2.0785	0.9901
21*	Burr	Burr	Burr	2.0970	0.9899
22*	Joe	Joe	Joe	2.2098	0.9888
23	Cubic	Cubic	Cubic	4.1200	0.9612
24	Independence	Independence	Independence	4.1240	0.9611

B.5. Copula Parameter

In Figure B.19 the impact of the copula parameter can be seen. For the Frank copula, four different values are been chosen to visualize the difference. As can be seen, for an increasing θ, the correlation between the two parameters is more defined.

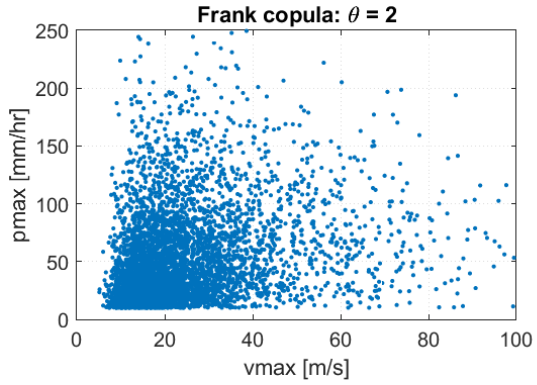

(a) Frank Copula; $\theta = 2.0$

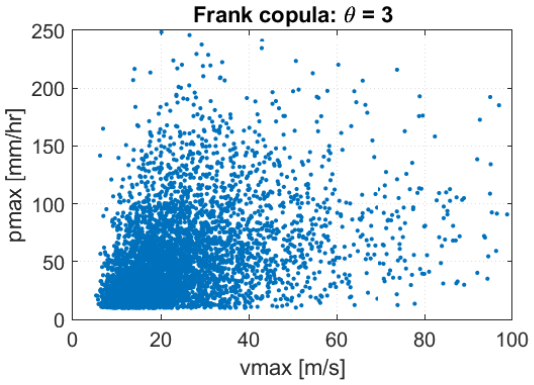

(b) Frank Copula; $\theta = 3.0$

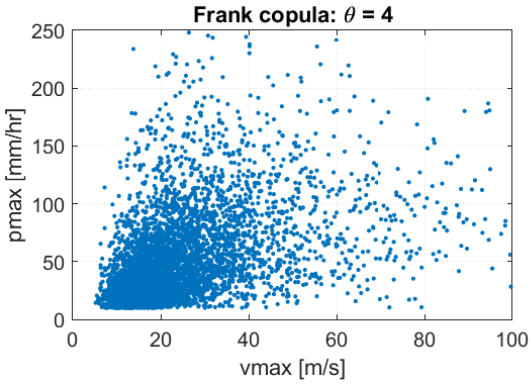

(c) Frank Copula; $\theta = 4.0$

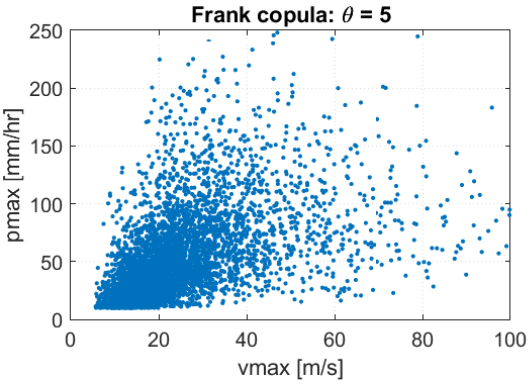

(d) Frank Copula; $\theta = 5.0$

Figure B.19: 5,000 randomly sampled values from a Frank Copula for different values of the copula-parameter θ.

B.6. Observed Radial Rainfall Profiles

Opposite to the previous section, this section contains the observations when plotting absolute values on the y-axis. Here it can be seen that for the high end *pmax* categories, the exponential-like radial rainfall profile is more distinguishable.

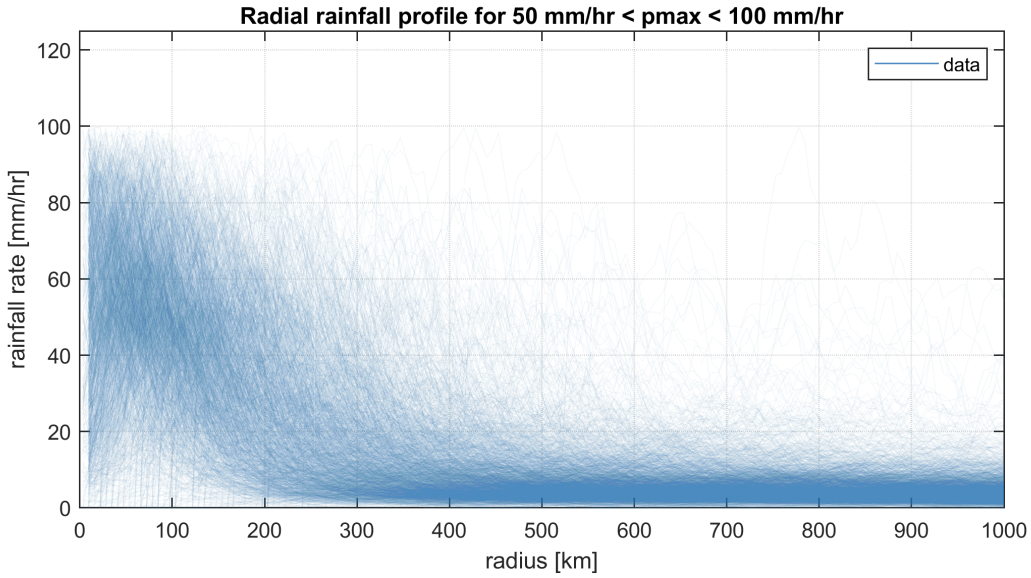

Figure B.20: Absolute radial rainfall profiles for observations with 50 mm/hr < *pmax* < 100 mm/hr of the QSCAT-R dataset. Blue lines are individuals observations, more frequent observations are shown in darker blue.

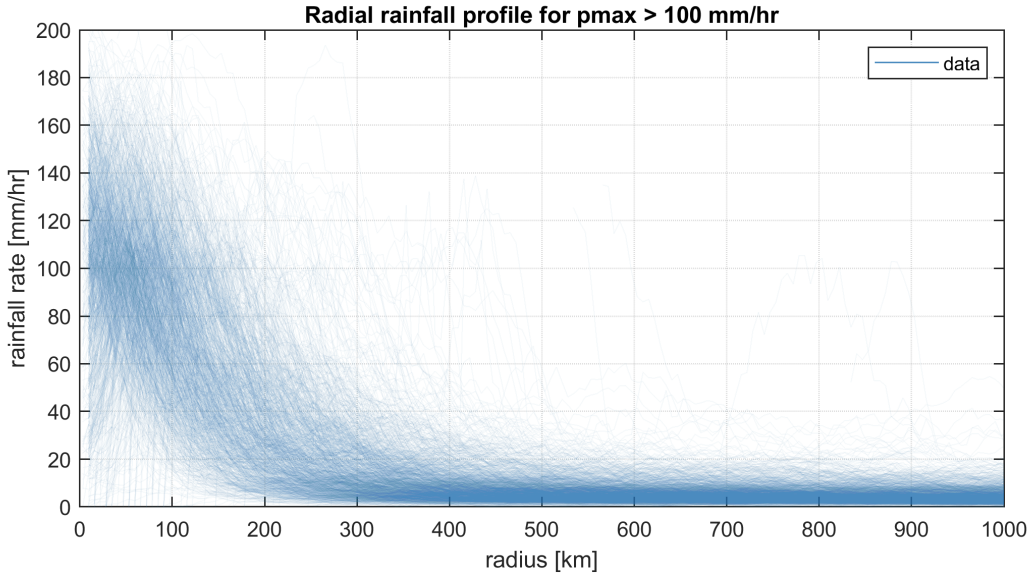

Figure B.21: Absolute radial rainfall profiles for observations with *pmax* > 100 mm/hr of the QSCAT-R dataset. Blue lines are individuals observations, more frequent observations are shown in darker blue.

B.7. Performance

Performance of the radial rainfall model for different performance metrics. It should be noted that only the *50%-sample fit* is shown for clarity.

Table B.4: Performance metrics for the 50%-sample fits for different categories of the maximum rainfall intensities. The table is split up in metrics for the original and modified rainfall model.

	RMSD [mm/hr]		bias [mm/hr]		MAE [mm/hr]	
fitted - sampled *pmax*	original	modified	original	modified	original	modified
pmax < 50 mm/hr	3.8	3.8	-3.13	-3.13	3.6	3.6
50 mm/hr < *pmax* < 100 mm/hr	3.1	3.1	-2.0	-2.0	2.7	2.7
pmax > 100 mm/hr	2.7	2.7	0.4	0.4	2.4	2.4
fitted - observed *pmax*						
pmax < 50 mm/hr	24.4	24.4	10.5	10.5	18.1	18.1
50 mm/hr < *pmax* < 100 mm/hr	34.3	34.3	-26.4	-26.5	28.7	28.7
pmax > 100 mm/hr	73.6	73.6	-68.1	-68.1	68.1	68.1
modelled - observed radial rain						
pmax < 50 mm/hr	8,438	7,434	4,447	459	7,084	5,718
50 mm/hr < *pmax* < 100 mm/hr	9,662	7,818	6,706	2,980	8,397	6,482
pmax > 100 mm/hr	12,271	9,781	10,276	6,896	11,081	8,609

B.8. Examples Adjustment

The figures presented below show three snapshots of the radial rainfall profile of Hurricane Isabel (2003). The figures on the left show the original rainfall model, whereas the right figures show the distributions of the adjusted rainfall model ($p_r(R) < 10$ mm/hr are set to zero).

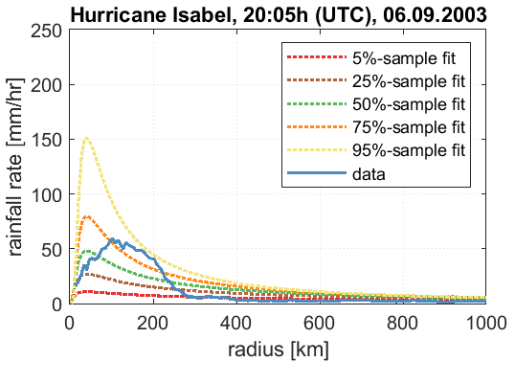

Figure B.22: Snapshot of rainfall distribution of Hurricane Isabel (solid blue line) and fits for different sampled values of the original rainfall model (1/3).

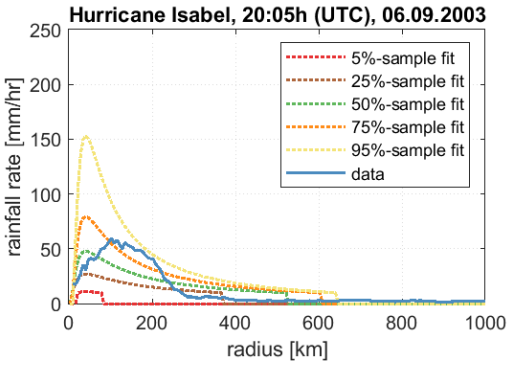

Figure B.23: Snapshot of rainfall distribution of Hurricane Isabel (solid blue line) and fits for different sampled values of the adjusted rainfall model (1/3).

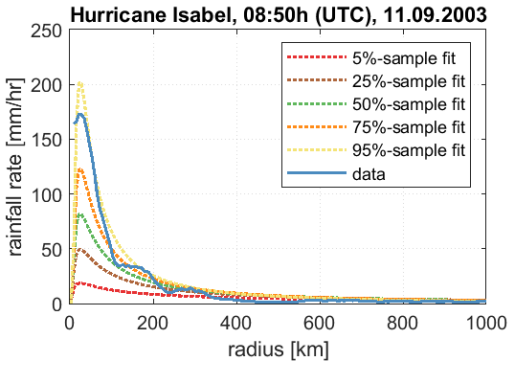

Figure B.24: Snapshot of rainfall distribution of Hurricane Isabel (solid blue line) and fits for different sampled values of the original rainfall model (2/3).

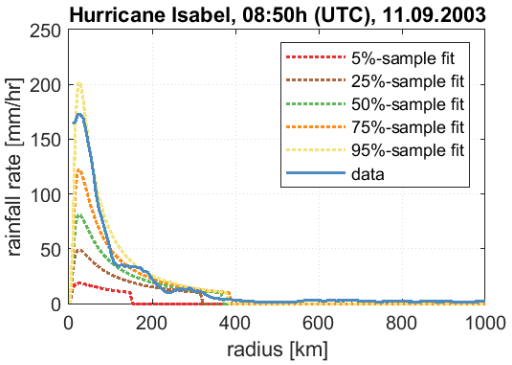

Figure B.25: Snapshot of rainfall distribution of Hurricane Isabel (solid blue line) and fits for different sampled values of the adjusted rainfall model (2/3).

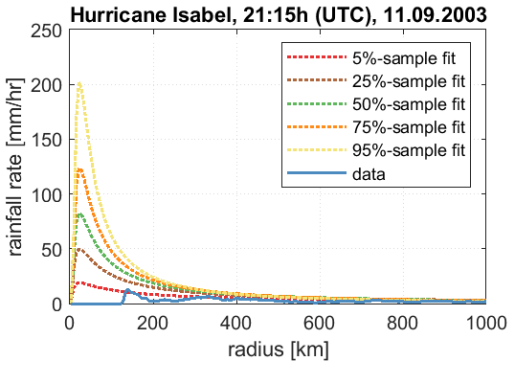

Figure B.26: Snapshot of rainfall distribution of Hurricane Isabel (solid blue line) and fits for different sampled values of the original rainfall model (3/3).

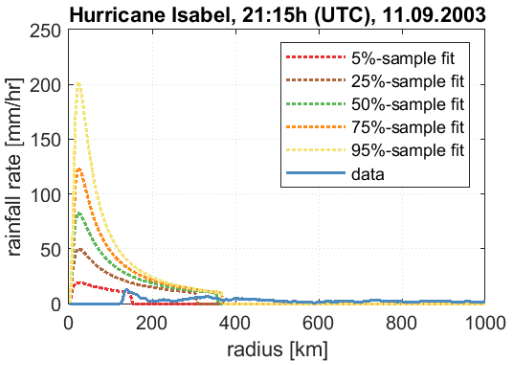

Figure B.27: Snapshot of rainfall distribution of Hurricane Isabel (solid blue line) and fits for different sampled values of the adjusted rainfall model (3/3).

B.9. Time Dependence

In Figures B.28 and B.29 the time dependence for the other two categories can be seen (initial *pmax* < 50 mm/hr and initial *pmax* > 100 mm/hr). For both categories no time dependence can be recognized. Furthermore, it is difficult to draw any conclusions for the latter category, because the amount of observations is limited.

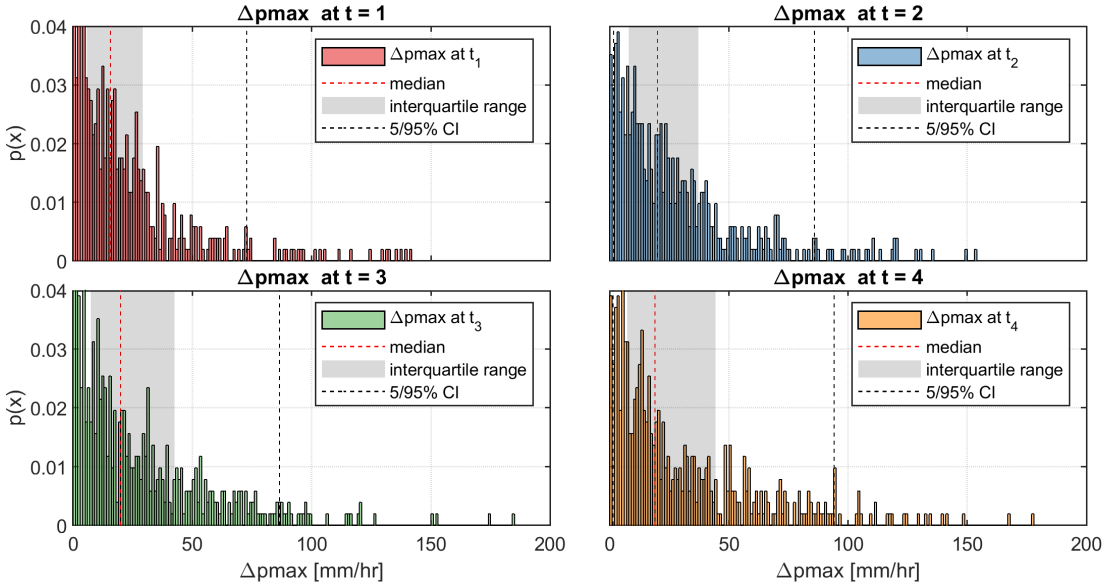

Figure B.28: Distribution of maximum rainfall intensities at different time steps. Only hurricanes with an initial *pmax* lower than 50 mm/hr are taken into account. The red dashed-line indicates the median value, the gray polygon represents the interquartile range and the black dashed lines indicate the 5% and 95% boundaries.

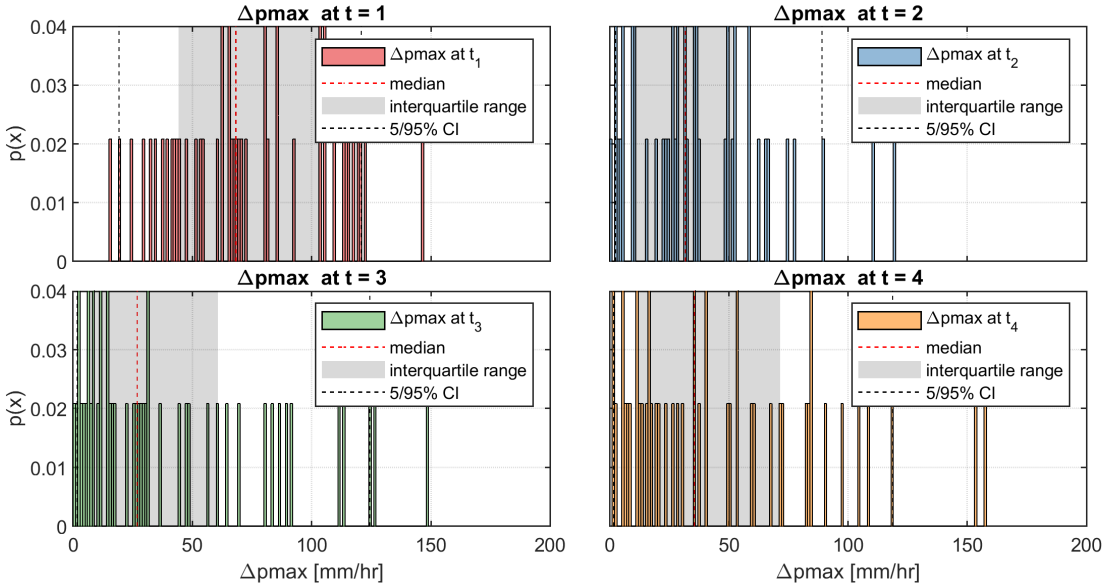

Figure B.29: Distribution of maximum rainfall intensities at different time steps. Only hurricanes with an initial *pmax* higher than 100 mm/hr are taken into account. The red dashed-line indicates the median value, the gray polygon represents the interquartile range and the black dashed lines indicate the 5% and 95% boundaries.

C

Application: Climate Variability Study

This appendix contains background information for the climate variability study. In Section C.1 the flowchart used for the TCWiSE tool is presented. Section C.2 contains the observed historical TCs over time. Lastly, in Section C.3 the used Delft3D-FM model is discussed. Section C.4 contains the validation of the used Delft3D-FM Model. Subsequently, Section C.5 contains a comparison of the 1 in 100-year flood extent with the flood extent during Hurricane Harvey. Lastly, Section C.6 contains a qualitative comparison between the derived 1 in 100-year flooding and the FEMA flood plain map.

C.1. Flowchart TCWiSE

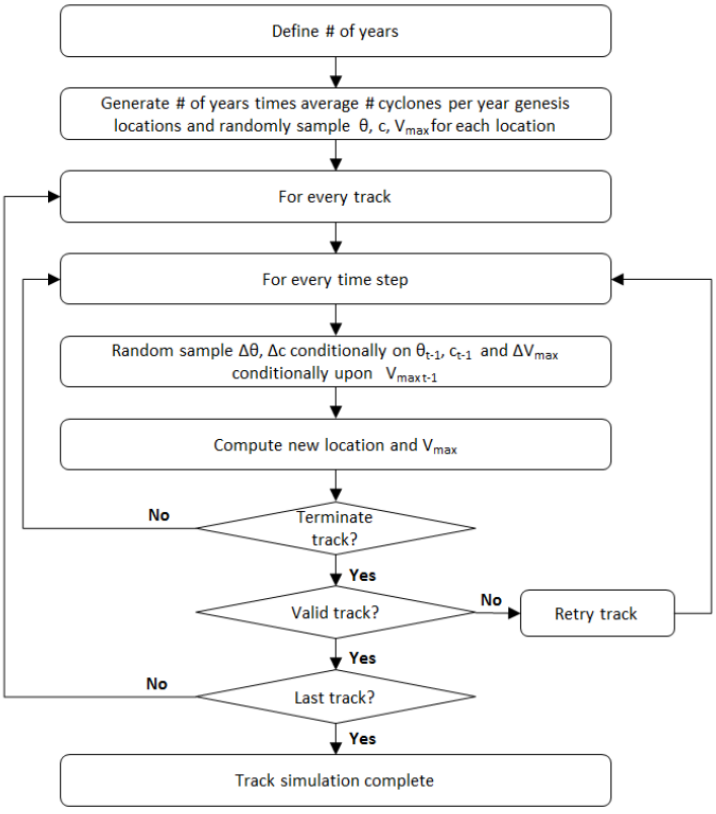

Figure C.1: Flowchart of the methodology used in the TCWiSE tool. Courtesy of Hoek (2018)

C.2. Historical Observations

The TCWiSE samples with a Monte Carlo sampling method an average number of cyclones per year for a user-specified amount of years. For this study a 1000 years is used and the sampling is based on Figure C.2.

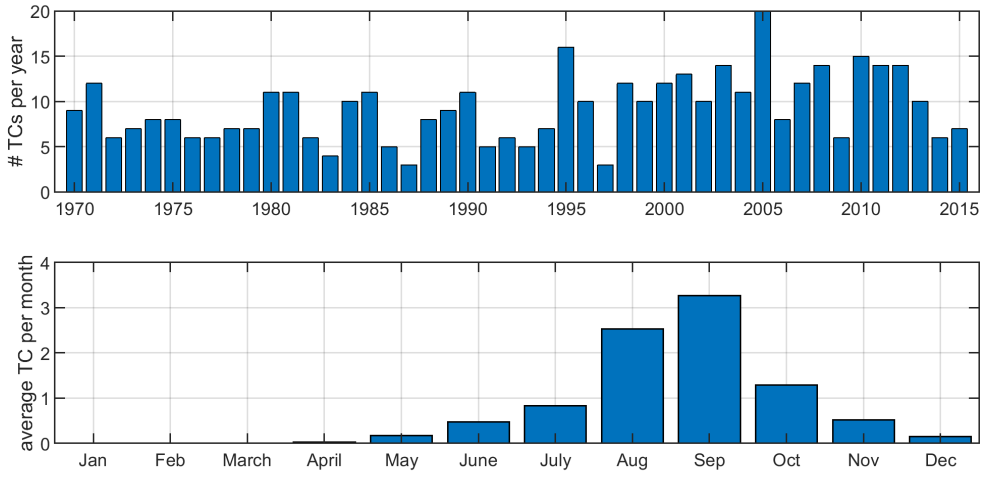

Figure C.2: Observed historical TCs per year and per month in the North Atlantic basin.

C.3. Delft3D-FM Model Setup

The Delft3D-FM model is setup as follows:

- The model domain can be seen in Figure C.3;
- The geographic coordinate system is WGS 84;
- The vertical coordinate system is NAVD88;
- The maximum cell size is 10,000 m;
- The minimum cell size is 300 m;
- The total number of nodes is 395,846;
- The tidal motion is included with the TPXO 8.0 model (Egbert and Erofeeva, 2002); and
- The bathymetry is based on the GEBCO dataset. Near the Galveston Bay, the bathymetry is further refined with the CRM.

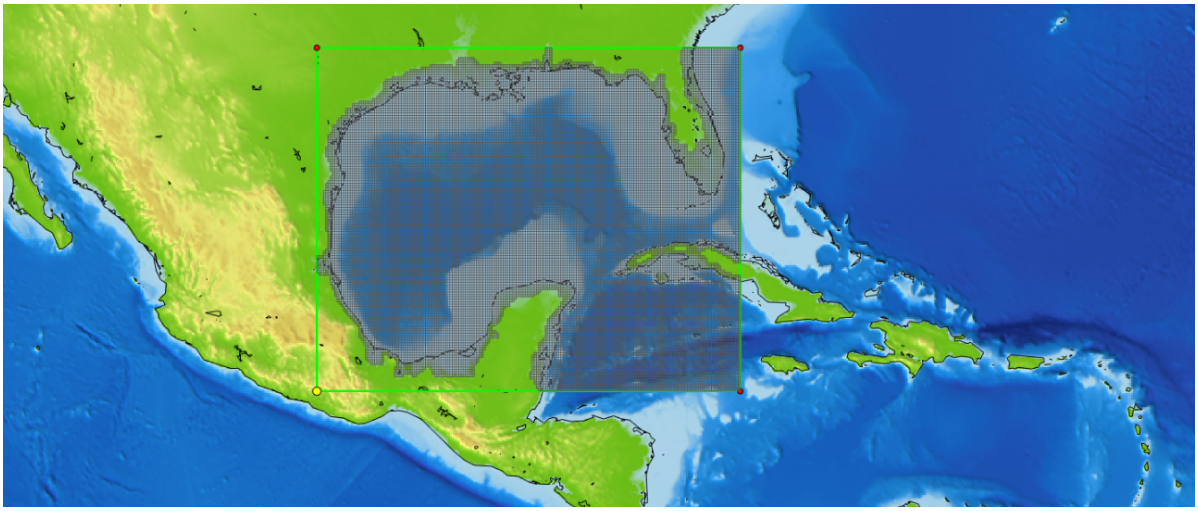

Figure C.3: Extent of Delft3D-FM model domain.

C.4. Validation

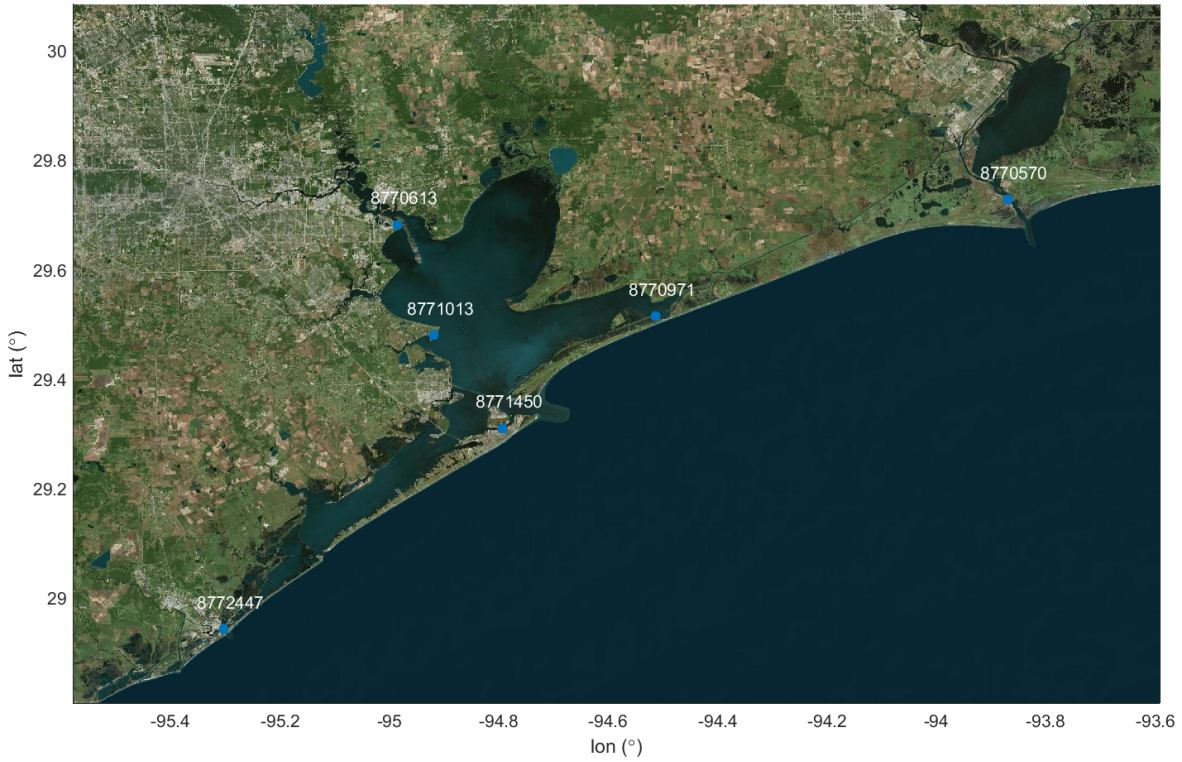

Figure C.4: Observation station used to validate the Delft3D-FM model results.

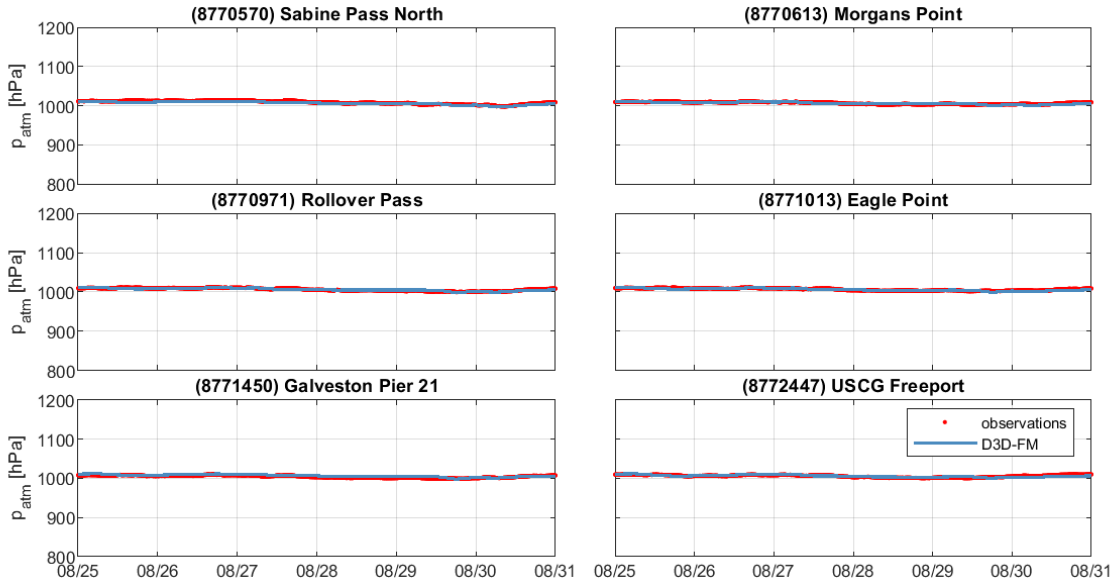

Figure C.5: Atmospheric pressure at the observations stations as observed (in red) and as modelled with the Delft3D-FM model (in blue).

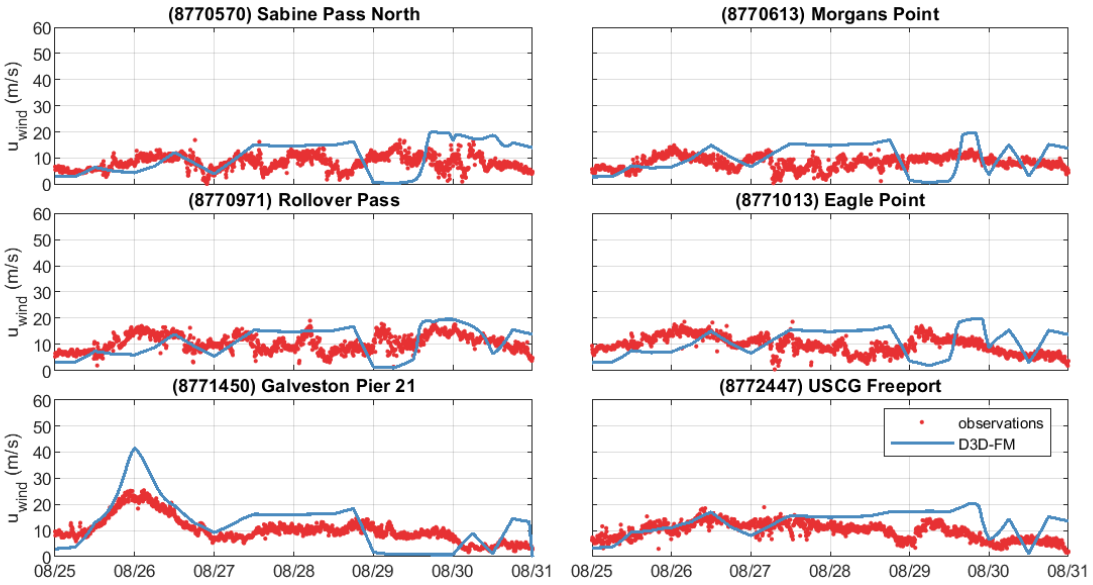

Figure C.6: Wind speed at the observations stations as observed (in red) and as modelled with the Delft3D-FM model (in blue).

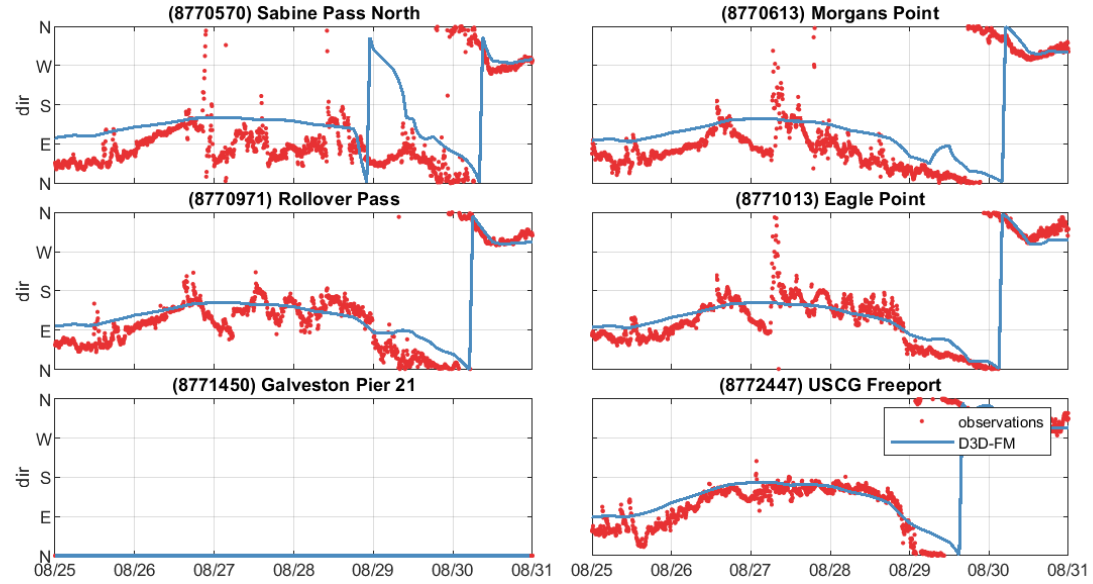

Figure C.7: Wind-direction at the observations stations as observed (in red) and as modelled with the Delft3D-FM model (in blue).

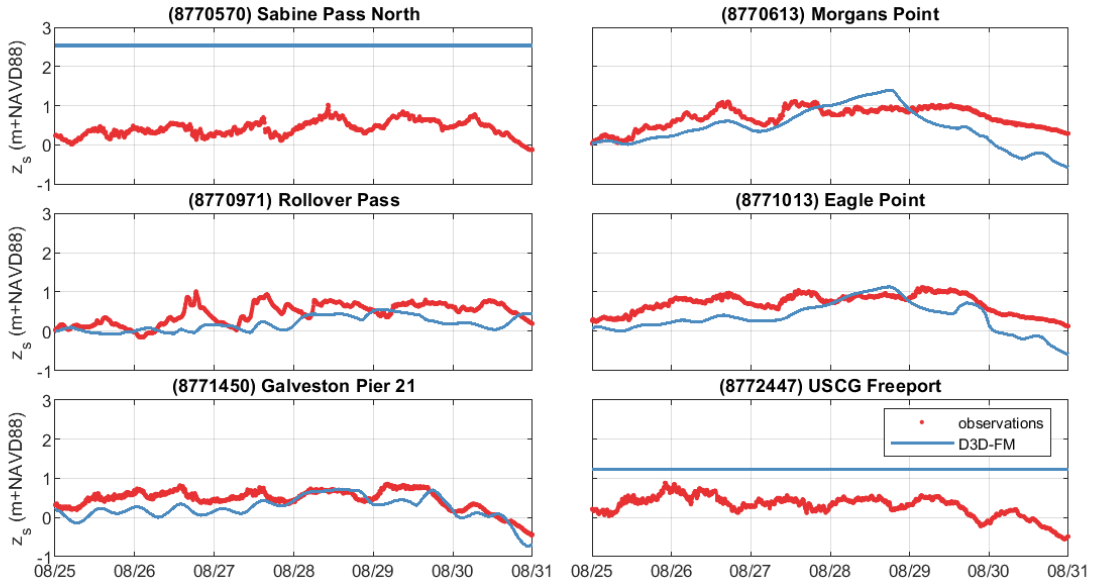

Figure C.8: Water levels at the observations stations as observed (in red) and as modelled with the Delft3D-FM model (in blue).

C.5. Comparison with Hurricane Harvey

When comparing the derived 1 in 100-year flood extent map with the flooding due to Hurricane Harvey, it can be seen that a 1 in 100-year event is much more severe.

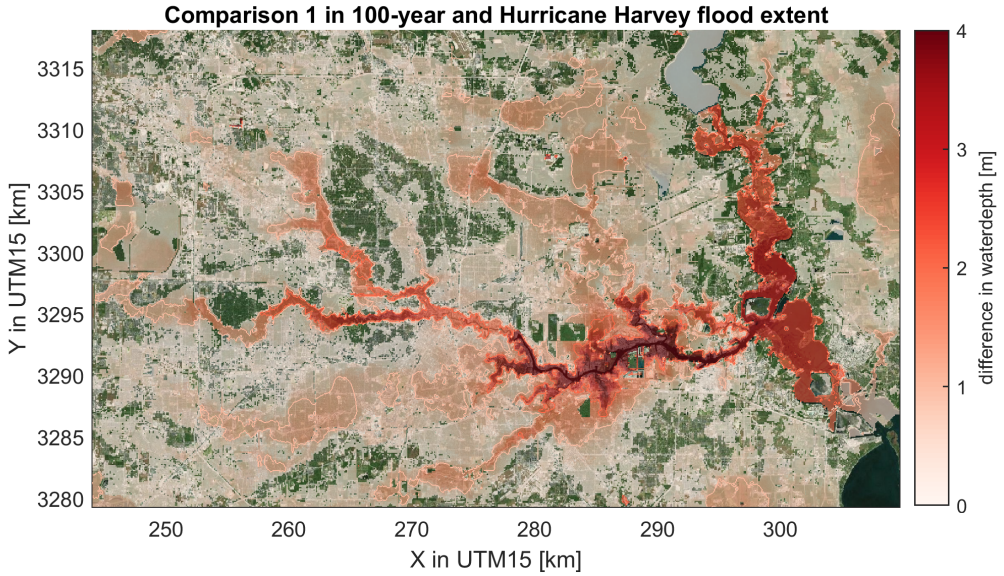

Figure C.9: The flood extent for a 100-year return period flood event compared to the flooding due to Hurricane Harvey in the urban areas of Houston. Differences in water depths lower than 0.15 m have not been plotted for visual purposes. Contour lines are given for the 1.0 and 2.0 m water depths.

C.6. Comparison with FEMA

The flood extent near Buffalo Bayou is shown in Figure C.10. Equal to the surrounding of Brays Bayou, most of the area is covered with at least 0.15 m water depth (white colors). The FEMA flood zone does only mark areas close to the river banks as flood prone, especially for the 500-year flood plain. In this figure, this area is marked with the 1.0 m water depth contour. Nevertheless, it seems that the FEMA flood plain does underestimate flooding due to a 1 in 100-year event according to the CVA. Another interesting observation is that it seems that during an extreme event, there is some interaction between the White Oak Bayou catchment and the Buffalo Bayou Catchment near their confluence (265 km < X in UTM15 < 270 km). This would suggest more severe flooding in the urban areas near the city center.

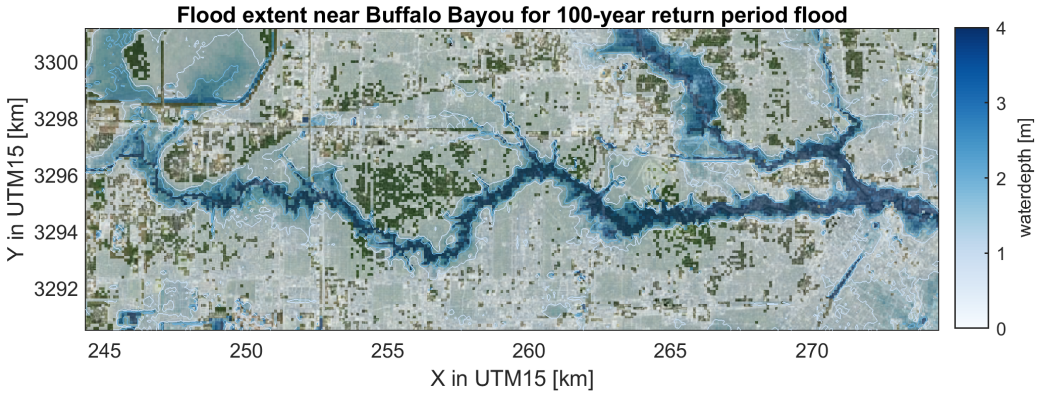

Figure C.10: The flood extent for a 100-year return period storm in the urban areas of Houston. Water depths lower than 0.15 m have not been plotted for visual purposes. Contour lines are given for the 1.0 and 2.0 m water depths.

The flooding in the vicinity of the White Oak Bayou is shown in Figure C.11. A large part of the upstream White Oak Bayou is marked as floodway by the FEMA map. According to the limited water depth shown by the model results, it seems that this floodway is not captured correctly in the DEM. The lack of water could also be explained by the fact that the catchment of the Whiteoak Bayou is not enclosed in the model domain entirely. Furthermore, similar to earlier analysis, the extent of the 100-year flood plain is captured in the model (with large water depths). However, the spatial distribution of the pluvial flooding is not included in FEMA.

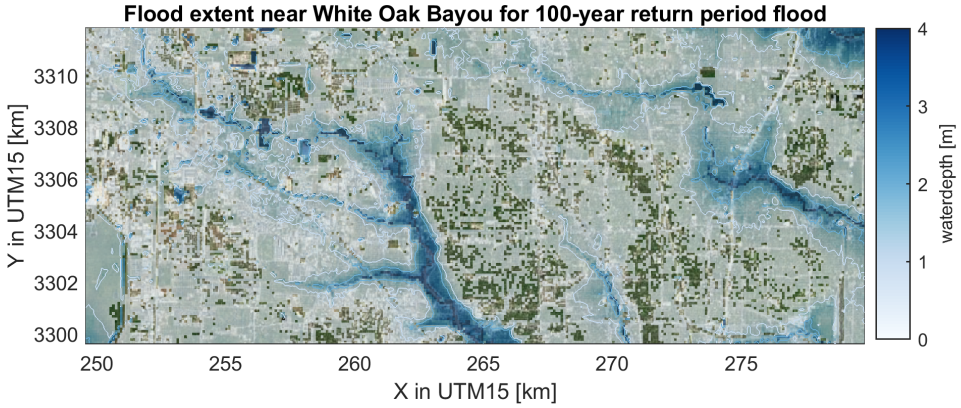

Figure C.11: The flood extent for a 100-year return period storm in the urban areas of Houston. Water depths lower than 0.15 m have not been plotted for visual purposes. Contour lines are given for the 1.0 and 2.0 m water depths.

Lastly, the flood extent near Greens Bayou is visualized in Figure C.12. Similar to White Oak Bayou, the Greens Bayou is seen as a floodway in the FEMA flood zone maps. This is recognized in the upstream part of the bayou (Y in UTM15 = 3,312 km), however not the entire bayou shows this behavior. Especially the lower branch seems to be lacking extreme water depths (X in UTM15 < 275 km), to be a floodway. Furthermore, the large flood extent as indicated by the 500-year flood plain map of FEMA is recognized when looking at the 1.0 and 2.0 m water depth contours. Nevertheless, the spatial variation of the precipitation shows that a wider area could potentially be affected by a 1 in 100-year flood event.

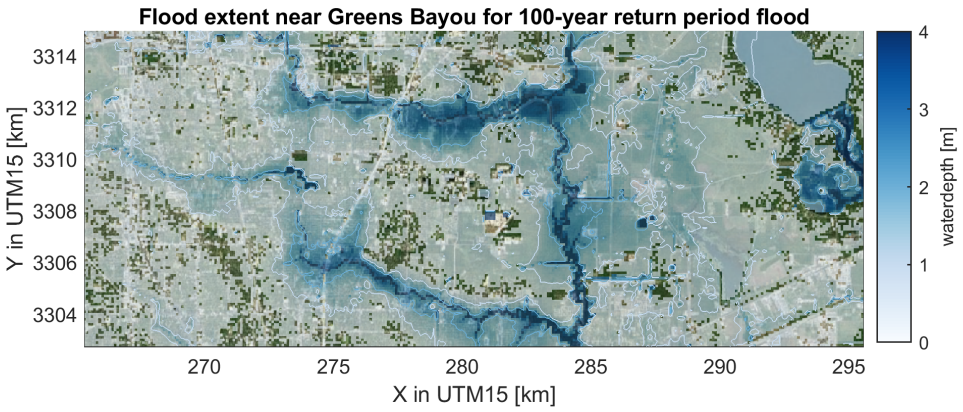

Figure C.12: The flood extent for a 100-year return period storm in the urban areas of Houston. Water depths lower than 0.15 m have not been plotted for visual purposes. Contour lines are given for the 1.0 and 2.0 m water depths.